Cooled Turbine Model

Development of a semi-empirical cooled turbine performance simulation model for aero engines

Gopal Kandiyoor

TU Delft

Delft
University of
Technology

Challenge the future

COOLED TURBINE MODEL

DEVELOPMENT OF A SEMI-EMPIRICAL COOLED TURBINE PERFORMANCE SIMULATION MODEL FOR AERO ENGINES

by

Gopal Kandiyoor

in partial fulfillment of the requirements for the degree of

Master of Science
in Aerospace Engineering

at the Delft University of Technology,
to be defended publicly on Friday 24th May, 2024 at 14:00

Cover: Acessed from Javier Vermaas under Unsplash License.

TUDelft Delft University of Technology

PREFACE

This thesis marks the end of my academic journey at TU Delft. The last 15 months have been a unique period in my life, full of learning and resilience. I am grateful for the vast support I have been lucky to receive throughout the process. A lot of thanks goes to my supervisory team: Carlo and Dabo, who I would like to thank for the numerous meetings, conceptual discussions, detailed feedback and useful suggestions. Their flexibility, and understanding made it possible for me to complete this thesis. I would also like to thank Matteo Pini for our exchanges on some of the challenges I encountered in the conceptual modelling involved in this work. Equally I would like to thank the entire team at NACO that made it possible for me to work there alongside my thesis. To Christine, Eoghan, Tom and Vivek, the understanding, flexibility and insights are something I truly appreciated in this period of my academic journey!

My time at TU Delft has been instrumental in shaping me both professionally and personally. There are numerous people to whom I owe a great deal of thanks for their endless support, friendship and advice. I want to specially thank those who have been there throughout this process (and prior) Alex, Aytek, Elena, Irmak, Kavya, Lorenzo, Manos, Manos, Mohammed, Octavian, Prajwal, Rahul and of course Reshma for always being my greatest supporters. I could not have finished this thesis without your support, encouragement and presence! I will carry the fond memories of our numerous days and nights filled with fun for many years to come.

Finally, my immense gratitude goes to my family, without whom none of this would have been possible. My heartfelt thanks go to my mother and father who have forever been my greatest source of strength and confidence. My brother, who continues to inspire me with his curiosity, drive and permanent ability to pick-up his phone regardless of the hour to lend a listening ear and offer splendid advice. This thesis is equally theirs as it is mine.

Gopal Kandiyoor
Delft, May 2024

ABSTRACT

A significant trend in aero engine design has been the rise in turbine inlet temperatures, as well as the drive to produce raise efficiency. Since the 1960s, turbine inlet temperatures have exceeded turbine material limits, with turbine cooling systems being used to bridge the gap. Modern engines require substantial amounts of cooling air, prompting a need to understand further the impact of turbine cooling on turbine and engine performance in cycle calculations.

Current models employed for performance analysis of cooled turbines are based on technical assumptions that are several decades old. This raises questions about the possibility of adapting models to more accurately represent modern engine technology. As such, this thesis aims to develop a cooled turbine model (CTM) for use in *PyCycle*, an open-source engine cycle analysis platform. The CTM is based on the cooled turbine blade row model defined by Young and Wilcox, which employs empirical constants to estimate cooling mass flow rates. The CTM can estimate the cooling flow requirements and the associated entropy rise for the turbine, accounting for the irreversibility in the turbine cooling process.

The implemented CTM models a complete turbine stage and multi-stage turbines based on three key aspects: the thermodynamics of a cooled turbine row, the work extraction in an equivalent uncooled turbine stage, and the conversion of thermodynamic properties between an absolute and rotating frame of reference. The CTM was verified and validated using three other cases, and it was found to accurately capture the effects of turbine cooling on bulk flow properties.

Following the implementation of the CTM, a study into the (semi-)empirical parameters and constants was performed to update existing parameters for modern engines. The limited availability of data relating to flow velocities and Mach numbers in aero-engine turbines forms a significant obstacle to the accurate specification of some empirical parameters. An estimation for the average Stanton number over turbine blades based on the gas temperature and Reynold's number was derived and validated with the Von Karman Institute's LS-89 turbine cascade results. The impact of updating the empirical parameters used in the CTM has been assessed by formulating the cooling flow estimation as an optimization problem. Using the updated ranges for the empirical parameters, the optimization study showed the potential for a significant reduction in the estimated cooling fraction.

CONTENTS

LIST OF FIGURES

LIST OF TABLES

NOMENCLATURE

ABBREVIATIONS

BPR	Bypass Ratio
CFD	Computational Fluid Dynamics
CET	Combustor Entry Temperature
COT	Combustor Outlet Temperature
CTM	Cooled Turbine Model
E3	Energy Efficient Engine
HPC	High Pressure Compressor
ICCT	International Council on Clean Transportation
LPC	Low Pressure Compressor
MDAO	Multidisciplinary Design, Analysis and Optimization
NGV	Nozzle Guide Vane
OPR	Overall Pressure Ratio
SC	Single Crystal
SLSQP	Sequential Least Squares Programming
TBC	Thermal Barrier Coating
TET	Turbine Entry Temperature
TIT	Turbine Inlet Temperature
Y&W	Young and Wilcox

SYMBOLS

Symbol	Definition	Unit
A	Area	m^2
Bi	Biot number	-
c	Chord	mm
c_p	Specific heat capacity	$J \cdot K^{-1} \cdot Kg^{-1}$
C	Absolute flow velocity	$m \cdot s^{-1}$
C_θ	Absolute tangential velocity	$m \cdot s^{-1}$
C_m	Meridional flow velocity	$m \cdot s^{-1}$
C_a	Axial flow velocity	$m \cdot s^{-1}$
FAR	Fuel to air ratio	-
$FACTOR$	Correction factor Gauntner model	-
h	Specific enthalpy	$J \cdot kg^{-1}$
$H_j^\circ(T)$	Enthalpy of chemical species as a function of temperature	$J \cdot kg^{-1}$
I	Momentum flux ratio	-
I_r	Specific rothalpy	$J \cdot kg^{-1}$
K_{comb}	Combustion pattern factor	-
K_{cool}	Cooling flow factor	-
K_{ext}	External flow parameter	-
K_{int}	Internal flow parameter	-
K_{swirl}	Rotor swirl factor	-
L	Length	m
m	Mass	kg
M	Mach number	-
M_c	Molar mass of Carbon	$g \cdot mol^{-1}$
M_H	Molar mass of Hydrogen	$g \cdot mol^{-1}$

M_O	Molar mass of Oxygen	$g \cdot mol^{-1}$
M_N	Molar mass of Nitrogen	$g \cdot mol^{-1}$
Nu	Nusselt number	-
o/c	Throat to chord ratio	-
P	Specific work	W
P_0	Total pressure	Pa
P_b	Airfoil perimeter	mm
Pr	Prandtl Number	-
Pt_{out}^{uc}	Total pressure at uncooled turbine stage outlet	Pa
Q	Heat transfer rate	$J \cdot s^{-1}$
R	Specific gas constant	$J \cdot K^{-1} \cdot mol^{-1}$
$R_{mass,i}$	Residual equation for minimization of Gibbs energy	-
$°R$	Degree of reaction	-
Re	Reynolds number	-
s	Specific entropy	$J \cdot K^{-1} \cdot Kg^{-1}$
St_g	Stanton number	-
$S_j^°(T)$	Entropy of chemical species as a function of temperature	$J \cdot K^{-1} \cdot Kg^{-1}$
T	Temperature	K
U	Blade velocity	$m \cdot s^{-1}$
V	Velocity	$m \cdot s^{-1}$
w	Relative flow velocity	$m \cdot s^{-1}$
$\dot{w}$	Mass flow rate	$kg \cdot s^{-1}$
w_c^+	Dimensionless cooling fraction - Holland and Thake	-
WT_{uc}	Work transfer of an uncooled turbine stage	W
w_c^+	Dimensionless cooling fraction - Holland and Thake	-

GREEK LETTERS

Symbol	Definition	Unit
α	Absolute flow angles	$deg°$
β	Relative flow angles	$deg°$
β_{uc}	Uncooled turbine stage pressure ratio	-
phi	Flow coefficient	-
Φ	Flow injection angle	$deg°$
δ	Change in variable quantity value	-
ΔP_t	Change in total pressure	Pa
$\Delta \Sigma$	Irreversible entropy creation rate	$J \cdot kg^{-1} \cdot K^{-1}$
ϵ_f	Film cooling effectiveness	-
$\eta_{c,int}$	Internal cooling efficiency	-
η_{cooled}	Cooled turbine efficiency	-
η_{is}^{uc}	Uncooled turbine stage isentropic efficiency	-
γ_c	Ratio of specific heats	-
μ	Dynamic viscosity	$kg \cdot m^{-1} \cdot s^{-1}$
Ψ	Stage loading coefficient	-
ρ	Density	$kg \cdot m^{-3}$
ζ	Equivalence ratio	-
ω	Angular frequency	$rad \cdot s^{-1}$
$\Omega^{(2,2)}$	Reduced collision integral	-
Ω_{stage}	Stage total cooling fraction	-
λ	Thermal conductivity	$W \cdot m^{-1} \cdot K^{-1}$
ΔT_{cc}	Combustor temperature rise	K
ϵ_0^{max}	Required cooling effectiveness	-
ϵ_0^{asymp}	Asymptotic cooling effectiveness	-
ϵ_0^{min}	Minimum cooling effectiveness	-
ϵ_f	Film cooling effectiveness	-

$\phi_{gauntner}$	Cooling effectiveness Gauntner model	-
σ	Molecular diameter	m
χ	Coolant to gas flow ratio	-

SUBSCRIPTS

Subscript	Definition
0	Total quantities
AP	Approach
aw	Adiabatic wall
b,rel	Relative blade (temperature)
c	Coolant
CO	Climb out
ext	External
F	Friction
g	Gas
$*$	Flow stream throat
i	Coolant condition at blade entry
ID	Idle
is	Isentropic
k	Coolant condition at bleed location
m or met	Metal
m,ext,eff	External effective metal temperature
m,int	Internal metal temperature
$mix(ed)$	Mixing or Mixture
q	Heat transfer
r	Radial
r,max	Maximum radial
$surf$	Surface
$stoich$	Stoichiometric
tbc	Thermal barrier coating
TO	Take-off
w	Wall
x	Coolant condition at blade exit

MOLECULES

O_2	Oxygen
N_2	Nitrogen
CO_2	Carbon Dioxide
H_2O	Water
CH_4	Methane
$C_{10.8}H_{21.6}$	Jet A1
$C_{12}H_{23}$	Kerosene

1

INTRODUCTION

1.1. PROBLEM BACKGROUND

In an increasingly connected world, aviation is a vital sector, often considered to be a driving factor in global prosperity [41]. At present, the sector is estimated to account for approximately 3% of global carbon emissions [42]. Passenger traffic is projected to grow at an average of 3.6% per year, up to 2042 [43]. In the face of this continuous growth and as a consequence of emissions reduction strategies being implemented in other sectors, aviation could account for 40-50% of global carbon emissions in the following decades [44].

For aviation to achieve net-zero carbon emissions in the coming decades, two distinct strategies are available. The first is the further improvement of existing aircraft by adopting advanced technologies and better exploiting of manufacturing techniques and operational practices. An example is the retrofit of existing air frames such as the case of Ryanair's 737-800 fleet, modified to include split scimitar winglets in 2023. The airline claims the retrofit will improve fuel efficiency by 1.5%, resulting in an annual carbon emissions saving of 165,000 tonnes [45].

A second example of incremental improvements in efficiency is that of the jet engine. The International Council on Clean Transportation (ICCT) indicates that fuel burn of jet engines dropped 45% between 1968 and 2014, [46] thanks to continuous improvements in technology in a compounded way.

Complementary to incremental improvement in aviation technology, are disruptive innovations. In particular, in recent years, the development of radically new propulsion systems fuelled by hydrogen or new air frames such as blended wing bodies have begun. A key example of such disruptive innovation is the blended wing body, hydrogen fuelled ZeroE concept by Airbus, expected to enter service by 2035 [47]. Combustion of hydrogen is free from carbon emissions, marking a quantum leap in emissions reduction for aviation propulsion systems.

While disruptive innovations have a high potential to reduce carbon emissions and reduce overall climate effects, the technology required is not currently ready for widespread use. The technical maturity and market adoption of these innovative technologies is dependent on various factors including commercial and operational feasibility. Until innovative technologies are adopted widely, incremental improvements to existing technology will be required. An existing technology expected to be suitable for such incremental improvement is the aero-engine gas turbine.

A key trend in the design of gas turbines is the sustained increase in the turbine inlet temperature [1]. The driver for this increase is the link between turbine inlet temperature and power output. The evolution of turbine inlet temperatures over time is exemplified in Figure 1.1.

However, while turbine inlet temperatures have increased, material capabilities have remained limited by comparison, as shown in Figure 1.2.

Figure 1.2 shows that turbine inlet temperatures have grown significantly faster than material capabilities, particularly since the 1970's. The reason lies in the advancements achieved in the cooling technology of turbine blades.In order to address the challenge of turbine inlet temperatures exceeding blade metal capabilities, turbine cooling systems are used. A variety of configurations exist, with the aim of protecting the material integrity of the turbine's blades. The materials used in modern turbines influence the design of cooling systems significantly. For modern aircraft engines, blade lifetime is of high importance due to the high operating costs associated with their replacement [48]. Blades used in turbines face various sources of
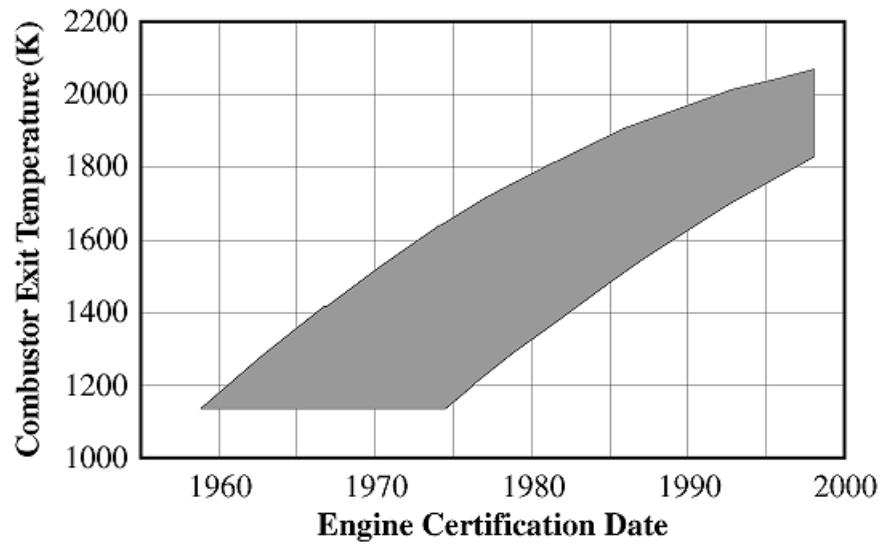
Figure 1.1: Growth of turbine inlet temperature over time [1]
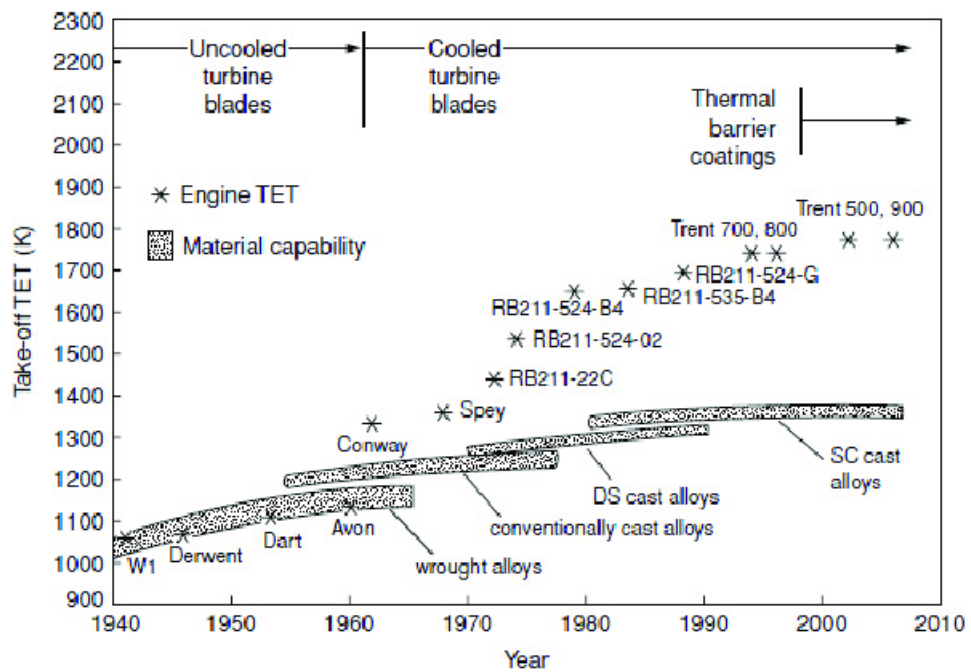
Figure 1.2: Evolution of take-off turbine inlet temperatures and material capabilities for Rolls Royce engines [2]

loading, which can be categorised into three main groups. These are: centrifugal loads, bending loads and vibrational effects [4]. In addition to this, high temperature conditions often drive failure through thermal creep [49].

The cooling air requirement can be significant, and have a quantifiable impact on the efficiency of the turbine. Kurzke indicates the importance of quantifying turbine cooling air requirements, due to the strong coupling to eventual fuel burn [15]. Young and Wilcox [17] present a model to calculate the required coolant fraction as well as irreversible entropy creation rates associated with cooling a single blade row. It is found to be one of the few turbine cooling models that directly quantify entropy creation rates, and this is of significant interest as it allows for immediate recognition of the cause of potential inefficiency in the cooling system.

Therefore, considering the desire to develop more powerful and efficient engines, it is of importance that the exact performance of engine concepts can be modelled. Particularly the turbine cooling system can penalize engine performance, therefore highlighting the need to consider the impact of this system earlier in the engine design process, at cycle design level. Furthermore, the increasing trend of using optimization in aircraft and engine conceptual design [50] highlights the need for the compatibility between engine and cycle design models and general optimization frameworks.

Therefore, motivated by these trends, the aim of this thesis is to implement a cooled turbine model into an engine cycle analysis platform. The target outcomes of such analysis are twofold, firstly the cooling flow requirement for a given turbine stage row, and secondly the stage performance degradation as a result of cooling. *PyCycle* is an open-source tool, providing a common platform for researches to evaluate novel engine design concepts and is the platform that will be used in this thesis.

1.2. Research Objective

The research objective is:

Developing a cooled turbine model for use in engine cycle analysis and optimization through implementation and adjustment of an entropy based approach to turbine cooling related performance degradation

The chosen method to investigate the research objective is through numerical modelling in *PyCycle*, a python based cycle analysis library [12].

1.3. Research Questions

In order to answer the research objective, the following research (sub-) questions have been formulated.

1. What is the state of the art in gas turbine blade cooling performance modelling?

   - What are various approaches that can be used to predict cooling mass flows?
   - What approaches can be used to predict efficiency degradation due to turbine blade cooling?

2. How sensitive are turbine cooling performance models to various parameters?

   - Which parameters drive the cooling mass flow requirements for turbine blade rows?
   - What is the sensitivity of turbine cooling models to design parameters?
   - What is the sensitivity of turbine cooling models to empirical parameters?

3. How can an entropy based performance degradation model be tuned to predict cooling system performance in aero-engine gas turbines?

   - What empirical and experimental data must be available to such a model?
   - What is the effect of tuning empirical parameters with modern gas turbine data on the accuracy of cooling flow estimations?

1.4. Thesis Overview

The thesis is structured as follows. In chapter 2, an overview of the theoretical background relevant to turbine cooling is presented. This overview includes an introduction to the modelling framework used in this thesis, *PyCycle*. Following this, chapter 3 presents the theoretical framework used to develop the cooled turbine model (CTM), specifically the model used to predict cooling flow requirements and performance degradation. Subsequently, chapter 4 presents the implementation and development of the cooled turbine model.

Verification and validation of the cooled turbine model are presented in chapter 5. Following this, chapter 6 deals with the assessment of the the numerous empirical parameters required to accurately model turbine cooling needs and performance effects. Key conclusions and recommendations are outlined in chapter 7.

2

GAS TURBINE COOLING & PERFORMANCE MODELLING

There are a number of factors that must be accounted for in the modelling of a cooled turbine for cycle calculations and optimization. The first is regarding the composition of the working fluid, shown in section 2.1. Following this, the main principles of preliminary design of turbine stages are discussed and the related duty coefficients are defined in section 2.2. Following this, an overview of turbine cooling techniques used in modern gas turbine engines is presented in section 2.3. Subsequently section 2.4 discusses a number of models found in literature that can be used to estimate required cooling flows and cooled turbine performance. The modelling framework, $OpenMDAO$, used in this thesis, as well as the engine modelling library $PyCycle$ are outlined in section 2.5. Finally, section 2.6 presents the development of a modelling component within $PyCycle$ required for the implementation of a cooled turbine model.

2.1. GAS COMPOSITION IN TURBINES

The turbine inlet temperature is dependent on the temperature of the combustion products in the combustion chamber. The most commonly used fuel used in aero-engine gas turbines is known as Jet-A1 [51]. Jet-A1 is a hydrocarbon fuel similar to kerosene, with a composition that has been defined by Wang [52, 53] as:

$$C_{10.8}H_{21.6}$$
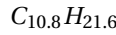
The amount of fuel used in the combustion chamber can be described using the fuel to air ratio, FAR, defined as the mass ratio of fuel to air, namely:

$$FAR = \frac{m_{fuel}}{m_{air}} \tag{2.1}$$

Another term commonly used to represent the quantity of fuel used is the equivalence ratio, ζ. The equivalence ratio represents the ratio of the fuel to air ratio present in a fluid, to the stoichiometric fuel to air ratio, namely:

$$\zeta = \frac{FAR_{mixture}}{FAR_{stoich}} \tag{2.2}$$

The stoichiometric fuel to air ratio of a fuel represents the FAR required for complete combustion. For Jet-A1 the combustion equation in air, modelled as an oxygen nitrogen mixture, reads:

$$C_{10.8}H_{21.6} + (O_2 + 3.76N_2) \rightarrow CO_2 + H_2O + N_2 \tag{2.3}$$
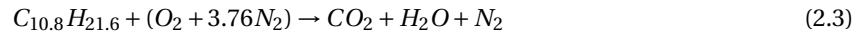
When balanced, this equation yields:

$$C_{10.8}H_{21.6} + 16.2(O_2 + 3.76N_2) \rightarrow 10.8 \cdot CO_2 + 10.80 \cdot H_2O + 121.82 \cdot N_2 \tag{2.4}$$
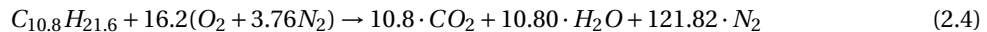
From this equation, the stoichiometric fuel to air ratio of Jet-A1 is calculated given the molar mass of each species (M):

$$FAR_{stoich,JetA1} = \frac{10.8M_C + 21.6M_H}{16.2 \cdot (2M_O + 2 \cdot 3.76M_N)} \tag{2.5}$$

Species	Molecular Mass [g/mol]
Carbon (C)	12.0107
Hydrogen (H)	1.00794
Oxygen (O)	15.9994
Nitrogen (N)	14.0067

Table 2.1: Molecular Mass of Various Species [28]
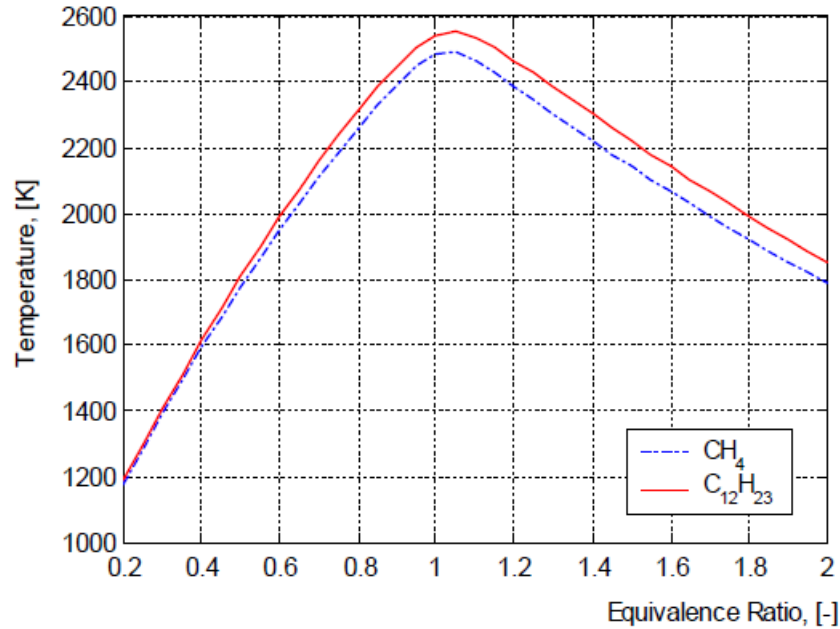
Figure 2.1: Variation in flame temperature with equivalence ratio [3] for Methane and $C_{12}H_{23}$. T = 700 Kelvin, P = 2.8 MPa

Using molecular mass values shown in Table 2.1. It results

$$FAR_{stoich,JetA1} = \frac{10.8M_C + 21.6M_H}{16.2 \cdot (2M_O + 2 \cdot 3.76M_N)} = 14.685 \tag{2.6}$$

Therefore, a stoichiometric fuel to air ratio for JetA1 is approximately 14.7. The equivalence ratio of the mixture in the combustion chamber is linked to the adiabatic flame temperature achieved, shown in Figure 2.1 for methane (CH_4) and $C_{12}H_{23}$, another common representation of the molecular composition of kerosene.

It is clear that for rich mixtures (ζ >1) the temperature peaks, before showing a decline in temperature. For lean mixtures where ζ is less than unity, temperature increases with increasing equivalence ratios. The influence of air temperature on the adiabatic flame temperature is shown in Figure 2.2 for methane. Furthermore, it can be seen that pressure has limited influence.

In aircraft engines, the equivalence ratio falls within a narrower band than the range shown in Figure 2.1 and Figure 2.2.For a given temperature, pressure and massflow delivered by the compressor system, there are extinction limits [54]. These are conditions where the combustion process stops, These can occur for both rich and lean conditions. Further discussion on typical equivalence ratios in modern engines will be presented in section 6.3. In general, the turbine inlet temperature will be lower than the highest adiabatic flame temperature achieved for a given ζ, due to the addition of air in secondary and tertiary combustor zones. Nonetheless, a higher temperature in the combustor is the driver for increased turbine inlet temperatures.

2.2. DESIGN OF TURBINES & DUTY COEFFICIENTS

Turbine stages consist of two blade rows, with the first a stationary row of stators, and the second a moving row of rotors. Stators in turbine stages are also known as nozzle guide vanes (NGV) [4]. The function of the
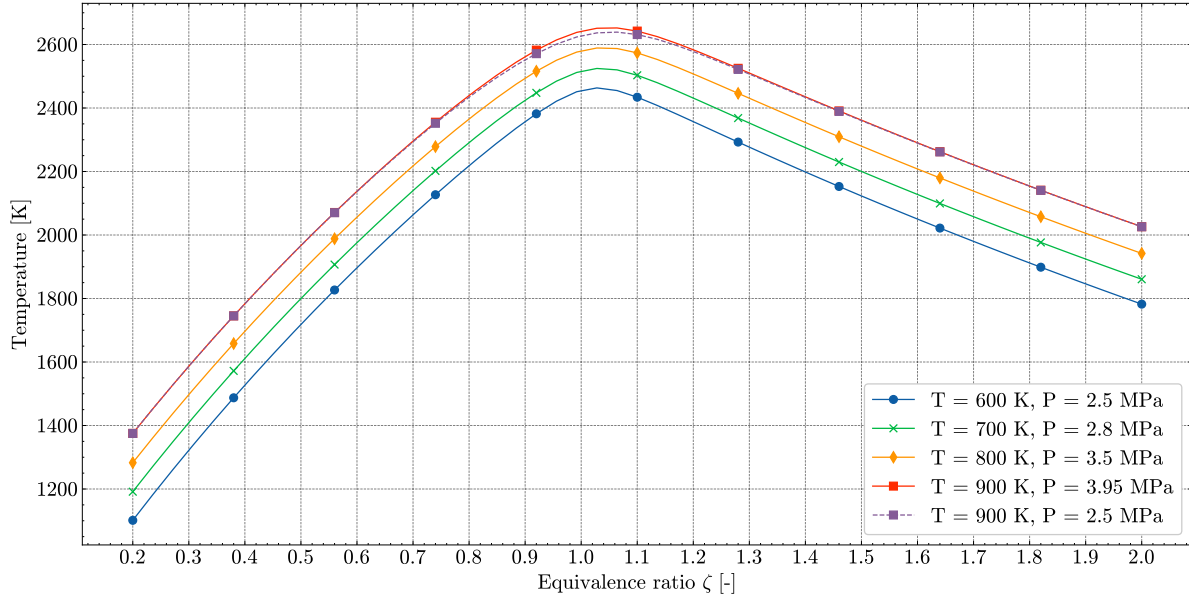
Figure 2.2: Variation in adiabatic flame temperature for combustion of methane in varying conditions. Air temperatures vary from 600 K to 900 K representing typical compressor delivery conditions. Calculated using *Cantera*.

stator rows is to add swirl to the incoming flow, and convert internal energy in to kinetic energy, while the rotor transforms this kinetic energy in work. [55].

The velocity diagram of an axial turbine stage is shown in Figure 2.3. Three stations are defined, 1 corresponds to stage inlet, 2 corresponds to inter-row and 3 is the stage outlet. Velocities in the absolute frame of reference are indicated with c, while the angle they form with respect to the axial direction is denoted by α. Relative velocities are denoted by w and the corresponding angles by β. The blade speed, U is the product of the rotational velocity of the turbine ω and the blade radius of interest.

Three duty coefficients are used extensively in the turbine design process [56]. The first is the stage loading coefficient, Ψ, representing the ability of the stage to perform work [57]. It is defined as the ratio of specific work, P, to the square of the blade velocity, U:

$$\Psi = \frac{P}{\dot{m}_g \cdot U^2} \tag{2.7}$$

The second is the flow coefficient, Φ, defined as the ratio of the absolute inlet velocity, C_1, see Figure 2.3, to the blade velocity, U, namely:

$$\Phi = \frac{C_1}{U} \tag{2.8}$$

The final parameter is the degree of reaction, $°R$, defining the fraction of the expansion occuring in the rotor compared to the total expansion [56]. It is often defined on the basis of static temperature or enthalpy, namely:

$$°R = \frac{T_2 - T_3}{T_1 - T_3} \tag{2.9}$$

In a turbine stage where the axial velocity C_a is constant, the duty coefficients can be expressed as a function of the flow angles [56], as:

$$°R = \frac{\Phi}{2}\left(\tan\beta_3 - \tan\beta_2\right) \tag{2.10}$$

and

$$\Psi = 2\Phi\left(\tan\beta_2 + \tan\beta_3\right) \tag{2.11}$$

Additionally, the flow coefficient and stage loading coefficient can be used to describe the isentropic efficiency of a stage, based on the Smith chart [4], shown in Figure 2.4. The figure presents lines of constant isentropic efficiency for combinations of Ψ and Φ. It is apparent that the highest efficiencies are obtained for low values of Φ and Ψ. However, Saravanamutto [56] points out that low Ψ requires more stages for the
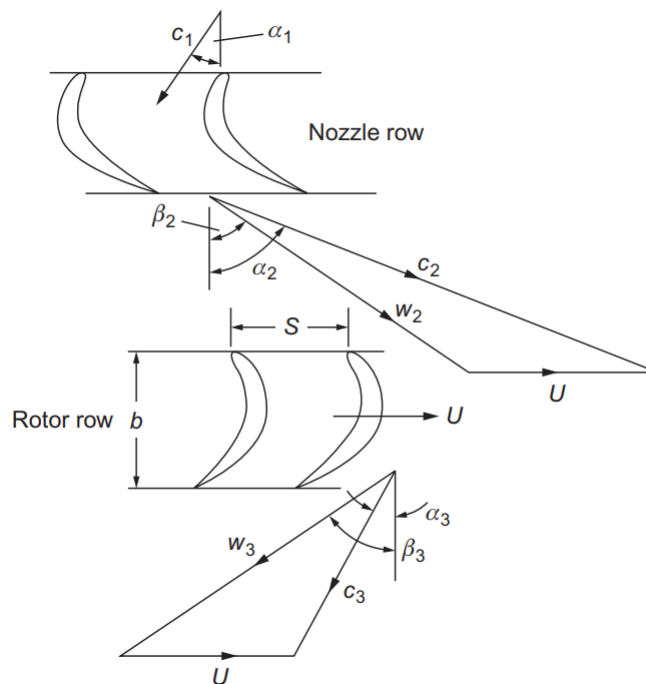
Figure 2.3: Velocity diagram for an axial turbine stage [4]

same work output of a turbine, and a low flow coefficient requires a larger turbine cross-section area . Typical values of Ψ range from 1.5 to 2.5 while typical Φ values are in the range 0.8 to 1.0 for current aircraft engines [56].

2.3. Turbine cooling techniques

Having addressed the aerodynamic design of turbines, this section presents an overview of common methods used to bridge the gap between material temperature limits and gas temperatures. The significant development of cooling systems used in gas turbines over time is shown in Figure 2.5, highlighting the corresponding growth in turbine inlet temperatures. While numerous cooling methods have been proposed, including the use of water/steam injection, air cooling is the most widely used form of blade cooling [58]. The air used to cool turbines is typically sourced from the compressor system, as coolant air must be delivered at an equivalent or slightly higher pressure than the gas pressure in the turbine [4]. Cooling air is used to cool blades and other elements of the turbine system including disks, seal segments and end walls [59]. Within air cooling techniques, a distinction can be made between internal and external cooling of turbine blades. The detailed mechanisms of heat transfer associated with each cooling technique are considered beyond the level of detail required for thermodynamic cycle calculations and will not be elaborately discussed. A range of literature exists describing these mechanisms including the work of Lakshminarayana [58], Han [6], as well the National Energy Technology Lab [7].

Internal cooling, typically applied for when gas temperatures are between 1300 and 1600 K [58], includes convection cooling and jet impingement cooling. Furthermore, convection cooling can be split into two sub-categories, namely rib-turbulated and pin-fin cooling [23]. A cross-section of a modern, internally cooled turbine blade is presented in Figure 2.6 [6].

The internal channels shown in Figure 2.6 showcase the complex internal geometry of a cooled blade. The rib-turbulated channels use a variety of shapes to raise convective heat transfer. Examples of rib configurations are shown in Figure 2.7.

The increased heat transfer is achieved in two ways, the first being the larger heat transfer surface and the second the increase in turbulence. An increased turbulence level has been shown to increase the heat transfer coefficient in internal cooling channels[60]. The quantity generally used to describe heat transfer is
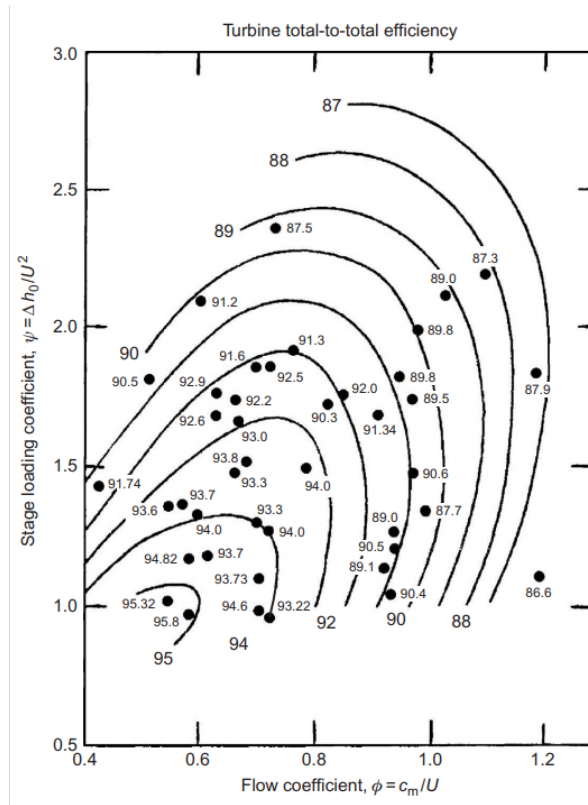
Figure 2.4: Smith chart showing lines of constant turbine stage isentropic efficiencies as a function of the flow coefficient, Φ and stage loading coefficient Ψ [4].
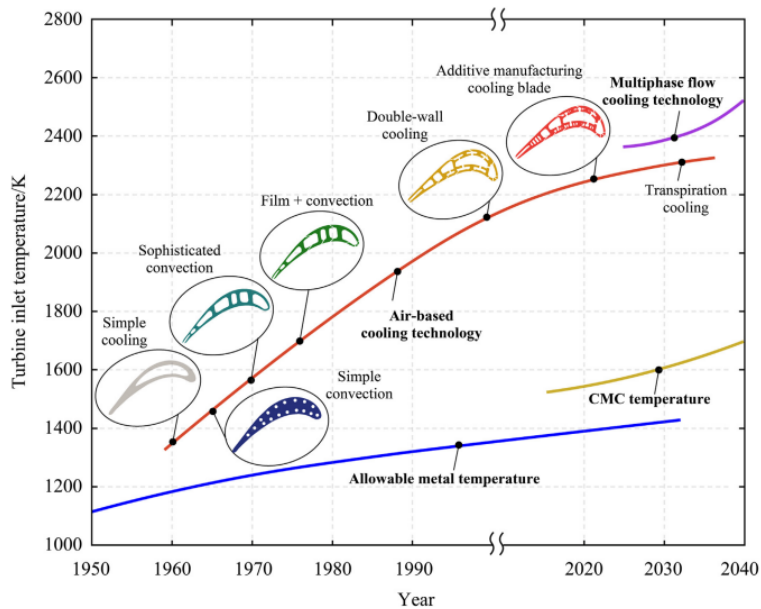
Figure 2.5: Development in cooling technologies over time [5]
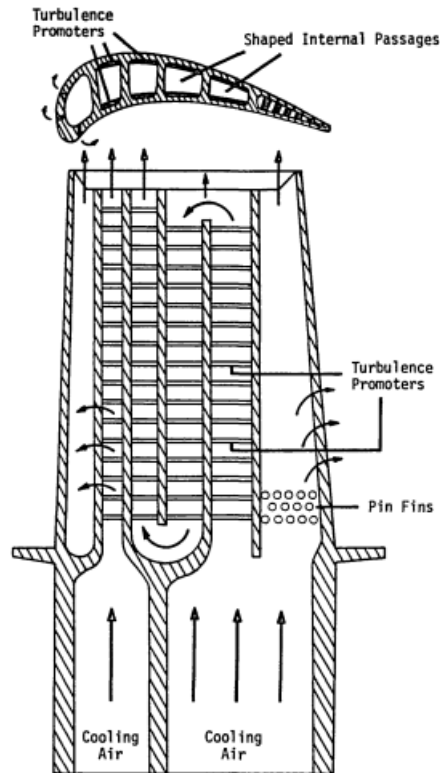
Figure 2.6: Cross section of a modern, internally cooled gas turbine blade [6].
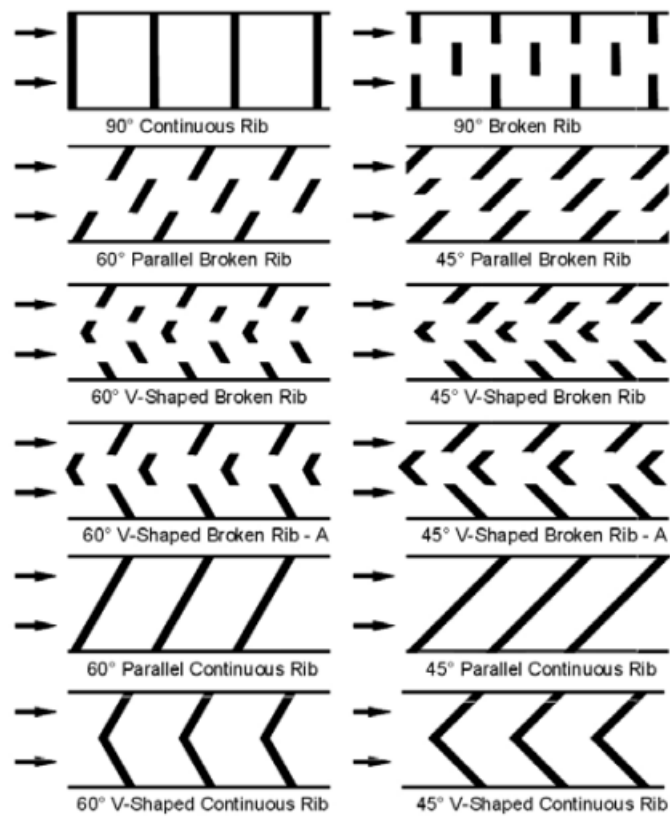
Figure 2.7: Rib turbulator shapes for internal cooling [7]
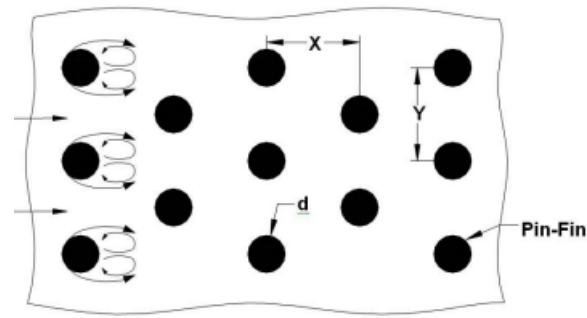
Figure 2.8: Schematic representation of pin-fin cooling array [7]
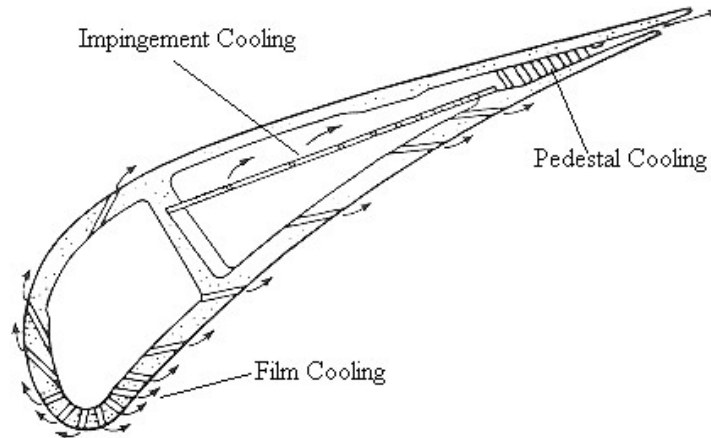
Figure 2.9: Turbine blade with impingement and film cooling [8].

the Nusselt number, Nu, a dimensionless heat transfer coefficient [61]. It is defined as:

$$Nu = \frac{h_c \cdot L}{k} \tag{2.12}$$

where h_c is the convective heat transfer coefficient, L is a characteristic length and k is the thermal conductivity of the fluid. Due to the complexity of the flow in the cooling channels, Nusselt numbers are typically calculated based on experimental data and semi-empirical correlations. In addition to the heat transfer, internal cooling channels with rib turbulation result in a pressure drop of the coolant flow, due to separation and reattachment of the flow over ribs. This pressure drop is also observed for pin-fin cooling.

Pin fin cooling is typically used in the trailing edge region of turbine blades [7], where manufacturing constraints may prevent the use of ribs or cooling channels. Pins can be used to promote the creation of horseshoe vortices, enhancing mixing, see in Figure 2.8. Additionally, Tiemstra [31] notes the importance of the spanwise position at which the coolant flow is injected into the bulk flow. Coolant flows used in pin fin arrays are injected into the bulk flow through a slot at the trailing edge of the blade. The shape of the slot can vary. The shape and location of the slot can influence the heat transfer within the array of pin-fins, with Lau et. al,[62] concluding that ejection of the cooling flow closer to the root of the blade results in a lower heat transfer coefficient.

The third internal cooling technique is jet impingement. With this technique, air is sprayed onto the inner wall of the blade. It can be applied locally, with one single spray orifice (nozzle) or multiple orifices arranged in an array [32]. An example of an impingement-cooled blade is shown in Figure 2.9. It can be seen that the flow used to impinge on the blade wall exits the blade through film cooling holes or a trailing edge slot, as with pin-fin or rib turbulated cooling channels. This cooling technique is usually used in areas of high thermal load due to the high heat transfer coefficients that can be achieved by jet impingement [56].

External cooling techniques aim to reduce the overall heat flux into the turbine blade. This can be achieved through film cooling and/or transpiration cooling [58]. Transpiration cooling is not widely used in aircraft engines [56] and therefore this discussion will only focus on film cooling.
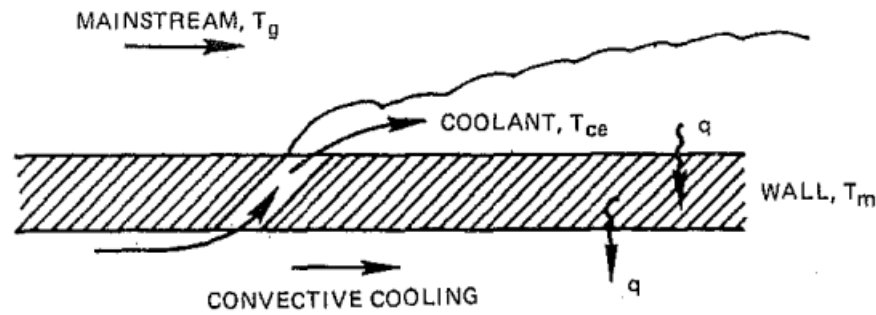
Figure 2.10: Simplified representation of film cooling in turbine blades [9].

Film cooling is typically used when gas temperatures exceed 1600 K [58]. As seen in Figure 2.9, film cooling can be applied locally with a single row of holes at a chord wise location, or over the entire blade section. The fundamental principle of film cooling is to introduce a barrier of cold air over the blade surface to protect this from the gas. The use of film cooling causes an interaction between the cooling flow and the gas flow as seen in Figure 2.10 resulting in a reduction in the heat flux into the blade. Additionally the effect of film cooling is a loss of total pressure over the cooled blade, due to mixing losses between the coolant and gas flow streams. The magnitude of this can vary depending on the amount of coolant flow and the pressure of both flow streams [63].

The performance of a film cooling system is described by the film cooling effectiveness, ϵ_f, whose definition is based on the temperature difference between the gas, T_g and the adiabatic wall temperature, T_{aw}, normalized by the temperature difference between the gas and coolant flows, T_c. This is:

$$\epsilon_f = \frac{T_g - T_{aw}}{T_h - T_c} \tag{2.13}$$

Film cooling effectiveness can vary significantly over a blade, as seen from Figure 2.11. The figure shows the local variation in ϵ_f around a row of 3 film cooling holes, and shows that the influence of film cooling is highest in proximity of the hole, and it reduces as the distance increases. Furthermore, a stronger decrease in ϵ_f is noted at the edges of the film cooling jet, shown by the sharpening of each ϵ_f contour with increased distance from the hole.

The value of ϵ_f is impacted significantly by the momentum flux ratio, I, defined as:

$$I = \frac{\rho_c V_c^2}{\rho_g V_g^2} \tag{2.14}$$

where ρ represents the density and V is the flow velocities of the coolant and gas indicated with the subscripts c and g, respectively. Based on the work of Sinha [64] the value of I is related to the capability of the film cooling jet to remain attached to the blade surface. For I less than 0.4, the film jet remains attached throughout, while for I between 0.4 and 0.8 the jet separates and then reattaches. Finally, for higher values of I, the film is fully separated. For this reason, the film cooling effectiveness is observed to reduce with I [31].

2.4. EXISTING TURBINE COOLING MODELS

Much experimental work on turbine cooling was performed from the late 1940's onwards, such as that of Lewis at NASA [65]. Following this, the first civil engines to make use of cooled turbines were the Tyne and Conway, developed by Rolls Royce [66], followed by the Spey, throughout the 1950's and 1960's. However, the competitive advantage afforded to commercial parties developing cooled turbines for aero-engines meant that models capable of predicting cooled turbine performance often remain(ed) classified, with limited access for scientific use. By the early 1970s, simplified models were developed. A brief overview of some of the major models used to describe cooled turbine performance is presented in Table 2.2. In order to understand the similarities and differences between these models, as well as the increase in model fidelity over time, each model is discussed further, from subsection 2.4.1 to subsection 2.4.4. The Young and Wilcox model implemented in this thesis is discussed at length in chapter 3 and will not be discussed at length in this section.
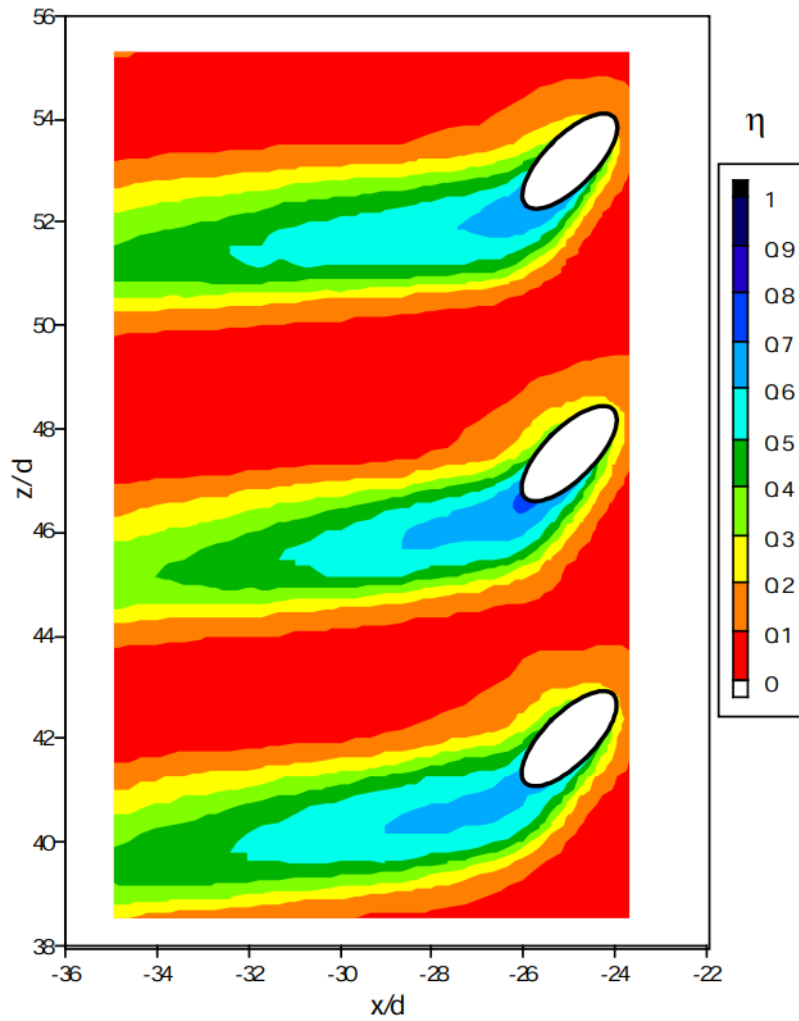
Figure 2.11: Variation in film cooling effectiveness surrounding film cooling holes on a turbine blade [7].

Cooling Model	Year of Publication	Country
Saravanamuttoo	1972	Canada
Holland & Thake	1980	UK
Gauntner	1980	USA
Massardo	2001	Italy/Sweden
Young & Wilcox	2002	UK

Table 2.2: Tabulated overview of major cooled turbine models

A brief summary of the models found in literature and their differences compared to the model implemented in this thesis is presented in subsection 2.4.5.

2.4.1. Saravanamuttoo's Cooled Turbine

The first, publicly available, model is that of Saravanamuttoo [56]. The model identifies two key issues with respect to cooled turbine performance. The first is defining the required amount of cooling air flow, and the second is the effect of cooling on turbine performance.

The first consideration is addressed through the use of a parameter known as the blade relative temperature, $T_{b,rel}$, defined as the ratio of two temperatures differences:

$$T_{b,rel} = \frac{T_b - T_{cr}}{T_g - T_{cr}} \tag{2.15}$$

Where T_b is the average temperature of the blade, T_g is the effective gas temperature (relative in the case of rotors), while T_{cr} is the temperature of the coolant at the entry of the blade, typically the root. The coolant flow rate required m_c is calculated by solving:

$$T_{b,rel} = 1 - \frac{e^{\frac{kl}{L}}}{1 + \frac{h_g S_g}{h_c S_c}} \tag{2.16}$$

where:

$$k = \frac{h_g S_g L}{m_c c p_c \left(1 + \frac{h_g S_g}{h_c S_c}\right)} \tag{2.17}$$

In this equation, h refers to the heat transfer coefficient, L is the blade length, l is the location along the blade length at which the cooling requirement is being calculated and S indicates the wetted perimeter area. For the gas, S_g is simply the blade perimeter, but for the coolant S_c refers to the perimeter of all internal coolant channels. Saravanamutto's model [56] requires the user to establish a target value of $T_{b,rel}$ and thereafter calculate the value of the cooling flow rate, m_c that allows this to be achieved at various spanwise locations along the blade, l/L. The model requires information about the internal blade geometry and heat transfer coefficients. In addition, this model does not quantify the influence of turbine cooling on the turbine performance.

2.4.2. Gauntner Cooling Model

The second model is that of Gauntner [22]. Apostolidis categorises this model as being fully empirical [67]. The model presents a series of empirical factors calibrated based on an experimental data set involving a fully film cooled turbine blade. This is one of the first models that is able to assess both the required cooling air fraction as well as the effect of cooling on turbine efficiency. The model quantifies the reduction in efficiency due to cooling by using empirical factors. For this purpose, the model assumes that all stages in multiple stage turbines have equal pressure ratios [22].

The Gauntner model calculates cooling fraction as a function of cooling effectiveness, namely:

$$\frac{m_c}{m_g} = Factor \cdot 0.022 \cdot \left(\frac{\phi_{gauntner}}{1 - \phi_{gauntner}}\right)^{1.25} \tag{2.18}$$

where $\phi_{gauntner}$ represents the cooling effectiveness,calculated as:

$$\phi_{gauntner} = \frac{T_g - T_m}{T_g - T_c} \tag{2.19}$$

The term *Factor* is specified discretely and varies between 0.8 and 2.0 depending on the adopted cooling technology, namely:

- A value between 1.4 and 2.0 represents blades cooled by internal convection with no film cooling. 1.5 represents an internally convection cooled blade with a thermal barrier coating.

- A value between 1.0 and 1.3 represents blades with film and internal convection cooling.

- Values between 0.8 and 0.9 represent blades that are transpiration cooled.

In addition to estimating the required cooling fractions, the model determines the cooled stage efficiency accounting for the additional fluid dynamic losses occuring in the stator and rotor due to blade cooling. The efficiency penalty is proportional to the cooling flow. The equation used for a stage is:

$$\eta_{cooled} = \eta_{uncooled} - \eta_{uncooled} \cdot \frac{m_c}{m_{g\;s}} \cdot K_{stator} - \eta_{uncooled} \cdot \frac{m_c}{m_{g\;r}} \cdot K_{rotor} \tag{2.20}$$

K_{stator} and K_{rotor} are the empirical factors tabulated by Gauntner [22] for each value of *Factor*. This model has been implemented at Delft University of Technology and will be used as a benchmark for the cooled turbine model developed in this thesis.

2.4.3. HOLLAND AND THAKE COOLING MODEL
The next model considered is the model by Holland and Thake, two Rolls Royce engineers, published in 1980 [10]. The model aims to estimate the required cooling fraction for a turbine blade, through the calculation of the non-dimensional mass flow coefficient w_c^+. The parameter is defined as:

$$w_c^+ = \frac{w_c cp_c}{h_g S_g l_g} \tag{2.21}$$

where w_c represents the coolant flow rate, h_g the heat transfer coefficient, S_g the blade surface area, and l_g the length of the blade.This parameter is used in other turbine blade cooling performance models as well, including that of Young and Wilcox, developed two decades later [17]. The model by Holland and Thake determines the cooling mass flow rate given the target blade temperature. Exemplary calculations and data points associated with Rolls Royce engines are shown in Figure 2.12.

However, the empirical factors required to calculate the mass flow are based on the Rolls Royce Spey and RB 211 engines operational at the time of publishing. Engines have changed significantly over time, thus making this model not the most optimal for modern engines [68]. Additionally, the model does not address the issue of turbine performance degradation.

2.4.4. MASSARDO COOLING MODEL
Another popular model is that developed by Massardo and Torbidoni. The model extends that of Holland and Thake described earlier, by integrating features of the model derived by Consonni [69, 70].

The coupled model provides significant insight into turbine blade cooling mass flow requirement and the total pressure loss. The authors claim the model is highly predictive also for alternative fluids other than exhaust gases, which may well prove a unique characteristic. Massardo's model is dependent on a parameter Z, whose value varies with the technology level of the blade [70]. It should be noted that this model also quantifies efficiency degradation through pressure drop. However, the complexity associated with this model makes it unfeasible to implement in PyCycle.

2.4.5. DISCUSSION
Following on from the numerous turbine blade cooling models, Young and Wilcox of the Whittle Laboratory in Cambridge developed a framework for the analysis of cooled gas turbines [17]. The main difference compared to other cooling models is the use of entropy creation to quantify performance losses, as opposed to the total
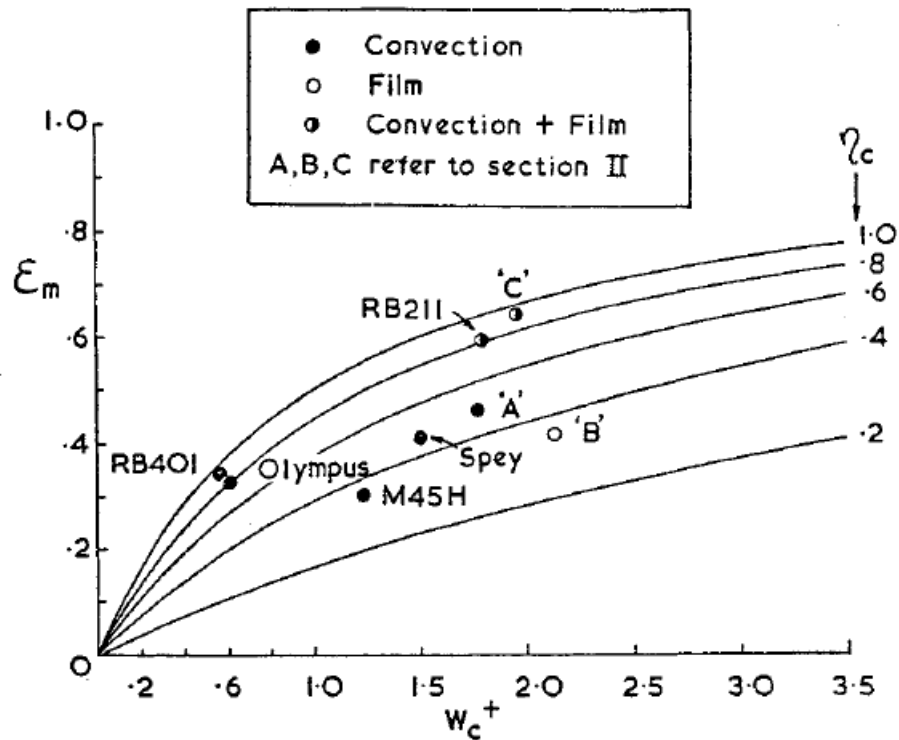
Figure 2.12: Cooling performance curves based on Holland and Thake cooling model, data points represent Rolls Royce engines [10].

pressure loss or efficiency penalties considered in previous models. Further details regarding the model are provided in chapter 3.

Most of the models presented can be used to calculate cooling requirements for a cooled blade, or row in a turbine stage. However, few are available in engine performance models, with most engine modelling programs such as GSP or GasTurb [15] requiring user specified cooling fractions. This further confirms the need for the integration of a turbine cooling model in cycle calculation programs such as PyCycle.

Additionally the majority of the cooling models require experimental data or empirical factors. These are often based on older engines, raising questions around their validity for next generation gas turbine design. The existing implementations of cooling models in gas turbine simulation programs, including Gauntner or Holland and Thake, makes use of pressure loss as representation of performance degradation. However, Young and Wilcox explicitly state the importance of working with entropy creation rates as oppose to pressure drops in their publication [14]. Thus, a research project that aims to implement the entropy creation based model, as well as work to update its empirical parameters for use in engine modelling programs complements the existing gap in the reviewed scientific literature.

2.5. MODELLING FRAMEWORK

This section will present the framework used to develop the cooled turbine model. The chosen modelling tool is *PyCycle*, a library designed for use with the *openMDAO* framework [71]. An introduction to the *openMDAO* framework is presented in subsection 2.5.1. The engine modelling library is presented in subsection 2.5.2. The development of a class for calculation of thermodynamic properties based on enthalpy-entropy pairs is discussed in section 2.6.

2.5.1. OPENMDAO

OpenMDAO is an open source framework developed for multidisciplinary design, analysis and optimization (MDAO), developed by Gray et al [11]. It is unique amongst MDAO frameworks for its ability to efficiently and rapidly calculate derivatives, making it well suited for applications involving gradient based optimization.

OpenMDAO is an objected oriented framework, and there are four parent classes used to develop problem models. These are: *Component,Group,Driver* and *Problem* [11].*Component* represent the lowest level
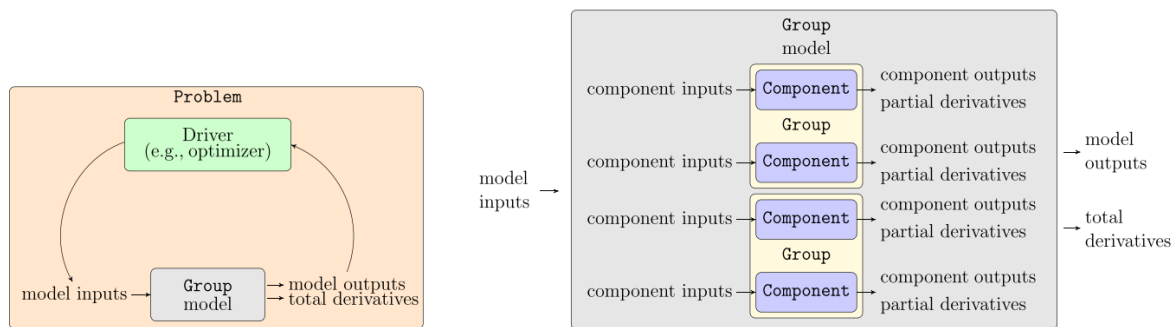
Figure 2.13: Simplified representation of the interaction between the fundamental classes of the openMDAO framework [11].]

class in the model, and consist of simple equations. These can be either explicit or implicit, and there are versions of the *Component* class specifically intended for each type. *Groups* include component libraries, and a subsystem of models made of a combination of component models. Groups can be nested within each other. The *Driver* group is used to iterate and solve the equations. Finally, all three aforementioned classes and their instances are part of a top level model, *Problem*. An example showing the interlinking of these parent classes is shown in Figure 2.13.

From Figure 2.13 it is seen that the driver takes outputs of *group* as an input and then provides new inputs to the model. Within *group*, the various components contribute to the definition of the model outputs and total derivatives of the output variables with respect to the input variables. The partial derivatives, on a component level, can be specified analytically by the user and this enhances computational speed. In the absence of user specified partial derivatives, OpenMDAO uses finite difference schemes to calculate them.

The derivatives associated with output variables and input variables at *component* level are referred to by Gray [11] as partial derivatives, while the derivatives at *problem* level are named total derivatives. The calculation of total derivatives is a distinguishing feature of the openMDAO framework. For objective functions that consist of only explicit *components*, the total derivative can be calculated by the chain rule of all component partial derivatives. However, for objective functions with implicit equations, two methods are used by the framework: direct and adjoint. Detailed derivations and proofs of the methods are shown by Gray [11], but for the purposes of this thesis it is sufficient to note that that the rapid calculation of total derivatives allows for implementation of newton-type solution methods. The work of Chauhan [72] points out that these methods are effective when applied to strongly coupled problem, where all problem variables are simultaneously updated.

2.5.2. PyCycle for engine modelling
PyCycle is a thermodynamic cycle analysis library developed for use within the openMDAO framework capable of providing analytical derivatives [12]. The realization of *PyCycle* is considered a significant step towards aircraft multidisciplinary design [11]. Originally developed and validated against NASA's Numerical Propulsion Simulation System (NPSS), *PyCycle* was found to be significantly faster in a benchmark study. The time taken by *PyCycle* was between 4.3% and 7.6% of that taken by NPSS [73]. The general structure of a cycle analysis problem implemented in *PyCycle* is shown in Figure 2.14.

In Figure 2.14 the first two blocks on the diagonal are the optimizer and solver. In an optimization problem in *PyCyle*, the solver is used to satisfy equality constraints, constraining the design space that the optimizer must search [12]. Furthermore, the cycle block contains the equations representing the engine thermodynamic cycle, while the balance block accounts for the definition of the balance equations and cycle specifications resulting in residual equations.*PyCycle* offers the user a set of pre-defined component models used in cycle analysis, representing various engine components such as compressors, ducts, fans, turbines and nozzles. The advantage is that the equations describing the thermodynamic processes in this components can be differentiated easily such that analytical derivatives can be implemented.

Akba [73] presents a summary of the various components that are pre-set in *PyCycle*. Most component models are built up in a similar way, with Figure 2.15 showing the internal structure of the compressor element. From the figure, it is seen that the element first calculates the total outlet pressure of the compressor element based on the total pressure of the flow entering and the pressure ratio. Following this, the specification of the entropy of the flow entering the compressor allows for the calculation of the ideal total thermodynamic
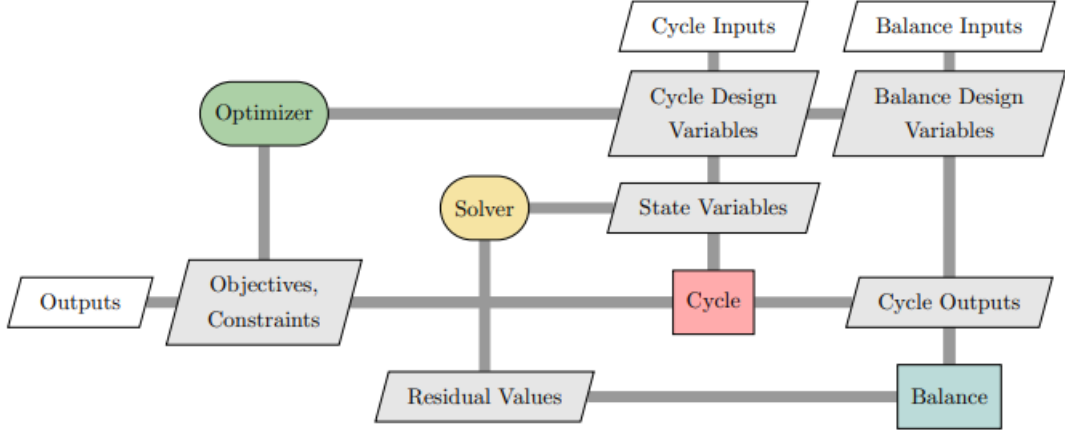
Figure 2.14: General setup of a cycle analysis problem in *PyCycle* [12].

quantities. Hereafter, the specification of the inlet specific enthalpy and the efficiency of the compressor allows the output enthalpy to be calculated. Subsequently, the outlet enthalpy is used to calculate real total thermodynamic quantities, as well as the power. The power can then be calculated given the air mass flow rate. Finally, the total temperature at compressor exit is combined with the outlet total pressure, given the Mach number and mass flow rate to calculate the static properties of the compressor exit flow. The turbine component is built up in a similar way [12].

Another key element of *PyCycle* is the thermodynamic model used to calculate flow properties. The class used for this is *Thermo* and differs from the thermodynamic calculations performed in NPSS [12]. The thermodynamic properties of a fuel-air mixture are calculated based on a minimization of the Gibbs free energy [12] assuming chemical equilibrium among the species in the mixture. The Gibbs free energy is the product of the concentration, n, and chemical potential of the species in a mixture, μ [74]:

$$g = \sum_{j}^{N_s} \mu_j \cdot n_j \tag{2.22}$$

where N_s is the number of chemical species, and the subscript j indicates the properties of the jth species in the mixture considered. The units for n are $kg-mol/kg\,mixture$. The chemical potential of a species is dependent on temperature, pressure and concentration. Gray [74] defines the chemical potential of the jth species in a mixture as:

$$\frac{\mu_j}{RT} = \frac{H_j°(T)}{RT} - \frac{S_j°(T)}{RT} + \ln\frac{P}{P_a} + \ln n_j - \ln\left(\sum_{k}^{N_s} n_k\right) \tag{2.23}$$

$H_j°(T)$ represents the enthalpy of the species as a function of temperature, while $S_j°(T)$ represents the entropy of the species. R is the universal gas constant and T the temperature. Both enthalpy and entropy can be calculated based on coefficients (c_0 to c_8) derived from the NIST lookup tables [28]:

$$\frac{H_j°(T)}{RT} = \frac{-c_0}{T^2} + \frac{c_1 \ln(T)}{T} + c_2 + \frac{1}{2}c_3 T + \frac{1}{3}c_4 T^2 + \frac{1}{4}c_5 T^3 + \frac{1}{5}c_6 T^4 + \frac{c_7}{T} \tag{2.24}$$

and

$$\frac{S_j°(T)}{RT} = \frac{-c_0}{2T^2} + \frac{c_1}{T} + c_2 \ln(T) + c_3 T + \frac{1}{2}c_4 T^2 + \frac{1}{3}c_5 T^3 + \frac{1}{4}c_6 T^4 + c_8 \tag{2.25}$$

The equilibrium composition of the mixture is obtained by minimizing the Gibbs free energy, without violating the conservation of mass, which is formulated as a constraint by Gray [74] in the form:

$$R_{mass,i} = \sum_{j=1}^{N_s} a_{ij} n_j - b_i° = 0 \tag{2.26}$$

In this equation, $b_i°$ represents the initial mole fraction of an element in the initial mixture composition. Furthermore, $a_{i,j}$ represents the coefficient used for an element in a species in the balanced chemical reaction.
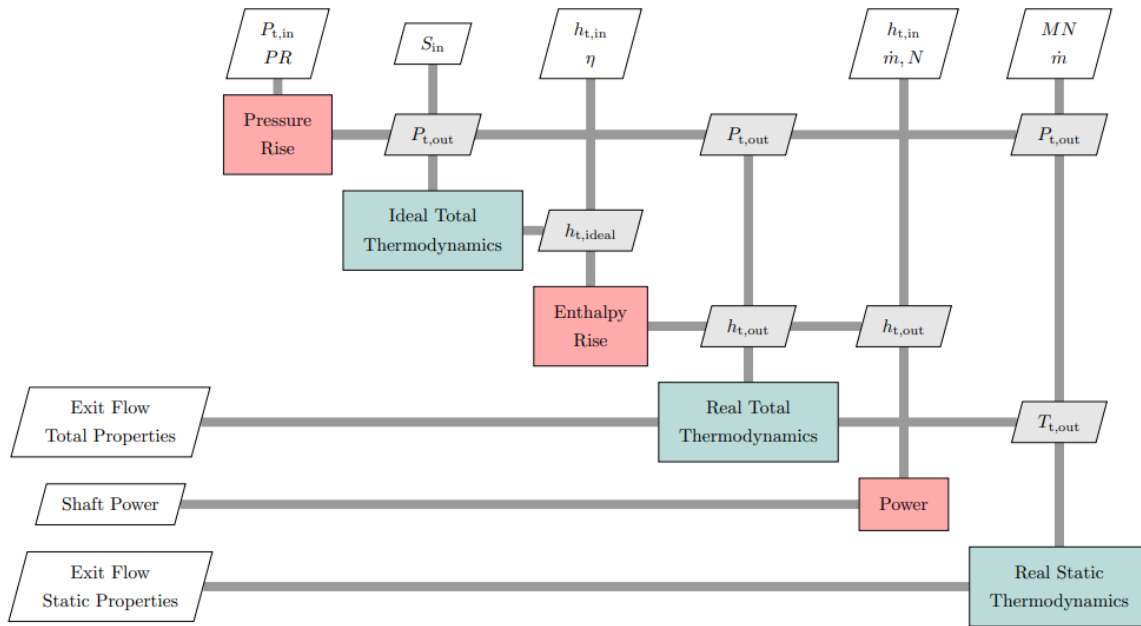
Figure 2.15: Structure of a compressor element class in *PyCycle* [12]. Blocks on the diagonal show components or groups performing calculations. Outputs are shown on the left, with shared variables passed between the groups. Inputs are shown on top.

Based on these mass conservation constraints, the minimization problem is well defined. Furthermore, once the equilibrium composition of the mixture is known, the thermodynamic properties can be calculated. This is visible from the setup of the XDSM of the *Thermo* element presented in Figure 2.16.

The process displayed in Figure 2.16 results in the specific heats at constant pressure and volume, C_p and C_v respectively. Together with n, the thermodynamic properties of the flow can be calculated from these quantities. For modelling purposes, PyCycle allows three combinations of input pairs, as shown in Table 2.3

In addition to the element *Thermo* to calculate thermodynamic properties, *PyCycle* provides an element to calculate the result of mixing two streams. This is the element *ThermoAdd*. The element requires three inputs for each flow being mixed: fuel to air ratio, FAR, enthalpy, h and mass flow rate $\dot{W}$. For two flows, labelled 1 and 2, the mixed properties are calculated in *ThermoAdd* as:

$$\dot{W}_{mixed} = \dot{W}_1 + \dot{W}_2 \tag{2.27}$$

$$FAR_{mixed} = \frac{FAR_1 \dot{W}_1 + FAR_2 \dot{W}_2}{\dot{W}_{mixed}} \tag{2.28}$$
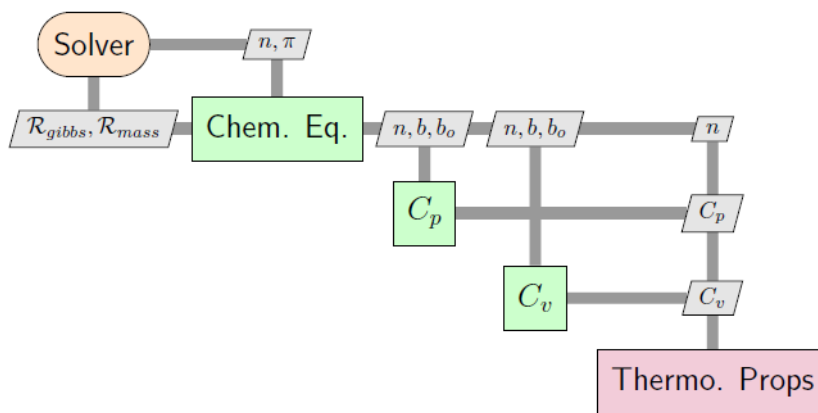
Figure 2.16: XDSM of Chemical Equilibrium used in PyCycle Thermo Element [13]

Input Pair	Symbol
Total Temperature & Total Pressure	pT
Total Enthalpy & Total Pressure	hP
Entropy & Total Pressure	sP

Table 2.3: Acceptable input pairs for PyCycle *Thermo*.
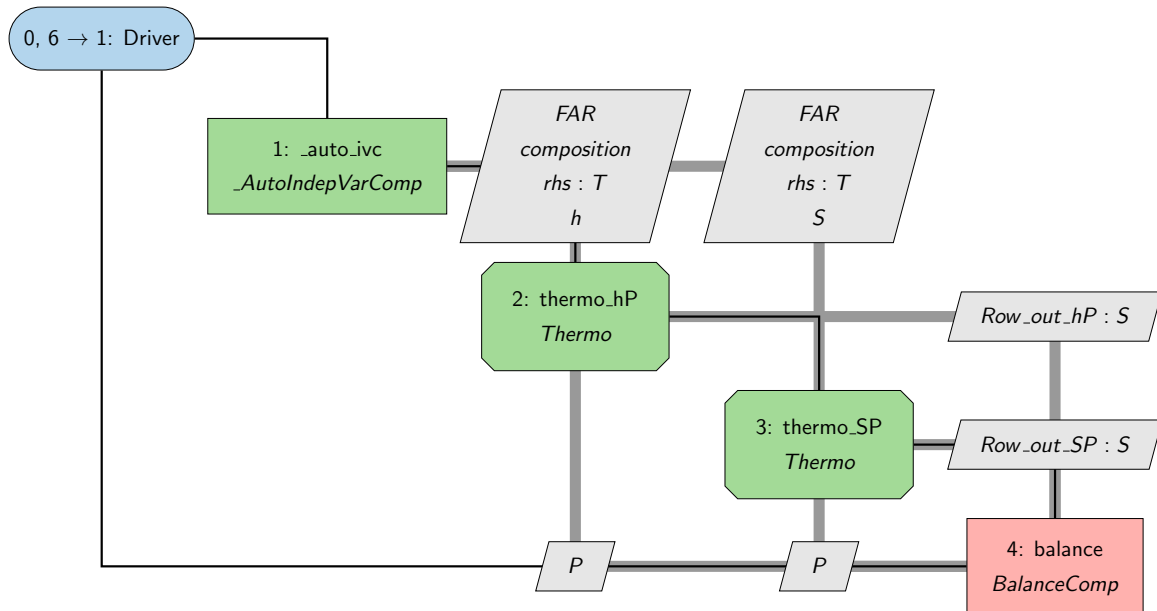
Figure 2.17: XDSM of Mollier group capable of $h - S$ thermodynamic input pairs

and

$$h_{mixed} = \frac{h_1 \dot{W}_1 + h_2 \dot{W}_2}{\dot{W}_{mixed}} \tag{2.29}$$

2.6. Development of h-S thermodynamic model

As discussed, the thermodynamic modelling of a working fluid in *PyCycle* is possible through defining a pair of variables. However, all three pairs that can be used include pressure. As the intended cooling model by Young and Wilcox explicitly calculates the entropy creation rates, and the mixing of flow streams results in enthalpy changes, it is foreseen that for the implementation of the blade cooling model it is beneficial to have a function determining the fluid thermodynamic properties given enthalpy-entropy as state variables. This section will describe the implementation of an enthalpy entropy, $h - S$, thermodynamic element in *PyCycle*. The combination of enthalpy and entropy will be referred to as a *mollier* pair, based on the name for an enthalpy-entropy diagram.

The fundamental working principle is to use two instances of *Thermo*, and making use of a Newton solver, to determine the pressure. Instances of *Thermo* that take hP or sP as input pairs consist of an iterative balance whereby a placeholder value of temperature is used as a state variable in order to match the enthalpy or entropy with the user specified input. Therefore, the thermodynamic element that takes the mollier pair as an input will feature balances on two levels. The first level will occur within the individual instances of *thermo*, as both elements 2 and 3 are calls of *Thermo* that take hP and sP as inputs respectively. The second level is the balance of the output of these elements themselves. The XDSM of the developed mollier group is shown in Figure 2.17.

The user must specify three characteristics of the working fluid, namely:

- enthalpy, h

- entropy, S

- Fuel to Air Ratio, FAR

Besides the user specified inputs, the auto-ivc component provides the dummy variable, $rhs : T$ to both instances of $Thermo$ to perform the lower level, internal, balancing procedure. Elements 2 and 3 of the group are instances of $Thermo$, linked through the 4th element, the balance component. The entropy is the target variable, while the pressure is the state variable. Thus, for a user specified pair of h and S, the pressure can be calculated. The mollier groups will also be referred to as the *ThermoBalancer* or *Mollier* group in further chapters. Tested over a range of conditions, the group is found to be highly accurate with absolute differences in values not exceeding order $e - 07$.

3

THEORETICAL FRAMEWORK- YOUNG & WILCOX COOLED BLADE ROW MODEL

Following numerous turbine blade cooling models, Young and Wilcox of the Whittle Laboratory in Cambridge developed a framework for the analysis of cooled gas turbines [17]. The main difference compared to other cooling models is the use of entropy creation to quantify performance loss, as opposed to the previous methods based on total pressure loss coefficients or efficiency penalties. The following subsections will present an overview of the model, which can be divided into two main modules. The first module pertains to the calculation of the cooling flow requirement of a turbine blade or row and the resulting temperatures, while the second quantifies the corresponding entropy generation, to properly account for losses associated with turbine cooling in cycle calculations.

The chapter initially presents the model's nomenclature in section 3.1, following which an overview of the inputs is presented in section 3.2. Furthermore section 3.3 presents the blade design characteristics and additional empirical constants required by the model. Finally, the cooling flow calculation scheme and related loss quantification framework are presented in section 3.4 and section 3.5.

3.1. MODEL NOMENCLATURE

For the purpose of simplification, Young and Wilcox subdivide a turbine stage into 4 stations, as shown in Figure 3.1.

The labels e, f, t and b are used to indicate the cooling flows associated with: end wall, film, trailing edge and blade surface. A station omitted in the figure is station x which represents the point at which cooling flows are mixed with the bulk flow. Further, it should be noted that the coolant flow is extracted from the compressor, at a station k,and it enters the blade at station i, before mixing with the gas flow at station x. The mixed flow enters then the following blade cascade. To provide an overview of the various flows in a cooled turbine stage, the reader is referred to Figure 3.2.

The stations related to the main gas path are indicated in red circles. For blades and disk cooling injections, the same station labels are used, but the subscripts s, r and dc are added to distinguish between stator, rotor and disk cooling flows respectively.

3.2. MODEL INPUTS

The model developed by Young and Wilcox requires the user to specify various inputs. A number of these are related to the flow conditions at the various stations, such as the compressor bleed off point and the row entry flow conditions. Additionally, a number of (semi-) empirical parameters must be specified. The following section will provide an overview of the model inputs and how their value can be specified.

The model inputs are listed in Table 3.1 and Table 3.2 and can be subdivided into two categories. The first are flow conditions while the second are thermodynamic properties.

Two observations can be made regarding these inputs. The first is that no thermodynamic conditions are specified for station i, the point at which the coolant flow enters the blade. This is because of the isentropic bleed assumption. Therefore thermodynamic conditions at the bleed off station, k and station i are the same. Hence:
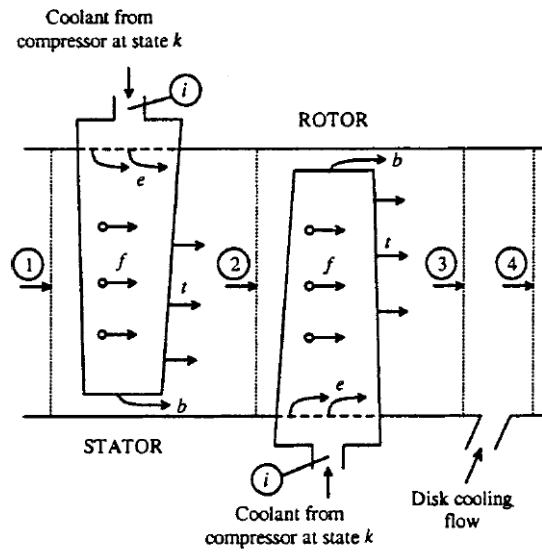
Figure 3.1: Cooled turbine stage as modelled by Young and Wilcox [14]
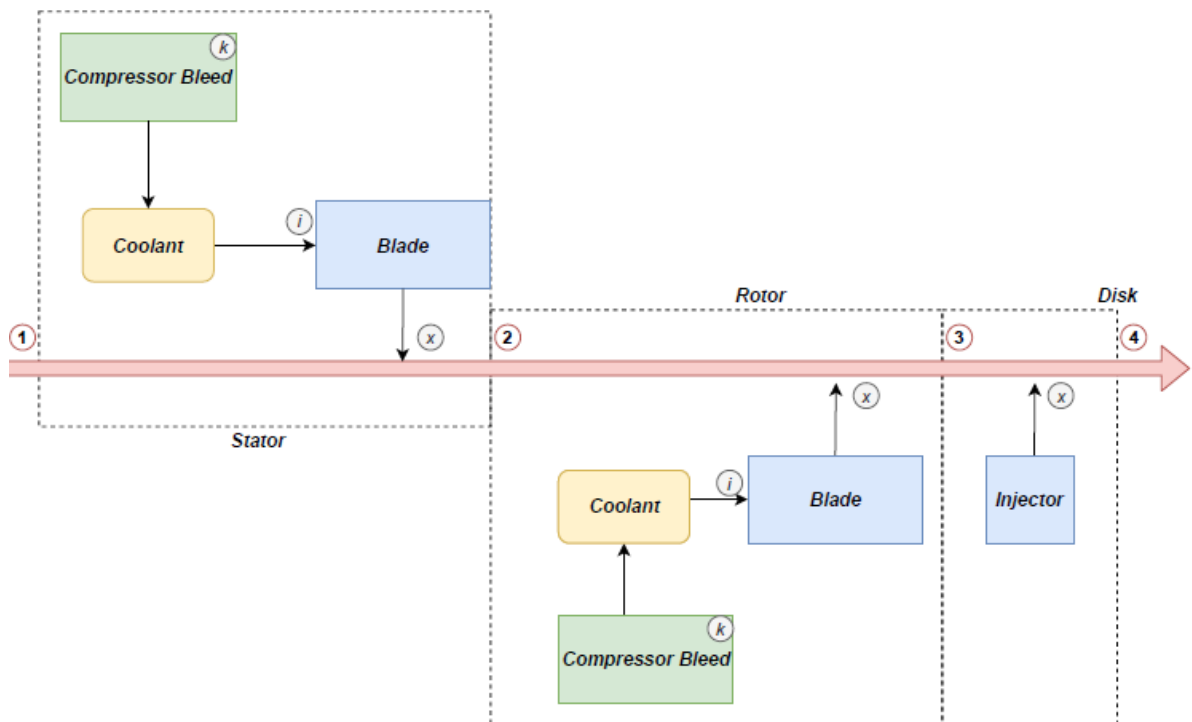
Figure 3.2: Overview of all flow stations for cooled turbine stage

Variable Symbol	Unit	Description
T_{0g}	K	Total temperature of mainstream flow into the row
T_m	K	Maximum permitted metal temperature
$T_{0c,k}$	K	Total temperature of compressor bleed flow at extraction point
ΔT_{cc}	K	Temperature difference between combustor inlet and outlet
P_{0g}	bar	Total pressure of mainstream flow into the row
$P_{0c,k}$	bar	Total pressure of flow at compressor bleed extraction point

Table 3.1: Flow condition inputs required for Young and Wilcox cooled turbine model [14]

Variable Symbol	Unit	Description
cp_c	J/(kg*K)	Specific heat capacity of the coolant
R_c	J/(kg*K)	Specific gas constant of the coolant
R_g	J/(kg*K)	Specific gas constant of the mainstream gas
γ_g	-	Ratio of specific heats at the blade row entry
γ_c	-	Ratio of specific heats of the coolant

Table 3.2: Flow thermodynamic properties required for Young and Wilcox cooled turbine model [14]

$$T_{0c,i} = T_{0c,k} \tag{3.1}$$

$$P_{0c,i} = P_{0c,k} \tag{3.2}$$

The second observation is that the user must specify the temperature rise across the combustor, ΔT_{cc}. Young and Wilcox do not explicitly state how this should be calculated [17]. However, the example presented in the original paper makes the assumption that the coolant bleed off station k is the same as the combustor inlet station. While this is possible for first and/or second turbine stages, the coolant bleed station can vary for multi-stage turbines. Finally,the user must also specify the maximum temperature the blade metal can reach, T_m.

3.3. Blade Design characteristics & empirical factors

The model also requires a number of inputs that are either (constant) design characteristics of the blade cascade, or empirical factors of the model.

Among the design constants shown in Table 3.3, the angle of flow injection, as well as the stage loading coefficient are required as inputs. In addition, the biot number of the blade and thermal barrier coating, if applicable, are needed. The biot number is a dimensionless representation of the heat transfer throughout a conducting material [75]. Young and Wilcox make use of two biot numbers, as follows:

$$Bi_m = \frac{\alpha_g}{\lambda_m} t_m \tag{3.3}$$

$$Bi_{tbc} = \frac{\alpha_g}{\lambda_{tbc}} t_{tbc} \tag{3.4}$$

Where α_g is the heat transfer coefficient in the mainstream flow path, λ refers to the thermal conductivity of the material. The subscript m and tbc refer to metal and thermal barrier coating respectively.

Variable Symbol	Unit	Description
Bi_m	-	Biot number blade metal
Bi_{tbc}	-	Biot number thermal barrier coating
Ψ	-	Stage loading coefficient
ϕ	deg	Flow injection angle

Table 3.3: Blade design characteristics required for Young and Wilcox cooled turbine model [14]

Variable	Description
K_{ext}	External flow variable
K_{int}	Internal flow variable
K_{cool}	Cooling flow factor
$\eta_{c,int}$	Internal cooling efficiency
ϵ_f	Film cooling effectiveness
K_{comb}	Combustion pattern factor

Table 3.4: Semi-empirical factors required for Young and Wilcox cooled turbine model [14]

The stage loading coefficient Ψ is also required as an input, to determine flow quantities in the rotating reference frames. The definition of the stage loading coefficients and other duty coefficients can be found in chapter 2. Finally, the flow injection angle must be provided as an input. Typically this refers to the angle formed by the vector normal to the film cooling holes and the mainstream flow.

A characteristic of low-fidelity blade cooling models is the frequent use of (semi-) empirical factors, typically fitted based on confidential engine performance data. Table 3.4 lists the empirical factors required for the calculation routines of the cooled turbine model developed by Young and Wilcox.

The first empirical factor is the combustion pattern factor, K_{comb}. Young and Wilcox prescribe values of 0.1 and 0.05 for stator and rotor rows respectively [14]. This factor, accounts for the temperature distribution at the outlet of a combustion chamber.

As can be observed from Figure 3.3 there is a significant variation in the gas temperature in the spanwise (radial) direction. T_{max} defines the maximum gas temperature, while T_r defines the mean circumferential temperature along the blade height, whose maximum is labelled $T_{r,max}$. For comparison, the figure reports T_4, the average combustor outlet temperature, that typically corresponds in cycle calculations to the high-pressure turbine inlet temperature.
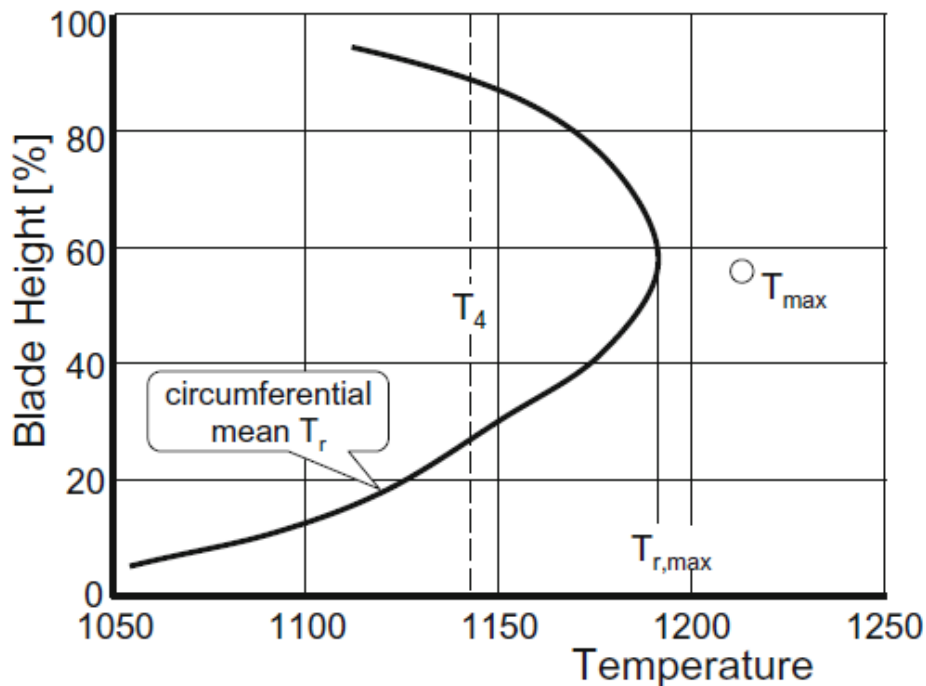
Figure 3.3: Distribution of temperatures at combustor outlet [15]

It is apparent that the blade cooling system cannot be correctly sized based on the average gas temperature. Hence the quantification of hot spots of the gas temperature distribution is key to ensuring the proper operation of the turbine and its cooling system. Further discussion on this topic will be presented in chapter 6.

The second set of empirical factors are related to the flow conditions. Static thermodynamic conditions are required to estimate the losses associated with the cooling flows. At the same time, the cycle calculations are performed using total quantities. Assuming an isentropic process, the relation between the coolant (subscript c) or gas (subscript g) total quantities and static quantities is as follows:

$$\frac{1}{T_c} = \left(1 + \frac{\gamma_c - 1}{2} M_c^2\right) \frac{1}{T_{0c}} \qquad (3.5)$$

$$\frac{1}{T_g} = \left(1 + \frac{\gamma_g - 1}{2} M_g^2\right) \frac{1}{T_{0g}} \qquad (3.6)$$

For simplicity, Young and Wilcox choose to label the bracketed terms as K_{int} and K_{ext} respectively, namely:

$$\frac{1}{T_c} = K_{int} \frac{1}{T_{0c}} \qquad (3.7)$$

$$\frac{1}{T_g} = K_{ext} \frac{1}{T_{0g}} \qquad (3.8)$$

The authors assumed values of 1.01 and 1.07 for K_{int} and K_{ext} respectively. Further considerations about the choice of these factors are reported in chapter 6.

For turbine blades featuring film cooling, the model introduces a performance parameter, defined as the film cooling effectiveness, ϵ_f.

$$\epsilon_f = \frac{T_{0g} - T_{aw}}{T_{0g} - T_{0c,x}} \qquad (3.9)$$

The numerator represents the difference between the mainstream gas temperature and the corresponding adiabatic wall temperature. The denominator is defined as the difference between the mainstream gas path temperature and the total temperature at which the coolant leaves the blade. All quantities are total.

Regardless of the adopted internal cooling enhancement devices such as pin fins or rib turbulators, the model accounts for their performance metric simply by defining an internal cooling efficiency, $\eta_{c,int}$, i.e:

$$\eta_{c,int} = \frac{T_{0c,x} - T_{0c,i}}{T_{m,int} - T_{0c,i}} \qquad (3.10)$$

The numerator represents the temperature of the coolant along the blade internal channels. The denominator is the difference between the internal wall temperature of the blade cooling channels and the total temperature of the coolant upon entering the blade. By defining this efficiency, there is no need to predict heat transfer within the blade cooling channels. This is the opposite of what is done by Rao et al in their paper [31], where a detailed model of the heat transfer within the cooling channels of the blade is implemented. The final parameter is the cooling flow factor, whose definition reads:

$$K_{cool} = \frac{A_{surf}}{A_g^*} \frac{cp_g}{cp_c} St_g \qquad (3.11)$$

Here A_{surf} represents the surface area of the blade, and A_g^* represents the cross sectional area of the flow at the blade cascade throat, and St_g is the Stanton number. Young and Wilcox state that the value of the Stanton number must be estimated from a suitable correlation or external heat transfer coefficient data at representative conditions.

3.4. COOLING FLOW CALCULATION ROUTINE

Young and Wilcox state that their calculation procedure to estimate the required cooling flow of a turbine stage is an extension of the methodology developed by Holland and Thake in the 1980's [10].

A high level overview of the inputs and outputs of the cooling flow calculation routine is presented in Figure 3.4. It should be noted that the cooling flow calculation is estimated for a single row at a time, and there are differences in the procedures adopted for stator and rotor rows although the quantities provided as output by the routine are the same.
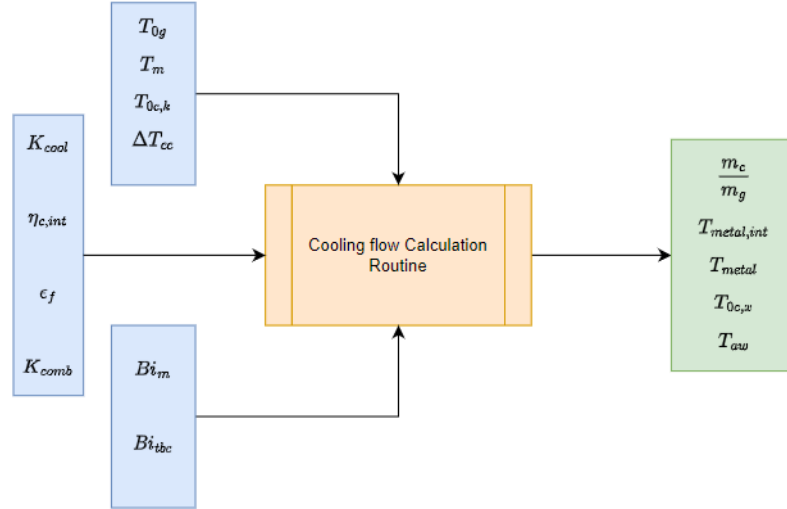
Figure 3.4: Inputs and outputs of cooling flow calculation routine

3.4.1. CALCULATION OF COOLING FLOW FRACTIONS

The first step of the calculation routine is targeted at estimating the temperature for which the cooling system is to be designed. With respect to a mission profile, the take-off condition is typically the design point. In addition, considering the non-uniformities of the combustor outlet flow, a maximum gas temperature is introduced:

$$T_{0g}^{max} = T_{0g} + K_{comb} * \Delta T_{cc} \tag{3.12}$$

Equation 3.12 implies that the maximum gas temperature is equal to the mean combustor outlet temperature (T_4 in cycle calculations) increased by a factor proportional to the temperature rise in the gas flow across the combustor. This is analogous to the method developed by Kawaike et al [76]. Subsequently, the value of the blade cooling effectiveness, ϵ_0^{max} is calculated:

$$\epsilon_0^{max} = \frac{T_{0g}^{max} - T_{m,ext}}{T_{0g}^{max} - T_{0c,i}} \tag{3.13}$$

The definition of the required blade cooling effectiveness allows for calculation of the dimensionless cooling flow rate, m_{c+}.

$$m_{c+} = \frac{\epsilon_0^{max} - \epsilon_f + \epsilon_f \eta_{c,int}(1 - \epsilon_0^{max})}{(1 + Bi_{tbc})\eta_{c,int}(1 - \epsilon_0^{max}) - Bi_m \eta_{c,int}(\epsilon_0^{max} - \epsilon_f)} \tag{3.14}$$

The actual cooling fraction, and subsequent cooling flow rate is determined by means of the cooling flow factor:

$$\frac{m_c}{m_g} = K_{cool} * m_{c+} \tag{3.15}$$

In order to understand the origins of Equation 3.14, let us consider the coolant flow path within the blade. The temperature rise of the coolant can be used to calculate the heat transfer from the gas to the coolant:

$$Q = m_c c p_c (T_{0c,x} - T_{0ci}) \tag{3.16}$$

In order to know the total temperature of the coolant flow at blade exit, the accurate modeling of the heat transfer in the cooling channels of the blade is required. An example of cooling models describing in detail the heat transfer process inside the blades is that developed by Rao et. al [31]. However, Young and Wilcox argue that the predition of the internal heat transfer coefficient can be affected by large uncertainity and prefer defining an integral quantity, the internal cooling efficiency, $\eta_{c,int}$. This parameter has been defined in Equation 3.10. Considering the mainstream flow, the heat transfer rate reads:

$$Q = \alpha_g A_{surf}(T_{aw} - T_w) \tag{3.17}$$

In order to estimate the adiabatic wall temperature in the presence of film cooling, the film cooling effectiveness, ϵ_f was defined earlier. Additionally, the following relations are defined for the dimensionless cooling mass fraction, m_{c+}, and the biot numbers of both metal and thermal barrier coating.

$$m_{c+} = \frac{m_c c p_c}{\alpha_g A_{surf}} = \frac{T_{aw} - T_w}{T_{0c,x} - T_{0c,i}} \tag{3.18}$$

$$Bi_{tbc} = \frac{\alpha_g t_{tbc}}{\lambda_{tbc}} = \frac{T_w - T_{m,ext}}{T_{aw} - T_w} \tag{3.19}$$

$$Bi_m = \frac{\alpha_g t_m}{\lambda_m} = \frac{T_{m,ext} - T_{m,int}}{T_{aw} - T_w} \tag{3.20}$$

Equation 3.14 is achieved through algebraic manipulation, by removing all temperature differences in Equation 3.18.

3.4.2. CALCULATION OF BLADE TEMPERATURES

In addition to the cooling fraction required for a blade or blade row, the calculation routine determines various temperatures characteristic of the considered blade row. These are:

- $T_{m,ext,eff}$ - The external temperature of the blade
- $T_{0c,x}$ - The coolant blade exit temperature
- $T_{metal,int}$ - Blade internal temperature

- T_{aw} - Adiabatic wall temperature
- T_w - Wall temperature
- $T_{0g,2}$ - Gas temperature at row exit, post mixing

Firstly, the external temperature of the blade is evaluated as:

$$T_{m,ext,eff} = T_{0g} - \epsilon_0^{max}(T_{0g} - T_{0c,i}) \tag{3.21}$$

Note that this is obtained through rearranging the definition of the cooling effectiveness ϵ_0^{max}, while also setting the value of the combustion pattern factor K_{comb} to 0, thereby using T_{0g} instead of T_{0g}^{max}. This is done to account for a representative average gas temperature.

Subsequently, the exit temperature of the coolant from the blade is determined as:

$$T_{0c,x} = \frac{T_{m,ext,eff} + T_{0c,i}\left(\dfrac{1}{\eta_{c,int}} - 1 + Bi_m m_{c+,max}\right)}{Bi_m m_{c+,max} + \dfrac{1}{\eta_{c,int}}} \tag{3.22}$$

which is the result of combining:

$$Bi_m\left(m_{c+,max}(T_{0c,x} - T_{0c,i})\right) = T_{m,ext} - T_{m,int} \tag{3.23}$$

and

$$\frac{1}{\eta_{c,int}}\left(T_{0c,x} - T_{0c,i}\right) + T_{0c,i} = T_{m,int} \tag{3.24}$$

The internal temperature of the blade is calculated using either Equation 3.23 or Equation 3.24 once $T_{0c,x}$ is known.

Following this, using the definition of the film cooling effectiveness, the adiabatic wall temperature T_{aw} is calculated, namely:

$$\epsilon_f = \frac{T_{0g} - T_{aw}}{T_{0g} - T_{0c,x}} \tag{3.25}$$

It follows that the wall temperature, T_w can be determined from:

$$m_{c+,max}(T_{0c,x} - T_{0c,i}) = T_{aw} - T_w \tag{3.26}$$
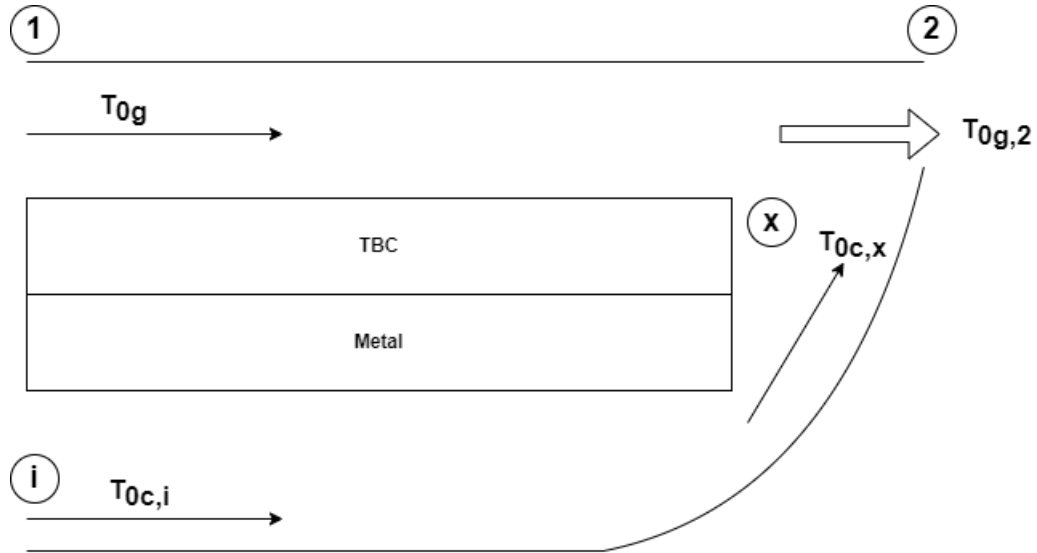
Figure 3.5: Simplified heat transfer model based on notation used by Young and Wilcox [14]

Finally, the total temperature of the mixed stream leaving the cascade must be calculated. Young and Wilcox assumed that both flow streams had identical specific heat capacities [17]. Therefore, the mixed total temperature is determined, based on :

$$T_{0g,2} = \frac{1}{2} * \left(\frac{T_{0g} + \frac{m_c}{m_{g,1}} * T_{0c,i}}{1 + \frac{m_c}{m_{g,1}}} + \frac{T_{0g} + \frac{m_c}{m_{g,1 \ max}} * T_{0c,i}}{1 + \frac{m_c}{m_{g,1 \ max}}} \right) \tag{3.27}$$

However, for the implemented cooled turbine model, this assumption is not necessary, and mixed temperature will be calculated based on a mixed enthalpy as described in chapter 2.

3.5. LOSS ACCOUNTING - ENTROPY GENERATION

The second purpose of the cooling model developed by Young and Wilcox is the quantification of the effect of cooling air flows on the turbine performance. While most of the models in the literature account for the penalty in efficiency by defining pressure loss coefficients, the Y&W model quantifies entropy increase. This is done through a detailed accounting system for the various mechanisms resulting in entropy creation due to blade cooling.

Defining the relevant nomenclature, $\Delta\Sigma$ is the total irreversible entropy creation rate, and is defined as the sum of the losses resulting from the expansion in an uncooled turbine and the loss associated with cooling [17]. These terms are $\Delta\Sigma_{basic}$ and $\Delta\Sigma_{cool}$.

$$\Delta\Sigma = \Delta\Sigma_{basic} + \Delta\Sigma_{cool} \tag{3.28}$$

Figure 3.5 recalls the mains stations of a blade row considered in the cooling model. Young and Wilcox assume that the variations in mainstream flow properties are negligible between station 1 and x [17].

Q is the heat transfer from the mainstream flow across the temperature difference T_{0g} to $T_{0c,i}$ through the thermal barrier coating and the blade metal. Due to the numerous heat transfer streams and temperature variations throughout the flows, Young and Wilcox define a number of terms that sum together to form the overall entropy creation rate term. An overview is shown in Figure 3.6. The following sections will provide an overview of the various entropy creation terms.

3.5.1. BASIC ENTROPY CREATION RATE

The basic entropy creation loss is the loss associated with an equivalent uncooled turbine stage. Young and Wilcox provide the definition this entropy creation rate on the basis of the uncooled polytropic efficiency of the equivalent uncooled machine.η_{basic} namely:

$$\Delta\Sigma_{basic} = m_g R_g (1 - \eta_{basic}) ln(\Pi_{stage}) \tag{3.29}$$
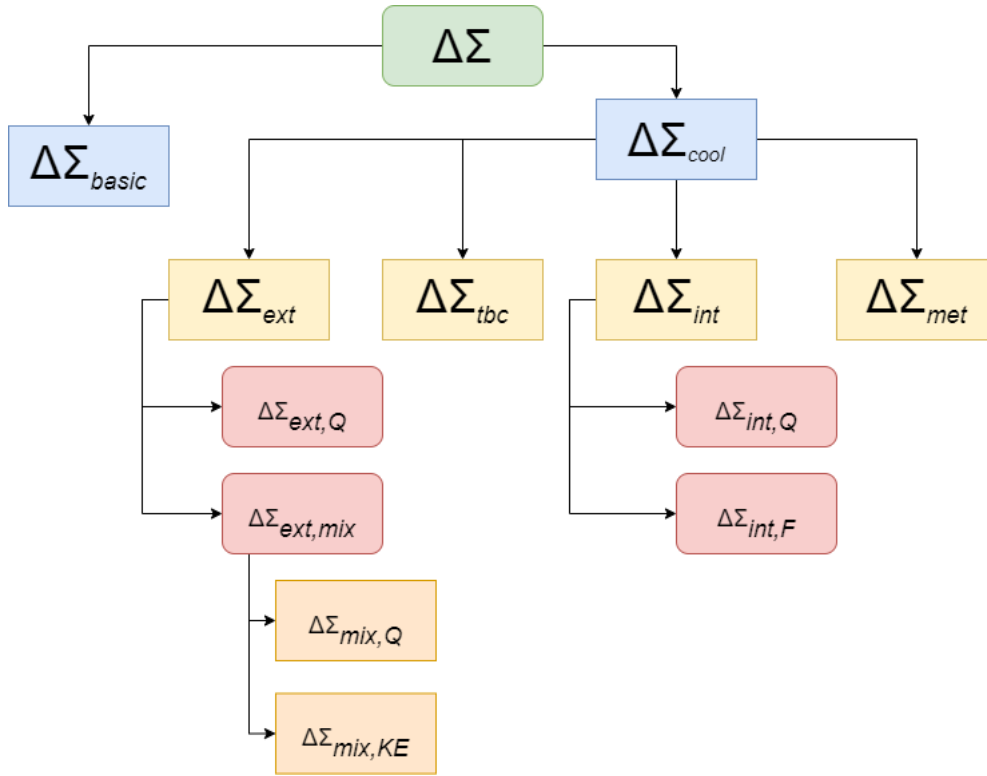
Figure 3.6: Breakdown of entropy creation terms

where Π_{stage} is the ratio between the total pressure at stage inlet and total pressure at stage outlet, $\frac{P_{0,1}}{P_{0,4}}$. A major assumption of the loss model is that the entropy generation due to the flow expansion in the blade cascade does not change in the case of cooling flows.

Figure 3.7 shows the variation in the basic entropy creation term with stage expansion ratio, for different polytropic efficiencies. It should be noted that this for a unit of massflow of bulk flow, and will scale linearly with massflows. As expected, higher total pressure drop across the stage results in higher entropy creation, and this effect is amplified in less efficient stages.

3.5.2. EXTERNAL FLOW ENTROPY CREATION

There are various processes associated with the mainstream flow which contribute to entropy creation. It is possible to divide them into three main categories. Due to heat transfer, friction as well as mixing of the streams.

In order to establish the entropy creation terms involving the gas flow, a control volume is defined, as depicted in Figure 3.8. Young and Wilcox establish that the momentum equation across the control volume in Figure 3.8 may be formulated as [14]:

$$\dot{m}_g \left(\frac{\delta P_g}{\rho_g} + V_g \delta V_g \right) = -V_c \delta F \tag{3.30}$$

Additionally, the energy equation reads:

$$\dot{m}_g \left(\delta h_g + V_g \delta V_g \right) = \delta Q \tag{3.31}$$

Finally, applying entropy balance across control volume gives:

$$\delta \Sigma = \dot{m}_g \delta s_g - \frac{\delta Q}{T_g} \tag{3.32}$$

The entropy created is the difference between the entropy change across the expansion and the entropy de-
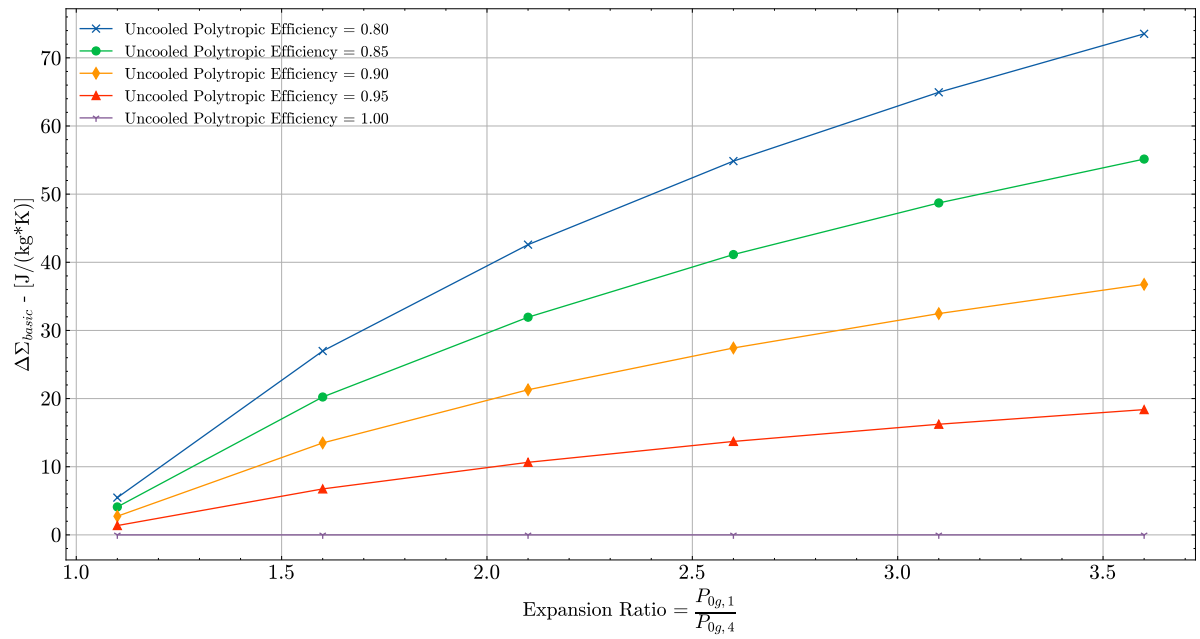
Figure 3.7: Variation in basic entropy generation as a function of stage expansion ratio and polytropic efficiency
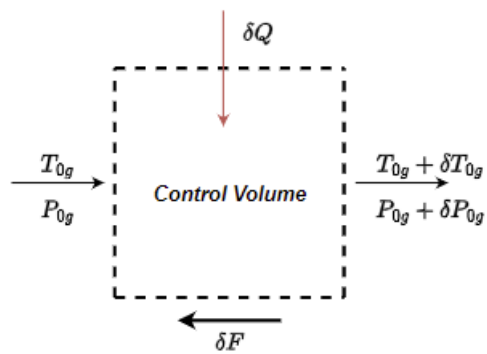
Figure 3.8: Definition of control volume for entropy calculations involving mainstream flow. The control volume includes the blade.
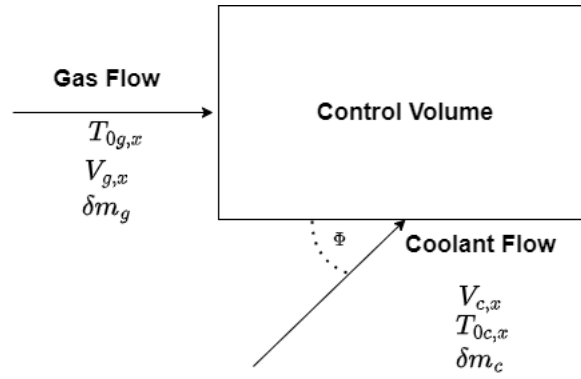
Figure 3.9: Control volume where the mixing of the cooling and main stream occurs

crease due to the cooling of the gas bulk flow. Equation 3.32 can be rearranged as:

$$T_g \delta s_g = \delta h_g - \frac{\delta P_c}{\rho_c} \tag{3.33}$$

Combining Equation 3.30 and Equation 3.33 gives the following formulation for the entropy creation terms:

$$\delta \Sigma_{ext} = \left(\frac{1}{T_w} - \frac{1}{T_g} \right) \delta Q + \frac{V_g}{T_g} \delta F \tag{3.34}$$

In Equation 3.34, it is possible to recognize the term associated with the heat transfer and that associated with the viscous effects. Young and Wilcox assume that the intensity of the frictional forces is not affected by the presence of cooling, and that they should therefore be captured by the basic entropy creation term, outlined in subsection 3.5.1. Hence, only the contribution of heat transfer is considered in $\Delta \Sigma_{ext,Q}$ resulting in:

$$\delta \Sigma_{ext,Q} = \left(\frac{1}{T_w} - \frac{1}{T_g} \right) \delta Q \tag{3.35}$$

It should be noted that the temperature differences Equation 3.35 pertain to static conditions, as opposed to the total conditions generally adopted in cycle calculations. The external flow factor, defined in section 3.3 is used to convert the total temperature of the gas bulk flow into the static one. It results that:

$$\delta \Sigma_{ext,Q} = \left(\frac{1}{T_w} - \frac{K_{ext}}{T_{0g}} \right) \delta Q \tag{3.36}$$

The integration of Equation 3.36 results in the final formulation for the entropy creation rate due to heat transfer:

$$\Delta \Sigma_{ext,Q} = \left(\frac{1}{T_w} - \frac{K_{ext}}{T_{0g}} \right) Q \tag{3.37}$$

The entropy creation rate in the gas bulk flow must also account for the entropy generation resulting from the mixing with the coolant stream. To derive the formulation for this entropy generation term, it is useful to define the control volume in Figure 3.9 where the mixing of the two streams occurs.

In this figure, Φ represents the angle formed between the direction of injection of the coolant and the mainstream flow. Conventional turbine cooling models define the penalty due to mixing as a loss of total pressure, based on a method defined by Hartsell, whose derivation is based on the one dimensional analysis of mixing flows performed by Shapiro [17, 77]. However, Young and Wilcox argue that total pressure losses are an ambiguous performance metric due to reversibility. Hence, they argue that working directly with the entropy generation is paramount, for all loss sources in a cooled turbine. This is supported by the work of Denton [16], as seen in Figure 3.10. The difference between the mass averaged $h - S$ and the actual mixed out state is attribute to irreversible entropy creation. It is this term that Young and Wilcox aim to quantify for a cooled turbine. In figure Figure 3.10 this is labelled Δs_{irrev}.
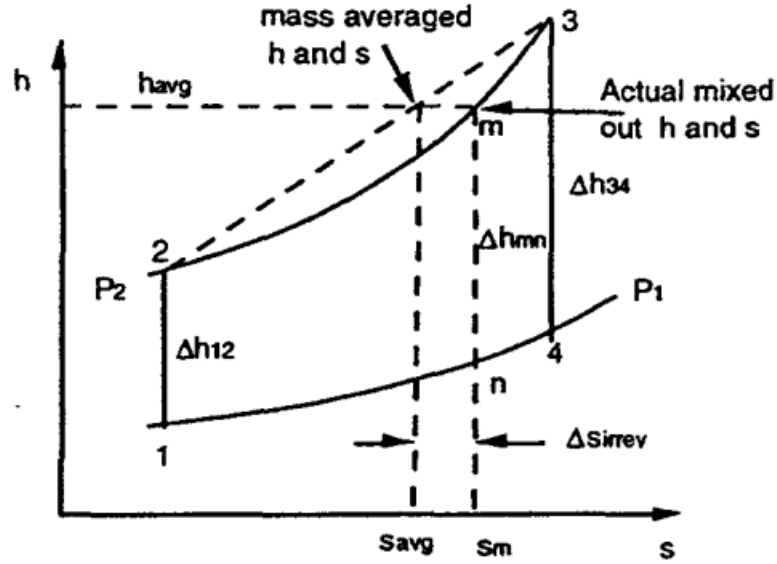
Figure 3.10: Mollier diagram of mixing flows showing the discrepancy in calculated outlet state, if irreversible entropy creation is not accounted for [16, 17].

The momentum balance across the control volume defined in Figure 3.9 reads:

$$\delta m_g \left(\frac{\delta P_g}{\rho_g} + V_g \delta V_g \right) + \delta m_c V_g \left(V_g - V_c \cos(\Phi) \right) = 0 \tag{3.38}$$

Additionally, applying energy conservation across the control volume gives:

$$m_g (\delta h_g + V_g \delta V_g) + \delta m_c \left(h_c(T_g) - h_c(T_c) + \frac{V_g^2 - V_c^2}{2} \right) = 0 \tag{3.39}$$

Furthermore, the mixing process is assumed to occur at the static pressure of the mainstream gas. Therefore, the corresponding entropy generation is as follows:

$$\delta \Sigma_{mix} = m_g \delta s_g + \delta m_c [s_c(T_g, P_g) - s_c(T_c, P_g)] \tag{3.40}$$

Where both temperature and pressure are static quantities. In analogy to the external heat transfer entropy creation term, it is useful to introduce:

$$T_g \delta s_g = \delta h_g - \frac{\delta P_g}{\rho_g} \tag{3.41}$$

RearrangingEquation 3.38 to Equation 3.41 results in:

$$\delta \Sigma_{mix} = \delta m_c \left\{ s_c(T_g, P_g) - s_c(T_c, P_g) - \frac{h_c(T_g) - h_c(T_c)}{T_g} \right\} + \delta m_c \left\{ \frac{(V_g - V_c \cos(\Phi))^2}{2T_g} + \frac{(V_c \sin(\Phi))^2}{2T_g} \right\} \tag{3.42}$$

Young and Wilcox treat the gases as ideal, and as such, the enthalpy is equal to the product of c_p and temperature, with a reference temperature of 0 K. Furthermore, the difference in entropy due to temperature change is neglected, leading to the following simplified expression.

$$\delta \Sigma_{mix} = \delta m_c \left\{ -\frac{h_c(T_g) - h_c(T_c)}{T_g} \right\} + \delta m_c \left\{ \frac{(V_g - V_c \cos(\Phi))^2}{2T_g} + \frac{(V_c \sin(\Phi))^2}{2T_g} \right\} \tag{3.43}$$

Two main contributions can be recognized in Equation 3.43: the first one due to heat transfer and the second one due to kinetic energy dissipation,namely:

$$\delta \Sigma_{mix} = \delta \Sigma_{mix,Q} + \delta \Sigma_{mix,KE} \tag{3.44}$$

$\delta\Sigma_{mix}$ can be rewritten in integral form as:

$$\delta\Sigma_{mix} = \delta m_c \int_{T_{c,x}}^{T_{g,x}} cp_c \left(\frac{1}{T} - \frac{1}{T_{g,x}} \right) dT + \delta m_c \left\{ \frac{(V_g - V_c \cos(\Phi))^2}{2T_g} + \frac{(V_c \sin(\Phi))^2}{2T_g} \right\} \tag{3.45}$$

The integral yields:

$$\Delta\Sigma_{mix,Q} = m_c cp_c \left(ln\left(\frac{T_{g,x}}{T_{c,x}} \right) - \left(1 - \frac{T_{c,x}}{T_{g,x}} \right) \right) \tag{3.46}$$

$$\Delta\Sigma_{mix,KE} = m_c \left\{ \frac{(V_g - V_c \cos(\Phi))^2}{2T_g} + \frac{(V_c \sin(\Phi))^2}{2T_g} \right\} \tag{3.47}$$

In summary, the external entropy creation rate consists of three terms. The first pertaining to the heat transfer in the external gas flow, the second is related to the heat transfer during mixing and the third one is related to the kinetic energy loss as a result of mixing two streams at different total conditions. These terms are defined in Equation 3.37, Equation 3.46 and Equation 3.47.

3.5.3. INTERNAL FLOW ENTROPY CREATION

Cooled blades feature complex internal geometry including pin-fins, ribs and other structures designed to enhance heat transfer by convection. While Tiemstra et. al [31] assess the performance of different blade internal geometries, Young and Wilcox treat the internal heat transfer of the blade with a lumped parameter modeling approach.

Sources of internal entropy generation are once again due to heat transfer and flow frictions within the internal blade channels. The corresponding entropy balance reads:

$$\Delta\Sigma_{int} = m_c \left(s_{c,x} - s_{c,k} \right) - \frac{Q}{T_{m,int}} \tag{3.48}$$

The equation shows that the entropy variation rate is the difference between the entropy rise due to friction in the internal channels and that associated to heat transfer. The heat transfer rate within the blade is defined using the temperature difference in the cooling flow across the blade

$$Q = m_c cp_c \left(T_{0c,x} - T_{0c,i} \right) \tag{3.49}$$

Furthermore, it is assumed by Young and Wilcox that the specific heat at constant pressure (cp_c) is temperature invariant. This results in the following formulation for $\Delta\Sigma_{int}$:

$$\Delta\Sigma_{int} = m_c cp_c \left\{ ln\left(\frac{T_{0c,x}}{T_{0c,k}} \right) - \frac{T_{0c,x} - T_{0c,i}}{T_{m,int}} \right\} - m_c R_c ln\left(\frac{P_{0c,x}}{P_{0c,k}} \right) \tag{3.50}$$

which can be split into the two following terms:

$$\Delta\Sigma_{int,q} = m_c * cp_c \left\{ K_{int} ln\left(\frac{T_{0c,x}}{T_{0c,i}} \right) - \left(\frac{T_{0c,x} - T_{0c,i}}{T_{m,int}} \right) \right\} \tag{3.51}$$

$$\Delta\Sigma_{int,F} = m_c * cp_c \left\{ ln\left(\frac{T_{0c,x}}{T_{0c,k}} \right) - K_{int} ln\left(\frac{T_{0c,x}}{T_{0c,i}} \right) \right\} - m_c R_c ln\left(\frac{P_{0c,x}}{P_{0c,k}} \right) \tag{3.52}$$

Assessing both equations, it is observed that all temperature terms are known from the cooling flow calculation routine. Other terms are specified by the user, apart from the total pressure at the cooling flow injection point, $P_{0c,x}$.

A rigorous modeling approach would be to the model the internal geometry of the blade to calculate the total pressure drop compared to the bleed off point ($P_{0c,k}$). Young and Wilcox argue that this is too complex for the purpose of the turbine cooling model. Instead, the devised method aims to specify $P_{0c,x}$ without modelling the internal geometry[14].

As mentioned before, when the mixing occurs, the two streams must have the same static pressure. To determine the total pressure at the cooling flow injection point a new quantity is introduced, namely the momentum flux ratio. This is defined as the ratio of the mass flux of the two flows, as in Equation 3.53:

$$I = \frac{\rho_{c,x} V_{c,x}^2}{\rho_{g,x} V_{g,x}^2} = \frac{\gamma_c M_{c,x}^2}{\gamma_g M_{g,x}^2} \tag{3.53}$$
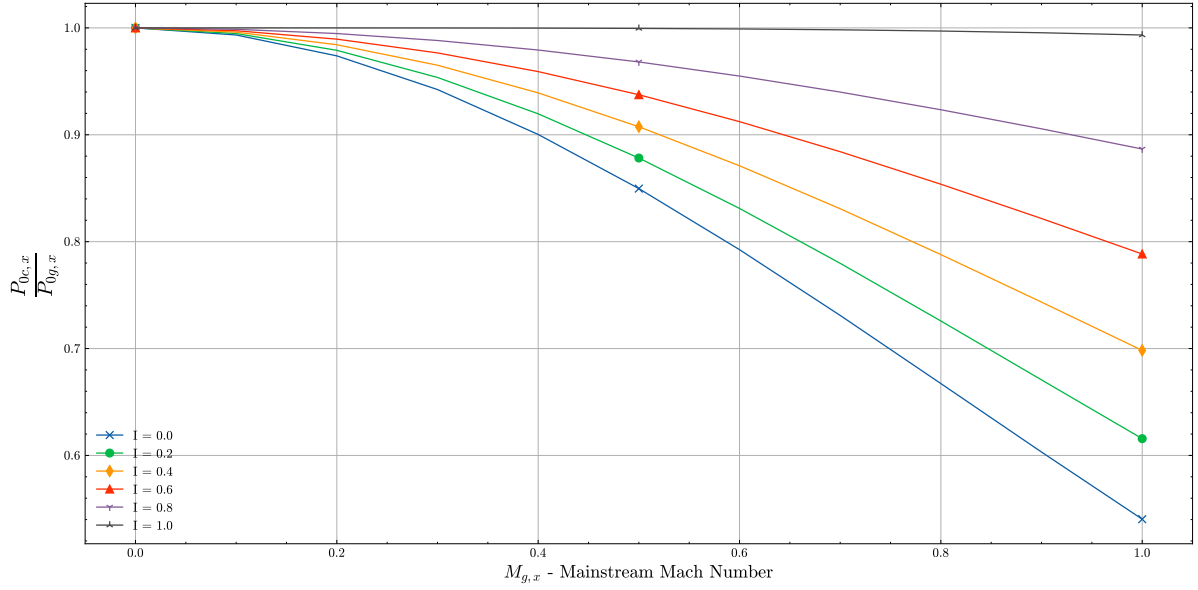
Figure 3.11: Variation in total pressure ratio at blade exit as a function of mainstream mach number

Furthermore, the ratio of the total pressure of the two streams may be defined as:

$$\frac{P_{0c,x}}{P_{0g,x}} = \frac{\left\{1 + 0.5\left(\gamma_c - 1\right)M_{c,x}^2\right\}^{\dfrac{\gamma_c}{\gamma_c - 1}}}{\left\{1 + 0.5\left(\gamma_g - 1\right)M_{g,x}^2\right\}^{\dfrac{\gamma_g}{\gamma_g - 1}}} \tag{3.54}$$

Combining Equation 3.53 and Equation 3.54, the pressure ratio can be expressed in terms of the momentum flux ratio.

$$\frac{P_{0c,x}}{P_{0g,x}} = \frac{\left\{1 + 0.5\left(\gamma_c - 1\right)\dfrac{\gamma_g}{\gamma_c}M_{g,x}^2 I\right\}^{\dfrac{\gamma_c}{\gamma_c - 1}}}{\left\{1 + 0.5\left(\gamma_g - 1\right)M_{g,x}^2\right\}^{\dfrac{\gamma_g}{\gamma_g - 1}}} \tag{3.55}$$

As visible from Figure 3.11, increasing the mainstream mach number results in a reduction of the overall pressure ratio. This effect is larger with lower momentum flux ratios. Due to the combustor pressure loss, the total pressure at the outlet of the last compressor stage will always be higher than the total pressure entering the first stage of the turbine.

As the bleed port supplying the cooling air for the first turbine stage is often placed at the outlet of the last compressor stage, the ratio of $P_{0c,x}$ to $P_{0c,k}$ will be less than 1. This results in the second term in Equation 3.52 adding to the entropy.

In summary, the specification of the momentum flux ratio and the mainstream mach number allow for the calculation of the internal entropy creation rate.

3.5.4. ENTROPY CREATION THROUGH HEAT TRANSFER - BLADES AND TBC

The third and fourth terms in the overall cooling entropy creation rate of a cooled turbine blade row are related to the heat transfer through the thermal barrier coating (TBC) and the blade itself. These terms are respectively $\Delta\Sigma_{tbc}$ and $\Delta\Sigma_{met}$.

Figure 3.12: Model of the heat transfer process through the thermal barrier coating and substrate blade metal

The accumulation of thermal energy in the two layers used to discretize the blade structure, see Figure 3.12, is neglected.

The temperature difference across the TBC is defined by T_w and $T_{m,ext,eff}$, while for the metal this is between $T_{m,ext,eff}$ and $T_{m,int}$. It results that the entropy variation in the two layers is as follows:

$$\Delta\Sigma_{tbc} = Q\left(\frac{1}{T_{m,ext,eff}} - \frac{1}{T_w}\right) \tag{3.56}$$

$$\Delta\Sigma_{tbc} = Q\left(\frac{1}{T_{m,int}} - \frac{1}{T_{m,ext,eff}}\right) \tag{3.57}$$

<div style="text-align: right">

4

</div>

COOLED TURBINE MODEL - DEVELOPMENT

This chapter will explain the adaptations of the Young & Wilcox (Y&W) method required for its implementation in *PyCycle*. The resulting model, the Cooled Turbine Model (CTM) is composed of several elements. Firstly, section 4.1 presents the conceptual structure of the CTM. The modelling of a cooled turbine row is presented in section 4.2. Following this, the modelling approach for the mixing of flows is outlined in section 4.3. The work extraction process in the cooled turbine is modelled similarly to an uncooled turbine as elaborated in section 4.4. Finally, considerations related to the transformation of the references frames for rotating blades are presented in section 4.5.

4.1. CONCEPTUAL MODELLING APPROACH - COOLED TURBINE MODEL

The main blocks of the cooled turbine model are shown in Figure 4.1.It should be noted that intermediate stations corresponding to the mixing of the main flow with the cooling air are indicated with the subscript with two digits 5 (stations 15 and 35).

The original Y&W model is developed for the analysis of a single blade row, and does not account for the work extraction process in the turbine. For this reason, the CTM treats the work extraction process as independent from the solution of the thermodynamic conditions across each blade row, as shown in Figure 4.1. This also simplifies the structure of the CTM, allowing the re-use of elements used in the stator row calculations for the rotor row.

To further understand the adopted modelling approach, Figure 4.2 shows the mollier diagram for a cooled turbine row, as reported by Dick and De Paepe [18] where the modeling of the process occuring in a cooled blade row involves three main steps: the expansion process from 1 to $2'$, the entropy reduction due to coolant addition between station $2'$-$2''$ as well as the entropy rise between $2''$ and 2 due to mixing, and the corresponding pressure drop from $P_{2'}$ to P_2. The modelling of mixing and cooling processes in the CTM will be treated in further detail in the coming sections.

4.2. TURBINE BLADE ROW COOLING REQUIREMENTS

As discussed in chapter 3, Young and Wilcox define the combustor temperature rise,ΔT_{cc}, as the difference between row inlet total temperature and total temperature at the cooling bleed off location [17]. However, this is not always a valid definition for the stages of a low pressure turbine, that may be more optimally cooled by bleed air from earlier compressor stages. Additionally, prescribing a fixed value for combustor temperature rise would prevent modelling of novel engine architectures, such as that with an inter-turbine burner (ITB), as shown in Figure 4.3. As the combustor temperature rise is used to account for temperature variations in the flow entering the turbine row, modelling the temperature rise for each combustion chamber provides more flexibility.

The temperature rise is determined in the CTM as the difference between the specified combustor outlet temperature (COT) and combustor entry temperature (CET). These temperatures may be user specified, or linked to the stations upstream and downstream of the combustor model. Finally, the calculation of the cooling flow rate. In kilograms per second this is calculated as the product of the cooling mass fraction estimated for a blade row and the gas mass flow rate at the inlet of that row. The XDSM of model elements developed to calculate both ΔT_{cc} and the cooling flow rate are shown in Figure 4.5 and Figure 4.6 respectively.
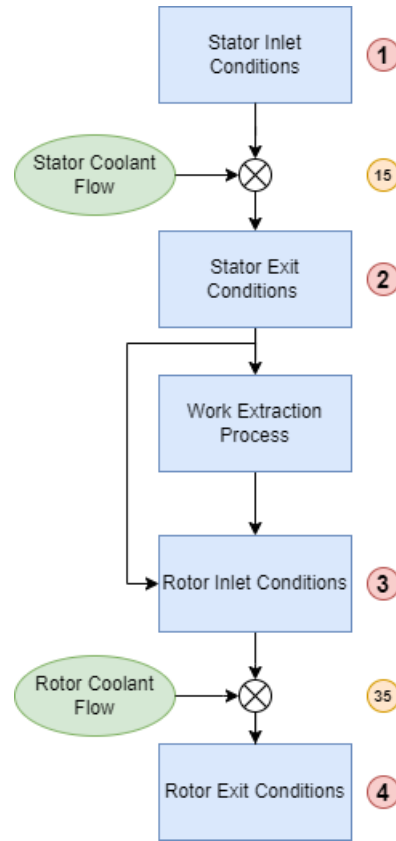
Figure 4.1: Conceptual model of cooling turbine stage
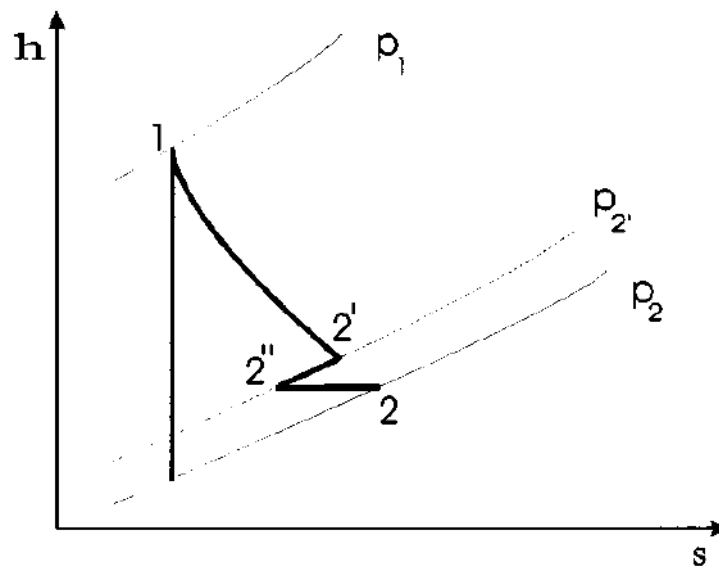
Figure 4.2: Modelling of the expansion in a cooled blade row as a cooling process followed by the mixing of the bulk flow with cooling air [18]
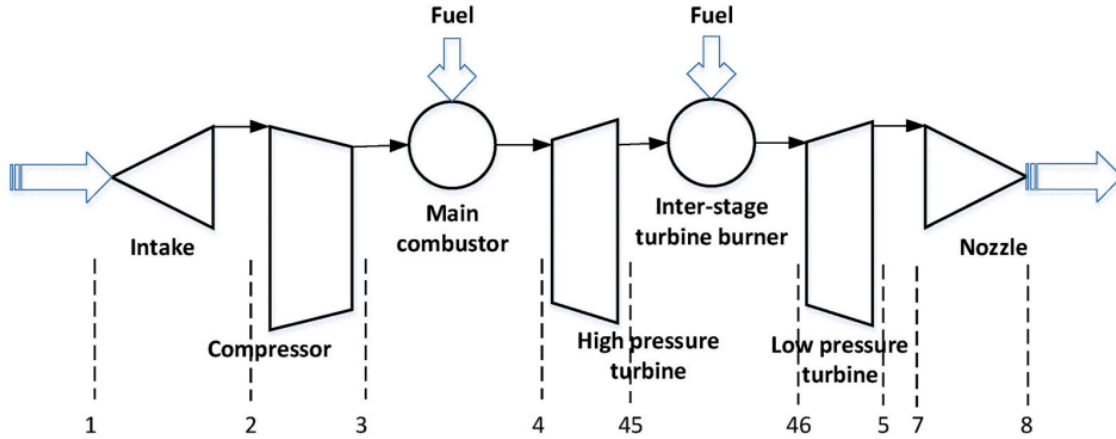
Figure 4.3: Simplified architecture of an engine with an inter-turbine burner (ITB). The main combustor and ITB may vary in temperature rise from inlet to outlet.[19]

Input Variable	Symbol	Option Variable	Symbol
Tt_primary	T_{0g}	Kcomb_stator & Kcomb_rotor	K_{comb}
T_metal	T_m	K_cool	K_{cool}
Tt_compbleed	$T_{0c,k}$	Bi_m	Bi_m
Tt_cool	Tt_{cool}	Bi_tbc	Bi_{tbc}
deltaT_cc	ΔT_{cc}	eta_c_int	$\eta_{c,int}$
P0g	P_{0g}	epsilon_f	ϵ_f
P_0C_k	$P_{0c,k}$	K_int	K_{int}
cp_c	cp_c	K_ext	K_{ext}
R_c	R_c	phi	Φ
R_g	R_g	T_factor	T_{factor}
gamma_g	γ_g		
gamma_c	γ_c		

Table 4.1: List of inputs and options of the CTM implementation of the Y&W model

The inputs to the Y&W model can be split into two categories. The first category includes variables related to the thermodynamic properties of the gas and cooling air flows, while the second category is composed of design characteristics of the blade row and empirical factors. The second category of inputs are defined as *options* in the current implementation of the CTM. When implemented as an option, a variable is treated as a constant in *PyCycle*. The inputs and options of the implemented CTM are shown in Table 4.1.

All input variables in Table 4.1 were presented in chapter 3, apart from the temperature multiplication factor, T_{factor}, that can be used to account for the overall increase in turbine inlet temperature due to a number of factors including the adoption of new fuels for future engines.

The Outputs of the Y&W model are presented in Table 4.2. Only the temperature after mixing of gas and coolant flow streams, $T_{0g,2}$, was not discussed in chapter 3. The methodology used to determine this quantity will be discussed in further sections.

Figure 4.4 shows a high-level representation of the CTM structure, while the expanded XDSM diagram is presented in Appendix A.

The CTM implementation of the Y&W model differs from the original in four key aspects. The first is the presence of a check of the cooling mass flow rate, while the second and third relate to calculation of the momentum flux ratio and flow velocities respectively. The final difference is the calculation of analytic derivatives, required for implementation of an element in *PyCycle*.

The main reason for the implementation of the cooling mass flow rate check is that the original Y&W model has no inherent mechanism to prevent calculation of negative cooling flow rates. Calculations of negative flow rates, for cases where the gas temperature is lower than the blade material limit, will create significant error in the cycle calculation. Therefore, a cooling check is implemented to ensure that the Y&W model
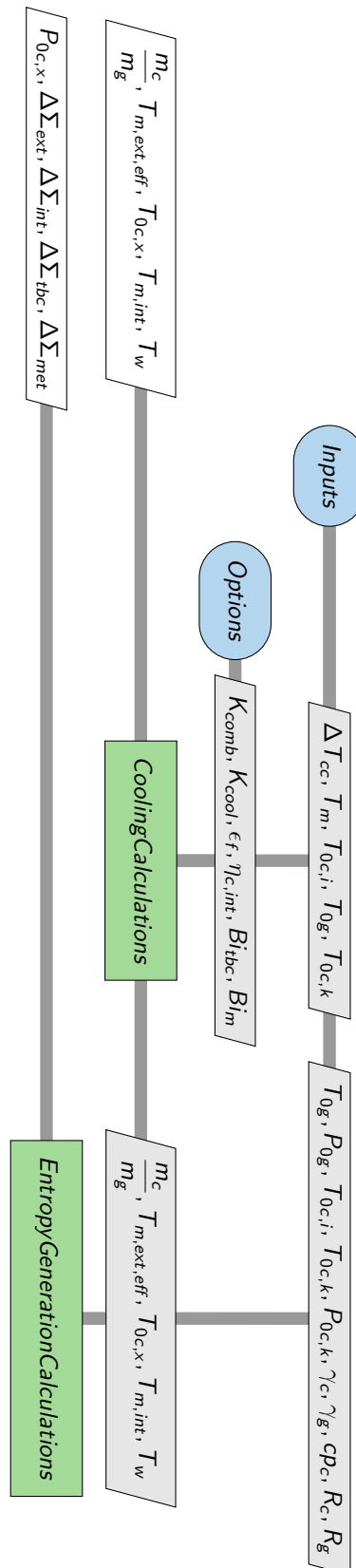
Figure 4.4: High Level XDSM of adapted Young and Wilcox model for use in cooled turbine model of *PyCycle*(*AdaptedYW*)

Output Variable	Symbol
Coolingflowfrac_max	$\dfrac{m_c}{m_g}$
T_metal_eff	$T_{metal,ext,eff}$
Tt_cool_postblade	$T_{0c,x}$
Tt_m,int	$T_{m,int}$
T_w	T_w
P0c_x	$P_{0c,x}$
Sig_int	$\Delta\Sigma_{int}$
Sig_ext	$\Delta\Sigma_{ext}$
Sig_met	$\Delta\Sigma_{met}$
Sig_tbc	$\Delta\Sigma_{tbc}$
Sig_cool	$\Delta\Sigma_{cool}$

Table 4.2: Output variables and symbols of cooling calculation component

will only be activated for cases where the blade material limit temperature is exceeded by the gas temperature.

Secondly, the CTM implementation of the Y&W calculates the momentum flux ratio based solely on thermodynamic properties and the flow factors, K_{int} and K_{ext}, whose definition is recalled here, namely:

$$K_{int} = \left(1 + \frac{\gamma_c - 1}{2} M_c^2\right) \tag{4.1}$$

$$K_{ext} = \left(1 + \frac{\gamma_g - 1}{2} M_g^2\right) \tag{4.2}$$

The flow mach numbers can be obtained from a user specified value of these flow parameters:

$$M_c = \sqrt{2} \cdot \sqrt{\frac{K_{int} - 1}{\gamma_c - 1}} \tag{4.3}$$

$$M_g = \sqrt{2} \cdot \sqrt{\frac{K_{ext} - 1}{\gamma_g - 1}} \tag{4.4}$$

As the ratio of specific heats for both flows is considered known in a cycle calculation, the momentum flux ratio can be specified as follows:

$$I = \frac{\gamma_c * \left(\sqrt{2} \cdot \sqrt{\frac{K_{int} - 1}{\gamma_c - 1}}\right)^2}{\gamma_g * \left(\sqrt{2} \cdot \sqrt{\frac{K_{ext} - 1}{\gamma_g - 1}}\right)^2} \tag{4.5}$$

Additionally, using the definition of the flow parameters and the definition of the Mach number, the flow velocities can be calculated, as shown below:

$$V_{c,x} = M_c * \sqrt{R_c \gamma_c \frac{T_{0cx}}{K_{int}}} \tag{4.6}$$

$$V_{g,x} = M_g * \sqrt{R_g \gamma_g \frac{T_{0g}}{K_{ext}}} \tag{4.7}$$

Hence, it is observed that the internal and external flow factors are used to quantify three variables: the flow velocities, the momentum flux ratios and the Mach numbers representing the coolant and bulk flow streams. Further discussion about suitable ranges for these flow factors will be addressed in chapter 6.

The final difference between the CTM implementation of the Y&W model and the original one is the necessity of analytical derivatives. *PyCycle* is specifically developed for use in gradient based optimisation, therefore the specification of analytic derivatives for every model component is required. The use of analytical derivatives allows significant reductions in computational times. This reduction is more prominent for complex component models with sparse Jacobians, where the majority of elements in the Jacobian are zero.
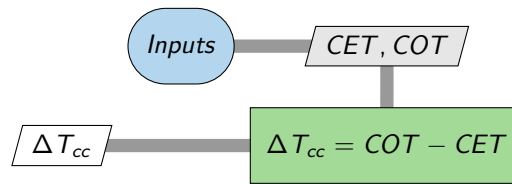
Figure 4.5: XDSM of element to calculate temperature rise over a combustor (*CombustorTempRise*)
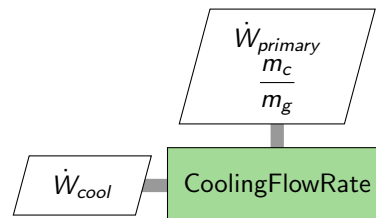
Figure 4.6: XDSM of element to calculate cooling flow rates (*CoolingFlowRate*)

Considering a function **F** with output variables g_1 and g_2, with input variables being x_1 and x_2, the Jacobian is the matrix of partial derivatives[78] given by:

$$J = \begin{bmatrix} \dfrac{\partial g_1}{\partial x_1} & \dfrac{\partial g_1}{\partial x_2} \\ \dfrac{\partial g_2}{\partial x_1} & \dfrac{\partial g_2}{\partial x_2} \end{bmatrix} \tag{4.8}$$

such that

$$\mathbf{F} = J \cdot \begin{bmatrix} x_1 \\ x_2 \end{bmatrix} \tag{4.9}$$

The CTM implementation of the Y&W model has 12 inputs and 11 outputs, resulting in 132 Jacobian entries. However, of these elements, only 65 are non-zero. Thus the Jacobian has a sparsity of 51%. The full Jacobian of the CTM, is presented in Table 4.3. Similar Jacobians have been constructed for every element within the CTM, to avoid the use of differencing schemes for numerical differentiation.

The XDSM of the grouped element, *YoungWilcoxCoolingCalcs* is shown in Figure 4.7. A key feature is the automatic passing of variables between components of the group, such as the combustor temperature rise into the adapted Y&W model and the cooling fraction into the cooling flow rate element. The group depicted allows the calculation of cooling fractions, cooling flows and entropy creation rates due to turbine cooling for a turbine blade row. The group forms the basis of the CTM as it can be used for both stator and rotor rows, with only reference frame conversions required. Reference frame conversions for rotor rows will be elaborated in further sections. As only a few of the outputs of each element in the group are required for further cycle calculations, few have been promoted to group-level outputs. In further sections, this group will be referred to solely as *CoolingCalcs*.

The CTM makes use of *PyCycle*'s own thermodynamic model, named *Thermo* to calculate the gas and air properties. The thermodynamic model is instantiated based on two state variables (e.g. temperature and pressure) and the fluid composition. For a cooled turbine blade row, two thermodynamic fluid models must be instantiated, one to represent the gas flow and the other for the cooling air flow. The resulting group is named *CooledTurbineRow* and depicted in Figure 4.8. This can be used to calculate cooling flows and entropy rise for both stators and rotors.

4.3. MODELLING OF COOLING AND BULK FLOW MIXING

The *CooledTurbineRow* block, presented in Figure 4.8 calculates the cooling requirements for a turbine blade row. However, this is not sufficient for use in a cycle calculation. The properties after mixing of bulk and

$$J =$$

∂T_{0g}	∂T_m	$\partial T_{0c,k}$	∂T_{tcool}	$\partial \Delta T_{cc}$	∂P_{0g}	$\partial P_{0c,k}$	∂cp_c	∂R_c	∂R_g	$\partial \gamma_g$	$\partial \gamma_c$
$\frac{\partial \frac{m_c}{m_g}}{\partial T_{0g}}$	$\frac{\partial \frac{m_c}{m_g}}{\partial T_m}$	0	$\frac{\partial \frac{m_c}{m_g}}{\partial T_{tcool}}$	$\frac{\partial \frac{m_c}{m_g}}{\partial \Delta T_{cc}}$	0	0	0	0	0	0	0
$\frac{\partial T_{metal,ext,eff}}{\partial T_{0g}}$	$\frac{\partial T_{metal,ext,eff}}{\partial T_m}$	0	$\frac{\partial T_{metal,ext,eff}}{\partial T_{tcool}}$	$\frac{\partial T_{metal,ext,eff}}{\partial \Delta T_{cc}}$	0	0	0	0	0	0	0
$\frac{\partial T_{0c,x}}{\partial T_{0g}}$	$\frac{\partial T_{0c,x}}{\partial T_m}$	0	$\frac{\partial T_{0c,x}}{\partial T_{tcool}}$	$\frac{\partial T_{0c,x}}{\partial \Delta T_{cc}}$	0	0	0	0	0	0	0
$\frac{\partial T_{n,int}}{\partial T_{0g}}$	$\frac{\partial T_{n,int}}{\partial T_m}$	0	$\frac{\partial T_{n,int}}{\partial T_{tcool}}$	$\frac{\partial T_{n,int}}{\partial \Delta T_{cc}}$	0	0	0	0	0	0	0
$\frac{\partial T_w}{\partial T_{0g}}$	$\frac{\partial T_w}{\partial T_m}$	0	$\frac{\partial T_w}{\partial T_{tcool}}$	$\frac{\partial T_w}{\partial \Delta T_{cc}}$	0	0	0	0	0	0	0
0	0	0	0	0	$\frac{\partial P_{0c,x}}{\partial P_{0g}}$	0	0	0	0	$\frac{\partial P_{0c,x}}{\partial \gamma_g}$	$\frac{\partial P_{0c,x}}{\partial \gamma_c}$
$\frac{\partial \Delta \Sigma_{ext}}{\partial T_{0g}}$	$\frac{\partial \Delta \Sigma_{ext}}{\partial T_m}$	0	$\frac{\partial \Delta \Sigma_{ext}}{\partial T_{tcool}}$	$\frac{\partial \Delta \Sigma_{ext}}{\partial \Delta T_{cc}}$	0	0	$\frac{\partial \Delta \Sigma_{ext}}{\partial cp_c}$	$\frac{\partial \Delta \Sigma_{ext}}{\partial R_c}$	$\frac{\partial \Delta \Sigma_{ext}}{\partial R_g}$	$\frac{\partial \Delta \Sigma_{ext}}{\partial \gamma_g}$	$\frac{\partial \Delta \Sigma_{ext}}{\partial \gamma_c}$
$\frac{\partial \Delta \Sigma_{int}}{\partial T_{0g}}$	$\frac{\partial \Delta \Sigma_{int}}{\partial T_m}$	$\frac{\partial \Delta \Sigma_{int}}{\partial T_{0c,k}}$	$\frac{\partial \Delta \Sigma_{int}}{\partial T_{tcool}}$	$\frac{\partial \Delta \Sigma_{int}}{\partial \Delta T_{cc}}$	$\frac{\partial \Delta \Sigma_{int}}{\partial P_{0g}}$	$\frac{\partial \Delta \Sigma_{int}}{\partial P_{0c,k}}$	$\frac{\partial \Delta \Sigma_{int}}{\partial cp_c}$	$\frac{\partial \Delta \Sigma_{int}}{\partial R_c}$	$\frac{\partial \Delta \Sigma_{int}}{\partial R_g}$	$\frac{\partial \Delta \Sigma_{int}}{\partial \gamma_g}$	$\frac{\partial \Delta \Sigma_{int}}{\partial \gamma_c}$
$\frac{\partial \Delta \Sigma_{tbc}}{\partial T_{0g}}$	$\frac{\partial \Delta \Sigma_{tbc}}{\partial T_{metal}}$	0	$\frac{\partial \Delta \Sigma_{tbc}}{\partial T_{tcool}}$	$\frac{\partial \Delta \Sigma_{tbc}}{\partial \Delta T_{cc}}$	0	0	$\frac{\partial \Delta \Sigma_{tbc}}{\partial cp_c}$	0	0	0	0
$\frac{\partial \Delta \Sigma_{metal}}{\partial T_{0g}}$	$\frac{\partial \Delta \Sigma_{metal}}{\partial T_m}$	0	$\frac{\partial \Delta \Sigma_{metal}}{\partial T_{tcool}}$	$\frac{\partial \Delta \Sigma_{metal}}{\partial \Delta T_{cc}}$	0	0	$\frac{\partial \Delta \Sigma_{metal}}{\partial cp_c}$	0	0	0	0
$\frac{\partial \Delta \Sigma_{cool}}{\partial T_{0g}}$	$\frac{\partial \Delta \Sigma_{cool}}{\partial T_m}$	$\frac{\partial \Delta \Sigma_{cool}}{\partial T_{0c,k}}$	$\frac{\partial \Delta \Sigma_{cool}}{\partial T_{tcool}}$	$\frac{\partial \Delta \Sigma_{cool}}{\partial \Delta T_{cc}}$	$\frac{\partial \Delta \Sigma_{cool}}{\partial P_{0g}}$	$\frac{\partial \Delta \Sigma_{cool}}{\partial P_{0c,k}}$	$\frac{\partial \Delta \Sigma_{cool}}{\partial cp_c}$	$\frac{\partial \Delta \Sigma_{cool}}{\partial R_c}$	$\frac{\partial \Delta \Sigma_{cool}}{\partial R_g}$	$\frac{\partial \Delta \Sigma_{cool}}{\partial \gamma_g}$	$\frac{\partial \Delta \Sigma_{cool}}{\partial \gamma_c}$

Table 4.3: Full Jacobian for adapted Young and Wilcox model based cooling calculation element, with sparsity of 51%
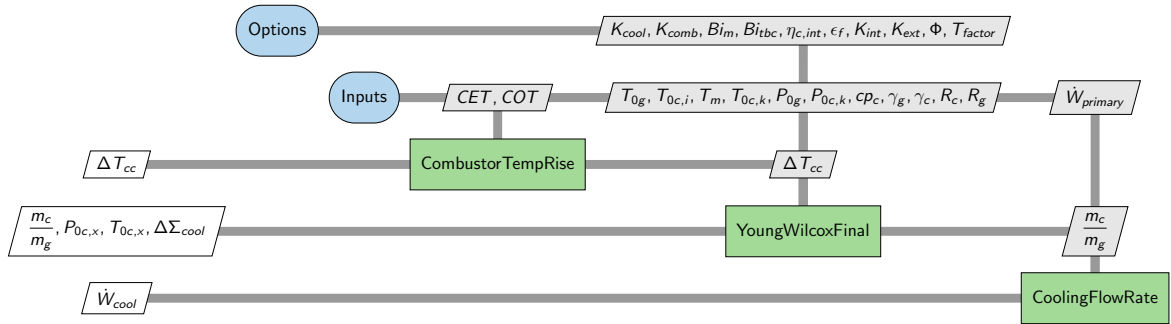
Figure 4.7: XDSM of *YoungWilcoxCoolingCalcs* grouped element
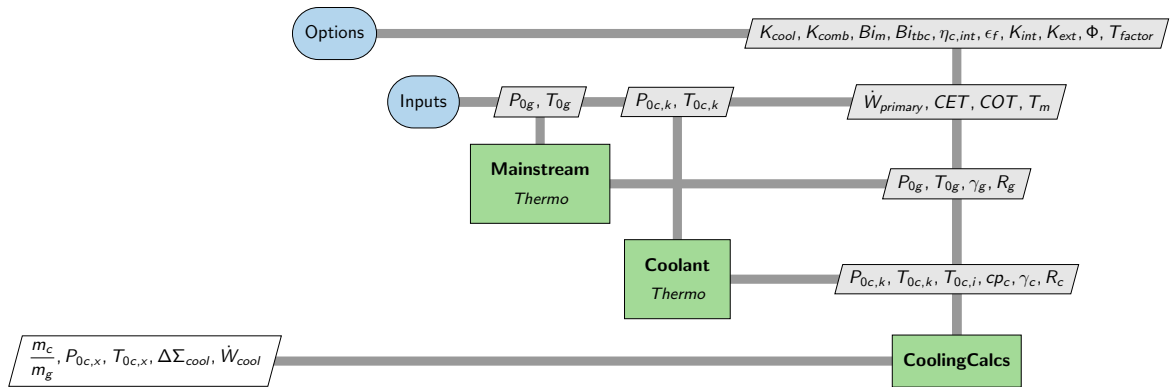
Figure 4.8: XDSM of *CooledTurbineRow* grouped element
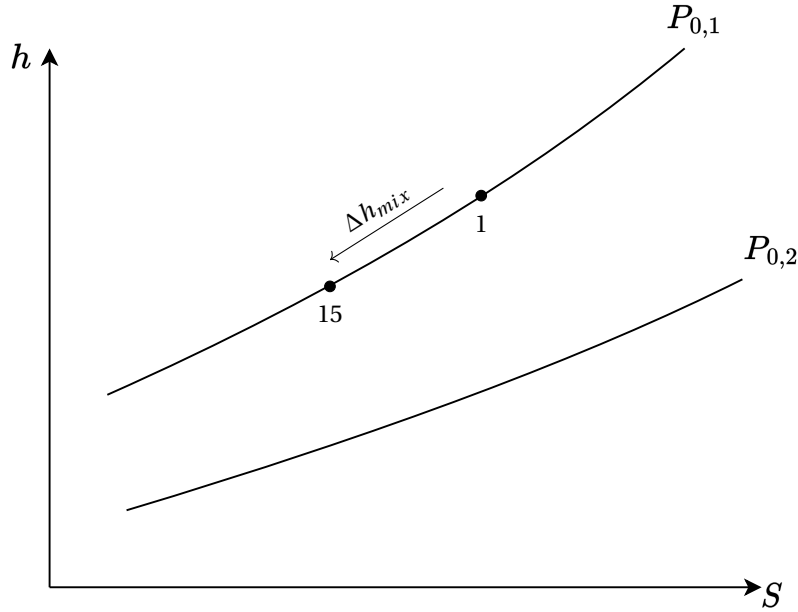
Figure 4.9: Enthalpy drop due to mixing of two flows with varying enthalpy, shown between stations 1 and 15.

coolant streams are needed to predict the engine performance. This requires modelling of the mixing process and the subsequent thermodynamic states.

Both enthalpy and entropy are state variables, with final state independent of path. It is chosen to model the mixing of both flow streams as a cooling process followed by a mixing process. The cooling process results in a decrease of enthalpy and change in bulk composition, while the mixing process results in an entropy rise, with a total pressure loss observed. This section will discuss both these processes, in subsection 4.3.1 and subsection 4.3.2, following which the the overall cooled row model is presented.

4.3.1. MIXED ENTHALPY & COMPOSITION
Firstly, the mixing of coolant air and bulk flow in the turbine will result in the reduction of the bulk flow enthalpy. Cooling air is typically drawn from compressor stages, where the air temperature is significantly lower than in the turbine, which results in a lower enthalpy for the coolant air than the hot gas. Station 15 is defined in Figure 4.1 as the point at which the mixed out enthalpy is known, but the mixed out total pressure is not known. At this station (or station 35) the enthalpy of the mixed flow is calculated using a mass-average, as shown:

$$h_{0,15} = \frac{\dot{W}_{primary} h_{0g} + \dot{W}_{cool} h_{0c}}{\dot{W}_{primary} + \dot{W}_{cool}} \tag{4.10}$$

where h_0 is the specific total enthalpy of either gas (g) or coolant (c). Depicting this process on a h-S diagram, it is observed that in the absence of any updated information on the pressure, it is assumed that the pressure of the bulk flow remains the same. Therefore Figure 4.9 shows an isobaric reduction in enthalpy, calculated as:

$$\Delta h_{mix} = h_{0,g1} - \frac{\dot{W}_{primary} h_{0g} + \dot{W}_{cool} h_{0c}}{\dot{W}_{primary} + \dot{W}_{cool}} \tag{4.11}$$

As the composition of the streams in *PyCycle* is specified by the user by means of the fuel to air ratio, *FAR*, the change in composition due to mixing is expressed in terms of this quantity. To understand the expected change in composition as a result of the injection of cooling flows, Figure 4.10 represents the variation in the outflow composition with increasing cooling fractions. The fuel to air ratio of the mixture, at station 15 (or 35) is calculated as follows:

$$FAR_{mix} = \frac{m_g}{m_g + m_c} \cdot FAR_{gas} \tag{4.12}$$

The composition calculated at this station 15 (or 35) is the composition that is taken as the inflow composition for the next turbine blade row.
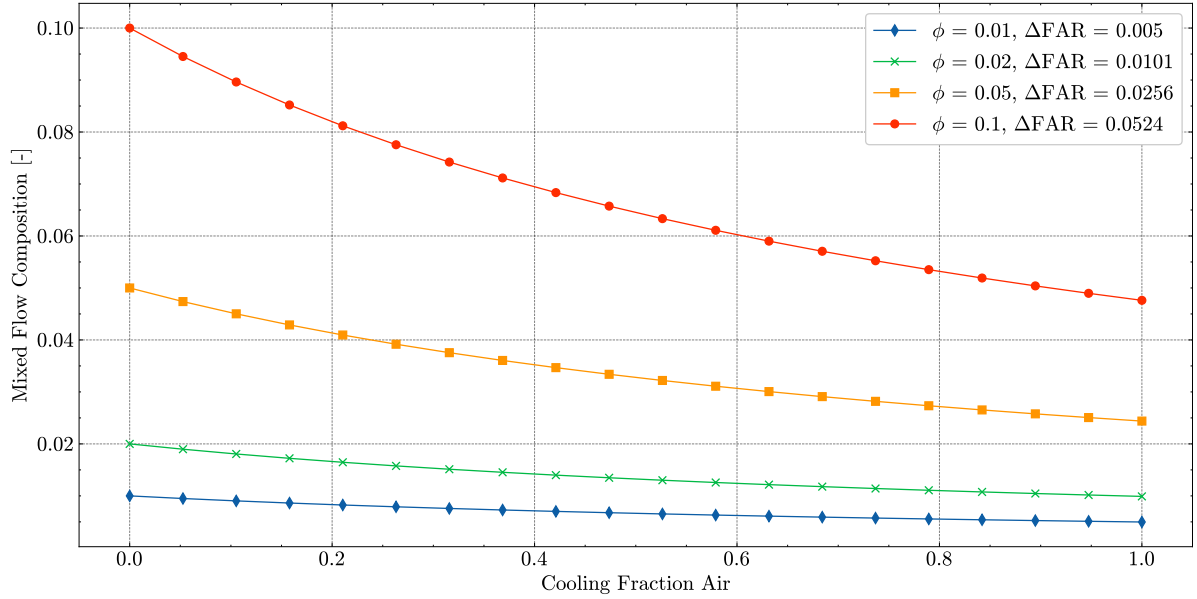
Figure 4.10: Variation in fluid composition with cooling air introduction for differing fuel to air ratios (ϕ). P_{0g} = 34 bar, T_{0g} = 1700 K, T_{0c} = 867 K and P_{0g} = 34 bar.

4.3.2. PRESSURE LOSSES DUE TO MIXING

The second process in the mixing of gas and coolant streams is the loss in total pressure due to entropy rise. The total entropy creation rate as a result of cooling is known for a cooled row as a result of the cooling calculations routine, $\Delta\Sigma_{cool}$. Referring to the h-S diagram, Figure 4.9, there are two key points to note:

- The entropy at station 15 is lower than the entropy associated with the mainstream flow at the blade row inlet

- The total pressure is the same as the mainstream flow

However, the various entropy sources accounted for in the cooling model need to be integrated into the thermodynamic cycle calculation. In order to do this, the entropy generation is added to the entropy of station 15, as defined on Figure 4.9. This results in a new point, associated with station 2, that corresponds to the row outlet condition. Therefore, at point two, the following information is known:

$$h_{0,2} = h_{0,15} = h_{0g,1} - \Delta h_{mix}$$

The entropy at station 15 is estimated given the enthalpy and the total pressure at the row inlet. Then, the entropy in station 2 is calculated as

$$S_2 = S_{15} + \Delta\Sigma_{cool}$$

Furthermore, the composition of the flow at the stator outlet is equal to the composition calculated at station 15 (or 35):

$$Comp_2 = Comp_{15}$$

Given the composition, total enthalpy and pressure and station 2, the total pressure of the stream leaving the blade row can be determined by means of the Mollier group described in section 2.6. Following this, the thermodynamic state, including all flow properties, at the row outlet, and mixing point are known.

The mixing process model described in subsection 4.3.1 and subsection 4.3.2 can be combined with the cooling requirement row model, *CooledTurbineRow*, shown in Figure 4.8. The result is an integrated model for a cooled turbine row which can be used for both stators and rotors. The structure of the integrated model is illustrated in Figure 4.11 for the case of a stator row, although the model structure is identical for a rotor row. The difference lies in the fact some flow quantities need to be defined in the rotating reference frame. As shown in the figure, for a specified mainstream flow (*g*), specified coolant flow (*c*), combustor temperature data and maximum blade temperature, the routine calculates the required cooling flows, the entropy generation and the thermodynamic properties at the blade row outlet.

Figure 4.11: XDSM of a cooled stator row
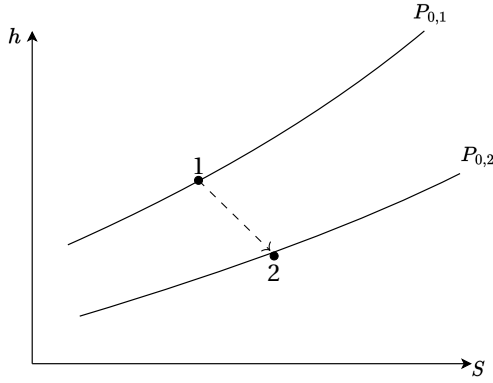
Figure 4.12: Expansion process in an uncooled turbine stage
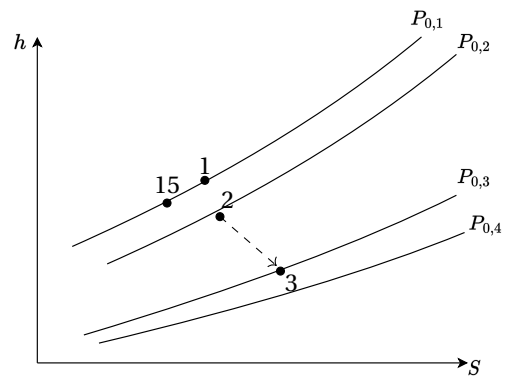
Figure 4.13: Expansion process in a cooled turbine stage

4.4. Modelling the work extraction process

The first step in modelling the work extraction process is to define an equivalent, uncooled stage to determine the operating conditions at which the cooled stage should operate. In this regard, it is assumed that the shaft power of the cooled stage should be equal to that of the uncooled stage, while the expansion occurs over the same pressure ratio of the uncooled stage. Therefore:

$$P_{cooled} = P_{uncooled}$$

$$\left(\frac{P_{0,2}}{P_{0,1}}\right)_{uncooled} = \left(\frac{P_{0,3}}{P_{0,2}}\right)_{cooled}$$

Moreover, blade angles are assumed to be unaffected by the coolant injection. Figure 4.12 shows the expansion process in an uncooled turbine stage and Figure 4.13 shows that in a cooled turbine stage.

Since the pressure ratio of the cooled stage and that of the uncooled one for work extraction are the same, any difference in stage pressure ratio can be attributed to the introduction of cooling flows and the subsequent loss of total pressure. This will facilitate the definition of cooled turbine efficiency, but also provides an immediate, quantifiable measure of performance degradation.

4.4.1. Modelling of the uncooled stage

The aim of the uncooled stage model is to determine the four outputs listed in Table 4.4 with the lowest computational effort.

Desired Output	Symbol	Unit
Uncooled stage outlet total pressure	Pt_{out}^{uc}	bar
Uncooled stage enthalpy drop	δh_t^{uc}	$\dfrac{J}{kg}$
Uncooled stage work transfer	WT_{uc}	W
Uncooled stage isentropic efficiency	η_{is}^{uc}	-

Table 4.4: Required outputs from uncooled stage model

The first output is obtained using the user-specified pressure ratio of the uncooled stage, given the inlet condition which is the same as that of the cooled stage, P_{0g}. Therefore:

$$Pt_{out}^{uc} = \frac{P_{0g}}{\beta_{uc}} \tag{4.13}$$

where β_{uc} is the ratio of the inlet total pressure to the outlet total pressure.

The next step is the evaluation of the entropy produced in the uncooled stage, with reference to Figure 4.14 this will define the difference in the horizontal coordinates of stations 1 and 3 (or 01 and 03 for total quantities). In order to do this, the user must specificy a polytropic stage efficiency. According to Young and Wilcox
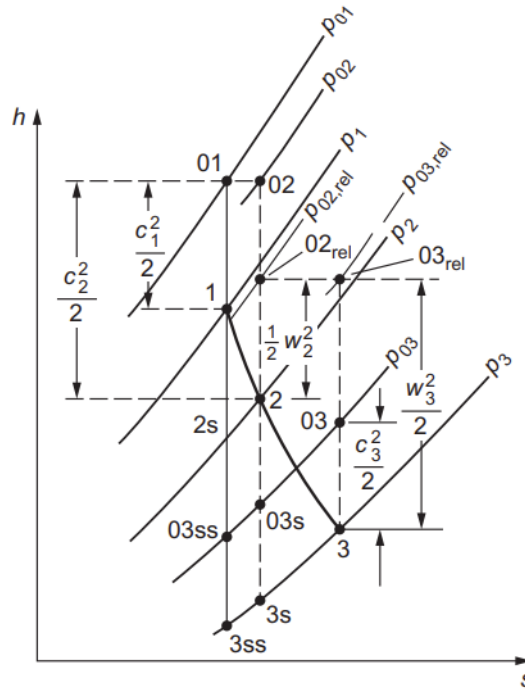
Figure 4.14: Mollier diagram of a turbine stage [4]

[17]:

$$\Delta\Sigma_{basic} = \dot{W}_{primary} \cdot R_g \cdot (1 - \eta_{p,uc}) \cdot \ln\left(\beta_{uc}\right) \tag{4.14}$$

To determine the outlet thermodynamic conditions of the uncooled turbine stage the first step is determining the thermodynamic conditions in a station *03ss*, resulting from an isentropic expansion of the working fluid over the specified pressure ratio. This is done by determining the thermodynamic state corresponding to the entropy in station and the target outlet pressure. The entropy at station 03 is then calculated as:

$$S_3 = S_{03ss} + \Delta\Sigma_{basic} \tag{4.15}$$

In the implemented CTM, defining the thermodynamic conditions at this uncooled stage outlet station requires another instance of *Thermo*, using the target outlet pressure and the newly calculated entropy at station 03.

The shaft power delivered by the stage is calculated based on the drop in specific enthalpy across the stage. Using the station numbering shown in Figure 4.14, it results that:

$$P_{uncooled} = \dot{W}_{primary} \cdot (h_{03} - h_{01}) \tag{4.16}$$

Finally, a parameter of interest is the isentropic efficiency of the uncooled stage. While the polytropic efficiency must be specified by the user, the isentropic efficiency is determined given the thermodynamic conditions estimated at the inlet and outlet of the uncooled stage, namely:

$$\eta_{is,uc} = \frac{h_{0,1} - h_{0,2}}{h_{0,1} - h_{0,2s}} \tag{4.17}$$

Examining the literature, Razak presents a formulation for the isentropic efficiency in terms of a specified polytropic efficiency [79]:

$$\eta_{is} = \frac{1 - \left(\dfrac{1}{\beta_{uc}}\right)^{\frac{\eta_{poly}(\gamma_g - 1)}{\gamma_g}}}{1 - \left(\dfrac{1}{\beta_{uc}}\right)^{\frac{(\gamma_g - 1)}{\gamma_g}}} \tag{4.18}$$

Comparing the results of the physically calculated isentropic efficiency, with the theoretically calculated isentropic efficiencies based on a number of polytropic efficiency values yields the results shown in Figure 4.15.
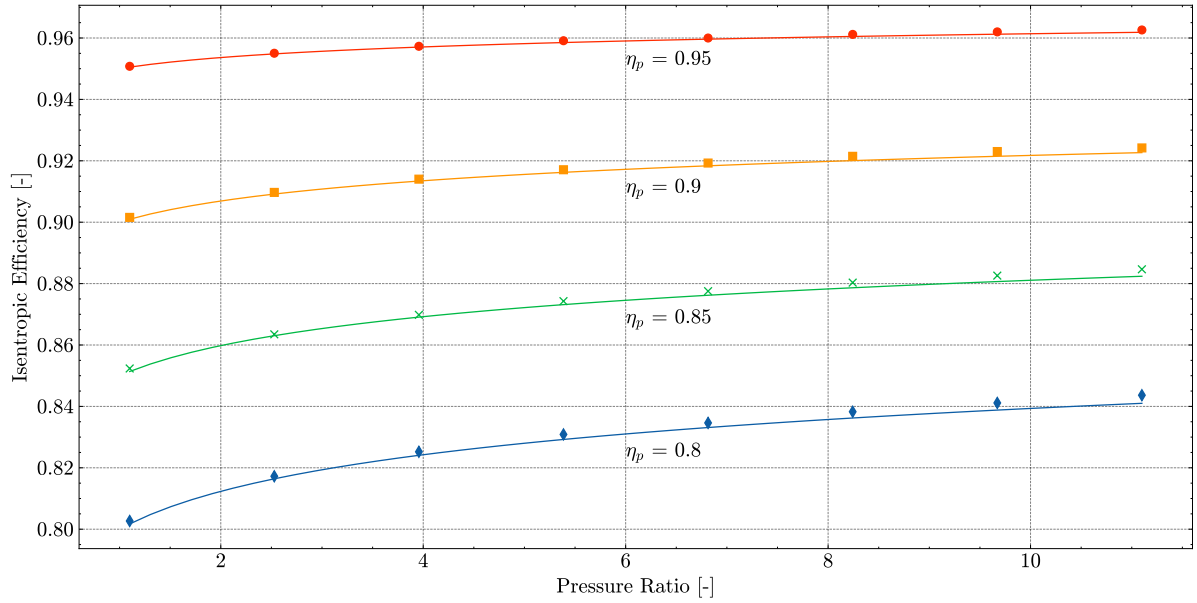
Figure 4.15: Variation of isentropic and polytropic efficiency of turbine stages with increasing pressure ratio. Markers used to represent outcome of uncooled stage model.

One significant note is the discontinuity when pressure ratio is 1, not shown on the chart. As the physically calculated isentropic efficiency works on the principle of enthalpy difference as perceived by the *Thermo* element, identical total pressures will result in identical enthalpies, therefore causing a false isentropic efficiency to be calculated of 1. Additionally, lower pressure ratios seems to yield closer outcomes of the uncooled stage model compared to the theoretical equation. This is due to the use of an averaged value for γ_g in the theoretical approximation. Examined over a large range of efficiencies and pressure ratios, the relative error between the uncooled stage model and the theoretical approximation never exceeds 1%. The results of this are shown in Appendix D.

4.4.2. Work Extraction Process in the Cooled Stage

Having solved the work extraction in the equivalent uncooled stage, the shaft power provided by the cooled stage is known. This means that it is possible to determine the enthalpy drop in the cooled turbine, dividing the shaft power by the massflow contributing to the work extraction.

It is necessary, then, to make an assumption with regard to the work done by cooling flow streams. It is assumed that:

1. Stator cooling flows do contribute to work extraction in the stage

2. Rotor cooling flows do not contribute to work extraction in the stage they are injected into, but they do contribute in the downstream stages.

Recalling the station numbering used in the implemented CTM, shown in Figure 4.1, station 2 is the stator exit and station 3 the rotor inlet. The enthalpy at station 3 is known by subtracting the enthalpy drop from the enthalpy at station 2. Additionally, as the work extraction process is assumed to occur over the same pressure ratio as the uncooled stage, the pressure at station 3 is also known. In mathematical terms:

$$h_{0g,3} = h_{0g,2} - \frac{P_{cooled}}{\dot{W}_{0g,2}}$$

$$P_{0g,3} = \frac{P_{0g,2}}{\beta_{uc}} \tag{4.19}$$

Given then enthalpy and pressure, all the thermodynamic properties at the rotor inlet station (3) can be determined by means of the *Thermo* block thereby concluding the procedure determining the work extraction

process. The XDSM of the model for work extraction is depicted in Figure 4.16, while that of the complete uncooled turbine stage is presented in Figure 4.17.

4.5. INERTIAL AND ROTATIONAL FRAMES OF REFERENCE

To apply the cooling model to a rotor row, the temperatures and enthalpies must be defined with respect to a frame of reference rotating with the blades [17]. A *PyCycle* group named *Adaptor* was implemented for this purpose. This section describes the transformations that need to be applied to the thermodynamic properties of both the mainstream and coolant flows. This will be discussed in subsection 4.5.1 and subsection 4.5.2. Following this the XDSM of the *Adaptor* group will be presented.

4.5.1. TRANSFORMATION OF MAINSTREAM FLOW REFERENCE FRAME

The heat transfer model of the CTM requires estimates of the rotor inlet flow enthalpy in a relative frame. The first step is to define the quantity rothalpy, I_r, whose definition according to Aungier [80] is:

$$I_r = H - \omega r C_\theta \tag{4.20}$$

where H represents the stagnation or total enthalpy of the flow in the absolute frame of reference. ω is the rotational velocity. r represents the radial position at which I_r is calculated. Finally, C_θ is the tangential velocity of the flow in the absolute frame of reference. This quantity is conserved along a streamline, provided that the sum of the shear work and heat transfer along the streamline are zero [81].

The definition of stagnation enthalpy in a rotating frame is analogous to the stagnation enthalpy of the flow in an absolute frame through the static enthalpy, which is equal for both frames. Defining the relative, specific, stagnation enthalpy ($h_{0,g}^{rel}$) and setting static enthalpies as equal, the relation between stagnation enthalpy in the rotating frame and in the absolute frame is as, as shown below:

$$h_g = h_{0,g}^{rel} - \frac{1}{2}W^2 = h_{0,g} - \frac{1}{2}C^2 \tag{4.21}$$

where C is the absolute velocity of the fluid, and W the relative velocity. Therefore, $h_{0,g}^{rel}$ can be expressed as:

$$h_{0,g}^{rel} = h_{0,g} - \frac{1}{2}C^2 + \frac{1}{2}W^2 \tag{4.22}$$

Using Aungier's definition of the relative velocity W in polar coordinate system, where [80]:

$$W_\theta = C_\theta - \omega r \tag{4.23}$$

$$W_m = C_m \tag{4.24}$$

and assuming no flow in the radial direction, the relative velocity is calculated:

$$W = \sqrt{W_m^2 + W_\theta^2} \tag{4.25}$$

Thus, Equation 4.22 can be rewritten:

$$h_{0,g}^{rel} = h_{0,g} - \frac{1}{2}C^2 + \frac{1}{2}\left(C_m^2 + C_\theta^2 - 2C_\theta\omega r + (\omega r)^2\right) \tag{4.26}$$

Since the absolute velocity in the polar coordinate system is equal to the square root of the sum of meridional (m) and tangential (θ) components, the above formula can be simplified to:

$$h_{0,g}^{rel} = h_{0,g} + \frac{1}{2}\left(-2C_\theta\omega r + (\omega r)^2\right) \tag{4.27}$$

$$h_{0,g}^{rel} = h_{0,g} + (-C_\theta\omega r) + \frac{1}{2}(\omega r)^2 = I_r + \frac{1}{2}(\omega r) \tag{4.28}$$

Which completes the derivation of the relationships between the relative and absolute frames.

The mean rotational velocity is defined as the product of the angular velocity and the radial position by Young and Wilcox [17]:

$$U_{mean} = \omega r \tag{4.29}$$
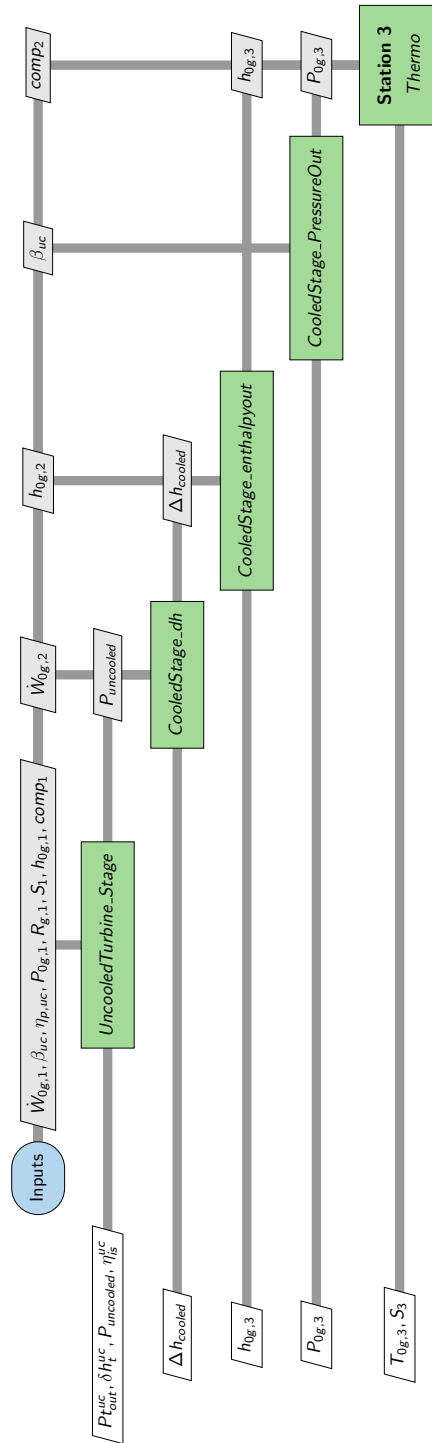
Figure 4.16: XDSM of module of elements used together to model the work extraction process between stations 2 and 3 of the cooled turbine stage
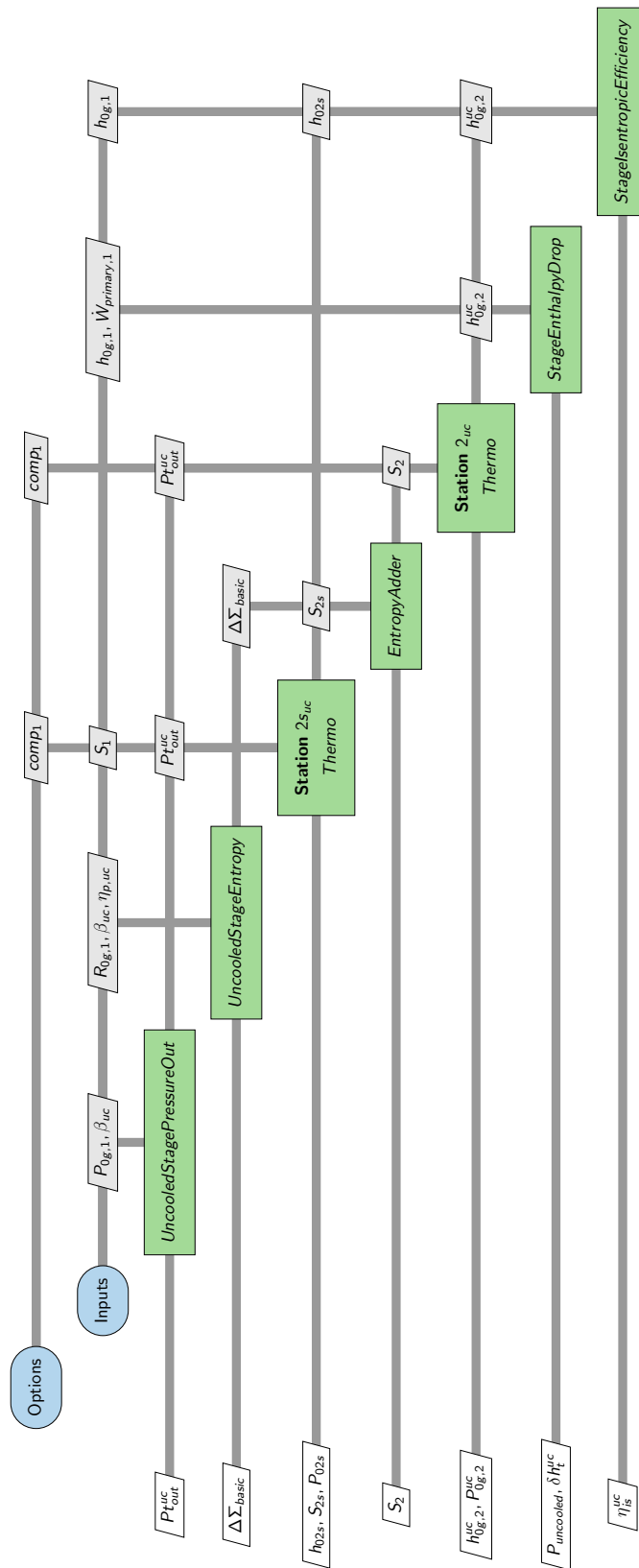
Figure 4.17: Expanded XDSM of *UncooledTurbine_Stage* group developed to model uncooled stage properties

Furthermore, Young and Wilcox denote C_θ by $(V_\theta)_{g,2}$, meaning that the prior expression for relative total enthalpy can be rewritten, namely:

$$h_{0g,2}^{rel} = h_{0g,2} + \frac{1}{2} U_{mean}^2 \left(1 - \frac{2(V_\theta)_{g,2}}{U_{mean}} \right) \tag{4.30}$$

Equation 4.30 represents the relation for the conversion of stagnation enthalpies between frames of reference. However, quantities such as $V_{\theta,g,2}$ and U_{mean} are unlikely to be known accurately in stages of design where cycle analysis is being performed. A simpler approach is, thus, required.

Defining a simplified control volume over the rotor row, as represented in Figure 4.18,
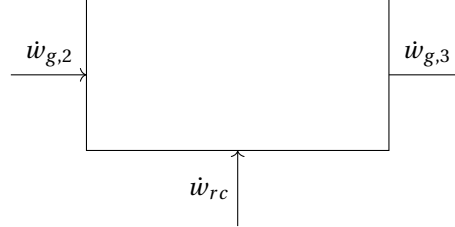
Figure 4.18: Control volume over rotor row

the power extracted over the rotor can be expressed as a balance of the mass averaged enthalpy differences:

$$P = \dot{W}_{g,2} \left(h_{0g,2} - h_{0g,3} \right) + \dot{W}_{rc} \left(h_{0rc,i} - h_{0g,3} \right) \tag{4.31}$$

By referring to the Euler turbine equations, the same quantity can be expressed as

$$P = \dot{W}_{g,2} \left((UV_\theta)_{0g,2} - (UV_\theta)_{0g,3} \right) + \dot{W}_{rc} \left((UV_\theta)_{0rc,i} - (UV_\theta)_{0g,3} \right) \tag{4.32}$$

Two major assumptions are made. The first is that the flow leaves the rotor control volume with no swirl velocity, meaning that V_θ is 0 at station 3. The second is that the addition of the rotor coolant is negligible. This assumption is coherent with those made in estimating the work extraction process, namely that the rotor cooling flow does not contribute to the shaft power of the stage. On the basis of these two assumptions, Equation 4.31 and Equation 4.32 can be simplified as follows:

$$P = \dot{W}_{g,2} \left(h_{0g,2} - h_{0g,3} \right) \tag{4.33}$$

and

$$P = \dot{W}_{g,2} \left((UV_\theta)_{0g,2} \right) \tag{4.34}$$

The power delivered by the stage can be then expressed as a function of the stage loading coefficient Ψ, whose definition is recalled as:

$$\psi = \frac{P}{\dot{W}_{0g,3} \cdot U_{mean}^2} \tag{4.35}$$

As the mass flow between stator outlet and stage outlet is constant if coolant flow to the rotor is neglected [17], it results that:

$$\psi = \frac{V_{\theta g,2}}{U_{mean}} = \frac{h_{0g,2} - h_{0g,3}}{U_{mean}^2} \tag{4.36}$$

Combining this expression with Equation 4.30 gives an approximate relation for reference frame conversion expressed in terms of a user specified stage loading coefficient:

$$h_{0g,2}^{rel} = \left(\frac{1}{2\psi} \right) h_{0g,2} + \left(1 - \frac{1}{2\psi} \right) h_{0g,3} \tag{4.37}$$

where $h_{0g,3}$ represents the outlet enthalpy of the stage. Therefore, to fully define the flow properties of the mainstream after stator outlet, in the rotating reference frame, it is necessary to know the load coefficient as well as the flow enthalpy at the outlet of the stage, calculated with respect to the mass flow rate leaving the stator. As the required shaft power contribution is known, as it is assumed equal to that of the equivalent uncooled stage, this information can be used to calculate the enthalpy at station 3, using the mass flow of the

stator outlet. Then, to determine the thermodynamic properties of station 2 in the relative frame, such that they may be used to determine the cooling properties of the rotor row, it is sufficient to use the *Thermo* group.

and thus can be used to calculate the enthalpy at station 3, using the mass flow of the stator outlet. Then, to instantiate the thermodynamic properties of station 2 in a relative frame, such that they may be used to determine the cooling properties of the rotor row, requires another instance of *Thermo*.

4.5.2. TRANSFORMATION OF COOLANT FLOW REFERENCE FRAME

The conversion of the coolant flow total enthalpy in the rotating frame follows the same procedure, with Young and Wilcox defining the difference between the enthalpies in the two different reference frames as follows [14]:

$$h_{0rc,i} - h_{0rc,i}^{rel} = (UV_\theta)_{rc,i} - \frac{U_{rc,i}^2}{2} \tag{4.38}$$

$h_{0rc,i}^{rel}$ is less than $h_{0rc,i}$ only if the swirl velocity of the coolant exceeds the mean rotational velocity. Utilizing the definition of the loading factor, Equation 4.38 is rewritten as:

$$h_{0rc,i} - h_{0rc,i}^{rel} = (K_{swirl} - \frac{1}{2}) \frac{P}{\dot{W}_{0g,3} \psi} \tag{4.39}$$

This formulation is used by Young and Wilcox, although Uysal argues that the 0.5 subtracted from K_{swirl} should be replaced by the degree of reaction of the stage [20]. For stages with no exit swirl, the degree of reaction and the stage loading coefficient are linked to each other by a simple relation:

$$\psi = 2 \cdot (1 - {}^\circ R) \tag{4.40}$$

with ${}^\circ R$ as the degree of reaction. For the case described in the original work, with a stage load coefficient of 1, the degree of reaction would be 0.5. Therefore, it is possible to determine the coolant enthalpy in the rotating frame by specifying the stage load coefficient, the mass flow rate after the stator and the stage shaft work contribution of the bulk flow.

The XDSM of the *Adaptor* group is presented in Figure 4.19.Note that the enthalpy out of the rotor uncooled stage is represented by $h_{0g,3}^{ucr}$, which differs from the exit enthalpy of a fully cooled stage, as stator cooling flow is accounted for in the frame transformation. Additionally, ψ and K_{swirl} must be user specified, as they are set constant, as options.
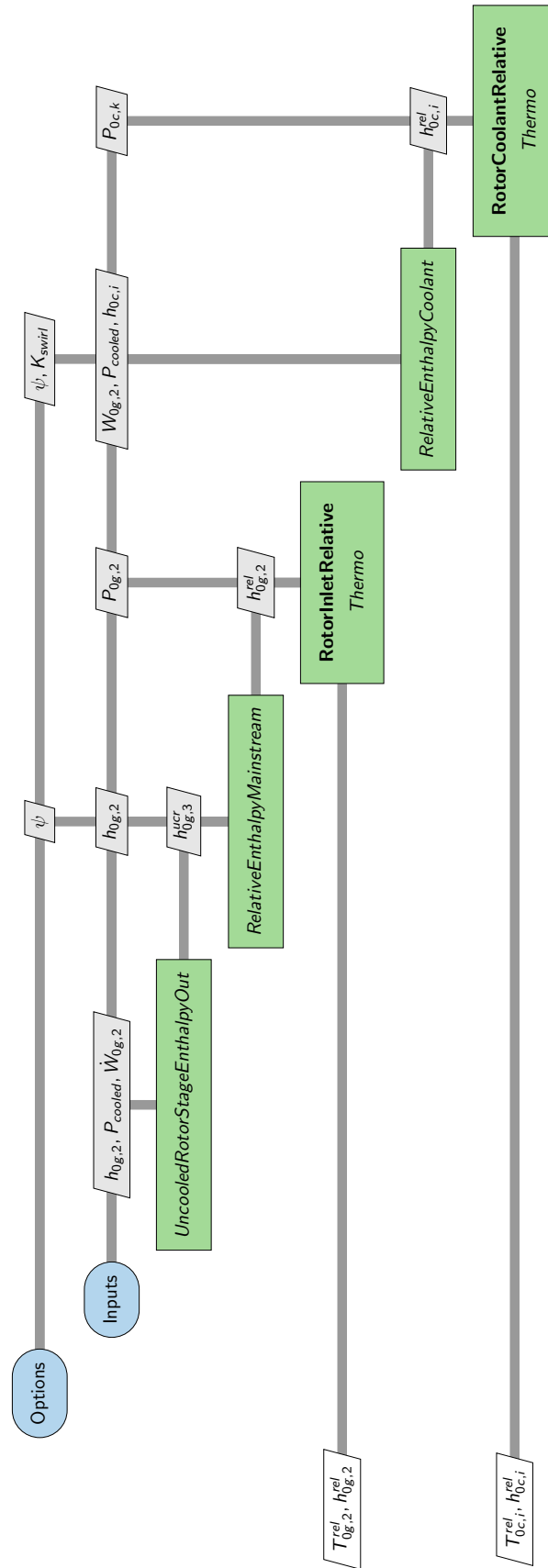
Figure 4.19: XDSM of *Adaptor* group used to transform stator outlet quantities into relative frame of reference for rotor entry

5

VERIFICATION & VALIDATION

PyCycle has been extensively verified and validated by its developers and compared with NPSS, a numerical propulsion system modeling tool [71]. This chapter presents the verification and validation tests performed on the Cooled Turbine Model (CTM) developed for use in cycle calculations in *PyCycle*. Verification is performed by comparing the test case presented by Young and Wilcox [17] in the original paper. Furthermore, the comparison is extended to the results obtained by Uysal [20] for the same test case. This comparison is presented in section 5.1. Following this, the model validation is performed using two test cases. The first one is based on the experimental results for a transonic nozzle guide vane (NGV), reported by Alfa Romeo [30]. This is presented in section 5.2. Furthermore, the CTM is validated against the results of NASA's Energy Efficient Engine (E3 Engine) program [21],presented in section 5.3. Following this, validation of the calculation of cooled turbine efficiency is presented in section 5.4. Finally, a discussion on the influence of the empirical parameters on the validity of the CTM cooling calculations is presented in section 5.5.

5.1. VERIFICATION - YOUNG & WILCOX TEST CASE

The first test case is the one presented by Young and Wilcox [14]. The number of output parameters that can be compared is limited, since the example in the original paper limits itself to row-wise properties. However, the comparison between the CTM results and the Y&W test case will serve as a verification of the CTM, in particular for the cooling calculation module. The input data for this test case are presented in Table 5.1.

Quantity	Value	Unit	Quantity	Value	Unit
$T_{0g,1}$	1700	K	$K_{comb,stator}$	0.1	-
T_{metal}	1100	K	$K_{comb,rotor}$	0.05	-
$T_{0c,k}$	867	K	K_{swirl}	0.5	-
P_{0g}	34	bar	K_{cool}	0.045	-
$P_{0c,k}$	34	bar	$\eta_{c,int}$	0.7	-
$\dfrac{P_{0g,1}}{P_{0g,4}}$	2.4	-	ϵ_f	0.4	-
ψ	1.0	-	Bi_m	0.2	-
η_p	0.9	-	Bi_{tbc}	0.0	-
K_{int}	1.01	-	ϕ	30	°
K_{ext}	1.07	-			

Table 5.1: Input parameters for test case presented by Young and Wilcox (YW)[14]

The data provided in Table 5.1 includes most of the inputs required by the CTM. However, thermodynamic flow properties such as the heat capacity,cp, and ratio of specific heats ,γ, is missing for both gas and coolant flows. In the CTM, such properties are specified by means of the fuel-to-air ratio, FAR. For the cooling air, this is set to 0. To obtain reasonable values for the gas flow, more recent work by Young & Horlock [29] presents

Quantity	Young & Wilcox	Cooled Turbine Model	Relative Error (%)
$\left(\dfrac{m_c}{m_g}\right)$	0.145	0.1447	0.21
ϵ_0	0.75	0.7457	0.57
$T_{0g,2}$	1603	1602.7665	0.01
$T_{0c,x}$	969	969.23	0.02
$T_{m,ext}$	1078	1078.818	0.08
$T_{m,int}$	1013	1013.04	0.00

Table 5.2: Comparison of outputs for stator rows in the YW testcase

Quantity	Young & Wilcox	Cooled Turbine Model	Relative Error (%)
$\left(\dfrac{m_c}{m_g}\right)$	0.049	0.0723	47.55
ϵ_0	0.58	0.645	11.21
$T_{0g,2}^{rel}$	1487	1481.801	0.35
$T_{0c,x}$	966	991.676	2.66
$T_{m,ext}$	1082	1085.216	0.3
$T_{m,int}$	1043	1045.109	0.2

Table 5.3: Comparison of outputs for rotor rows in the YW testcase

typical values for these quantities, namely:

$$cp_g = 1200 \frac{J}{kg \cdot K} \tag{5.1}$$

$$\gamma_g = 1.32 \tag{5.2}$$

However, attempts to replicate these values in combination with the gas properties in Table 5.1 in *PyCycle*'s thermodynamics solver showed that this is not possible for any reasonable value of FAR. It should be noted that the values suggested by Young & Wilcox are representative of a simple air-gas mixture, with methane as the fuel. For engine modelling, the default fuel modelled in *PyCycle* is JetA1. It was chosen to retain this, to more accurately model the conditions in aero-engine turbines as well as to avoid having to specify chemical properties of methane-air mixtures within *PyCycle*. For JetA1, Van Buijtenen et. al [3] place the equivalence ratio of the CFM-56, a turbofan used for single-aisle commercial aircraft such as the 737, at approximately 0.27 at take-off. Thus, taking an equivalence ratio of 0.27, the fuel to air ratio would be:

$$FAR = 0.27 * \frac{1}{14.7} = 0.0183 \tag{5.3}$$

where 14.7 is the stoichiometric fuel to air ratio for JetA1 as derived in chapter 2.

5.1.1. VERIFICATION RESULTS - COOLING FLOW RATES & TEMPERATURES

Using the input data provided in section 5.1, the results for the stator and rotor row as calculated by the CTM are shown in Table 5.2 and Table 5.3, respectively.

Observing the stator row results in Table 5.2, it is seen that there are no significant discrepancies, with all terms within 1% of the results of Young and Wilcox [17]. This suggests that the calculation procedure for a cooled row, including mixing of flow streams has been implemented accurately.

Results for the rotor row, in Table 5.3 show significant discrepancies with the results of Young and Wilcox [17]. Most significantly, the CTM overestimates the cooling fraction by 48%. Additionally, the cooling effectiveness parameter, ϵ_0, shows an 11% variation. As ϵ_0 is used in the calculation of the cooling fraction as well, it is likely that the reason of this discrepancy lies in the calculation of ϵ_0. Recalling the definition of the cooling effectiveness parameter:

$$\epsilon_0 = \frac{T_{0g} - T_{m,ext}}{T_{0g} - T_{0c,i}} \tag{5.4}$$

it is observed that the value of ϵ_0 depends on the mainstream and coolant temperatures. From the results of the stator row, it is reasonable to assume that the assumed value for the metal temperature is reasonable for the rotor row as well. The gas temperature and coolant temperatures must be specified in the relative frame of reference for rotors. Table 5.3 shows that the calculated value for the relative temperature of the mainstream flow entering the rotor row, $T_{0g,2}^{rel}$, is within acceptable limits of the results presented by the test case. Therefore, the source of the error is likely to lie in the conversion of the reference frame for the coolant flow. The conversion equation for coolant flow reference frame is given by:

$$h_{0rc,i} - h_{0rc,i}^{rel} = (K_{swirl} - \frac{1}{2}) \frac{P}{\dot{W}_{0g,3}\psi} \qquad (5.5)$$

where P is the specific power of the stage. The CTM calculates the power based on the work transfer required from an equivalent uncooled stage. The work transfer of the equivalent uncooled stage is used to define the uncooled stage outlet enthalpy, $h_{0g,3}$, which, in turn, is used to define the mainstream properties in the rotating reference frame. As the results for the mainstream flow are acceptably accurate, the value calculated for power is unlikely to be the source of the discrepancy. The mass flow rate $\dot{W}$ at station 3 is equivalent to the stator outflow mass flow rate since Equation 5.5 neglects the rotor coolant addition. Furthermore, the stage load coefficient is user specified. Therefore, the source of error is likely to lie in the value specified for the rotor swirl factor, K_{swirl}.

The rotor swirl factor is defined as the ratio of the swirl velocity of the coolant entering the blade (V_θ) to the blade speed (U), namely:

$$K_{swirl} = \frac{(V_\theta)_{rc,i}}{U_{rc,i}} \qquad (5.6)$$

From Equation 5.5 it can be seen that when K_{swirl} is 0.5, the relative enthalpy is the same as the relative total enthalpy. While Young and Wilcox indicate that the parameter can take values between 0 and 2.5, the work of Yanhua et. al [82] suggests significant benefits exist to swirling of cooling flows with higher values of K_{swirl}. Swirling of cooling air can raise cooling effectiveness over the entire blade surface area significantly, and as such it is unlikely that any realistic cooling system design will account for K_{swirl} less than 0.5. Furthermore, Kurzke [15] suggests that relative temperatures are often 90% of absolute temperatures in cooled turbine stages. Rearranging Equation 5.5 to represent the ratio of enthalpies, $\frac{h_{0rc,i}^{rel}}{h_{0rc,i}}$, we obtain:

$$1 - \frac{h_{0rc,i}^{rel}}{h_{0rc,i}} = \left(K_{swirl} - \frac{1}{2}\right) \frac{P}{\dot{W}_{0g,3}\psi \cdot h_{0rc,i}} \qquad (5.7)$$

$$\frac{h_{0rc,i}^{rel}}{h_{0rc,i}} = 1 - \left(K_{swirl} - \frac{1}{2}\right) \frac{P}{\dot{W}_{0g,3}\psi \cdot h_{0rc,i}} \qquad (5.8)$$

The ratio of the specific, total enthalpy in the relative reference to the specific total enthalpy in the fixed reference frame can be plotted as a function of the swirl parameter. Calculated parameters are shown in Table 5.4. The mass flow rate that must be used for this conversion is the mass flow after the stator cooling flow has been introduced. Enthalpy of the coolant at condition i is defined using *PyCycle*'s built-in thermodynamics model.

Quantity	Value	Unit
P	352	kW
$\dot{W}_{0g,3}$	1.447	kg/s
ψ	1.0	-

Table 5.4: Parameters used to define the ratio of specific total enthalpy of the coolant in rotating and fixed references frames. These are used to calculate the ratio for variations in rotor swirl parameter, K_{swirl}.

The variation in the ratio is seen in Figure 5.1, confirming that values of 0.5 result in no difference between the coolant total enthalpy in the two reference frames. Additionally it is observed that for values lower than 0.5, a lower stage power contribution results in a higher ratio of relative to absolute specific total enthalpy. Values of K_{swirl} between 0.7 and 0.8 satisfy the approximated ratio suggested by Kurzke.
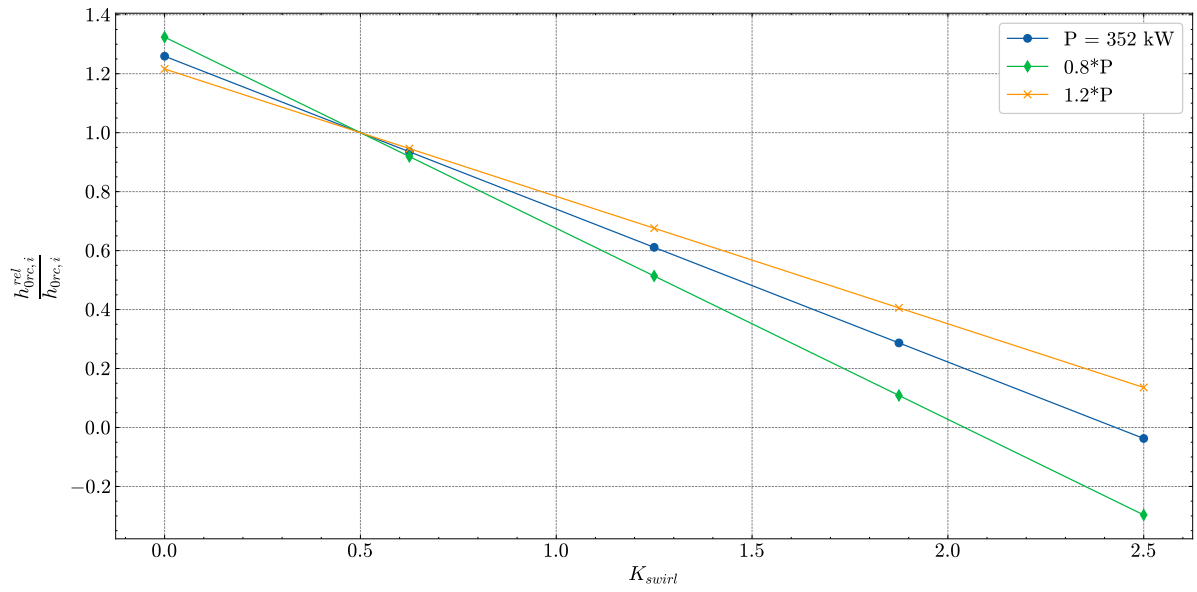
Figure 5.1: Variation in framewise enthalpy ratio with rotor swirl parameter for varying shaft work contributions
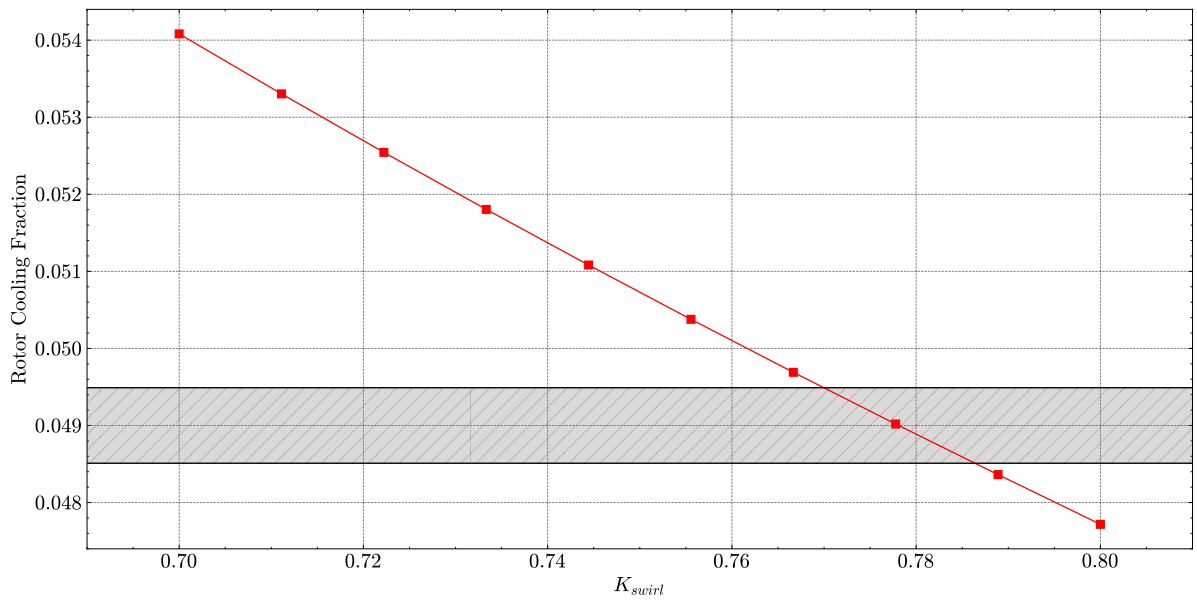
Figure 5.2: Variation in rotor cooling fraction with rotor swirl factor for single turbine stage. Shaded band indicates ± 1% from provided data [14]
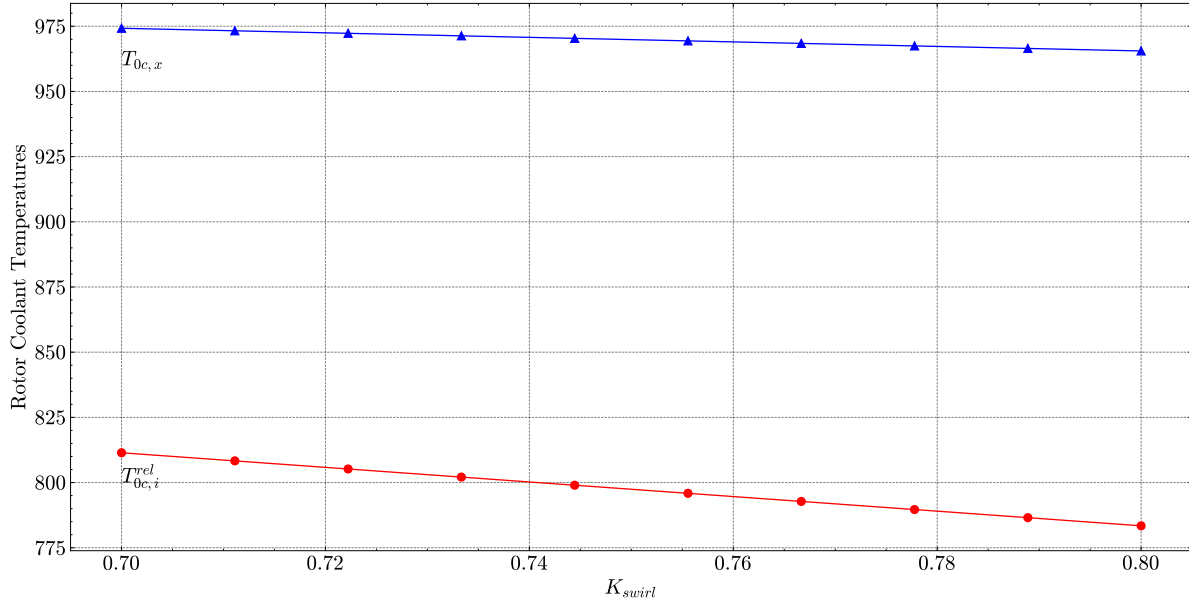
Figure 5.3: Variation in relative rotor coolant entry and exit temperatures with rotor swirl factor

Within this range, the effect of the value of K_{swirl} on the cooling fractions of the rotor and the coolant inlet and exit temperatures is shown in Figure 5.2 and Figure 5.3.

The linear relationship between the swirl factor and coolant fraction seen in Figure 5.2 is the result of the direct relationship between the swirl factor and the coolant inlet temperature. In turn, this coolant inlet temperature is used to define the cooling effectiveness parameter which drives the coolant fraction. Additionally, it is observed that the variation in the coolant exit temperature, $T_{0c,x}$, the temperature with which it exits the blade varies less with K_{swirl} than the relative inlet temperature.

Furthermore, Figure 5.2 shows that an appropriate value for K_{swirl} for the Y&W test case is 0.77. Running the CTM with this updated K_{swirl} value results an almost perfect match of the values reported by the authors, as shown in Table 5.5.

Quantity	Young & Wilcox	Cooled Turbine Model	Relative Error (%)	Change in rel. error (%)
$\left(\dfrac{m_c}{m_g}\right)$	0.049	0.0494	0.82	98
ϵ_0	0.58	0.5787	0.22	98
$T_{0g,2}^{rel}$	1487	1481.801	0.35	0
$T_{0c,x}$	966	968.126	0.22	92
$T_{m,ext}$	1082	1082.456	0.04	87
$T_{m,int}$	1043	1043.681	0.07	65

Table 5.5: Comparison of the results for the rotor row in the YW testcase with updated value of K_{swirl} = 0.77

As shown in Table 5.5, altering the swirl parameter significantly changes the outcome of the rotor module calculations, with up to 98% reduction in relative error for the cooling fraction. Regarding the blade temperatures, it is observed that while they are affected by the swirl parameter, the change and gain in calculation accuracy are not significant. Nonetheless, adapting the value of K_{swirl}, the CTM is able to predict results within 1% of maximum deviation with respect to the results reported by Young and Wilcox, meeting an acceptable level of accuracy.

5.1.2. Verification Results - Entropy Generation

The second step in verification of the CTM involves the entropy generation calculation module. Young and Wilcox [17] provide an overview of the variation of entropy terms with changes in the cooling parameter K_{cool}, see Figure 5.4. The verification of the CTM is done for two points in the chart. The first is when K_{cool} is 0.045,
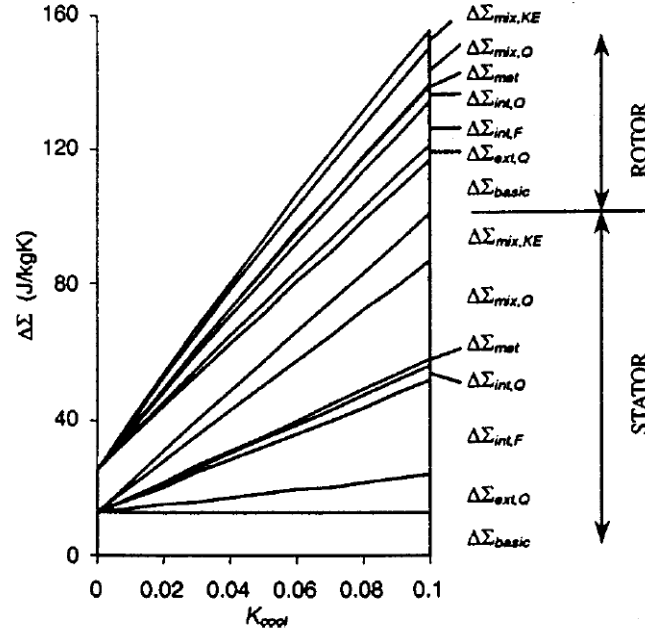
Figure 5.4: Variation in loss sources with K_{cool} [14]

as prescribed in the original test case. The second is when K_{cool} is 0.08. Data is obtained through digitisation of the chart. Entropy generation estimates for both values of K_{cool} are presented in Figure 5.5 and Figure 5.6.

The figures Figure 5.5 and Figure 5.6 show that the magnitude of the loss terms is identical to that in Figure 5.4, namely:

$$\Delta\Sigma_{mix,q} > \Delta\Sigma_{int,f} > \Delta\Sigma_{mix,KE} > \Delta\Sigma_{ext,q} > \Delta\Sigma_{int,Q} > \Delta\Sigma_{met} \qquad (5.9)$$

These trends are confirmed in Figure 5.7 and Figure 5.8, which illustrate the variation in the entropy terms with K_{cool}. Figure 5.8 compares the trend of a few entropy generation terms with K_{cool} against the trend reported by Y&W.

Observing Figure 5.5 and Figure 5.6, it is seen that the term describing external heat transfer, $\Delta\Sigma_{ext,Q}$ is matched quite accurately. Additionally, basic entropy generation terms match well for both values of the cooling parameter. Considering other terms, it is seen that the CTM under-predicts the internal entropy generation terms, most significantly $\Delta\Sigma_{int,f}$. The terms describing losses associated with mixing ($\Delta\Sigma_{ext,mix,q}$ and $\Delta\Sigma_{ext,mix,KE}$) are over-predicted. Furthermore, considering the entropy generation due to heat transfer through the blade ($\Delta\Sigma_{met}$), a over-prediction is noted, although this is seen to reduce with increasing value of K_{cool}. Overall, the CTM over-predicts the total entropy rise due to cooling, $\Delta\Sigma_{cool}$ by approximately 7-8%. The variation of individual entropy generation terms with K_{cool} can be found in Appendix B.

Another source for the CTM verification is the work of Uysal [20], based on the Young and Wilcox model. Uysal presents entropy results for the case where K_{cool} is 0.045. Figure 5.9 presents a comparison of the CTM's results with Uysal's data and the average of the digitized data sets reported in Figure 5.5 and those provided by Uysal [20], for his verification analysis.

From Figure 5.9 it is seen that the mixing heat transfer entropy term, $\Delta\Sigma_{mix,q}$ is over-predicted significantly by both Uysal's model and the CTM. Relative errors of both models (CTM & Uysal) are shown in Table 5.6, suggesting that the CTM is generally accurate. A significant outlier is the term representing entropy rise due to heat transfer through blade metal, $\Delta\Sigma_{met}$, although the small magnitude of this term limits its influence on the overall calculation.

Having compared the CTM performance with Y&W data and Uysal's model, the next step is to investigate potential error sources. Firstly, considering the term $\Delta\Sigma_{mix,q}$ representing entropy rise due to heat transfer during mixing of coolant and gas flow streams. The term is defined as:

$$\Delta\Sigma_{mix,q} = m_c c p_c \left(ln\left(\frac{T_{g,x}}{T_{c,x}}\right) - \left(1 - \frac{T_{c,x}}{T_{g,x}}\right) \right) \qquad (5.10)$$

The flow parameters defined in Equation 3.7 and Equation 3.8, K_{int} and K_{ext} allow the conversion of static to
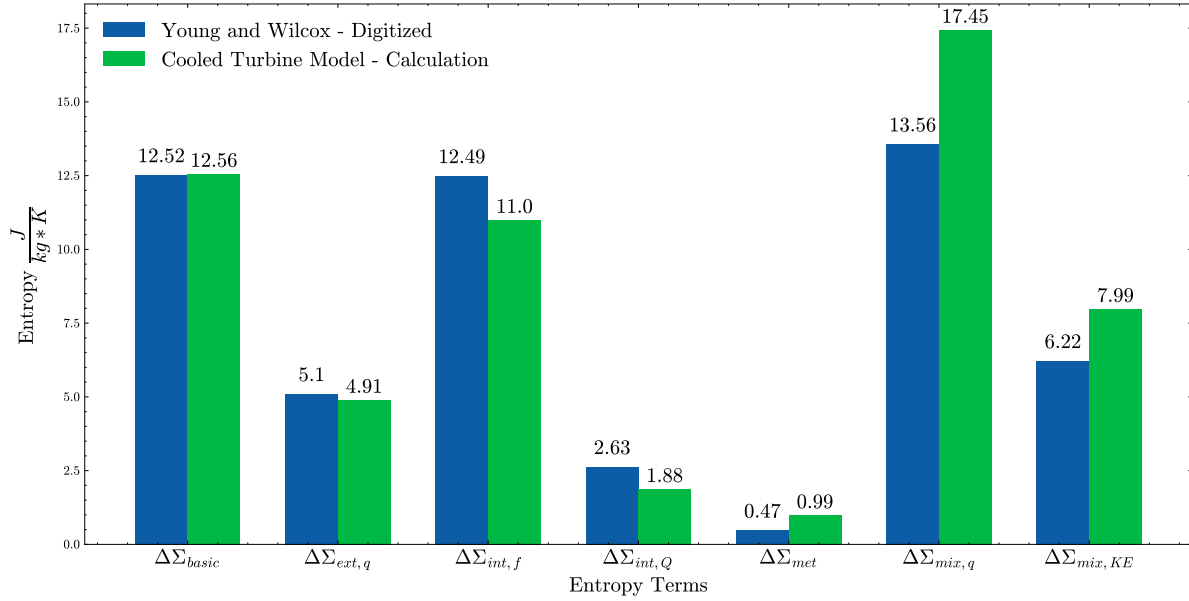
Figure 5.5: Comparison of entropy terms for $K_{cool} = 0.045$, $T_{0g} = 1700$ K, $T_{0c,i} = 867$ K, $T_{metal} = 1100$ K, $\epsilon_f = 0.4$ and $\eta_{c,int} = 0.7$
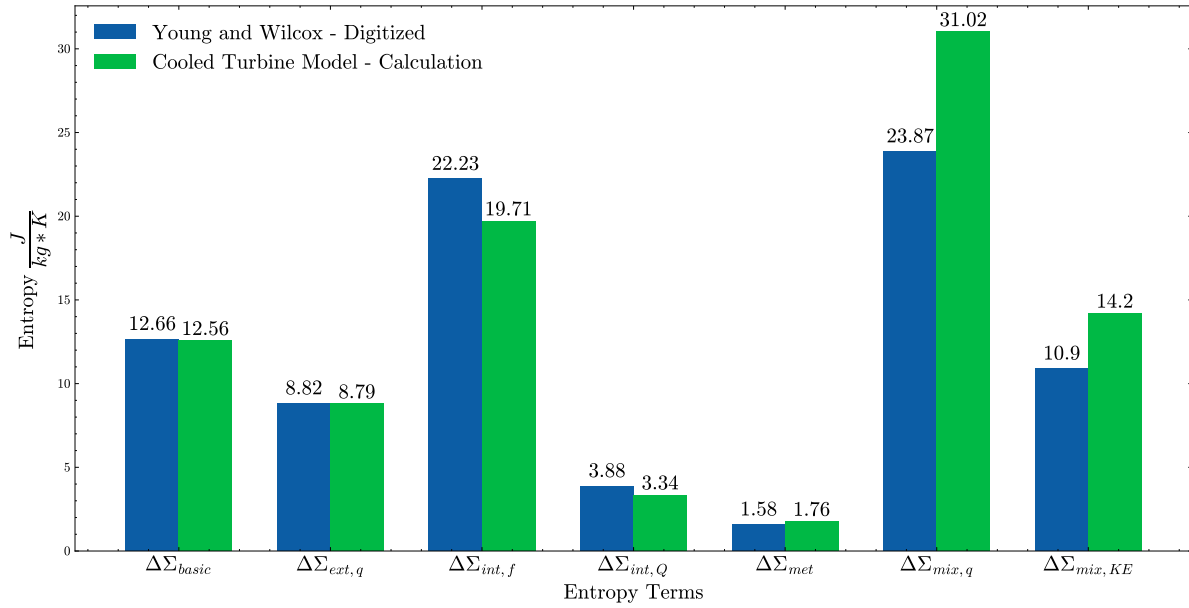
Figure 5.6: Comparison of entropy terms for $K_{cool} = 0.08$, $T_{0g} = 1700$ K, $T_{0c,i} = 867$ K, $T_{metal} = 1100$ K, $\epsilon_f = 0.4$ and $\eta_{c,int} = 0.7$

Entropy Term	CTM	Uysal	Average	Relative Error CTM	Relative Error Uysal
$\Delta\Sigma_{ext,Q}$	4.91	5.46	4.99	-2%	9%
$\Delta\Sigma_{int,f}$	11.00	10.02	10.75	2%	-7%
$\Delta\Sigma_{int,Q}$	1.88	2.44	2.27	-17%	8%
$\Delta\Sigma_{met}$	0.99	1.06	0.72	37%	47%
$\Delta\Sigma_{mix,q}$	17.45	16.68	15.50	13%	8%
$\Delta\Sigma_{mix,KE}$	7.99	8.34	7.17	11%	16%

Table 5.6: Relative error of entropy terms according to the CTM and Uysal [20] compared to Y&W digitized data [17].
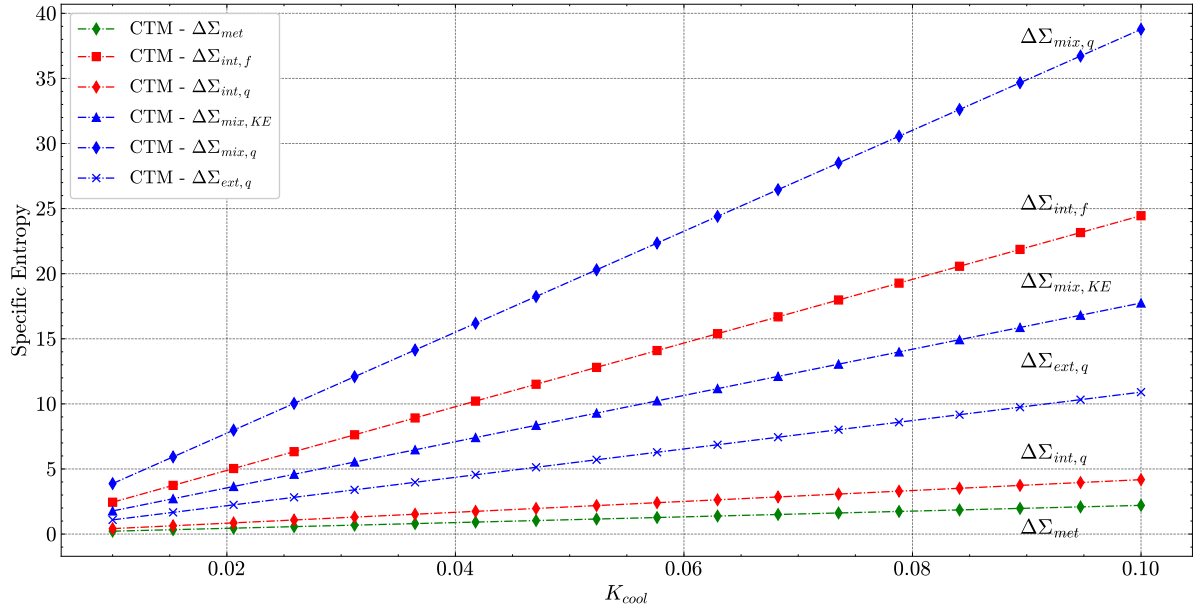
Figure 5.7: Variation of loss terms with variation in cooling parameter K_{cool}
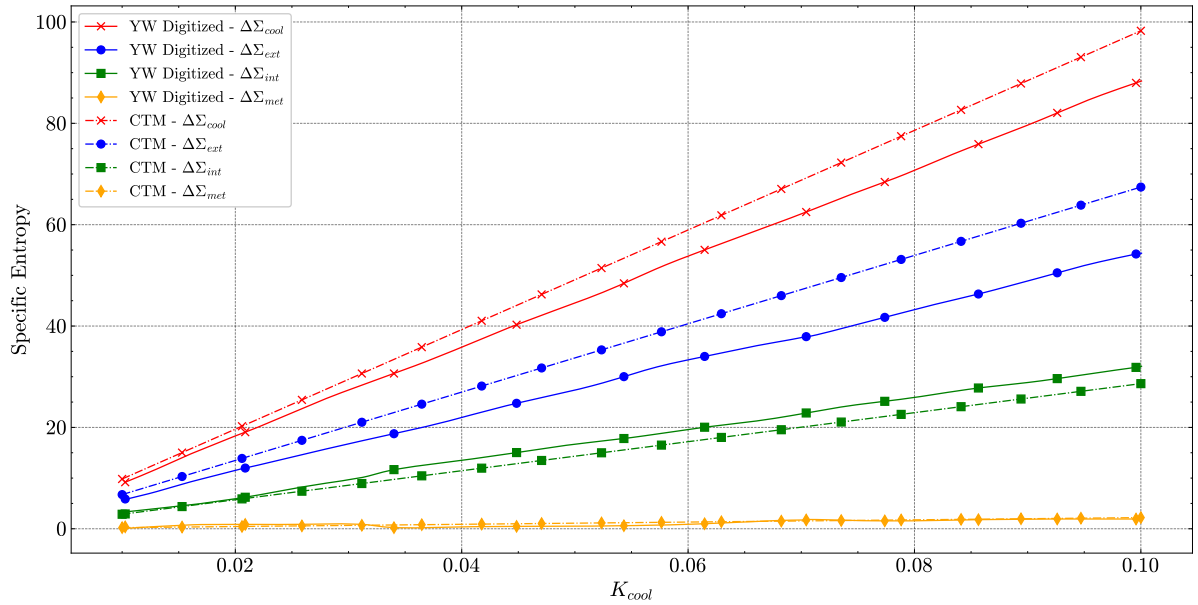
Figure 5.8: Variation of $\Delta\Sigma_{ext}$, $\Delta\Sigma_{int}$ and $\Delta\Sigma_{cool}$ with varying K_{cool}
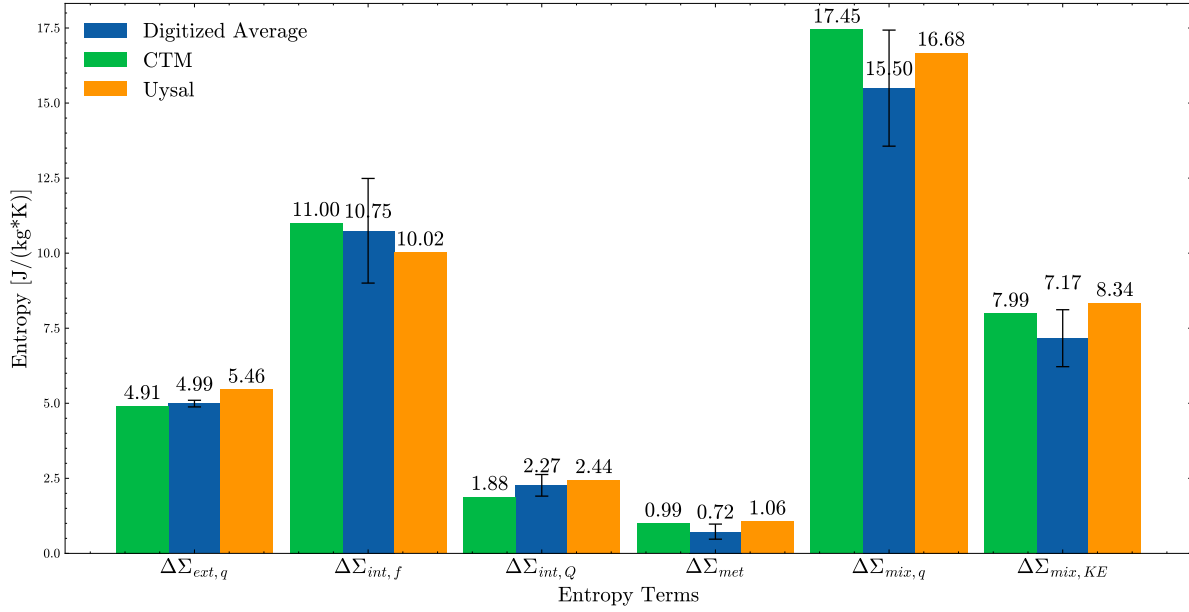
Figure 5.9: Comparison of entropy terms with averaged digitized data, and with Uysal's results [20]. The bars indicate the range of the digitized data obtained through digitization of the original paper and the results obtained by Uysal. $K_{cool} = 0.045$.

total flow quantities. As such, Equation 5.10 can be rewritten as:

$$\Delta\Sigma_{mix,q} = m_c cp_c \left(ln\left(\frac{T_{0g}K_{int}}{T_{0c,x}K_{ext}} \right) - \left(1 - \frac{T_{0c,x}K_{ext}}{T_{0g,x}K_{int}} \right) \right) \tag{5.11}$$

The known values in Table 5.2 can be substituted into this equation, namely:

$$\Delta\Sigma_{mix,q} = (0.1445) \cdot cp_c \left(ln\left(\frac{1700 \cdot 1.01}{969 \cdot 1.07} \right) - \left(1 - \frac{969 \cdot 1.07}{1700 \cdot 1.01} \right) \right) = cp_c * 0.01569 \tag{5.12}$$

The heat capacity of the cooling air flow, cp_c, can be defined at two stations. The first is the blade entry, i, while the second is x, the coolant injection station. Temperatures at these stations are 867 K and 969 K respectively. The heat capacity of the cooling air can be calculated based on temperature and composition as shown in Figure 5.10, using *PyCycle*'s built in thermodynamics model.

The cp_c values for air, at 867 K and 969 K, and the corresponding entropy terms are shown in Table 5.7. When K_{cool} is 0.08, $T_{0c,x}$ is also 969 K while the cooling fraction of the stator is 0.257. Results are also provided for a standard value of 1050 $\frac{J}{kg*K}$, based on recommendations in literature [29]. A comparison of the values presented in Table 5.7 and Figure 5.9 show that the CTM results are accurate.

Temperature	cp_c [J/(kg·K)]	$\Delta\Sigma_{ext,mix,q}(K_{cool} = 0.045)$	$\Delta\Sigma_{ext,mix,q}$ $(K_{cool} = 0.08)$
867	1114.1	17.48	31.0
969	1134.8	17.82	31.6
-	1050	16.5	29.2

Table 5.7: Upper and lower bounds for $\Delta\Sigma_{ext,mix,Q}$ based on variations in gas temperature. Temperature in Kelvin, Cp and entropy term in J/(kg*K)

Regarding the internal entropy terms, the first one to be analyzed is the term representing entropy rise due to friction within the blade cooling channels, $\Delta\Sigma_F$, defined earlier as:

$$\Delta\Sigma_{int,F} = m_c * cp_c \left\{ ln\left(\frac{T_{0c,x}}{T_{0c,k}} \right) - K_{int} ln\left(\frac{T_{0c,x}}{T_{0c,i}} \right) \right\} - m_c R_c ln\left(\frac{P_{0c,x}}{P_{0c,k}} \right) \tag{5.13}$$

Similarly to the external entropy term considered before, a number of the elements in Equation 5.13 are known, from the publication by Young and Wilcox, or as output of the Cooled Turbine Model. Substituting
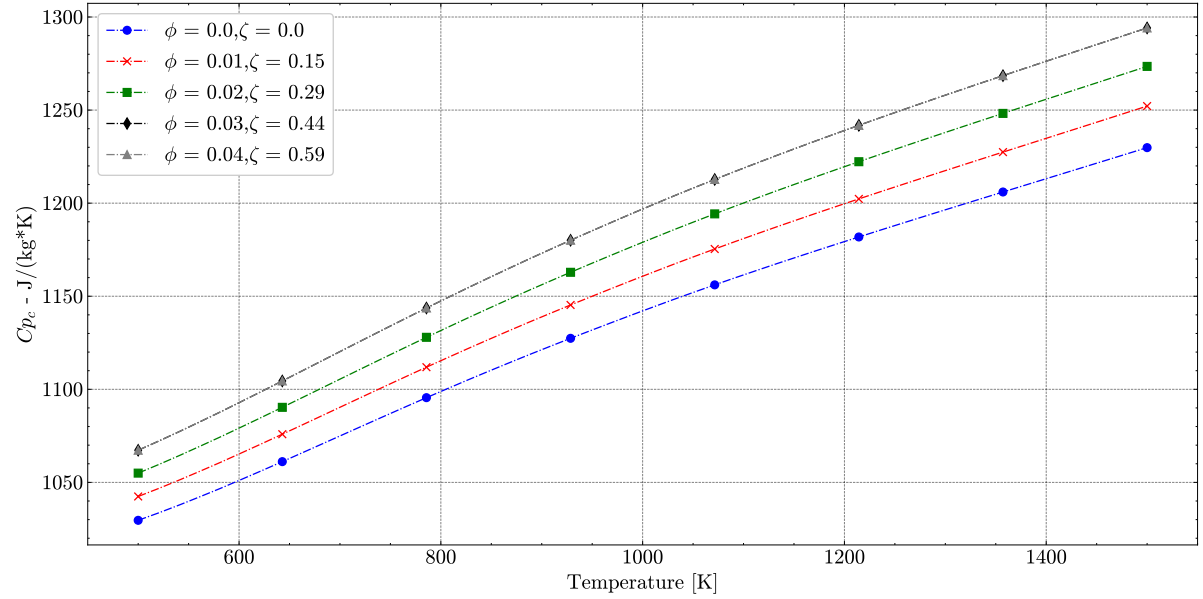
Figure 5.10: Variation of specific heat of gases with fuel to air ratios ϕ between 0 and 0.04, for temperatures in the range 500-1500 Kelvin. Pressure = 34 bar.

the known values, it is obtained that:

$$\Delta\Sigma_{int,F} = (0.145) * cp_c \left\{ ln\left(\frac{969}{867}\right) - 1.01 \cdot ln\left(\frac{969}{867}\right)\right\} - (0.145) \cdot R_c \cdot ln\left(\frac{P_{0c,x}}{34}\right) \tag{5.14}$$

While not specified by Young and Wilcox [14], the value of the coolant exit total pressure is calculated by the cooled turbine model to be 25.98 bar. To isolate the effect of variations in thermodynamic parameters, this value will be used:

$$\Delta\Sigma_{int,F} = (0.145) * cp_c \left\{ ln\left(\frac{969}{867}\right) - 1.01 \cdot ln\left(\frac{969}{867}\right)\right\} - (0.145) \cdot R_c \cdot ln\left(\frac{25.98}{34}\right) \tag{5.15}$$

Furthermore, the value of R_c is found to be effectively temperature invariant for either station i or x and is thus taken to be 287.04 J/(kg*K) throughout. Once again, this leaves the definition of the entropy term dependent on the specific heat capacity used for the coolant. Similarly to the analysis of the external mixing term, values of the entropy generation are tabulated for varying coolant heat capacity values in Table 5.8, showing agreement with the CTM results.

Temperature	Cp_c	$\Delta\Sigma_{int,F}(K_{cool} = 0.045)$	$\Delta\Sigma_{int,F}(K_{cool} = 0.08)$
867	1114.1	11.02	19.53
969	1134.8	11.01	19.52
-	1050	11.03	19.55

Table 5.8: Upper and lower bounds for $\Delta\Sigma_{int,F}$ based on variations in gas temperature. Temperature in Kelvin, Cp and entropy term in J/(kg*K).

Analysis of $\Delta\Sigma_{mix,q}$ and $\Delta\Sigma_{int,F}$ showed dependency on the fluid models used. Further investigation shows all entropy terms defined are dependent on the fluid model and combined with the digitization discrepancies, this justifies the differences observed during the CTM verification for the test case where K_{cool} is 0.045. To assess the accuracy of the CTM without the influence of the gas properties, an analytical verification was performed. Generic gas properties found in literature [29] are used in both the CTM and the original Y&W model. The gas properties used are shown in Table 5.8, with results of the verification shown in Figure 5.11. The results indicate a high level of accuracy of the CTM. The overall error in the entropy calculations is 5%.

Quantity	Value	Unit
cp_g	1200	J/(kg*K)
γ_g	1.32	-
cp_c	1050	J/(kg*K)
γ_c	1.38	-
$R_c = R_g$	287	J/(kg*K)

Table 5.9: Generic gas properties used, as defined by Young and Horlock[29]
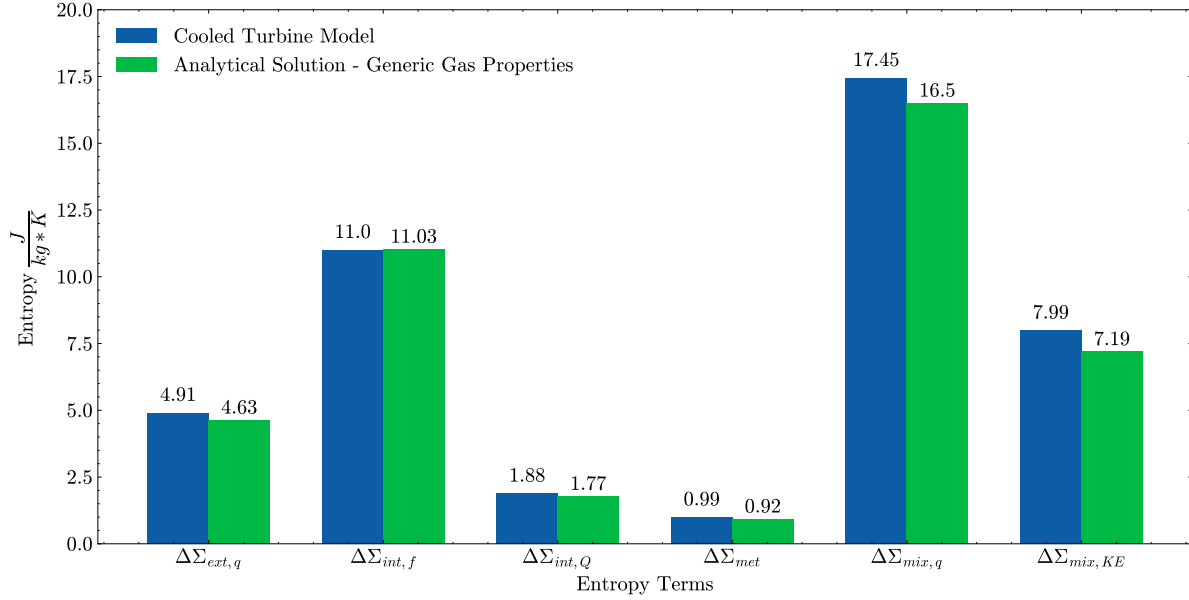
Figure 5.11: Comparison of entropy terms between cooled turbine model and analytical solutions using generic gas properties. K_{cool} = 0.045.

5.1.3. VERIFICATION - TOTAL PRESSURE LOSSES

A third quantity that needs to be verified is the calculated total pressure loss in the bulk flow due to the addition of cooling flows. In cycle calculations, stator blade rows are typically modelled as resulting in no loss of total pressure, as the frictional effects are neglected [56]. Therefore, in the CTM, any total pressure loss over the stator blade row in the turbine is attributed to the addition of the cooling flows.

As discussed in chapter 4, the CTM uses the cooling entropy, $\Delta\Sigma_{cool}$ to determine the total pressure loss. This entropy rise term is linearly proportional to the cooling fraction. The relationship between the cooling fraction and the total pressure loss over the stator are shown in Figure 5.12, for a number of values of coolant injection angle, ϕ. The vertical axis indicates the fractional drop in total pressure over the stator. The gas and coolant flow conditions that were used to calculate the pressure loss are shown in Table 5.10.

The total pressure loss grows significantly with increasing cooling fraction. Additionally, the pressure loss is larger with increasing cooling flow injection angle. This is because the kinetic energy of the coolant flow normal to the flow is lost in the mixing process. As the injection angles defines the proportion of the injected coolant flow that is aligned with the mainstream flow, an increased angle implies a lower contribution of the coolant velocity and higher losses.

Verification of the total pressure drop calculations can be done through a comparison with the work of Hartsell and Shapiro [77, 83]. An assumption common to the CTM and Hartsell's model is that mixing of two streams occurs at identical static pressure. Hartsell defines the total pressure drop in a flow due to the injection of another flow based on flow velocities, temperatures, angles and mass flow rates, as:

$$\frac{\Delta P_t}{P_{t,g}} = \frac{-\gamma}{2} M_g^2 \cdot \chi \left(1 + \frac{T_{0c}}{T_{0g}} - 2\frac{V_c}{V_g} \cdot \cos\phi \right) \tag{5.16}$$

where χ is the ratio of coolant to mainstream gas flow, while ϕ is the injection angle of the fluid. Furthermore, the flow velocities and mach number of the bulk flow are known from the CTM calculations and the definition

Quantity	Mainstream	Coolant	Unit
T_0	1700	867	K
P_0	34	34	bar
h_0	826.5	593.6	KJ/kg
S	7871.5	6967.7	J/(kg*K)
cp	1306.2	1114.1	J/(kg*K)
γ	1.28	1.35	-
FAR	0.0183	0.00	-

Table 5.10: Thermodynamic properties of coolant and mainstream flows based on test case temperature, pressure and estimated fuel to air ratio
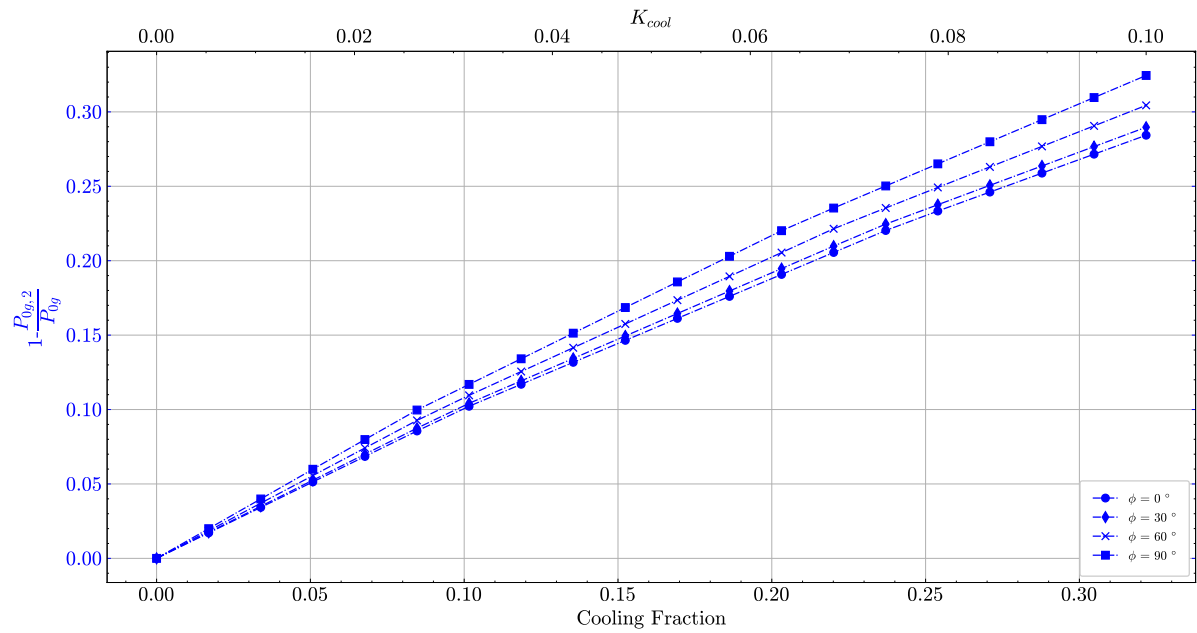
Figure 5.12: Variation in total pressure loss factor over the stator
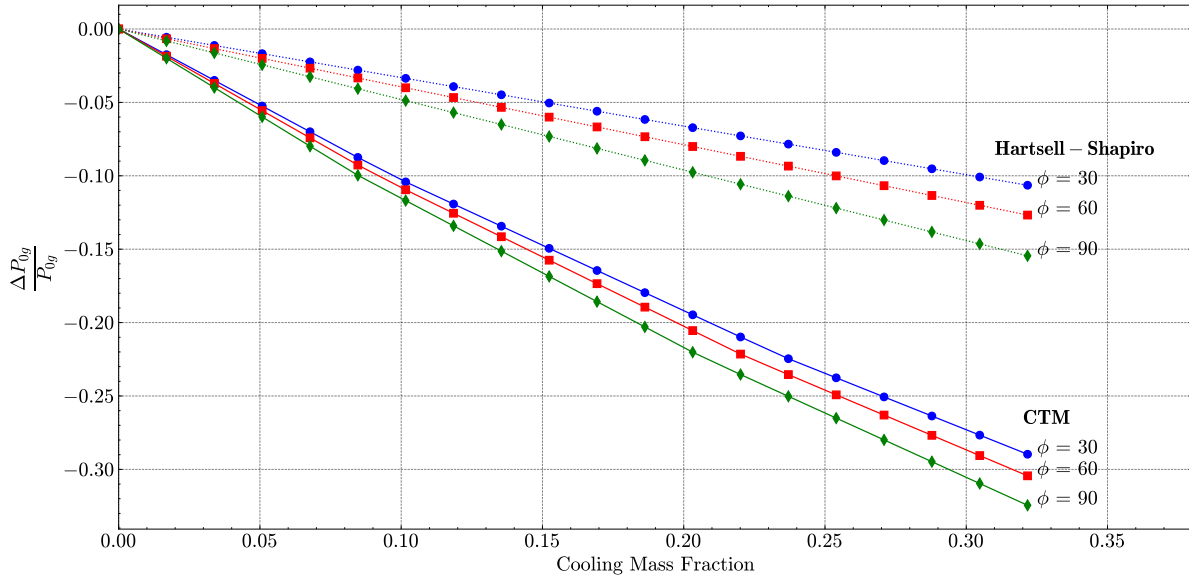
Figure 5.13: Variation in total pressure drop over stator, as predicted by Hartsell and the Cooled Turbine Model, for injection angles of 30, 60 and 90 degrees

of K_{int} and K_{ext}. These values are presented in Table 5.11.

Quantity	Value	Units
V_c	146.2	$m \cdot s^{-1}$
V_g	538.9	$m \cdot s^{-1}$
M_g	0.705	—

Table 5.11: Parameters required for Hartsell & Shapiro pressure loss model

Figure 5.13 shows the variation in total pressure loss as predicted by Hartsell's analytical equation, compared to the results obtained by the CTM for a range of cooling fractions and flow injection angles. The figure reveals that both models predict a trend of increased total pressure loss with increasing cooling mass fraction, and the increase in this loss with increasing flow injection angle. However, the absolute value of total pressure drop varies significantly, with growing discrepancy as the cooling mass fraction increases.

The primary reason for this is that the CTM accounts for the loss in total pressure as a result of multiple loss mechanisms, including mixing. On the contrary, Hartsell accounts only for the total pressure loss due to the mixing and injection procedure, see Equation 5.16. As seen from Figure 5.7, the external entropy terms only form a portion of the total cooling entropy which defines the pressure drop in the CTM.

This is confirmed by Figure 5.14 which shows the direct link between the magnitude of cooling entropy generation and the predicted pressure drop over the stator row. The pressure drop associated to the entropy generated due to heat transfer in the mixing process ($\Delta\Sigma_{mix,q}$) is large as compared to the kinetic energy dissipation entropy term. This also supports the theory that the Hartsell model only accounts for a portion of the overall pressure drop, and does not include e.g. the effect of entropy generation within the blade due to cooling. The resulting pressures when comparing the Hartsell model with the predicted pressures when accounting only for the kinetic energy mixing term are shown in Figure 5.15. Significantly better fits are achieved with the Hartsell predictions when only the effects of the mixing entropy generation terms are accounted for in the total pressure drop estimate. It should be noted that these pressures are calculated using the thermodynamic balance group developed earlier to take $h - S$ input pairs. The enthalpy and entropy used to calculate the pressure are based on the mixing of both flow streams. In the case of entropy, this is denoted by:

$$S = S_{15} + \Delta\Sigma_{cool,s} \tag{5.17}$$

where station 15 is the equilibrium station of a mixed flow with no entropy creation accounted for and the delta term represents: $\Delta\Sigma_{ext,mix,KE}$, or $\Delta\Sigma_{ext,mix,Q}$ or the sum of both.
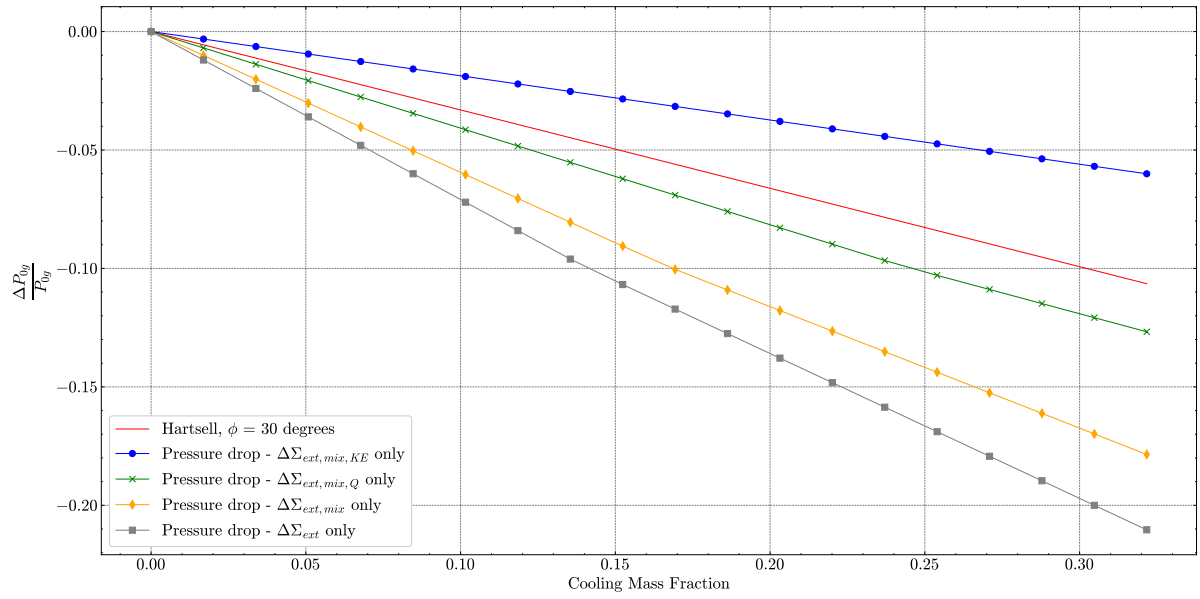
Figure 5.14: Predicted pressure drop according to Hartsell's model and the cumulative effect of various external entropy generation components for conditions corresponding to Y&W test case as presented in Table 5.1
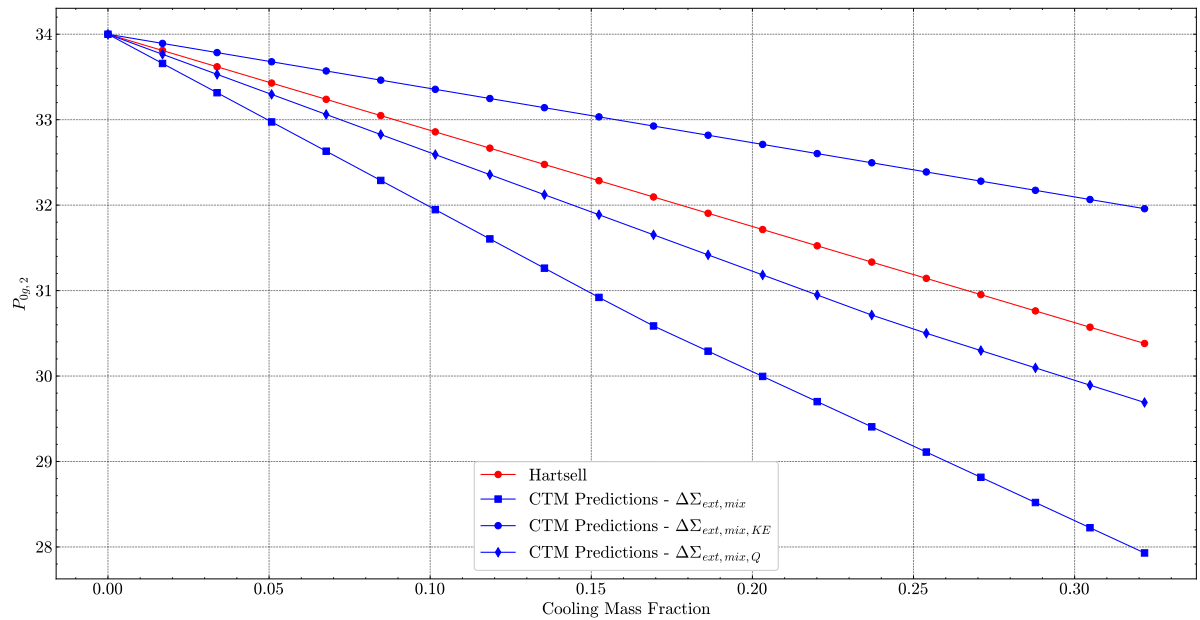
Figure 5.15: Predicted outlet total pressures by Hartsell and CTM when CTM accounts only for various external entropy terms $\phi = 30$

Having addressed the cooling flow estimates, the entropy calculation model and the total pressure losses modelled, the CTM can be considered verified to an acceptable level of accuracy.

5.2. VALIDATION - ALFA ROMEO NGV TEST CASE

The first validation case is based on the work of Colantuoni et. al [30], which presents the aerothermal design and experimental testing of a cooled, transonic turbine nozzle guide vane. Data provided by the authors is shown in Table 5.12.

Quantity	Value	Unit
P_{0g}	681	Kpa
T_{0g}	1450	K
$\dot{W}_{primary}$	2.82	kg/s
P	825	kW
U_{mean}	381000	RPM
PR_{uc}	2.45	-
η_{total}	86.3	%
ψ	1.86	-
$P_{0c,k}$	709.4	Kpa
$T_{0c,i}$	575	K
$T_{m,max}$	1050	K
Φ	45	deg

Table 5.12: Input parameters provided by Colantuoni [30] and Tiemstra [31]

In the absence of further information, certain parameters are estimated based on typical values for turbine stages, see Table 5.13.

The provided value for total efficiency is converted to polytropic efficiency [79], resulting in a value of 0.85. The predicted cooling fraction results are shown in Table 5.14.

The CTM shows high levels of accuracy with respect to the original paper, with an error percentage of 2.5%. However, this relative error could be reduced further through changing the film cooling effectiveness or internal cooling efficiency or K_{cool}. This highlights the importance of parameter selection, and will be discussed in further detail in chapter 6.

5.3. VALIDATION - ENERGY EFFICIENT ENGINE TEST CASE

The second validation case is NASA's Energy Efficient Engine (E3) [21, 32]. Designed as a proof of concept for an efficient, next generation engine in the 1980's, the E3 engine program has resulted in technical reports with high levels of detail, including those pertaining to the cooling system for the turbine. For the purposes of validation, the high pressure turbine (HPT) will be considered. The HPT of the E3 consists of 2 stages, providing the opportunity to compare the cooled turbine model for four different rows: first stage nozzle guide vane (NGV), first stage rotor, second stage stator and second stage rotor. Validation studies of both stages are presented in subsection 5.3.1 and subsection 5.3.2 respectively.

Quantity	Value	Unit	Reasoning
FAR_{in}	0.0183	-	Corresponds to equivalence ratio of 0.3 for Jet A1.
ϵ_f	0.3	-	Midpoint of range prescribed by[14]
$\eta_{c,int}$	0.7	-	Midpoint of range prescribed by [14]
K_{cool}	0.045	-	Initial guess based on [14]
Bi_m	0.2	-	see above
Bi_{tbc}	0	-	No mention of TBC

Table 5.13: Parameters estimated for validation of CTM against the Alfa Romeo NGV test case

Model or Paper	Cooling Flow Rate	Unit
Colantuoni	0.121	kg/s
Tiemstra	0.152	kg/s
Cooled Turbine Model (CTM)	0.124	kg/s

Table 5.14: Comparison of predicted cooling fractions by CTM and Tiemstra's model [31] for the Alfa Romeo NGV test case.

5.3.1. STAGE 1

Thermodynamic conditions for both rows (NGV and rotor) of the first high pressure turbine (HPT) stage are shown in Table 5.15. Furthermore the stage pressure ratio is 2.25 [21], while the uncooled polytropic efficiency is 0.93 [21]. The first validation of the CTM will use parameter values that are either the mid-point of the range provided by Y&W, or original values in case a range is not provided. These are values are shown in Table 5.16. Results are shown in Table 5.17.

Quantity	Symbol	NGV Row	Rotor Row	Unit
Gas temperature	T_{0g}	2012	1950	K
Gas pressure	P_{0g}	2.526	2.551	MPa
Coolant temperature	$T_{0c,i}$	883	883	K
Coolant pressure	$P_{0c,k}$	2.59	2.59	MPa
Maximum blade temperature	$T_{met,max}$	1356	1226	K

Table 5.15: E3 Engine - Stage 1 thermodynamic conditions for validation study [21, 32]

Parameter	Value	Parameter	Value
ϵ_f	0.3	K_{int}	1.01
$\eta_{c,int}$	0.7	K_{ext}	1.07
Bi_m	0.2	ϕ	45 deg
Bi_{tbc}	0.0	$K_{comb,s}$	0.1
K_{cool}	0.045	$K_{comb,r}$	0.05
K_{swirl}	0.77	T_{factor}	1.0

Table 5.16: Standard values used to instantiate CTM for validation study of E3 HPT stage 1

It is clear that there are major discrepancies between the CTM and the E3 technical reports. Firstly, the stator (NGV) cooling fraction is significantly over predicted, resulting in an under-predicted stator outlet temperature. Additionally, the rotor cooling fraction is over-predicted, although the magnitude of variation is smaller than for the NGV. These discrepancies can be attributed to the selection of the model parameters (Table 5.16). It is likely that some of these are too low, as this would explain the overestimation of cooling flow. To check this, the values of ϵ_f and $\eta_{c,int}$ are raised, to 0.45 and 0.8 respectively. New results are shown in Table 5.18 and show significantly improved accuracy. The largest deviation is observed in the rotor cooling fraction, likely due to the change of reference frame calculated in the CTM. The parameter influencing this is K_{swirl}, used to calculate thermodynamic quantities in the rotating frame of reference. Reducing this parameter to 0.67 results in a significantly more accurate calculation of the rotor cooling fraction, as shown in Table 5.18. Overall, it is seen that the CTM is able to estimate results close to the measurements from the E3 experimental campaign, provided the required parameters are specified accurately.

5.3.2. STAGE 2

Thermodynamic conditions for both rows (NGV and rotor) of the second high pressure turbine (HPT) stage are shown in Table 5.19. For this stage, the expected pressure ratio is 2.11, with polytropic efficiency given to be 0.93 [21, 32]. As with the first stage, the validation study will use mid-range values for each of the parameters, or original values presented earlier, shown in Table 5.16. The second stage of the E3 HPT does not have a film cooled NGV, meaning that ϵ_f must be set to 0. Results of the CTM are shown in Table 5.20. Once again, it is observed that the standard values for parameters are not suitable to accurately estimate the

Quantity	E3 Value	CTM	Difference	Rel. Difference	Unit
NGV cooling fraction	0.095	0.168	0.0734	+77.5%	[-]
Rotor cooling fraction	0.039	0.053	0.014	+35.9%	[-]
Stator Outlet Temperature	1950	1866	84	-4.3%	K

Table 5.17: Results of CTM validation study with standard input parameters of Table 5.16 for first stage of E3 engine HPT.

Quantity	E3 Value	CTM	Difference	Rel. Difference	Unit
NGV cooling fraction	0.095	0.098	0.002	+2.1%	[-]
Rotor cooling fraction	0.039	0.036	0.003	-7.6%	[-]
Stator Outlet Temperature	1950	1922	28	-1.4%	K
Rotor cooling fraction ($K_{swirl} = 0.67$)	0.039	0.038	0.001	-2.5%	[-]

Table 5.18: Results of CTM validation study with updated input parameters: ϵ_f = 0.45 and $\eta_{c,int}$ = 0.8. Remaining parameters based on Table 5.16

required cooling fractions. In order to improve the model predictions, the parameters are adapted through a trial and error process resulting in: $\eta_{c,int}$ = 0.95, Bi_m = 0.1 and Bi_{tbc} = 0.5, while the corresponding CTM results are presented in Table 5.21. While the tuned parameters allow for significant improvement, the CTM is not able to replicate the E3 results with these parameter values. The likely cause is the absence of film cooling, which impacts the overall effectiveness of the cooling system.

Quantity	Symbol	NGV Row	Rotor Row	Unit
Gas temperature	T_{0g}	1463	1416	K
Gas pressure	P_{0g}	2.38	2.35	MPa
Coolant temperature	$T_{0c,i}$	761	866	K
Coolant pressure	$P_{0c,k}$	2.45	2.40	MPa
Maximum blade temperature	$T_{met,max}$	1201	1202	K

Table 5.19: E3 Engine - Stage 2 thermodynamic conditions for validation study [21, 32]

A further validation can be obtained through comparison of the CTM with other cooling models for the E3 test case. For the first stage, the CTM can be compared with the Gauntner model [22], while the second stage can be compared with the results of Tiemstra [31]. This comparison is shown in Figure 5.16. It is apparent that for the first stage of the E3 engine, the results of the CTM provide an accurate estimation of cooling flows. For the second stage, this is not the case, with larger relative discrepancies noted. Tiemstra's model [31], compared for stage 2, is based on detailed modelling of internal cooling channels. This would explain the higher accuracy of this model for the second stage, where the absence of film cooling makes the estimate of cooling fraction more dependent on internal cooling. Overall, the CTM can be considered acceptable as long as parameters are specified properly. This will be discussed further in chapter 6.

5.4. Validation - Cooled turbine efficiency

A significant figure of merit is the efficiency of the cooled turbine stage. While there has been much literature about the appropriate definition of cooled turbine efficiency, the discussion will be limited here primarily to the definitions discussed by Young and Horlock [29].

The reference efficiency definition is that defined by Hartsell for a cooled turbine [83]:

$$\eta_{c,hart} = \frac{P_{gross}}{m_g(h_{01g} - h_{03Sg} + m_{c,s} * (h_{01ci-h_{03Sci}}) + m_{c,r} * (h_{01ci-h_{03Sci}}))} \tag{5.18}$$

where:

$$P_{gross} = (m_g h_{01g} + m_{c,s} h_{01ci} + m_{c,r} h_{01ci}) - (m_g + m_{c,s} + m_{c,r}) h_{03} \tag{5.19}$$

The formulation of Hartsell's cooled turbine efficiency is based on the gross power delivered by a stage relative to the idealized work potential of each stream. As is visible from the formulation, the gross power is

Quantity	E3 Value	CTM	Difference	Rel. Difference	Unit
NGV cooling fraction	0.02	0.066	0.046	+230%	[-]
Rotor cooling fraction	0.0076	0.018	0.0104	+136%	[-]
Stator Outlet Temperature	1416	1423	7	+0.5%	K

Table 5.20: Results of CTM validation study with standard input parameters of Table 5.16 for E3 engine HPT 2nd stage, with $\epsilon_f = 0.0$

Quantity	E3 Value	CTM	Difference	Rel. Difference	Unit
NGV cooling fraction	0.02	0.028	0.01	+40%	[-]
Rotor cooling fraction	0.0076	0.0099	0.0024	+30%	[-]
Stator Outlet Temperature	1416	1445	29	+2%	K

Table 5.21: Results of CTM validation study for E3 Engine HPT 2nd stage with updated input parameters: $\eta_{c,int} = 0.95, Bi_m = 0.1$ and $Bi_{tbc} = 0.5$. Remaining parameters based on Table 5.16

the enthalpy drop of the mainstream flow from stage inlet to outlet, with the additional contribution of the coolant of stator and rotor which are assumed expanding from their delivery state $01ci$ to the stage outlet condition 03.

While this formulation offers a thermodynamically valid insight into the cooled efficiency of the turbine, the cooled turbine model developed in this work requires a modification of this definition. The cause for this alteration is the work potential of the rotor coolant stream. The cooled turbine model is modelled on the basis that rotor coolant flow does not contribute to the work potential of the stage in which it is injected. Therefore, a definition of efficiency acknowledging the ideal work potential of the rotor coolant stream would be inconsistent with the model assumptions. As such, the definition of the Hartsell efficiency is modified as follows:

$$\eta_{CTM} = \frac{P_{gross}}{m_g \cdot (h_{0g,1} - h_{0g3s}) + m_{c,s} \cdot (h_{0c,i} - h_{oc,3s})} \tag{5.20}$$

Over a range of stage cooling fractions Ω_{stage}, the two efficiencies vary as shown in Figure 5.17. As is visible, the addition of cooling flows significantly degrades the efficiency of a turbine stage. The stage shown has an uncooled polytropic efficiency of 0.9 and a designed pressure ratio of 2.4. This corresponds to an isentropic efficiency of 0.91. η_{CTM} exhibits a trend where a 1% drop in stage efficiency is approximately observed for 1% of cooling flow added. This is in line with the results presented by Denton [16].

It should be noted that the Hartsell efficiency, as well as η_{ctm} are isentropic efficiencies, and therefore vary with pressure ratio. Conversion of isentropic to polytropic efficiencies is done through the formula presented in earlier sections, with dependency on pressure ratio, isentropic efficiency and ratio of specific heats.

Another factor that impacts the efficiency degradation of a cooled stage is the technology level of the cooling system used. This is represented by $\eta_{c,int}$ and ϵ_f. To investigate the impact of cooling technology, a variation of turbine inlet temperature is tested. Other values remain fixed, with the variation in turbine inlet temperature driving the change in coolant mass flow ratios. To set an upper bound and lower bound, the upper and lower bounds of both parameters will be used, respectively:

- **High** : $\eta_{c,int} = 0.8$ and $\epsilon_f = 0.4$

- **Low** : $\eta_{c,int} = 0.6$ and $\epsilon_f = 0.2$

Additionally a simulation is performed for a turbine stage with no film cooling. Turbine inlet temperatures are varied from 1300 to 1800, with a maximum metal temperature of 1100 Kelvin. Uncooled turbine polytropic efficiency is 90%, corresponding to an isentropic efficiency of 91.8% for an uncooled pressure ratio of 2.4. Results are shown in Figure 5.18.

As is visible from the figure, the efficiency degradation is minimized the more sophisticated the cooling technology. However, degradation is still present, with even the most advanced cooling system modelled resulting in an approximately 20% reduction in efficiency for a 20% stage cooling fraction. However, this emphasizes the importance of optimal cooling system design, by tuning the geometric and thermodynamic properties such as rib spacing, film hole spacing and others. Further information on detailed cooling configuration and design are discussed by Tiemstra [23].
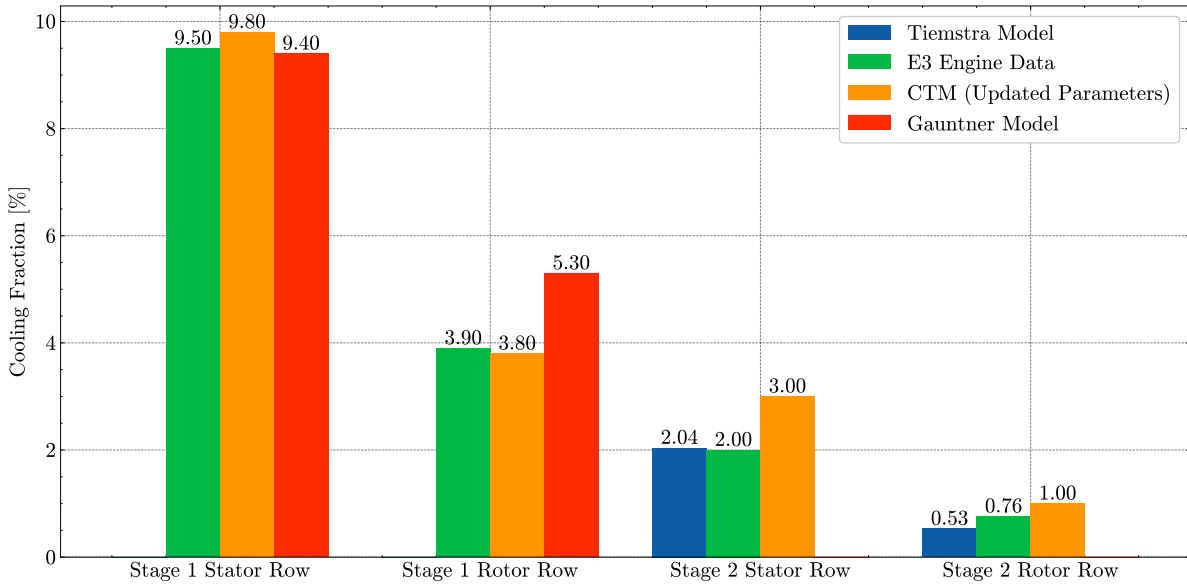
Figure 5.16: Comparison of CTM results with E3 engine data [21], Gauntner's cooled turbine model [22] and Tiemstra's cooled blade model [23] CTM instantiated with updated parameters for stage 1 (ϵ_f = 0.45 and $\eta_{c,int}$ = 0.8.) and stage 2($\eta_{c,int}$ = 0.95, Bi_m = 0.1 and Bi_{tbc} = 0.5). Remaining CTM parameter values in Table 5.16.
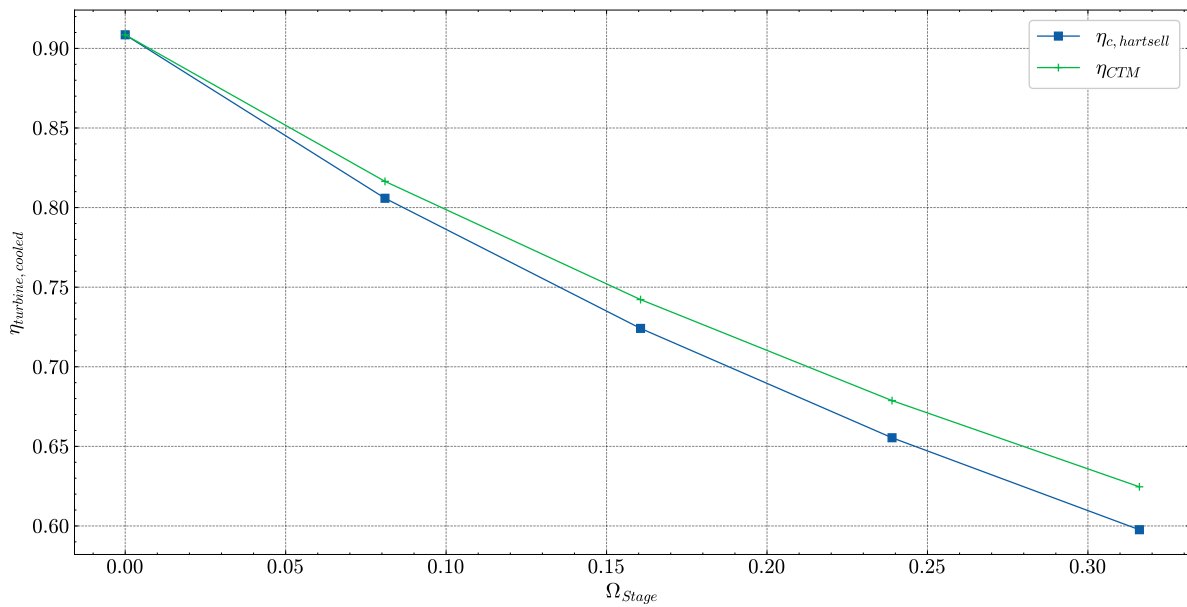
Figure 5.17: Variation in cooled turbine efficiency (Hartsell and CTM) with stage cooling fraction. Uncooled stage designed for expansion ratio 2.4 at polytropic efficiency 0.9
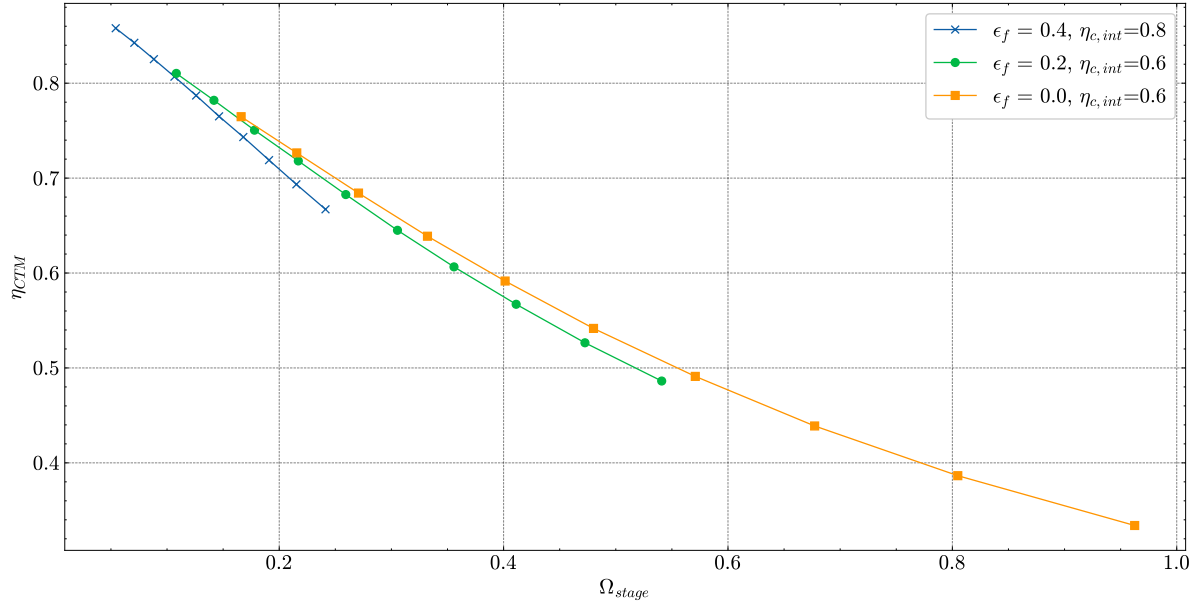
Figure 5.18: Variation in stage isentropic efficiency, as found by the cooled turbine model for various cooling technology configurations. Turbine gas temperature varied from 1300 to 1800 kelvin in steps of 50. Maximum metal temperature 1100 kelvin.

5.5. INFLUENCE OF EMPIRICAL PARAMETERS ON CALCULATION VALIDITY

The empirical parameters presented in chapter 4 are important in establishing the validity of the cooling fraction calculation. The driving factor in the cooling fraction calculations is the cooling effectiveness, ϵ_0^{max}, defined earlier as:

$$\epsilon_0^{max} = \frac{T_{0g}^{max} - T_{m,ext}}{T_{0g}^{max} - T_{0c,i}} \tag{5.21}$$

From this, the non-dimensional cooling fraction, m_{c+} is derived, namely:

$$m_{c+} = \frac{\epsilon_0^{max} - \epsilon_f + \epsilon_f \eta_{c,int}(1 - \epsilon_0^{max})}{(1 + Bi_{tbc})\eta_{c,int}(1 - \epsilon_0^{max}) - Bi_m \eta_{c,int}(\epsilon_0^{max} - \epsilon_f)} \tag{5.22}$$

The variation in m_{c+} with ϵ_0^{max} is significant, as demonstrated in Figure 5.19. Note that the values used to perform this calculation are those presented in Table 5.1.The variation in ϵ_0^{max} is achieved by raising the gas temperature, T_{0g}, while maintaining all other variables constant.

Figure 5.19 shows four issues that should be addressed, in relation to model validity. The first is the case for when ϵ_0^{max} drops below 0. This is only possible when the gas temperature does not exceed the allowable metal temperature and is a case for which a turbine blade row would not need to be cooled. As described in chapter 4, the original Y&W model is not designed for cycle calculations, and as such does not check whether cooling is required. For cases where ϵ_0^{max} is negative, the original Y&W model produces negative cooling fractions. To avoid this, the CTM has a built in cooling check to ensure that performance remains identical to the uncooled equivalent stage, as intended.

The second issue is related to cases where ϵ_0^{max} exceeds 1. This can occur when the coolant temperature chosen is not low enough to sufficiently cool the bulk flow. Both the Y&W model and the CTM return very large, unrealistic cooling fractions in excess of 1 in these cases. The solution to this issue is to modify the simulated coolant temperature in the cycle calculation & CTM.

The third issue relates to the asymptotic behaviour of the non-dimensional cooling fraction m_{c+}, observed in Figure 5.19. The formula used to define m_{c+}, Equation 5.22, can be rearranged to calculate the value of ϵ_0^{max} to which m_{c+} is asymptotic,ϵ_0^{asymp}, namely:

$$\epsilon_0^{asymp} = \frac{(\eta_{c,int} + Bi_{tbc}\eta_{c,int}) + \eta_{c,int}Bi_m\epsilon_f}{\eta_{c,int} + Bi_{tbc}\eta_{c,int} + Bi_m\eta_{c,int}} \tag{5.23}$$

ϵ_0^{asymp} is a function of only the empirical parameters (ϵ_f, $\eta_{c,int}$) and material properties (Bi_m,Bi_{tbc}). The variation of ϵ_0^{asymp} with these parameters is shown in Figure 5.20 and Figure 5.21.
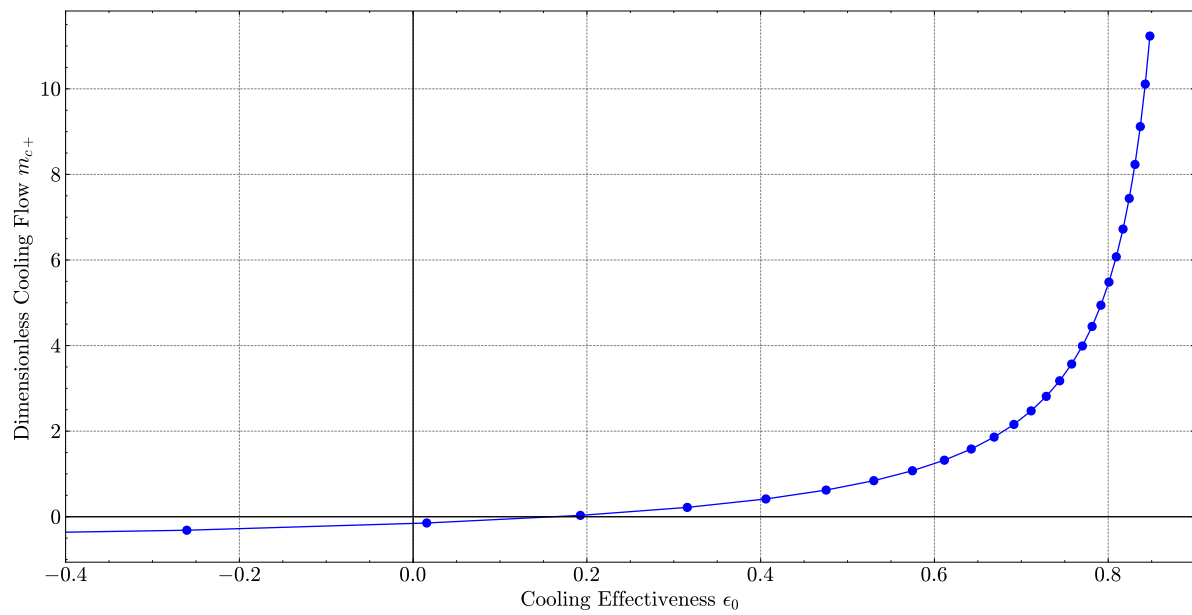
Figure 5.19: Variation in m_{c+} with ϵ_0^{max} for $\epsilon_f = 0.4$, $\eta_{c,int} = 0.7$, $T_{0c,i} = 867$ K and $T_{met,max} = 1100$ K.
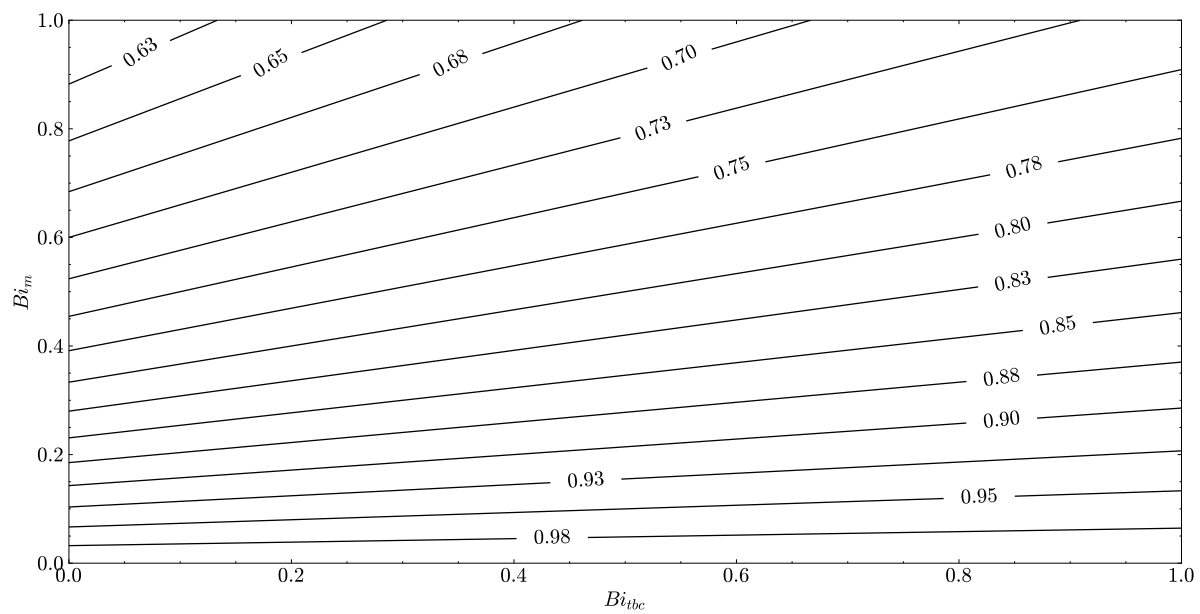
Figure 5.20: Contour plot of asymptotic cooling effectiveness, ϵ_0^{asymp}, for $\epsilon_f = 0.2$, $\eta_{c,int} = 0.6$
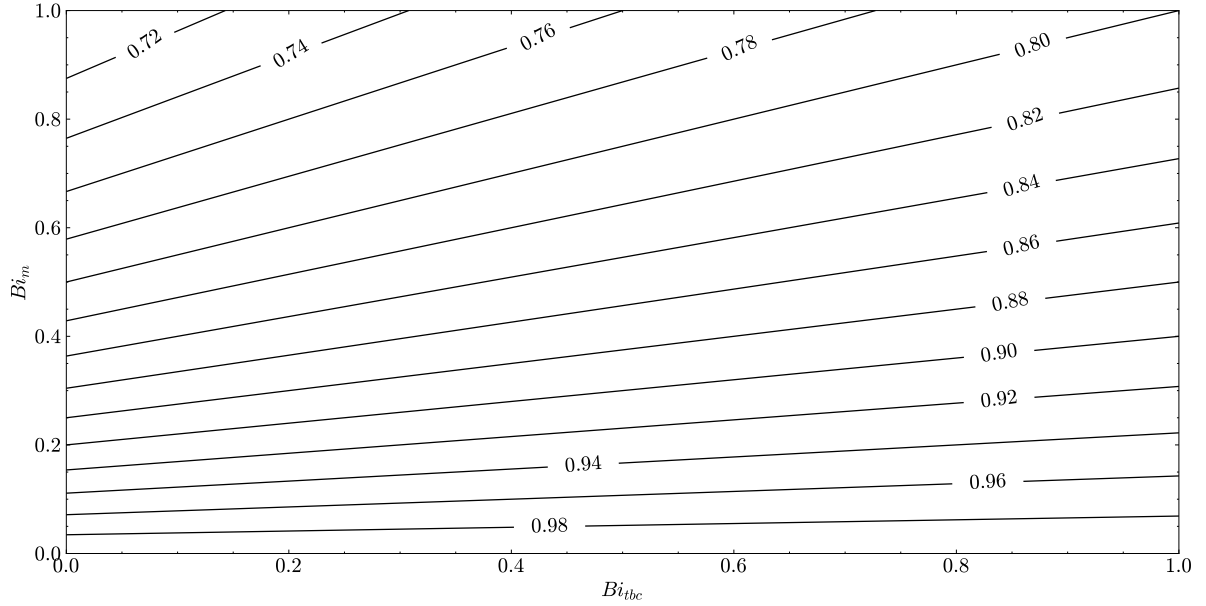
Figure 5.21: Contour plot of asymptotic cooling effectiveness,ϵ_0^{asymp}, for $\epsilon_f = 0.4$, $\eta_{c,int}$=0.8

ϵ_0^{asymp} represents the cooling effectiveness that the chosen combination of empirical parameters cannot attain. In the Y&W test case,ϵ_0^{asymp} is 0.9. This means divergence in cooling air requirement predictions is expected if the temperature difference between gas and blade allowance is in excess of 90% of the temperature difference between the gas and coolant air. This asymptotic behaviour inherently accounts for the inability of any real cooling system to use 100% of the temperature potential to effectively cool the blade.

If the calculated value of ϵ_0^{max} for a given combination of gas, coolant and allowable metal temperatures approaches ϵ_0^{asymp}, there are a number of potential ways to rectify this from a design perspective. The first is to lower the temperature of the gas, which would reduce the required cooling effectiveness, but this would impact the cycle efficiency. The second is to raise the maximum allowable blade temperature, either by changing the blade material, or through the introduction of a thermal barrier coating although this may not always be possible. The third is to lower the temperature of the cooling air flow stream. This can be achieved in two ways. The first is to move the bleed-off point supplying the cooling air to an earlier compressor stage, where temperature will be lower. However, cooling air must be supplied at total pressures higher than the total pressure of the bulk flow with which it will be mixed. Bleeding cooling air off earlier may not always be possible due to the dual, opposing, constraints posed on temperature and pressure. The second way to lower cooling air temperature is to cool the cooling air stream prior to delivery to the turbine, as evaluated by Velthausz [84]. In order to avoid excessively large cooling flow estimates when using the CTM, it is recommend to select parameters such that the required ϵ_0^{max} is not within 5-10% of ϵ_0^{asymp}.

The fourth issue that must be addressed is the possibility for m_{c+} to be negative when ϵ_0^{max} is greater than zero. This would lead to negative cooling fractions in cases where the temperature difference between the gas and blade limit are small relative to the difference between the gas and the coolant temperature.Figure 5.19 shows that the intercept of m_{c+} with the horizontal axis is when ϵ_0^{max} is 0.18. For values of ϵ_0^{max} less than this, but greater than 0, the Y&W model does not estimate cooling flows are needed, even when gas temperatures exceed the allowable metal temperature. The intersection of the non-dimensional cooling fraction with the horizontal axis, is obtained by setting Equation 5.22 equal to 0 and solving for ϵ_0^{max}. The resulting, minimum cooling effectiveness for the model to work is found to be entirely a function of ϵ_f and $\eta_{c,int}$, namely:

$$\epsilon_0^{min} = \frac{\epsilon_f - \epsilon_f \eta_{c,int}}{1 - \epsilon_f \eta_{c,int}} \tag{5.24}$$

ϵ_0^{min} is equal to 0 in all cases where ϵ_f is equal to 0, therefore in all cases where film cooling is not modelled. The impact of varying values of ϵ_f and $\eta_{c,int}$ on ϵ_0^{min} is shown in Figure 5.22. Clearly, each combination of the parameters demarcates a minimum ratio of the temperature difference between gas and metal to the temperature difference between gas and coolant streams. This minimum ratio must be satisfied for a valid

cooling fraction calculation. Furthermore, as the issue of non-zero minimum cooling effectiveness, Equation 5.25 can be rearranged to calculate the mathematically permitted maximum value of the film cooling effectiveness ϵ_f^{cap}. This maximum permitted value is defined for a known required cooling effectiveness, ϵ_0, and internal cooling efficiency, $\eta_{c,int}$, namely:

$$\epsilon_f^{cap} = \frac{\epsilon_0}{\epsilon_0 \eta_{c,int} + 1 - \eta_{c,int}} \tag{5.25}$$

The consequence of this requirement is that the Y&W model, and in turn the CTM, cannot effectively model the use of film cooling for small temperature differences. It should be noted however that this is unlikely to occur in practice due to the costs and production complexity of film cooling. Internal convection is the solution generally applied in such operating conditions.
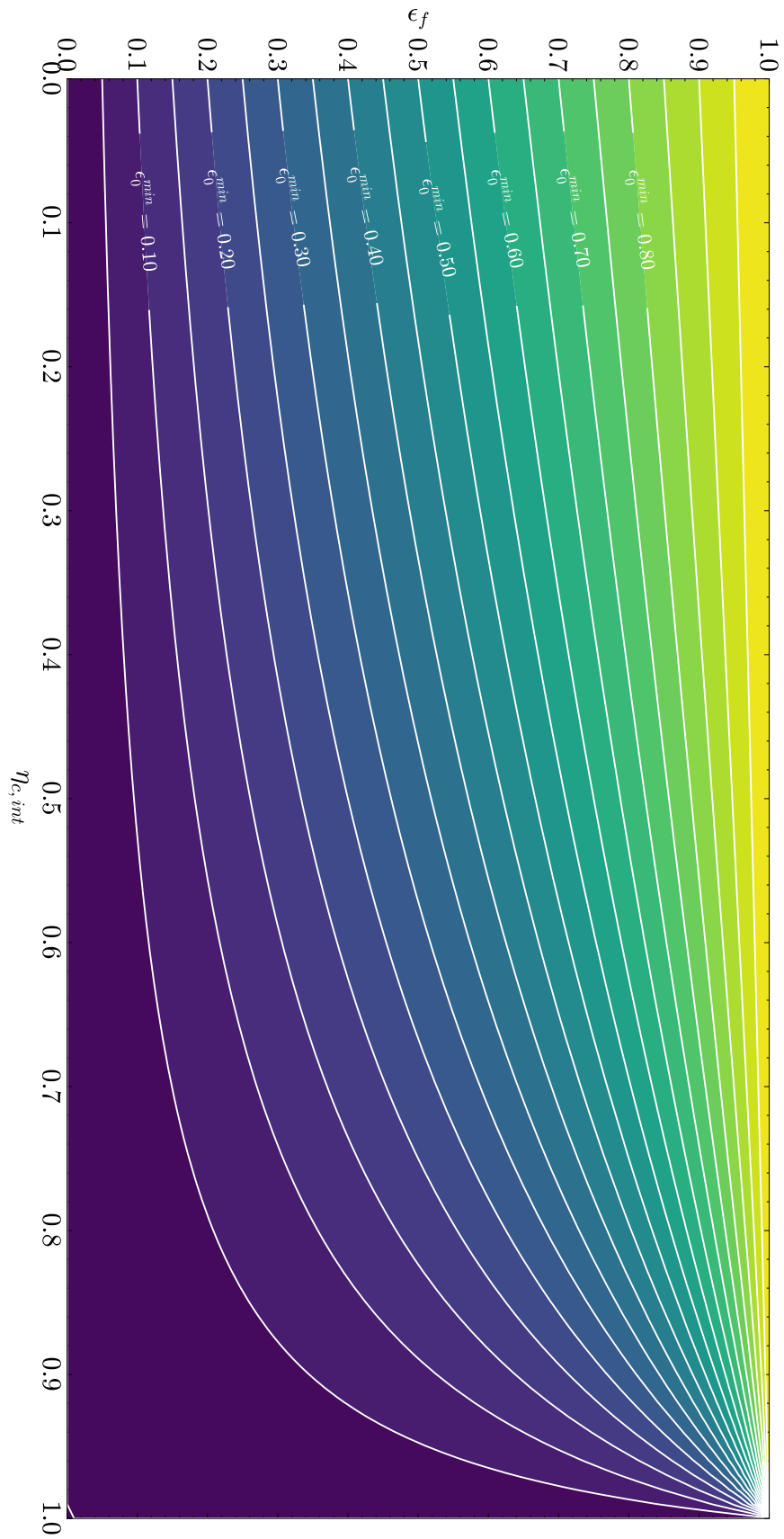
Figure 5.22: Contours of minimum required cooling effectiveness for variations in international cooling efficiency $\eta_{c,int}$ and film cooling effectiveness ϵ_f

6

DISCUSSION - EMPIRICAL PARAMETERS

The empirical parameters are key elements of the cooled turbine model (CTM). These include the film cooling effectiveness, ϵ_f, internal cooling efficiency, $\eta_{c,int}$ and the Biot numbers Bi_m and Bi_{tbc}. This chapter will present their influence on the outcome of the cooled turbine model. Firstly, section 6.1 will present a sensitivity analysis of the CTM outputs to various inputs. Following this, the results of the CTM will be compared to the Gauntner model in section 6.2. Thereafter, section 6.3 and section 6.4 discuss potential ranges for the external and internal flow parameters K_{ext} and K_{int}. The cooling flow parameter is examined in section 6.5 to narrow the potential range of values that can be used. The Biot numbers, as well as $\eta_{c,int}$ and ϵ_f are analyzed in section 6.6 and section 6.7. The cooling fraction calculation is structured as an optimization problem and treated with updated bounds in section 6.8. Finally, a parametric analysis of the CTM is presented in section 6.9.

6.1. SENSITIVITY ANALYSIS

A sensitivity analysis is performed on the CTM's cooling flow estimations to understand the influence of various factors. Using the default values of the Young and Wilcox paper, with the addition of a thermal barrier coating, each parameter is varied within a fixed range. The initial input conditions and parameter ranges are presented in Table 6.1.

Considering the temperatures, Figure 6.1 shows that increasing gas and coolant temperatures raise the estimated cooling fraction. In contrast, increasing the allowable metal temperature reduces the required cooling airflow significantly. Furthermore, it is observed that the cooling fraction is more sensitive to an increase in $T_{0c,i}$ than T_{0g}. A 50 K increase in T_{0g} causes a 0.015 increase in the estimated cooling fraction, whereas the same temperature increase for $T_{0c,i}$ causes a rise of 0.05 in the estimated cooling fraction. Furthermore, it is seen that increasing both ϵ_f and $\eta_{c,int}$ results in a cooling fraction reduction. The cooling fraction is more sensitive to changes in ϵ_f suggesting that design efforts to reduce the cooling fraction should focus on improving ϵ_f, except in cases where $\eta_{c,int}$ is very low. It is noted that Bi_{tbc} has a positive influence on the cooling fraction, while Bi_m raises the required cooling fraction significantly.

The sensitivity analysis can be extended by analysing the derivatives of the cooling fraction function,

Parameter	Initial Value	Lower Bound	Upper Bound	Step-size	Units
T_{0g}	1700	1200	2200	50	K
$T_{0c,i}$	867	367	967	50	K
T_m	1100	1000	1600	50	K
ϵ_f	0.4	0.0	1.0	0.1	[-]
$\eta_{c,int}$	0.7	0.0	1.0	0.1	[-]
Bi_m	0.2	0.1	0.7	0.1	[-]
Bi_{tbc}	0.1	0.0	0.1	0.1	[-]
K_{cool}	0.045	0.0	0.09	0.015	[-]

Table 6.1: Table of initial input values and parameter ranges for sensitivity analysis of cooling flow fraction estimates.
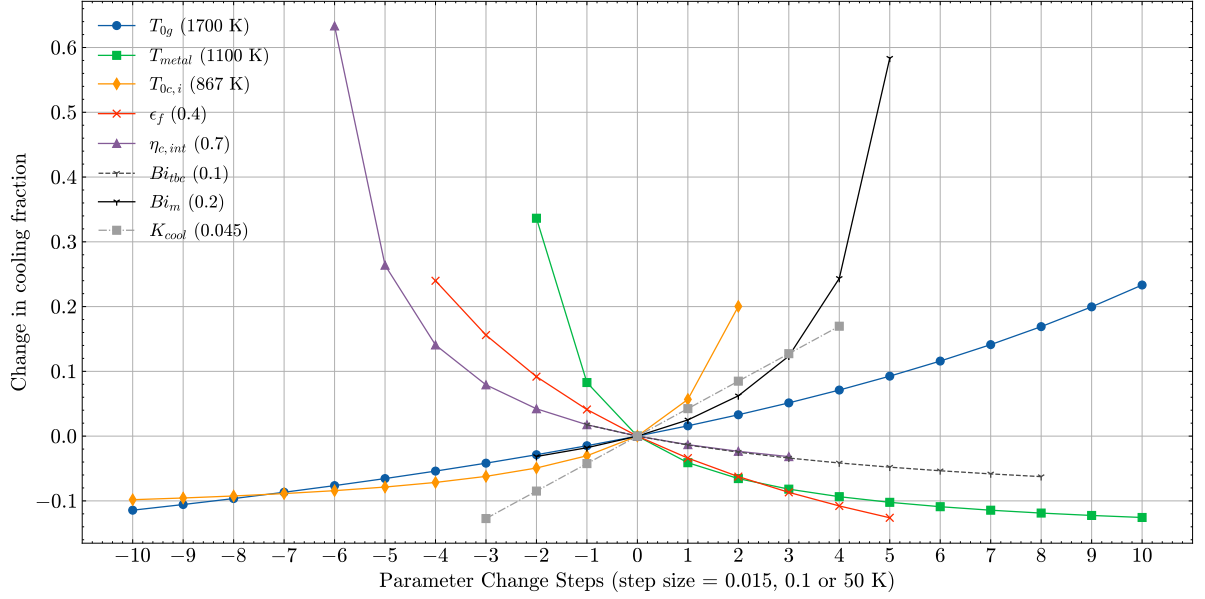
Figure 6.1: Sensitivity analysis of cooling flow fraction to all input parameters. Step size of 0.015 for K_{cool}, 0.1 for all other non-temperature parameters and 50 K for temperatures. Initial parameter values are in brackets.

known from the implementation of the CTM in *PyCycle*. The magnitude of the derivatives shows to which inputs the cooling fraction is most sensitive in the defined test case. These results are shown in Figure 6.2 and Figure 6.3. The sensitivity to temperature is three orders of magnitude less than the sensitivity to any of the other terms. An unexpected similarity is the magnitude of sensitivity to $\eta_{c,int}$ and Bi_{tbc}, seen in both Figure 6.1 and Figure 6.3. Plotting the derivatives over an extensive gas temperature range shows that the relative magnitudes of the derivatives remain similar. However, it is observed that as the gas temperature increases, the partial derivatives with respect to $\eta_{c,int}$ and Bi_{tbc} converge. This results in the two crossing each other at a gas temperature of approximately 1950 Kelvin. In general, the magnitudes of the derivatives are seen to increase with gas temperature. Results for the derivatives at various gas temperatures are shown in Figure 6.4, with tabulated values shown in Appendix C.

6.2. Comparison of CTM & Gauntner cooling model

In order to assess the performance of the CTM, it can be compared to an existing cooled turbine model. The Gauntner model presented in subsection 2.4.2 will be used. It was shown earlier that the Gauntner model calculates the required cooling fraction as a function of the cooling effectiveness, namely:

$$\frac{m_c}{m_g} = Factor \cdot 0.022 \cdot \left(\frac{\phi_{gauntner}}{1 - \phi_{gauntner}} \right)^{1.25} \tag{6.1}$$

where $\phi_{gauntner}$ represents the cooling effectiveness, calculated as:

$$\phi_{gauntner} = \frac{T_g - T_m}{T_g - T_c} \tag{6.2}$$

The variable, *Factor*, is a discrete parameter corresponding to the cooling technology used. The variable varies between 0.8 and 2.0. The variation in cooling fraction calculated by the Gauntner model with increasing gas path temperature is shown in Figure 6.5, for a fixed metal temperature of 1100 K and coolant temperature of 800 K. Figure 6.5 shows an almost linear variation in cooling fraction with gas temperature, due to the low exponent used in the last term of Equation 6.1.

The first case that can be compared is the standard Young & Wilcox case, as it specifies all required values for the CTM while leaving only *Factor* to be determined for the Gauntner model. Parameters used are presented in Table 5.1. The CTM predicts a cooling flow requirement of 0.1447 while matching this with the Gauntner Model requires *FACTOR* to be 2.01, a value that represents a blade without film cooling, while the original Y&W test case includes film cooling. In order to compare the CTM with the Gauntner model fully,
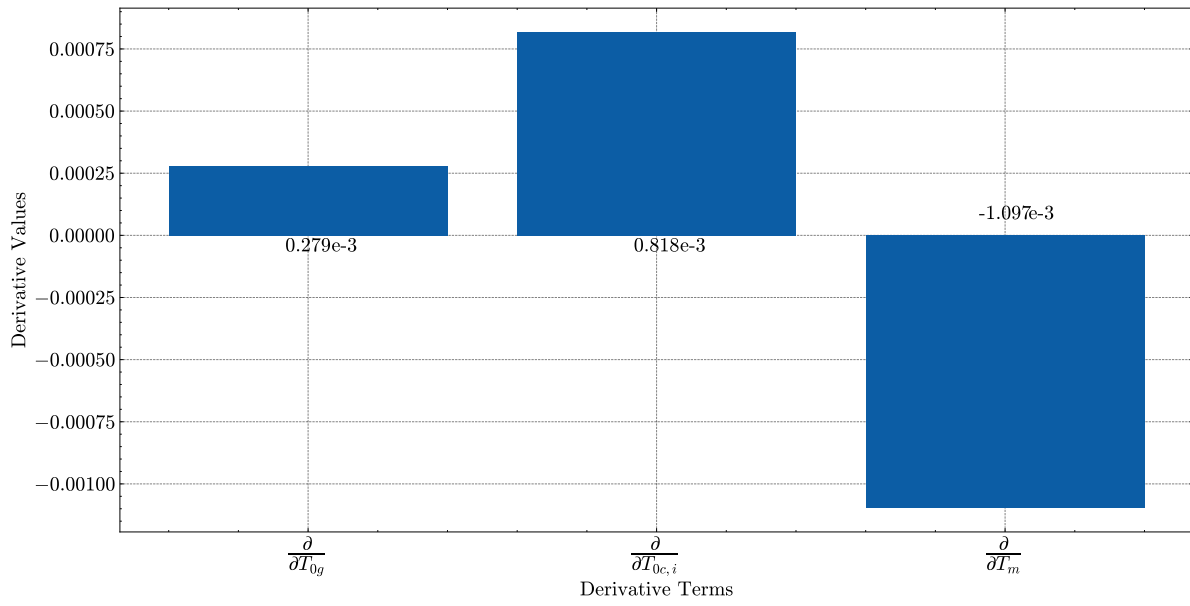
Figure 6.2: Derivatives of $\dfrac{m_c}{m_g}$ with respect to temperature terms evaluated at sensitivity analysis test case conditions, T_g = 1700 K, T_m = 1100 K, $T_{0c,i}$ = 867 K. Remaining parameters shown in Table 6.1
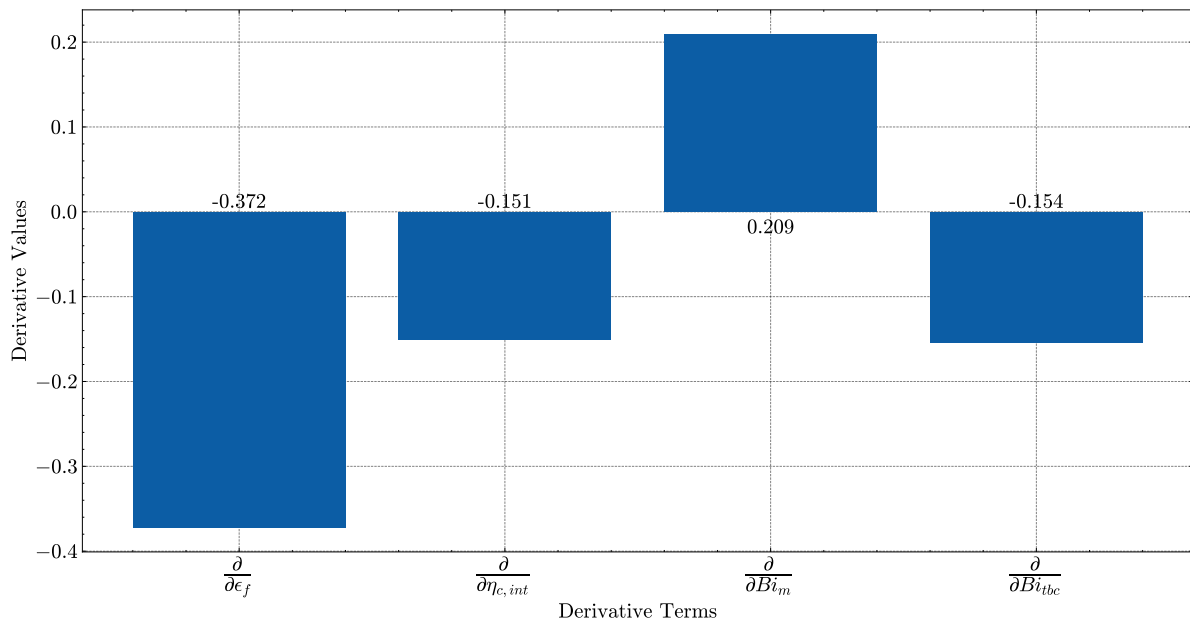
Figure 6.3: Derivatives of $\dfrac{m_c}{m_g}$ with respect to cooling system design terms evaluated at sensitivity analysis test case conditions, T_g = 1700 K, T_m = 1100 K, $T_{0c,i}$ = 867 K. Remaining parameters shown in Table 6.1
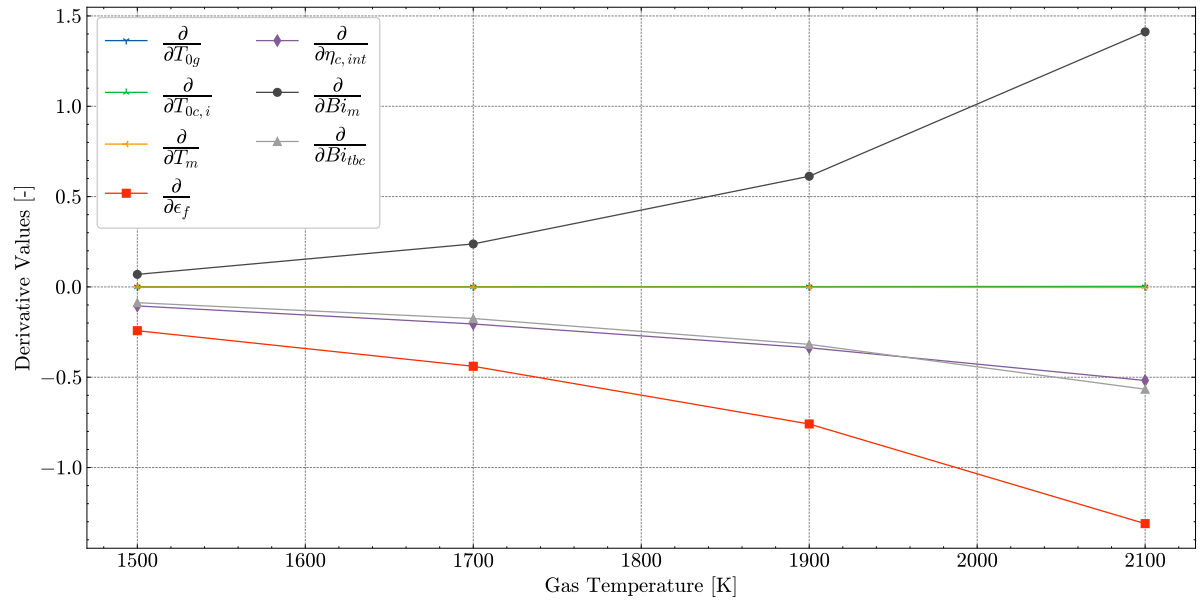
Figure 6.4: Variation in partial derivatives of $\dfrac{m_c}{m_g}$ with gas path temperature.
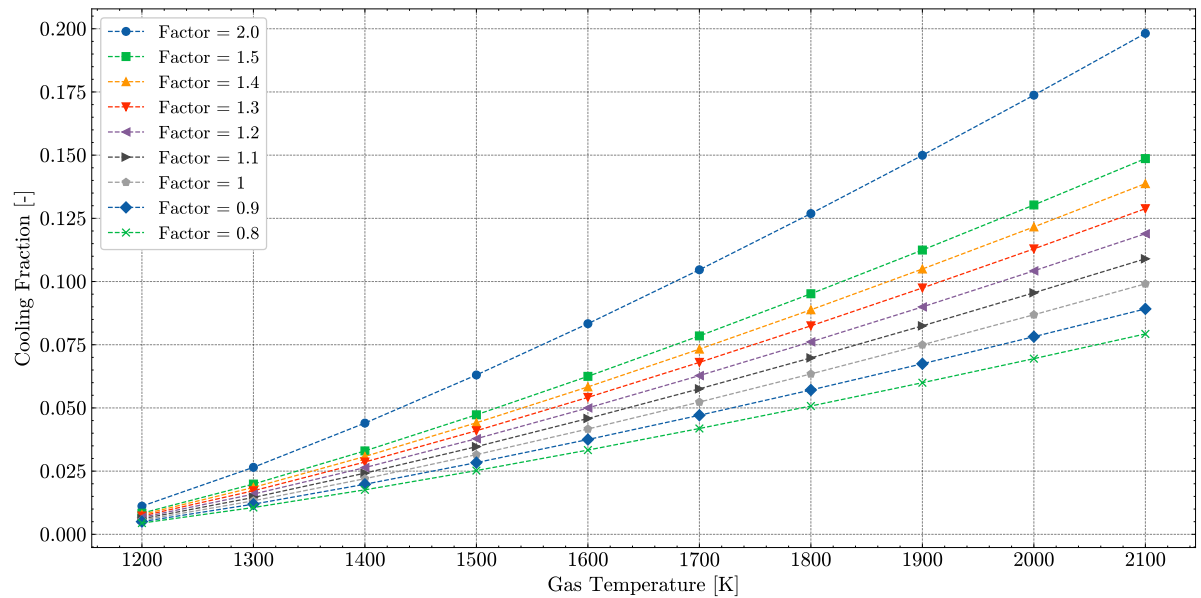
Figure 6.5: Variation in calculated cooling fractions with gas path temperature, for $T_m = 1100$ K and $T_{0c,i} = 800$ K by Gauntner model.
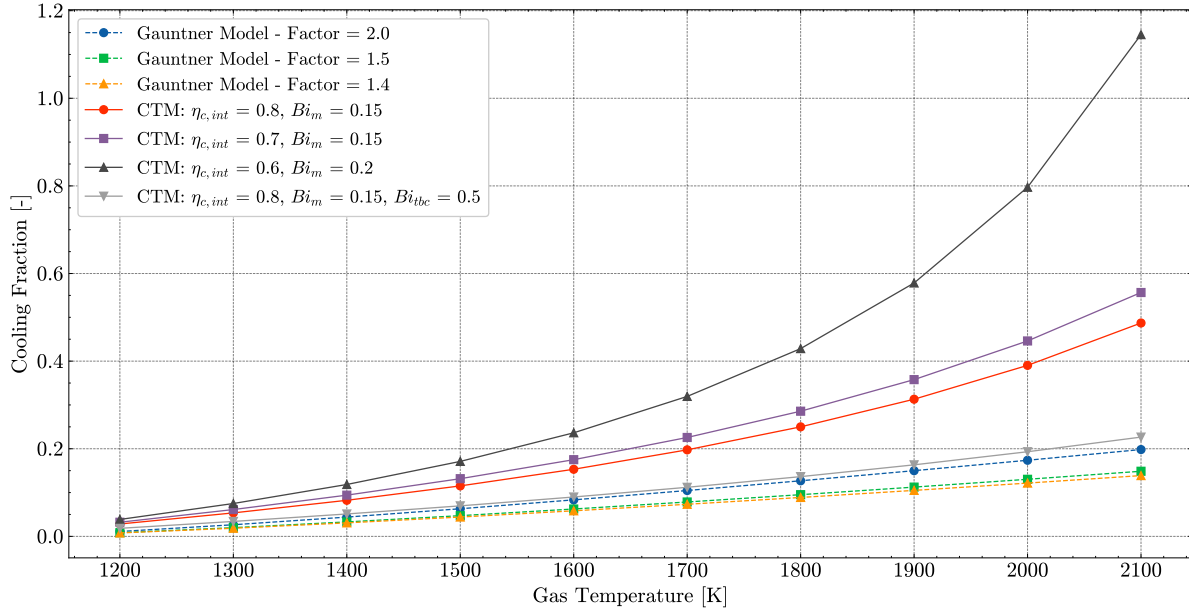
Figure 6.6: Comparison of CTM with Gauntner model for cooled blades with internal convective cooling mechanisms, $T_m = 1100$ K and $T_{0c,i} = 800$ K.

two steps will be taken. The first is to compare outcomes of the two models when the CTM is used with values for ϵ_f, $\eta_{c,int}$, Bi_{tbc} and Bi_{met} within the ranges specified by Young and Wilcox in the original publication. The second step is to tune the CTM parameters to match the Gauntner model, as it is validated against experimental data [22]. These two tasks are further elaborated in subsection 6.2.1 and subsection 6.2.2.

6.2.1. MODEL COMPARISON - STANDARD PARAMETER VALUES

For each group of values for *Factor*, a comparison can be made with the CTM. For the first group, film cooling is absent, meaning that ϵ_f can be set to 0 in the CTM. Furthermore, $\eta_{c,int}$ can be varied between 0.6 and 0.8, as suggested by Y&W [17]. Values used for Bi_m range from 0.15 to 0.2 based on literature. All comparisons will be performed using a value of 0.045 for K_{cool} in the absence of more detailed heat transfer data in the Gauntner model. Results for this group of cooling technologies are shown in Figure 6.6.

Figure 6.6 shows that using standard values for the parameters in the CTM results in significant differences between models. All combinations of CTM parameters used result in over predictions of cooling flows, with the difference between the CTM and Gauntner model growing at higher gas temperatures. The least error is observed in the case where the CTM is instantiated using $\eta_{c,int} = 0.8$, $Bi_m = 0.15$ and $Bi_{tbc} = 0.5$. However, the use of the Bi_{tbc} means that the comparison should be made by setting *Factor* = 1.5 in the Gauntner model. This still shows significant over-prediction. The most likely cause is that the experimental conditions used to calibrate the Gauntner model differ substantially from conditions where $K_{cool} = 0.045$. Reducing the value of this parameter would result in a significant downward shift of all CTM curves. In addition, beyond the absolute values, the CTM shows a significantly higher, non-linear growth in estimated cooling fraction with increased gas temperature. However, this is not considered a discrepancy, as the non-linearity of cooling fraction with gas temperature has been discussed in literature [31].

The second set of values for *Factor* represent blades with film and internal convective cooling. Here Bi_{tbc} is set to 0 and ϵ_f can vary between 0.0 and 0.4, while $\eta_{c,int}$ can vary between 0.6 and 0.8 [17]. Bi_m will be varied between 0.15 and 0.2, with K_{cool} still set at 0.045. The upper and lower bounds of the cooling fraction estimate achievable with the CTM over the Gauntner model predictions is shown in Figure 6.7.

Once again, Figure 6.7 shows the CTM is over-predicting required cooling fractions. However, the lower CTM curve shows a trend with gas temperature similar to that of the Gauntner model. As with Figure 6.6, this suggests that the value of K_{cool} is likely the source of the discrepancy. However, the original data used to calibrate the Gauntner model is insufficient to calculate a new value of K_{cool}. The following section, subsection 6.2.2, deals with the tuning of the CTM parameter values. If the tuned values of K_{cool} are within an acceptable range of existing values but are closer in predicted cooling fraction, this will facilitate further comparison of the CTM and the Gauntner model.
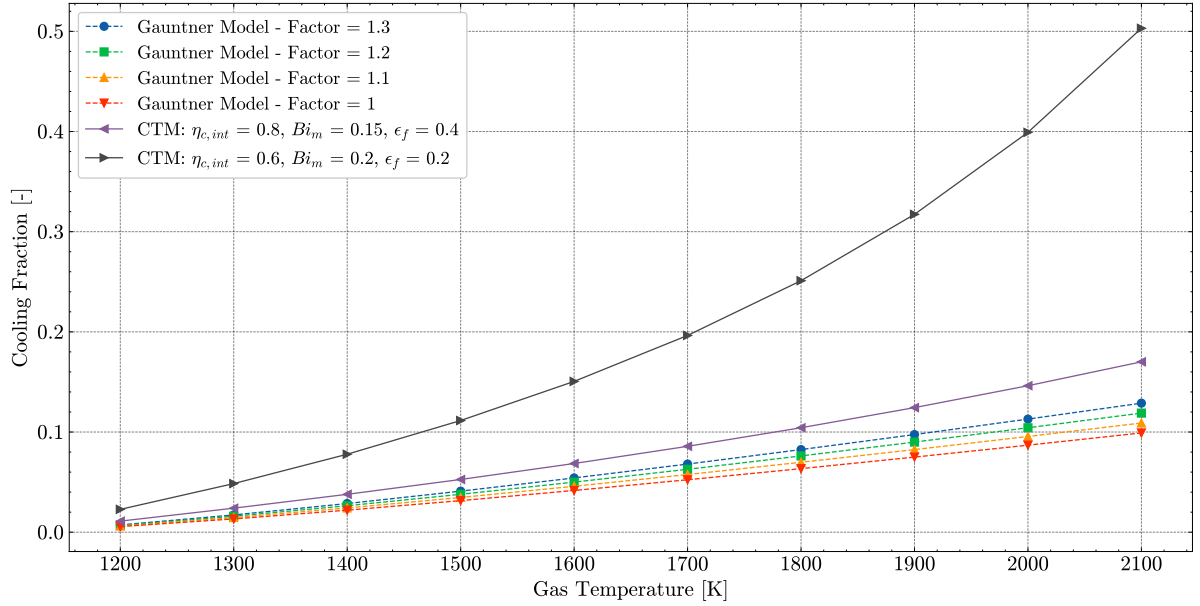
Figure 6.7: Comparison of CTM with Gauntner model for cooled blades with internal convective cooling mechanisms and film cooling, $T_m = 1100$ K and $T_{0c,i} = 800$ K.

Factor	Cooling Type	T.E Ejection %	K_{cool}	$\eta_{c,int}$	ϵ_f	Bi_m	Bi_{tbc}
2.0	Convection	100	x	x	-	x	-
1.5	Convection with coat	100	x	x	-	x	x
1.4	Advanced convection	100	x	x	-	x	-
1.3	Film with convection	75	x	x	x	x	-
1.2	Film with convection	50	x	x	x	x	-
1.1	Film with convection	25	x	x	x	x	-
1.0	Full cover film	0	x	x	x	x	-

Table 6.2: Table of parameters used in regression to tune CTM to Gauntner model. x indicates parameters being used, while $-$ shows a parameter that is not used.

6.2.2. CTM and Gauntner model matching

The matching of the CTM and Gauntner model predictions requires that the parameters of the CTM are tuned to replicate the outcomes of the Gauntner model. Using *Scipy*'s *curvefit* method the CTM parameters ($\eta_{c,int}$, Bi_{tbc}, Bi_{met} and K_{cool}) have been fitted to replicate the results of the Gauntner model over a range of gas temperature values. Table 6.2 indicates which CTM parameters are used in the regression, depending on the value of the parameter $FACTOR$ in the Gauntner model. For the case where the parameter $FACTOR$ has a value of 1.0, representing a film cooled blade with no internal cooling, it is still chosen to use $\eta_{c,int}$ in the regression. This is required as the CTM is not able to run in cases where $\eta_{c,int}$ is set to 0.0, as would be expected for a blade with no internal cooling mechanisms.

Considering the Y&W test case with a maximum metal temperature of 1100 K and a coolant temperature of 867 K, the results of the regression are shown in Table 6.3. A chart of the Gauntner model compared with the tuned CTM results is shown in Figure 6.8. It is clear that the tuned values match the Gauntner model well.

The same procedure is repeated for various combinations of metal and coolant temperature, with T_m varying between 950 and 1250 K and $T_{0c,i}$ varying between 600 and 900 K. From the results, a range of values for each parameter has been found, seeTable 6.4.

Table 6.4 shows that values for K_{cool} can vary from 0.023 to 0.06. The original range of K_{cool} was between 0.01 and 0.1, which the shown results match. $\eta_{c,int}$ has been prescribed as being between 0.6 and 0.7 by Young and Wilcox [17], while the tuned parameter results suggest that a higher range, between 0.78 and 0.85, is more appropriate. For ϵ_f, the provided range was 0.2-0.4 [17], whereas results in Table 6.4 show a range between 0.49 and 0.53. The subsequent work of Horlock [85] suggests a value of 0.5 is feasible for ϵ_f. Finally, the Biot numbers for blades are lower than Y&W prescribe, while Bi_{tbc} is slightly higher. However, these values still

Factor	K_{cool}	$\eta_{c,int}$	ϵ_f	Bi_m	Bi_{tbc}	R^2
2.0	0.031	0.80	0.00	0.10	0.00	0.988
1.5	0.036	0.76	0.00	0.10	0.40	0.999
1.4	0.023	0.85	0.00	0.10	0.00	0.988
1.3	0.062	0.79	0.53	0.10	0.00	1.00
1.2	0.057	0.79	0.52	0.10	0.00	1.00
1.1	0.055	0.81	0.54	0.10	0.00	1.00
1.0	0.052	0.82	0.55	0.11	0.00	1.00

Table 6.3: Regression results for CTM parameters required to replicate Gauntner model over gas temperature range 1300 K - 2100 K. Maximum metal temperature T_m = 1100 K and coolant temperature, $T_{0c,i}$=867 K.
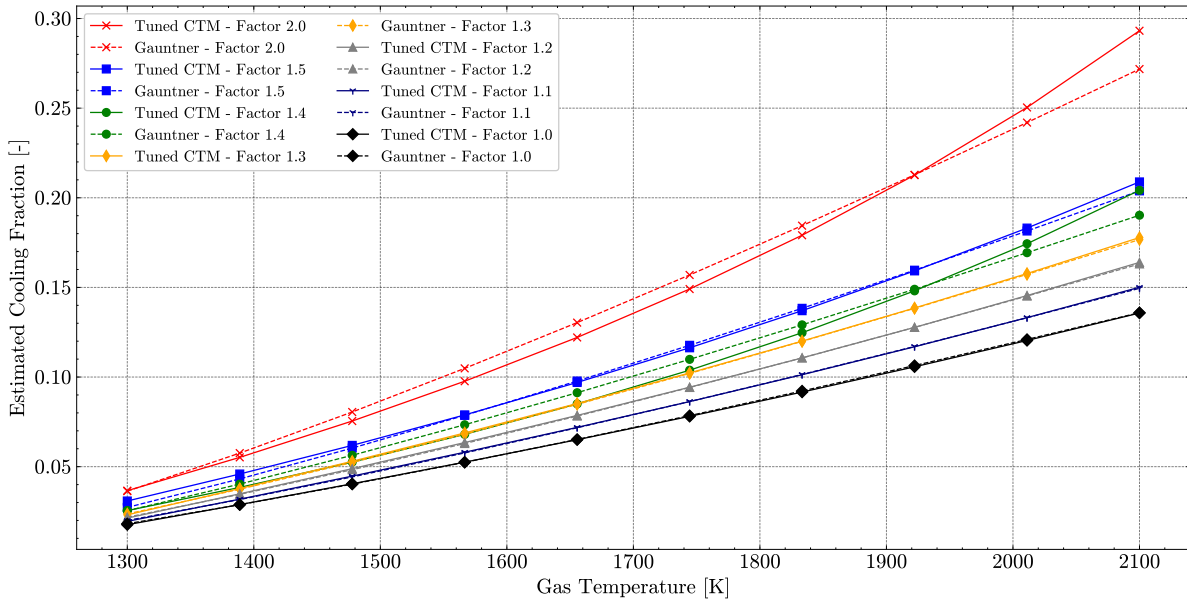
Figure 6.8: Comparison of tuned CTM compared to Gauntner model over gas temperature range 1300 K to 2100 K, T_m = 1100 K and $T_{0c,i}$ = 867 K

Factor	Quantity	K_{cool}	$\eta_{c,int}$	ϵ_f	Bi_m	Bi_{tbc}
	Min.	0.029	0.79	0.00	0.10	0.00
2	Max.	0.032	0.80	0.00	0.12	0.00
	Average	**0.031**	**0.79**	**0.00**	**0.11**	**0.00**
	Min.	0.029	0.76	0.00	0.10	0.23
1.5	Max.	0.036	0.81	0.00	0.15	0.40
	Average	**0.033**	**0.78**	**0.00**	**0.12**	**0.33**
	Min.	0.022	0.84	0.00	0.10	0.00
1.4	Max.	0.024	0.85	0.00	0.12	0.00
	Average	**0.023**	**0.85**	**0.00**	**0.11**	**0.00**
	Min.	0.041	0.79	0.37	0.10	0.00
1.3	Max.	0.085	0.86	0.62	0.16	0.00
	Average	**0.060**	**0.81**	**0.50**	**0.12**	**0.00**
	Min.	0.037	0.79	0.36	0.10	0.00
1.2	Max.	0.079	0.85	0.62	0.16	0.00
	Average	**0.056**	**0.81**	**0.49**	**0.12**	**0.00**
	Min.	0.037	0.80	0.39	0.10	0.00
1.1	Max.	0.072	0.87	0.62	0.17	0.00
	Average	**0.053**	**0.82**	**0.51**	**0.12**	**0.00**
	Min.	0.037	0.81	0.43	0.10	0.00
1.0	Max.	0.066	0.89	0.62	0.18	0.00
	Average	**0.050**	**0.83**	**0.53**	**0.13**	**0.00**

Table 6.4: Tuned CTM parameter values based on Gauntner model for gas temperatures ranging between 1300 K and 2100 K. Metal temperature varied between 950 and 1250 K, and coolant temperature varied between 600 K and 900 K.

fall within ranges reported in the literature and can be considered acceptable.

6.3. EXTERNAL FLOW PARAMETER
The first semi-empirical parameter to be analyzed is the external flow parameter, K_{ext}. It has previously been defined as the conversion factor between total and static conditions for the bulk flow, namely:

$$K_{ext} = 1 + \frac{\gamma_g - 1}{2} M_g^2 \tag{6.3}$$

Where γ_g is the ratio of specific heats of the mainstream gas entering the stage in question. The parameter is mostly used in defining the entropy terms related to the gas-path flow: $\Delta\Sigma_{ext,q}, \Delta\Sigma_{ext,mix,q}$ and $\Delta\Sigma_{ext,mix,KE}$. It has no influence on the estimation of cooling fraction. While not a direct design variable in the design process of the cooling system, γ_g is still important due to its role in entropy modelling.

Figure 6.9 presents the variation of K_{ext} with the Mach number and γ_g, as well as the value 1.07, presented by Young and Wilcox [17] in their test case. The Mach number is a property of the flow speed, while γ_g is determined by the composition and thermodynamic state of the flow at stage entry. The impact of both these variables on K_{ext} will be discussed in subsection 6.3.1 and subsection 6.3.2 respectively.

6.3.1. VARIATION IN GAS PROPERTIES
The ratio of specific heats is a gas property, primarily dependent on the temperature of the hot gases entering the turbine blade row. For the first stages of high pressure turbines, the value of γ_g is driven by the equivalence ratio and the combustor outlet temperature. Figure 6.10 shows the variation in γ_g over a large temperature range, with different curves for differing fuel-to-air ratios, using *PyCycle*'s inbuilt thermodynamic model. Results align well with results found in literature, including that of Sethi et al. [3, 86]. Total pressure has a negligible impact on the value of γ_g, except in cases with high fuel-to-air ratios and temperatures over 1800 K.

Turbine inlet temperatures vary significantly depending on engine type and thrust class [87], although
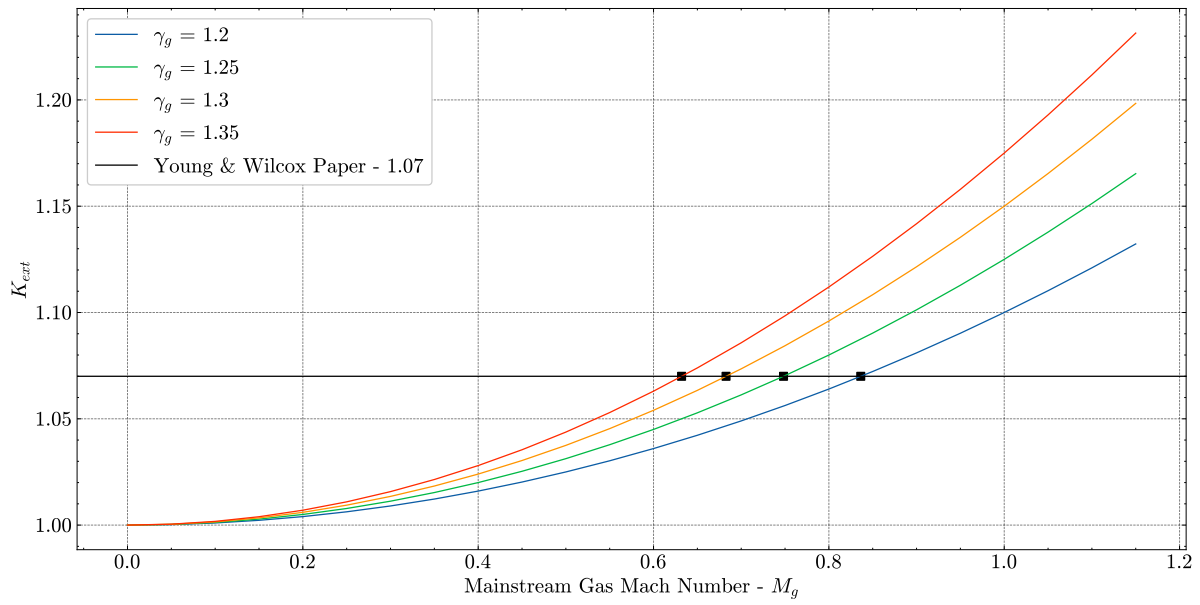
Figure 6.9: Variation in K_{ext} with stage inlet mach number and varying gas composition γ_g. Squares indicate intersection with a test case value of 1.07 [14]
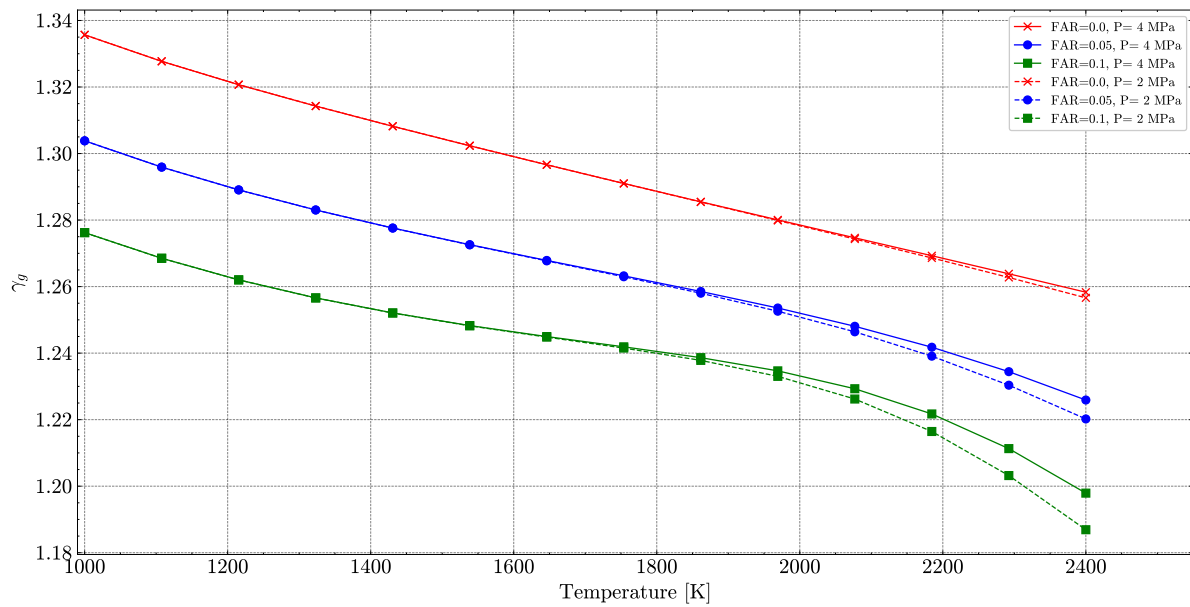
Figure 6.10: Variation in γ_g with temperature for increasing fuel-to-air ratios. Solid lines correspond to a gas total pressure of 4 MPa; dashed lines indicate a total pressure of 2 MPa.
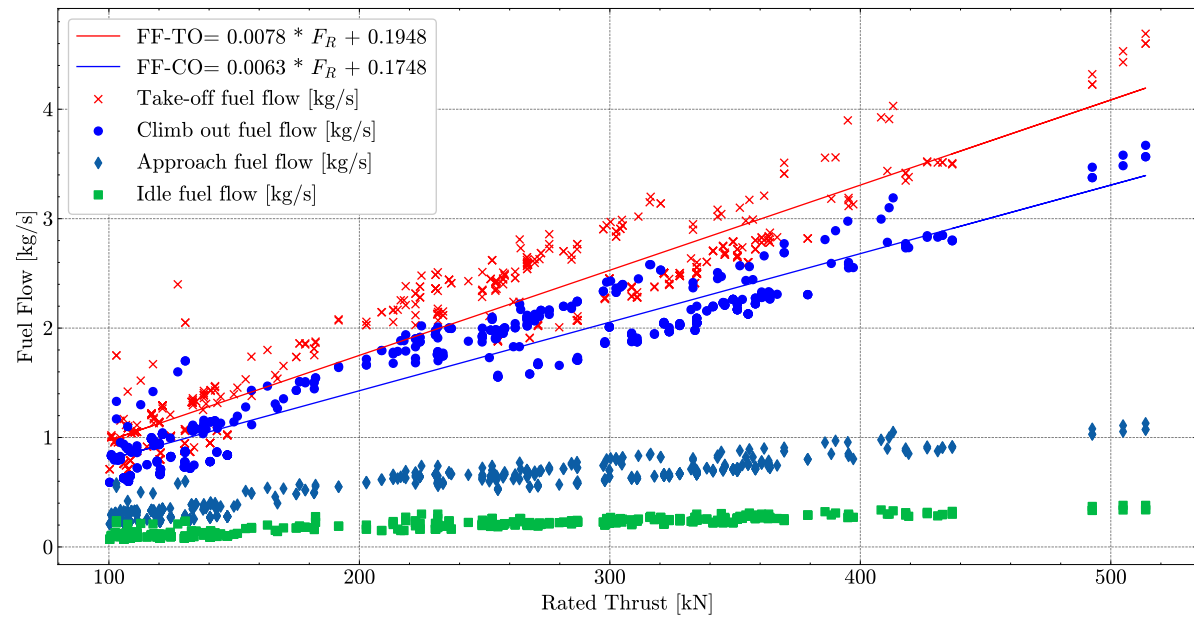
Figure 6.11: Variation in fuel flow with rated thrust, at take-off, climb-out, approach and idle engine settings. Data from ICAO [24]

Engine Type	Model	Take-off Thrust (kN)	Bypass Ratio (BPR)	Air Mass Flow (kg/s)
CFM 56	3C1	104.5	4.8	322
CFM 56	5A1	111.2	6	386
CFM 56	5C2	138.8	6.4	483
CFM 56	7B20	91.6	5.5	483
GE90	85B	400.3	8.4	1378
Rolls Royce Trent	772	316.3	4.89	897
Rolls Royce Trent	892	406.1	5.74	1234
PW	4152	231.3	4.85	773
PW	4168	302.5	5.1	877

Table 6.5: Selected representative engines and bypass ratio, mass flows and take-off thrust levels. Data from ICAO databank [24] and Jenkinson et. al. [33]

the trend of increasing temperatures has been observed across classes [19]. The fuel-to-air ratio in the combustion chamber is a driving factor in turbine inlet temperatures and must be analyzed in order to derive appropriate expected ranges of γ_g. Derivation of reasonable ranges starts with understanding typical mixture compositions in modern aero-engines. The first step is to examine the typical fuel flows in different flight conditions, presented in Figure 6.11. The clusters represent specific flight conditions, which correspond to certain throttle percentages [88]. In descending order: 100% (take-off), 85% (climb), 30% (approach) and 7% (idle).

Figure 6.11 shows a clear increase in absolute fuel flow with the rated thrust of an engine across all four flight phases considered. Particularly for higher throttle settings, the increase is steeper. Additionally, for higher thrust engines, the variation between take-off and climb fuel flow is larger, as shown through the divergence of the blue and red lines.

With fuel flows known, calculation of γ_g requires the calculation of the composition of the gas, based on the equivalence ratio, ζ. A sample of representative engines, with take-off thrusts ranging from 104 kN to 406 kN, are taken to calculate the equivalence ratio based on known air intake mass flow ratios and bypass ratios. Where mass flows were not available at all flight conditions, available mass flows were used. Generally, this is at take-off conditions, which provides an upper bound estimate. The sample of representative engines is presented in Table 6.5. The calculated equivalence ratios are shown in Figure 6.12.

As seen, there is little variation across engine thrust rating and the equivalence ratio for the various engine samples, suggesting that the equivalence ratio is in a similar range for existing turbofan engines in the 100 kN+
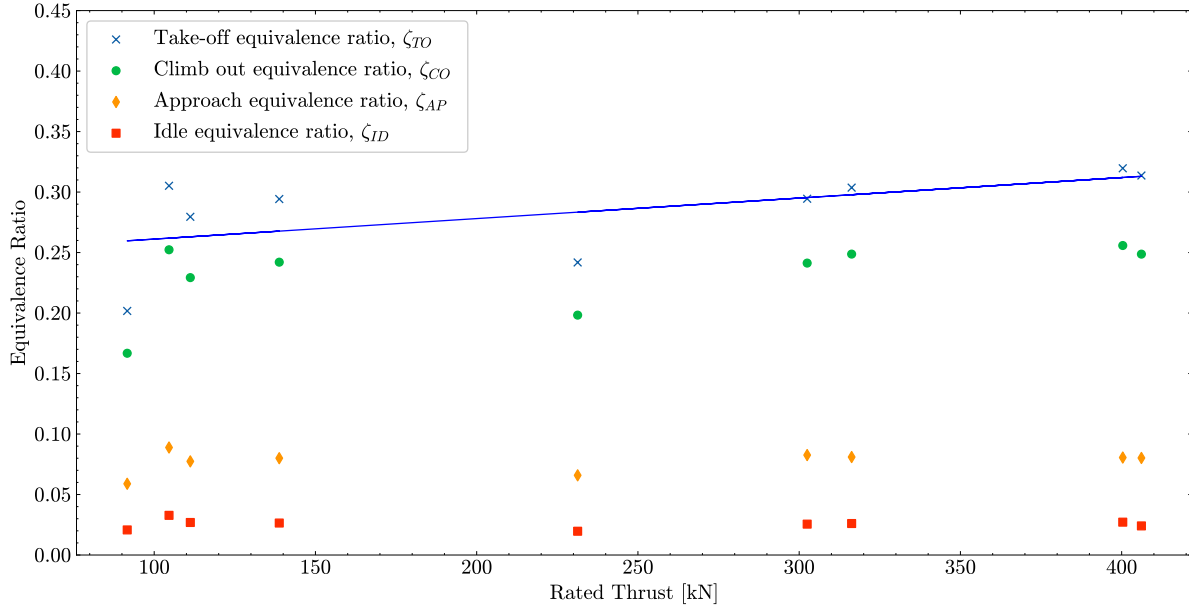
Figure 6.12: Equivalence ratios, ζ for different power settings for sample of representative engines [24, 25]

category. As expected based on Figure 6.11, it is seen that the equivalence ratio is highest at take-off, between 0.2 and 0.3. For certain engines, such as the Pratt & Whitney 4000-112, the take-off equivalence ratio reaches 0.34 [3], with el Abbassi [89] suggesting an upper limit of 0.4 for modern engines.

Based on this information and the data in Figure 6.10, a typical range of γ_g for the first stage of high pressure turbines would be 1.20-1.34. A contour chart of the variation in γ_g with equivalence ratio and temperature is shown in Figure 6.13. As visible, γ_g is more sensitive to temperature than equivalence ratio, and as such, the variation in γ_g across a multistage turbine will be influenced primarily by the expansion ratio of the stage and the resulting temperature drop. Overall, for a multistage turbine system, the value of γ_g will increase following the gas path. Considering the example of the CFM56-5B, Kurzke reports a turbine outlet temperature of 1577 Kelvin and a LPT entry temperature of 1162 Kelvin, which would give γ_g equal to 1.288 and 1.32, respectively taking an equivalence ratio of 0.35.

6.3.2. GAS PATH MACH NUMBER

Considering first Figure 6.14, the value of the K_{ext} parameter is shown to increase with the Mach number for all gas compositions. The chart also reports the value used in the test case of Young and Wilcox, namely K_{ext} = 1.07. It is seen that depending on the composition, the associated Mach number entering the turbine stage can vary from 0.63 to 0.85.

Furthermore, assuming γ_g to be between 1.2 and 1.34, the corresponding range for K_{ext} is between 1.01 and 1.25, as shown in Figure 6.15. The definition of $_{ext}$ for the 1st stage of the high pressure turbine therefore depends on the mainstream Mach number. From Figure 6.15, it is clearly visible that for lower mainstream Mach numbers, there is a negligible effect of γ_g on the value of K_{ext}. At higher mach numbers, there is significantly more dependency, with K_{ext} varying from 1.14 to 1.28 when the gas Mach number is 1.2, as compared to a constant K_{ext} of 1.01 for M < 0.5. The experimental work by Nealy [90] shows Mach numbers varying between approximately 0.2 and 1.05, suggesting that a valid range of K_{ext} would lie between 1.02 and 1.17 approximately. However, further research and validation of gas path mach numbers in aero-engines is needed prior to drawing conclusions. Nonetheless, K_{ext} has no influence on the cooling flow estimates and has negligible influence on entropy calculations.

6.4. INTERNAL FLOW PARAMETER

The internal flow factor, K_{int}, is defined similarly to K_{ext} but is characteristic of the coolant flow. It is a function of flow temperature and Mach number, namely :

$$K_{int} = 1 + \frac{\gamma_c - 1}{2} M_c^2 \tag{6.4}$$
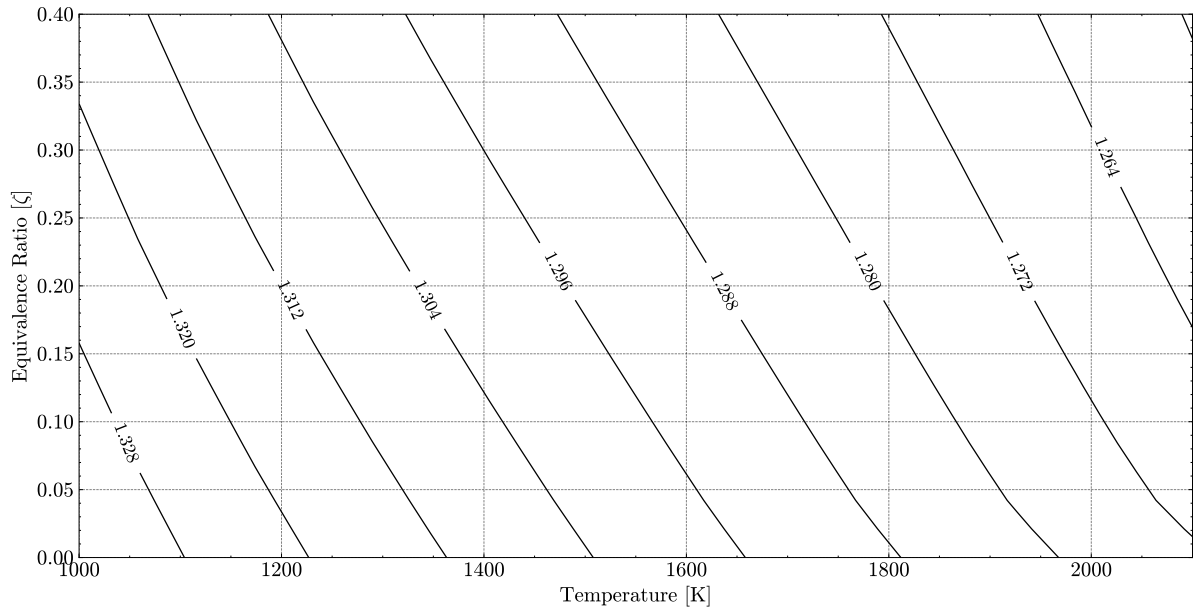
Figure 6.13: Variation in ratio of specific heats for temperatures between 1000 and 2100 kelvin, equivalence ratios between 0.0 and 0.4, at P = 2325 kPa, the turbine inlet pressure of the CFM56 [15]
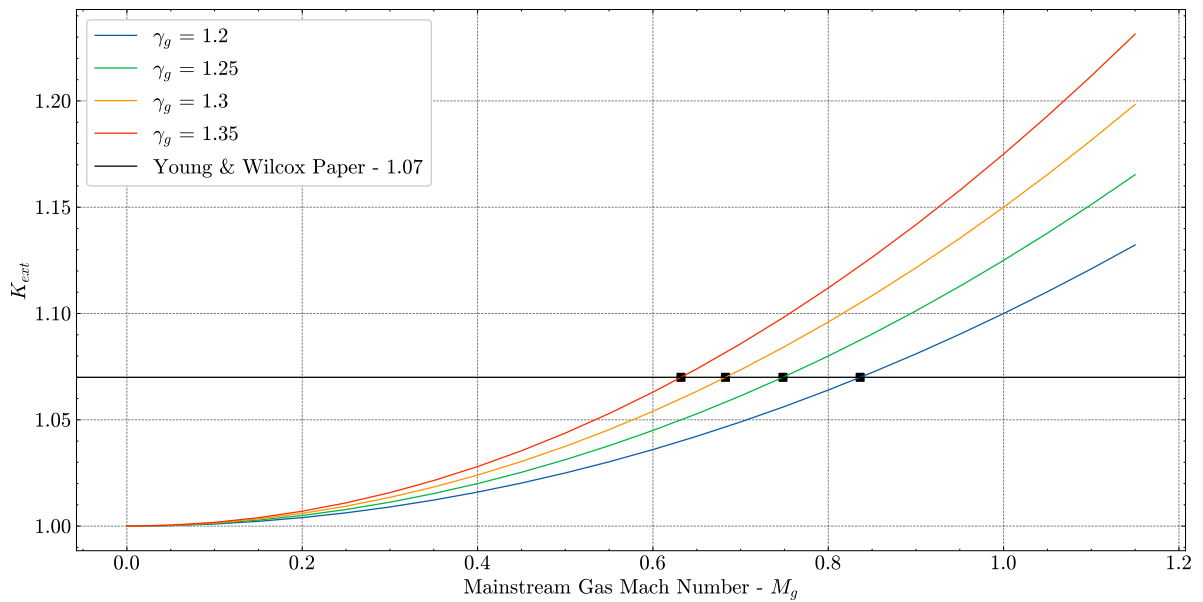
Figure 6.14: Variation in K_{ext} with stage inlet mach number and varying gas composition γ_g. Squares indicate intersection with a test case value of 1.07 [14]
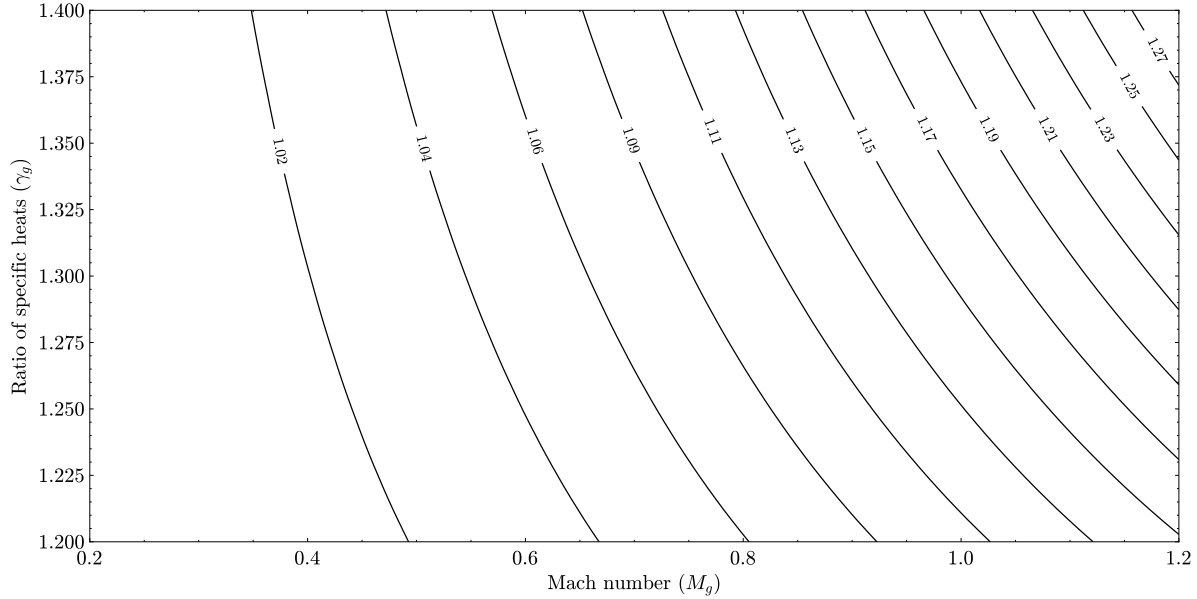
Figure 6.15: Contour plot of K_{ext} with M_g and γ_g, M_g between 0.2 and 1.2

A significant assumption is that the coolant velocity is homogeneous and can be described through an averaged Mach number [14].In order to analyze possible ranges for this value, a number of factors must be accounted for. The first is general engine trends in compressor architecture, as coolant air is drawn along the gas path. As compressor architecture varies significantly amongst engine classes and families, this analysis is limited to modern turbofans used for civil aerospace applications.

An overview of existing, certified engines is obtained through the ICAO emissions database. Engines are filtered such that the lowest thrust rating is 100 kN, in line with the Pratt and Whitney PW1921G engine used to power the A220 family of narrow-body aircraft [91]. The relationship between thrust rating and overall pressure ratio is shown in Figure 6.16. Clearly, there is a direct relation between rated thrust and the overall pressure ratio, although it is not possible to identify a constant ratio between these two quantities. There is a clear dependency on aircraft type as proven by the cluster of engines with OPRS in excess of 35 and rated thrusts between 250 and 350 kN, consisting mainly of engines such as the Rolls Royce Trent 1000 and GE90, used to power large, widebody aircraft.

Bleed air is typically extracted on the basis of the required supply pressure. However, having demonstrated the benefit of lowered cooling air temperature on overall cooling flow fractions, it is desirable to extract cooling air as early as possible depending on the pressure drop in the cooling air path, as discussed by Pfitzner and Waschka [92].

Modelling the total temperature rise through a compressor (stage) is done through the use of Saravanamuttoo's formulation, given the isentropic efficiency of the machine [56]:

$$\Delta T_0 = \frac{1}{\eta_s} \cdot T_{0,1} \left(OPR^{\frac{\gamma_c - 1}{\gamma_c}} - 1 \right) \tag{6.5}$$

This quantity can be rewritten as a function of polytropic efficiency[93], namely:

$$\Delta T_0 = T_{0,1} \left(OPR^{\frac{\gamma_c - 1}{\gamma_c \cdot \eta_{c,p}}} - 1 \right) \tag{6.6}$$

The total temperature rise across the compressor of an engine can be calculated, given the ambient conditions, overall pressure ratio (OPR) and γ_c. Considering the cruise condition, at an altitude of 12000 metres and Mach number of 0.8, the total temperature rise is plotted as a function of engine OPR in Figure 6.17. Ambient temperature is calculated based on the International Standard Atmosphere. Figure 6.17 shows that total temperature rise can vary between 350 K and 550 K for OPRs in the range 25-40, which captures the
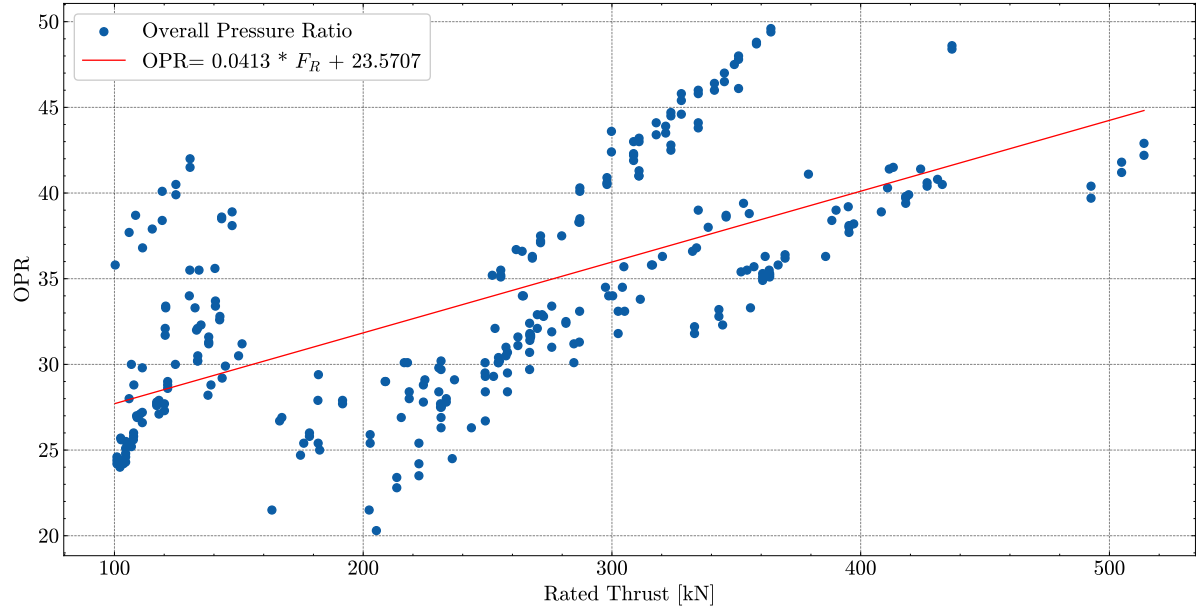
Figure 6.16: Variation in overall pressure ratio with the rated thrust of civil turbofans as per ICAO databank [24]

typical OPR values as seen in Figure 6.16. For modern engines, including the GE90, the pressure ratios at varying flight phases can vary, as seen in Table 6.6. Extending the calculation of total temperature rise across the compressor gas path to various altitudes results in the contour plot shown in Figure 6.18.

It is known from discussions in previous chapters that γ varies very little with pressure and for the purposes of calculating K_{int} can be purely treated as a function of temperature. Based on Figure 6.18, at 12,000 metres, an OPR of 20 results in a total temperature rise of 350 K. Ambient temperature at this altitude is 216.65 K, meaning the temperature at the outlet of the final compressor stage is approximately 567 K. For higher OPR's at lower altitudes, the compressor delivery temperature (CDP) will be higher. For temperatures between 550 and 1000 K, γ_c varies between 1.39 and 1.3, as seen in Figure 6.19. This range of γ_c means that typical K_{int} values for cooling air extracted from final compressor stages is 1.01-1.02. This is calculated based on the coolant Mach number assumed in the original paper by Young and Wilcox (0.22) [17]. For extraction from earlier stages, K_{int} is likely to be higher, due to an increase in γ_c. Limited information is available regarding flow velocities and Mach numbers in cooling air systems, thereby limiting further discussion into possible ranges for K_{int}. However, as with K_{ext}, the internal flow factor K_{int} has little to no influence on the calculation outcomes of the CTM.

Pressure Ratio	Cruise	Take-off
Inlet	1.59	1.00
Inner Fan	1.65	1.58
LPC	1.14	1.10
HPC	21.5	23.0
OPR	40.44	39.97

Table 6.6: Cruise and take-off pressure ratios for the GE90 engine [31]

6.5. COOLING FLOW PARAMETER

One of the most important empirical factors used in the CTM is the cooling flow factor, K_{cool}, as it is a linear scaling factor for the cooling fraction. It is defined as the product of three terms:

$$K_{cool} = \frac{A_{surf}}{A_{g*}} \frac{cp_g}{cp_c} St_g \qquad (6.7)$$
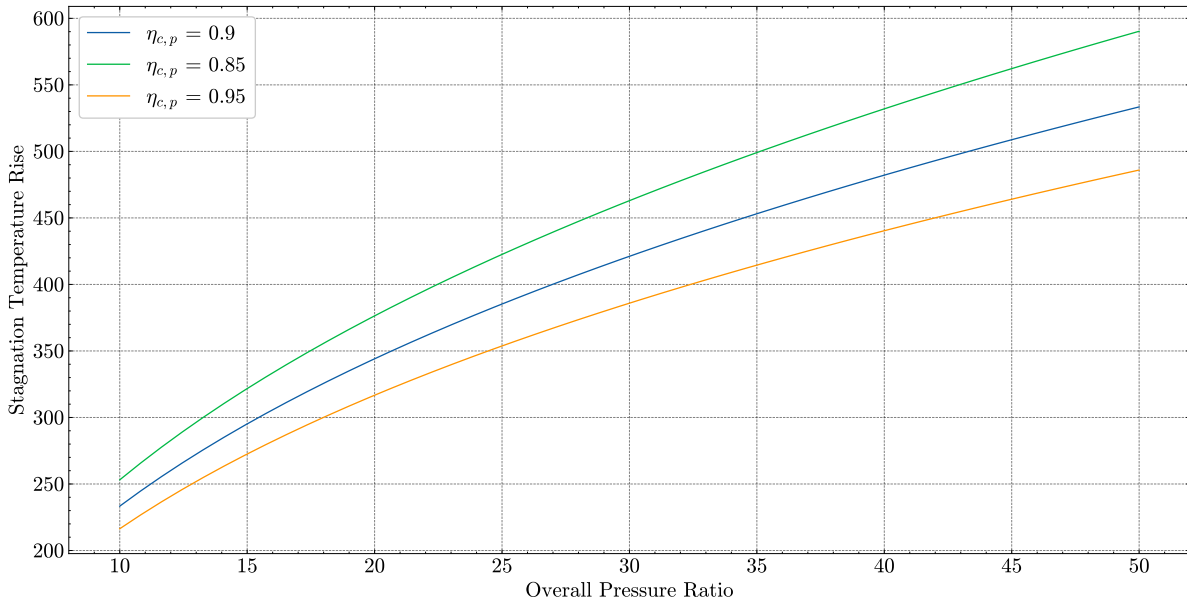
Figure 6.17: Variation in stagnation temperature rise with variation in overall pressure ratio for polytropic efficiencies in the range 0.85-0.95, at altitude of 12000 metres.
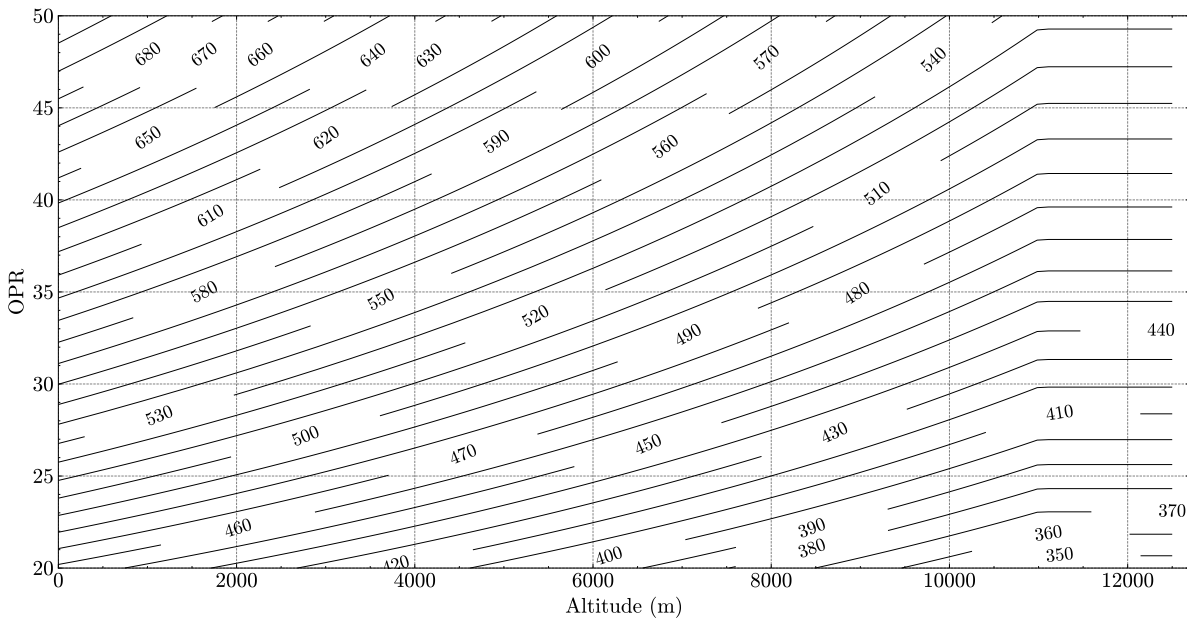
Figure 6.18: Variation in stagnation temperature rise with OPR for altitudes between sea level and 12000 metres, $\eta_{c,p} = 0.9$ and $\gamma_c = 1.4$
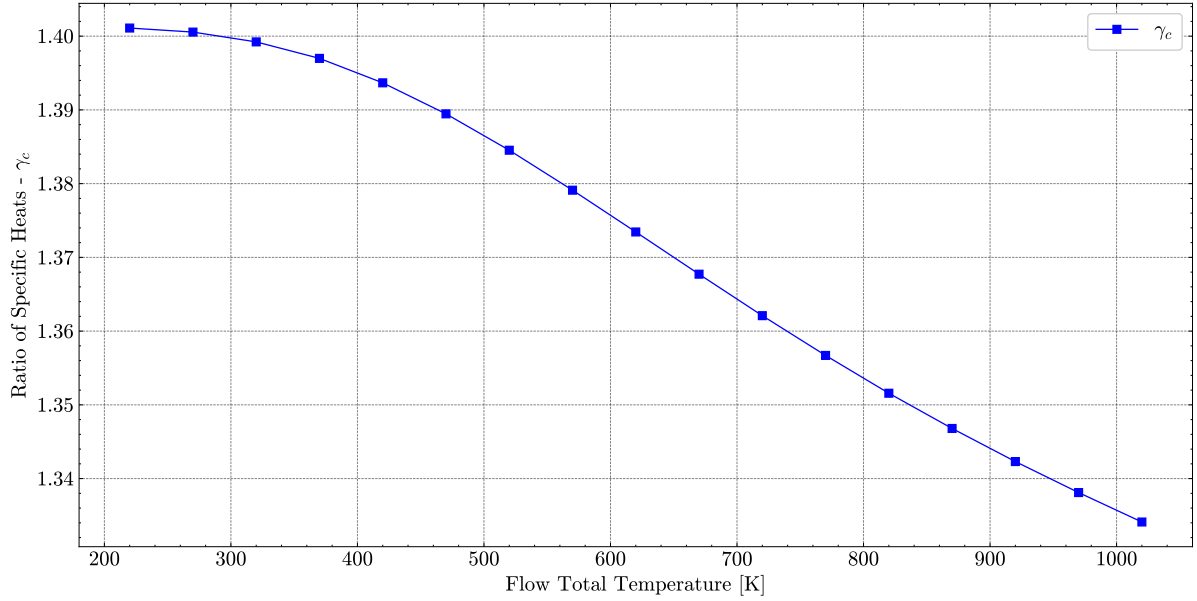
Figure 6.19: Variation in ratio of specific heats for air with temperature.

Where the first term is the ratio of the blade surface area to the blade throat area. Furthermore the second term is the ratio of the specific heat capacities of the gas and coolant. Finally, the third term is the Stanton number, St_g, which is based on an average external heat transfer coefficient [14]. Young and Wilcox considered a range between 0.01 and 0.1 for K_{cool}, see Figure 5.4, while subsequent work by Horlock et. al,[29] suggests a value of K_{cool} of 0.045 is suitable for current, advanced and super-advanced technology levels. The tuning of the CTM to replicate the prediction of the Gauntner model, discussed in subsection 6.2.2, suggests a range of K_{cool} between 0.02 and 0.06. Given the high influence of this parameter on the predictions of the CTM, further analysis of K_{cool} will be presented in this section. An analysis of effects of gas composition and geometric parameters on K_{cool} will be presented in subsection 6.5.1, while the Stanton number will be discussed in subsection 6.5.2 allowing specification of a suitable range for K_{cool}.

6.5.1. Gas composition & Turbine Geometry

Considering the second term in Equation 6.7 , the ratio of specific heats at constant pressure, $\frac{cp_g}{cp_c}$, this is influenced by the composition and temperature of the gas entering the turbine stage. The analysis of a set of engines (Table 6.5) shows that equivalence ratios for modern high bypass ratio turbofans vary between 0.15 and 0.3 in the climb and take-off phases of flight. For a mid-range equivalence ratio, ζ, of 0.26 the ratio $\frac{cp_g}{cp_c}$ is plotted in Figure 6.20. From this, it can be seen that typical values of this ratio are in the range 1.1 - 1.3.

Young and Wilcox take a value of 30 as the product of the first two terms used to define K_{cool}, with the $St_g = 0.0015$[17]. The first term represents the ratio of the blade surface area to the throat area. In a turbine row, the throat is defined as the minimum area of the blade passage [94] and is the narrowest point in the gas path between two blades in a turbine row. Limited data is available regarding precise blade dimensions, as this is typically engine manufacturers' proprietary information. However, such data can be found in the Von Karman Institute's (VKI) technical note presenting turbine row tests [34]. Geometric characteristics of the tested blade are shown in Figure 6.21 and Table 6.7.

Airfoil coordinates are also present in the original technical report [34] and can be used to calculate the perimeter of the blade, which is used in place of the surface area in this simplified, 1D treatment of the external heat transfer. The perimeter, P_b, is calculated by taking the sum of the distance between each consecutive pair of coordinates, n in number, namely:

$$P_b = \sum_{i=0}^{n} \sqrt{(x_{i+1} - x_i)^2 + (y_{i+1} - y_i)^2} \tag{6.8}$$

While this involves a linear approximation of the curves described by the airfoil, the uncertainty introduced
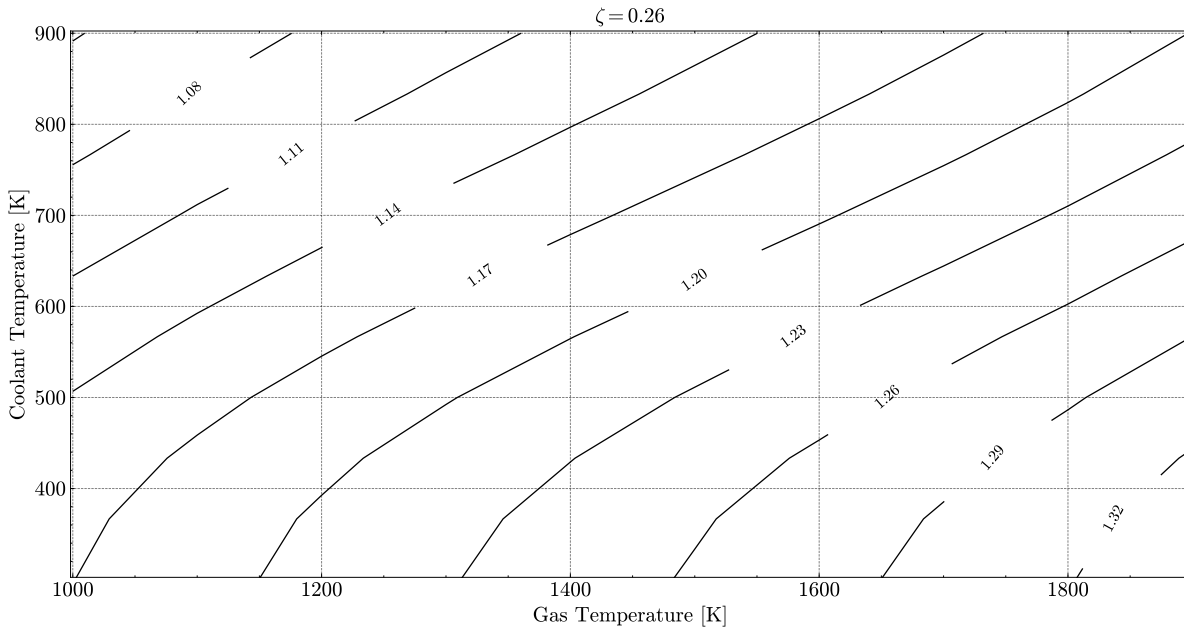
Figure 6.20: Variation in ratio of specific heats at a constant pressure of gas and cooling air with temperatures ($\frac{cp_g}{cp_c}$), $\zeta = 0.26$
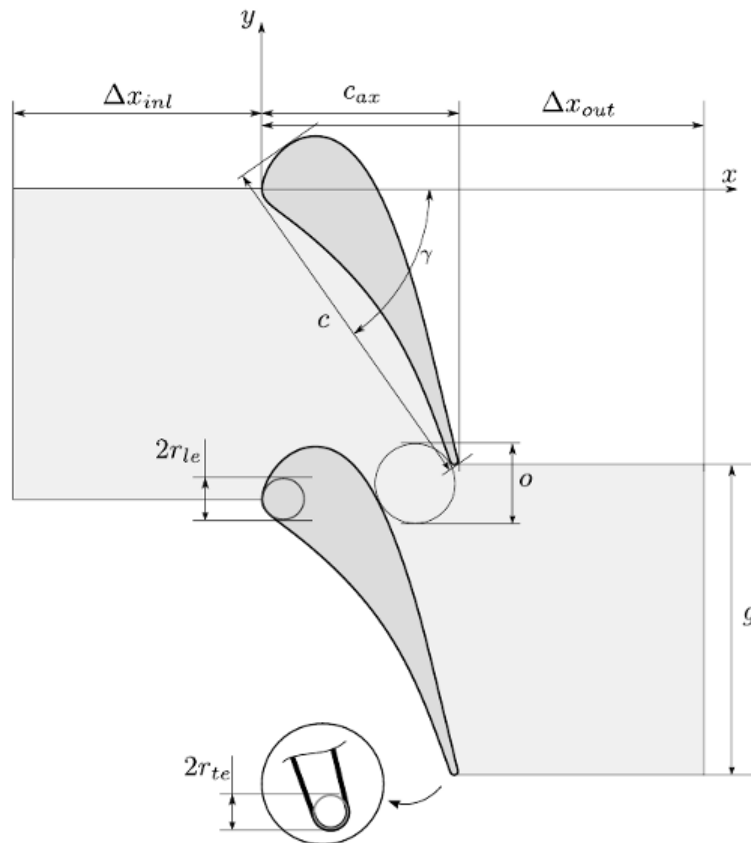
Figure 6.21: Geometry of LS89 turbine test configuration [26]

Parameter	Symbol	Value	Unit
Chord	c	67.647	[mm]
Throat to Chord ratio	o/c	0.2207	[-]
Number of coordinate pairs	n	405	[-]
Calculated Perimeter	P_b	152.2	[mm]
Calculated Perimeter-Throat ratio	$\frac{A_{surf}}{A_{g*}}$	10.2	[-]
Estimated cooling flow parameter	K_{cool}	0.019 - 0.02	[-]

Table 6.7: Geometric parameters of LS89 turbine blade [34] and calculated properties.

is acceptable due to the high number of coordinate points available. The results of the calculation show an approximate value of 10.2 for the perimeter-to-throat ratio. Young and Wilcox's original value of 30 would require the ratio to be 25-27 depending on the exact value of $\frac{cp_g}{cp_c}$. Taking the prescribed St_g (0.0015) the value for K_{cool} would be approximately 0.02. This aligns quite well with the results obtained while tuning the CTM based on the Gauntner model predictions. Furthermore, for turbine blades with larger camber and higher thickness, the expected value of the area ratio will be higher for the same throat-to-chord ratio.

6.5.2. STANTON NUMBER

This section will address the Stanton number, St_g. Defined as the ratio of heat transfer to thermal capacity [61] it is a dimensionless property. It can be expressed as the ratio of the external heat transfer coefficient to flow properties, as done by Young and Wilcox [17], namely :

$$St_g = \frac{\alpha_g}{cp_g \rho_{g*} V_{g*}}$$ (6.9)

ρ is the gas density, and α_g is the external heat transfer coefficient. Young and Wilcox take an average value for α_g over the blade, despite significant variation based on chordwise position. The superscript "$*$" indicates properties at the throat. This formulation of St_g requires detailed knowledge of flow velocity and geometric conditions at the nozzle throat, which are often unknown. Therefore, to develop a range of values for K_{cool}, a method to estimate St_g based on higher level parameters is required. St_g can be written in terms of the Nusselt number[61]:

$$St_g = \frac{Nu}{RePr}$$ (6.10)

Where Nu is the Nusselt number, Pr is the Prandtl number and Re the Reynolds number. The Reynolds number is the ratio of inertial to viscous forces in a fluid [61], defined based on a characteristic length, L. It is calculated as:

$$Re = \frac{1}{2}\frac{\rho_g v L}{\mu_{gas}}$$ (6.11)

where v represents flow velocity and μ_{gas} is the dynamic viscosity of the fluid considered.For gas turbine blades the characteristic length is the chord, c, therefore:

$$Re = \frac{1}{2}\frac{\rho_g v c}{\mu_{gas}}$$ (6.12)

Furthermore, the Prandtl number is defined as:

$$Pr = \frac{cp_g \mu_{gas}}{\lambda_g}$$ (6.13)

where λ_g is the thermal conductivity of the gas.

Pilidis et al present a correlation for St_g for flow over gas turbine blades [95], based on Re and Pr. The correlation is based on the assumption of turbulent boundary layer flow over the blade, which may not always fully represent flow conditions. However it is considered appropriate due to its conservative nature [95]. Therefore, this correlation will be considered for Reynold's numbers in excess of $5 \cdot 10^5$ [23]. The correlation is:

$$St_g = 0.285 Re^{-0.37} Pr^{-2/3}$$ (6.14)
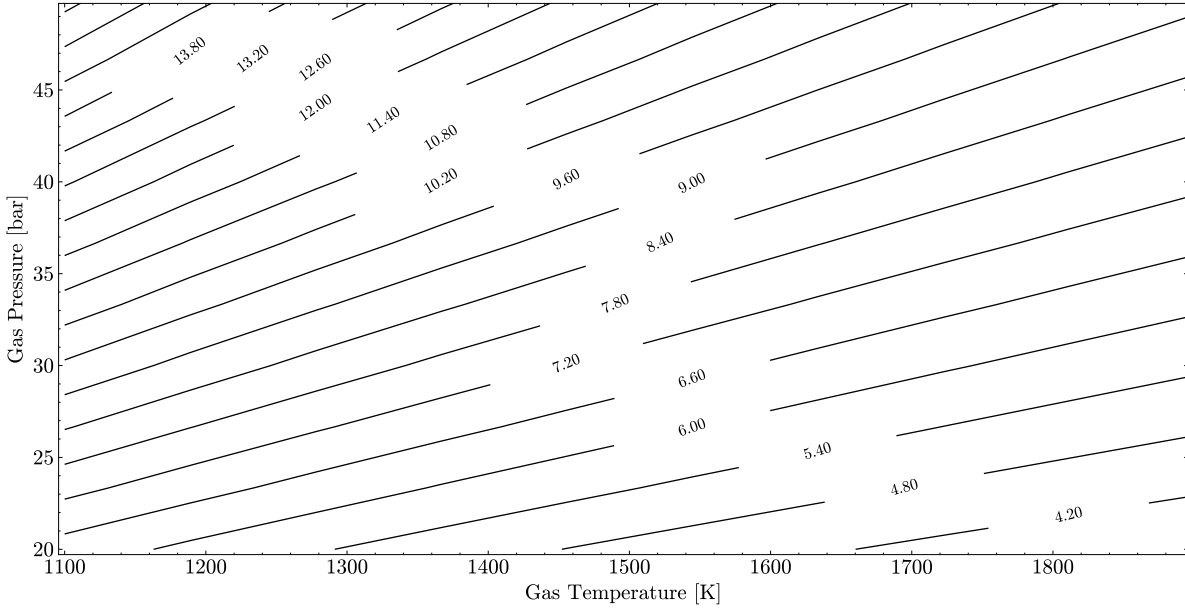
Figure 6.22: Variation in JetA1 combustion product density with temperature and pressure, equivalence ratio of 0.3.

Based on the definitions of Pr the correlation can be rewritten to:

$$St_g = 0.285 \cdot (Re)^{-0.37} \cdot \left(\frac{cp_g \mu_{gas}}{\lambda_g}\right)^{-2/3} \tag{6.15}$$

The density of the gas is known upon specification of pressure, temperature and composition. Considering an equivalence ratio of 0.3, representative of take-off conditions, gas densities vary between 4 and 13.5 kg/m^3, see Figure 6.22. Furthermore, cp_g is also known based on pressure, temperature and composition. This leaves the dynamic viscosity, μ_g and thermal conductivity of the gas, λ_g to be calculated. Both these quantities can be expressed as a function of the molar mass, M and molecular diameter, σ of the gas. Warnatz [35] provides an empirical correlation for both quantities with temperature, T. For dynamic viscosity, this is:

$$\mu = 2.6693 \cdot 10^{-8} \frac{\sqrt{MT}}{\sigma^2 \Omega^{(2,2)}} \tag{6.16}$$

For thermal conductivity the correlation is:

$$\lambda = 8.232 \cdot 10^{-4} \frac{\sqrt{T/M}}{\sigma^2 \Omega^{(2,2)}} \tag{6.17}$$

Both correlations allow for real gas behaviour (inter-molecular interaction) to be modelled through $\Omega^{(2,2)}$, the reduced collision integral [35]. However, for the purpose of this discussion, this will not be considered. Furthermore, the correlations presented are valid for a single element, while the gas in a turbine is a mixture of combustion products and air. For mixtures, both quantities can be written as a function of the average molar mass of the constituent elements. For μ_g this is:

$$\mu_{g,mix} = \frac{1}{2}\left(\sum_i \chi_i \mu_i + (\sum_i \frac{\chi_i}{\mu_i})^{-1}\right) \tag{6.18}$$

A similar expression is defined for λ_g. χ_i is the mole fraction of each constituent species of the mixture. The combustion products of the complete combustion of Jet-A1 were shown to be:

$$10.8CO_2 + 10.8H_2O + 121.8N_2 \tag{6.19}$$

For each of these species, the properties required to calculate μ_g and λ_g are shown in Table 6.8.

With these parameters specified, expected value of St_g can be calculated based on the external flow Re and the gas temperature, as expected by the Reynolds analogy [96]. As an example, the original value for St_g

Species	Diameter [nm]	Molar mass [g/mol]	mol fraction
CO_2	0.376	44.0095	0.0755
H_2O	0.260	18.0153	0.0755
N_2	0.362	28.0134	0.8491

Table 6.8: Molar mass and molecular diameter of combustion product species [28, 35]
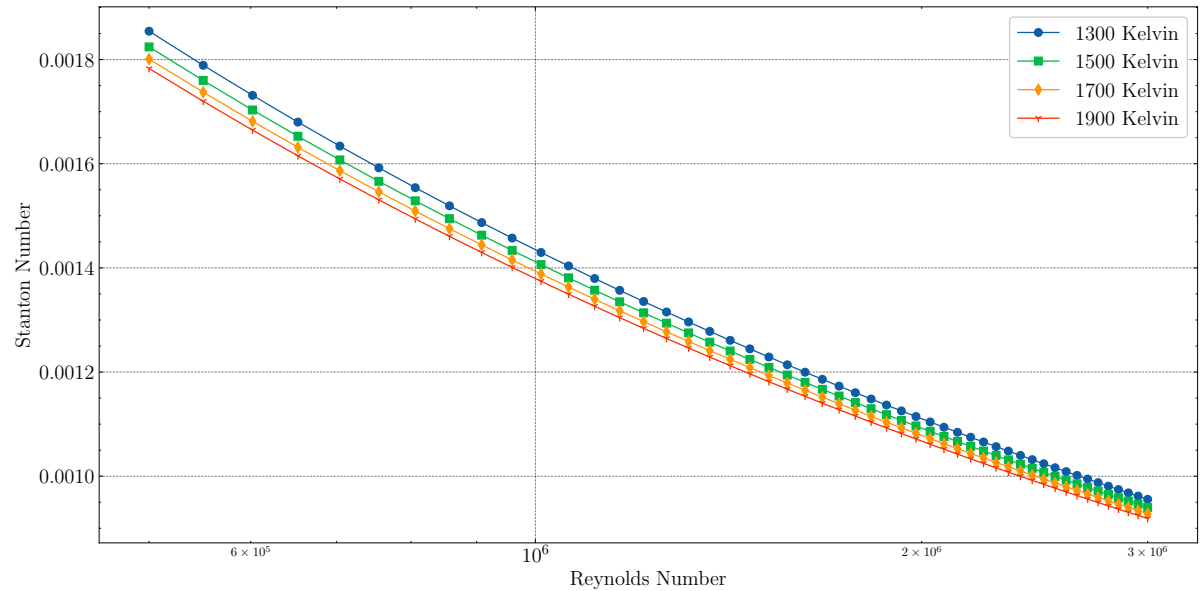
Figure 6.23: Variation in St_g with Reynolds number for external heat transfer over gas turbine blades for various gas temperatures.

[17], 0.0015 can be used to back calculate the value of Re required at the gas temperature of 1700 K, using the correlation in Equation 6.14. At this temperature, a Re of between 8e5 and 9e5 satisfies the correlation. This range is realistic in transonic turbines and fall within the experimental range of the LS89 test campaign where Re varied between 5e5 and 2e6 [34]. Considering a range of Reynolds numbers up to 3e6 [97], and gas temperatures between 1300 K and 1900 K, the estimated corresponding range of St_g is between 0.00185 and 0.00095, as shown in Figure 6.23.

Therefore, a suitable range for the three terms defining K_{cool} are:

- $10 \leq \dfrac{A_{surf}}{A_{g*}} \leq 27$

- $1.1 \leq \dfrac{cp_g}{cp_c} \leq 1.3$

- $0.00095 \leq St_g \leq 0.00185$

A plausible range for K_{cool} is then between 0.01 and 0.065. Once again, this matches the range of K_{cool} found through the tuning the CTM based on the Gauntner model results. However, using the lower end of this range of K_{cool} is unlikely to accurately represent turbine conditions due to increased turbulence in turbines [58]. This concludes the discussion on feasible ranges of K_{cool}.

6.6. BIOT NUMBERS

Developments in cooling system design have been complemented by advancements in material properties [98] as well as blade design, with material capabilities influencing cooling air flow requirements and therefore the performance of turbines. The CTM accounts for blade design and material properties through Biot numbers, defined earlier for blade metal and thermal barrier coatings, as:

$$Bi_m = \frac{\alpha_g}{\lambda_m} t_m = \frac{T_{m,ext} - T_{m,int}}{T_{aw} - T_w} \tag{6.20}$$
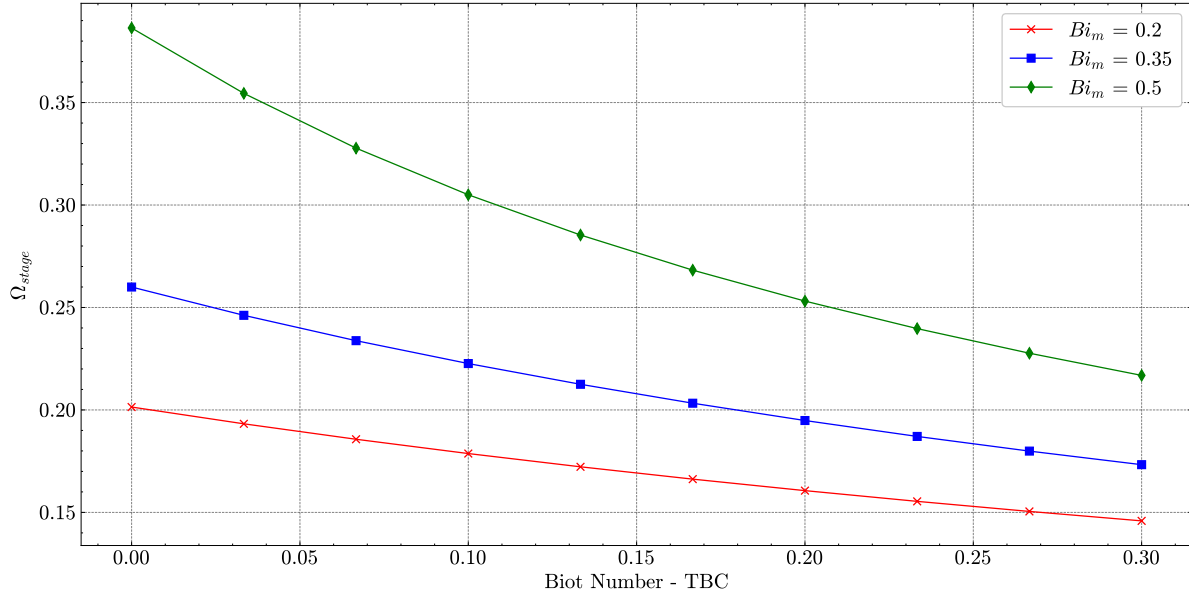
Figure 6.24: Variation in stage total cooling fraction with thermal barrier coating Biot number.Gas temperature of 1700 K, maximum metal temperature of 1100 K, with film cooling.

$$Bi_{tbc} = \frac{\alpha_g}{\lambda_{tbc}} t_{tbc} = \frac{T_w - T_{m,ext}}{T_{aw} - T_w} \tag{6.21}$$

Where α_g represents the mean external heat transfer coefficient of the mainstream gas flow, λ the thermal conductivity of the materials and t the thickness. The Biot numbers indicate the ratio of the temperature difference due to conduction in the concerned material, as compared to the overall temperature difference due to convection and conduction. To assess the role of the Biot numbers on CTM results, subsection 6.6.1 will investigate the relationship between Biot numbers and cooling flow estimates. Following this, subsection 6.6.2 will investigate the influence of temperature on material thermal conductivity, while subsection 6.6.3 will aim to quantify reasonable ranges for both Biot numbers.

6.6.1. BIOT NUMBERS AND COOLING FLOW REQUIREMENTS

To assess the influence of Biot numbers on the cooling flow estimates, we define the total coolant fraction of the stage, Ω_{stage}, as the sum of the stator and rotor coolant flows, normalized by the stage inlet massflow rate. Ω_{stage} is then defined as:

$$\Omega_{stage} = \frac{\dot{W}_{c,s} + \dot{W}_{c,r}}{\dot{W}_{primary}} \tag{6.22}$$

where $\dot{W}_{c,s}$ and $\dot{W}_{c,r}$ represent stator and rotor coolant mass flow rates respectively, while $\dot{W}_{primary}$ represents the massflow rate entering the turbine stage.

The CTM is instantiated with values of the Young & Wilcox test case, shown in Table 5.1. The variation in Ω_{stage} with Biot numbers are shown in Figure 6.24 and Figure 6.25. The range of Biot numbers considered for thermal barrier coatings (tbc) is 0 to 0.3. 0 is the value used in the CTM to represent a blade without a tbc. The upper bound of 0.3 is chosen to represent the variation in thermal conductivity amongst tbc materials, up to a factor 2 [38], compared to the typical value given by Horlock et. al.[85] of 0.15. Ranges for metal Biot numbers are initially based on prescribed ranges by Young and Wilcox [17].

From Figure 6.24 and Figure 6.25 it can be seen that the effects of both Biot numbers on stage cooling fraction are opposing. An increase in the tbc Biot number, Bi_{tbc}, strongly decreases Ω_{stage}, while an increase in the metal Biot number, Bi_m increases Ω_{stage}. The influence of a thermal barrier coating is larger, the higher the metal Biot numbers, as proven by the divergence of the curves of Ω_{stage} for prescribed values of Bi_{tbc} in Figure 6.25. The Biot number is a lumped parameter, meaning that an increase could represent a thickening of the material, an increase in convective heat transfer coefficient α , or a reduction in thermal conductivity λ.

For a fixed total stage cooling fraction, multiple combinations of metal and tbc Biot numbers can produce the same outcome. When Ω_{stage} is 0.2, a design with Bi_m of 0.2 does not require a thermal barrier coating.
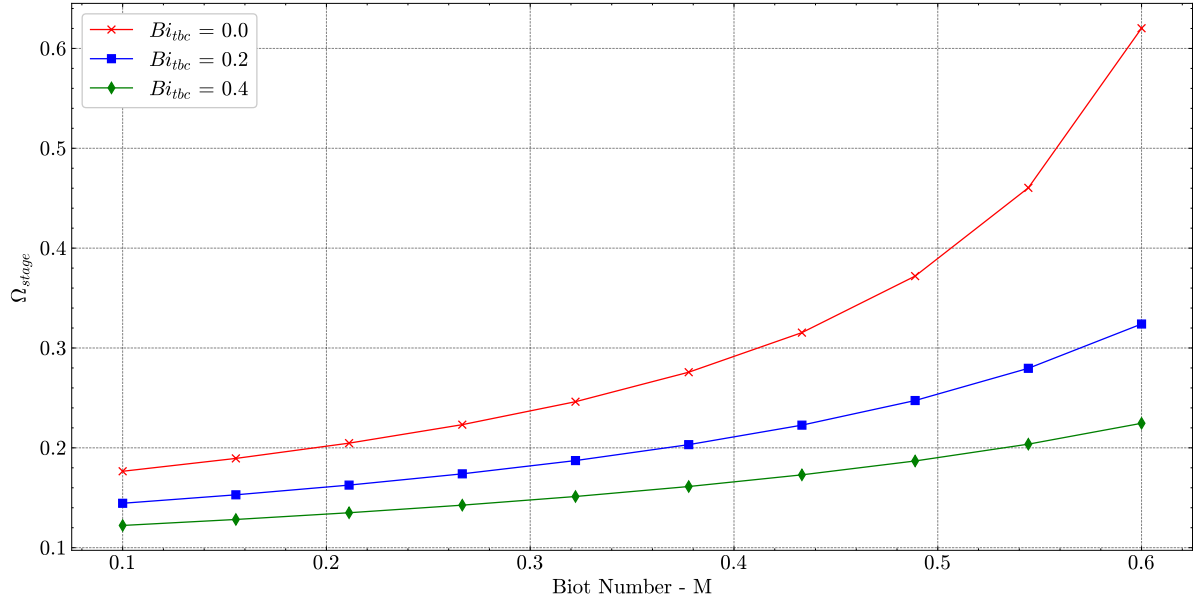
Figure 6.25: Variation in stage cooling fraction with metal Biot number. Gas temperature of 1700 K, maximum metal temperature of 1100 K, with film cooling.

However, when Bi_m is 0.35, Bi_{tbc} must take a value of 0.18 to ensure Ω_{stage} remains 0.2. Finally, for Bi_m of 0.5, $\Omega_{stage} = 0.2$ can only be achieved with Bi_{tbc} closer to 0.4, exceeding the initially specified upper bound of 0.3. The relationship between the two Biot numbers is dictated by some technical aspects such as thermal expansion [99], and will be discussed further in subsection 6.6.3.

6.6.2. THERMAL CONDUCTIVITY RELATIONSHIPS

A key variable in the definition of the Biot numbers for the CTM is the thermal conductivity of the blade and tbc materials. Thermal conductivity, λ is a function of temperature, with units $W/(mK)$.

Gas turbine blades are typically made out of high performance Nickel alloys, with Inconel 718 being the most common [100, 101]. Experimental work by Agazhnov et. al.[102] to quantify the temperature dependence of thermal conductivity of this material results in the following functions:

$$\lambda_m(T) = \begin{cases} 5.291 + 0.0152 \cdot T + 1.382 \cdot 10^{-6} \cdot T^2, & \text{for } 298 < T < 800 \text{ K} \\ 11.75 + 0.011 \cdot T - 9.237 \cdot 10^{-7} \cdot T^2, & \text{for } 1173 < T < 1375 \text{ K} \end{cases} \tag{6.23}$$

For temperatures above 1375 K, Alvarez et. al [103] suggest a value of 30.75 $W/(mK)$, as measured at 1573 K.

The calculation of the thermal conductivity of tbc materials is based on the experimental results produced by Xiwen et. al [36]. Through the experimental testing of a large number of yttria stabilized zirconia ceramics, used in a large number of aero engines as the tbc topcoat [104], it was shown that for lower yttria concentrations, the thermal conductivity varies substantially over large temperature ranges.

Xiwen et. al. tested yttria concentrations from 12-20 mol %, while Liu and Raghavan suggest that a weight fraction around 8% is desirable for high-end tbc performance [104, 105]. The derivation of a relationship for a representative tbc required an in-depth analysis of the mass of the compounds tested by the authors of both sources. This is done in Table 6.9, using a molar mass of 91.22 g/mol and 88.91 g/mol for zirconium and yttrium respectively [37].

The target mole fraction of yttria in the tbc is 11 (11Y), as this corresponds to an 8% mass fraction. Moreover calculation of the related thermal conductivity as a function of temperature requires that the experimental data in Table 6.9 are normalized for porosity of the samples [106]. In order to calculate expression relating the thermal conductivity of an 11Y tbc to the temperature, two steps are needed. The first is a linear extrapolation of the thermal conductivity of known yttria fractions at fixed temperatures to construct a series of discrete λ values. The second step is a linear regression of the discrete series to derive the function. The

Compound Name	Symbol	Molar Mass g/mol	Weight Fraction Yttria
12YSZ	$Zr_{0.88}Y_{0.12}O_{1.94}$	121.98	0.087
14YSZ	$Zr_{0.86}Y_{0.14}O_{1.93}$	121.77	0.010
16YSZ	$Zr_{0.84}Y_{0.16}O_{1.92}$	121.57	0.012
18YSZ	$Zr_{0.80}Y_{0.18}O_{1.91}$	119.54	0.013
20YSZ	$Zr_{0.80}Y_{0.20}O_{1.90}$	121.16	0.015

Table 6.9: Weight fractions of yttria in various thermal barrier coatings given molar compositions [36]. The molar masses of zirconium and yttrium are 91.22 g/mol and 88.91 g/mol respectively [37]
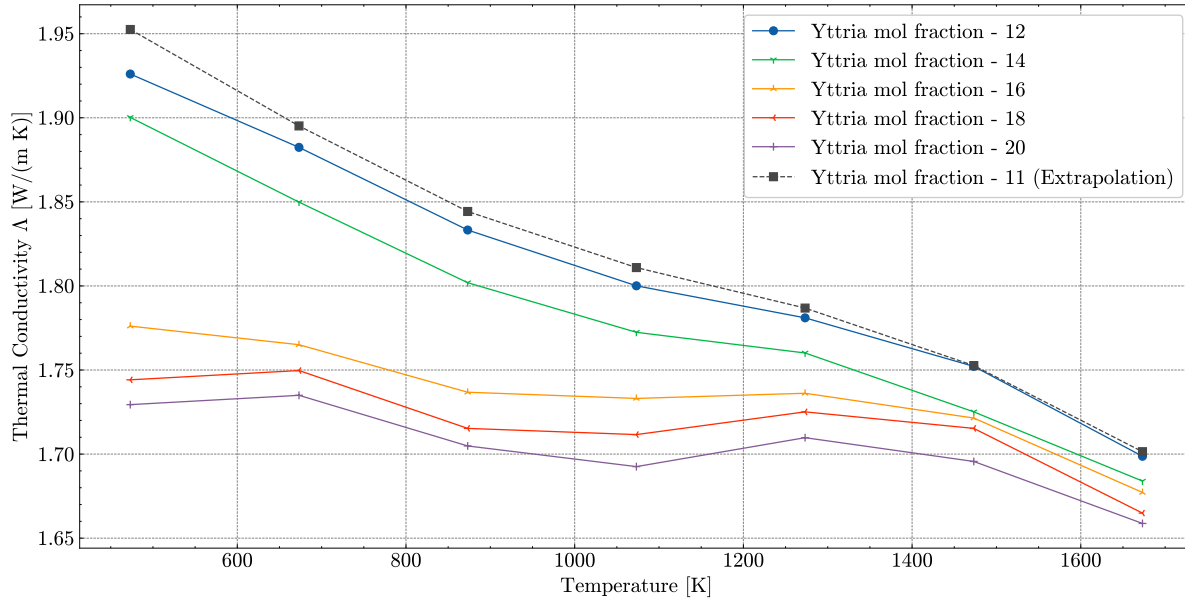
Figure 6.26: Variation in thermal conductivity of yttria stabilized topcoat

resulting function is found to be:

$$\lambda_{tbc,11Y} = -0.0002 \cdot T + 2.0305 \tag{6.24}$$

with an R^2 of 0.98. The prediction of such an empirical correlation are compared to Xiwen et. al's results [36] in Figure 6.26.

The relation in Equation 6.24 is valid for conventional yttria stabilized zirconia ceramics. Recent advances in tbc deposition technology, combined with variations in chemical composition, have led to significant reductions in the thermal conductivity of tbc topcoats. Research at Cranfield University and Rolls Royce, using various lanthenides, in addition to the yttria partially stabilised zirconia (PYSZ), has resulted in a reduction of thermal conductivity of the tbc, as shown in Table 6.10.

TBC	Thermal Conductivity	Unit
Reference Case	1.63	W/(mK)
Nickel Oxide	1.61	W/(mK)
Erbia	1.24	W/(mK)
Ytterbia	1	W/(mK)
Neodymia	0.95	W/(mK)
Gadolinia	0.88	W/(mK)

Table 6.10: Thermal conductivity of advanced thermal barrier coatings through modification of PYSZ [38]

6.6.3. BIOT NUMBER RANGES

With the thermal conductivity behaviour of typical blade and tbc materials established, the next step in assessing feasible value ranges for the Biot numbers is to consider the heat transfer, α_g. Both Biot numbers are
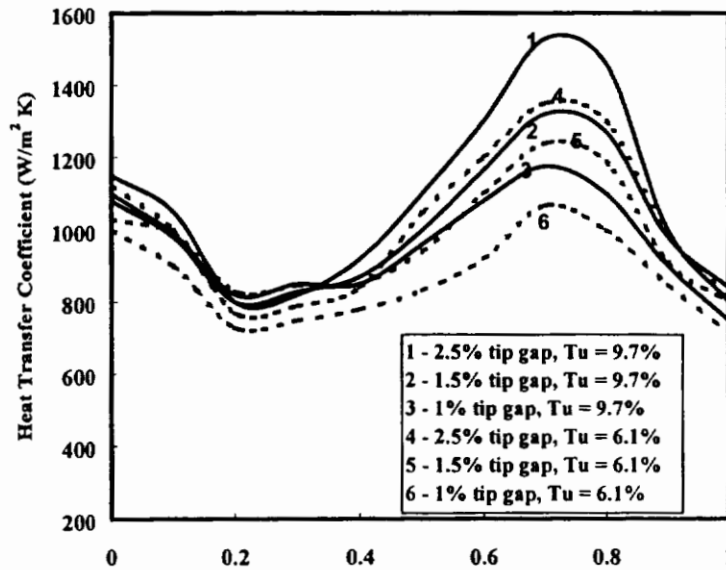
Figure 6.27: Averaged heat transfer coefficient as a function of normalized axial location for E3 Engine turbine blades. Re=1.1e6, turbulence intensity: 6.1% or 9.7% with varying tip clearance expressed as a percentage of blade spans.

defined using the same average external heat transfer coefficient, and this allows for the ratio between the Biot numbers to be formulated as:

$$\frac{Bi_m}{Bi_{tbc}} = \frac{\lambda_{tbc} \cdot t_{tm}}{\lambda_m \cdot t_{tbc}} \tag{6.25}$$

The E3 engine program, developed partially by General Electric (GE), provides experimental results for heat transfer over a set of turbine blades [107]. The results are based on a stage with an expansion ratio of 1.32, row exit Reynolds number of 1.1e6 (within the turbulent flow regime) at two different turbulence intensity levels: 6.1% and 9.7%. Additionally, the tip clearance of the blades is varied between 1% and 2.5% of the blade span [107]. The average heat transfer coefficient for each of the trials is shown in Figure 6.27.

Digitization of the curves in Figure 6.27 allows calculation of the average heat transfer along the blade. It results that this quantity varies between 866 and 1085 W/m^2K for curves 1 to 6. Additionally, computational results obtained by Garg [108] for a range of test cases suggest an α_g range between 500 and 1200 W/m^2K. This wider range is reflective of a variety of test conditions, as well as the spanwise variation of the heat transfer coefficient. The results presented in Figure 6.27 are instead based on measurements taken only at turbine blade tips [90]. Similar ranges are observed in the experimental data presented by Lakshminarayana [58].

The final variable required to define the Biot number is the thickness of the blade metal and thermal barrier coating. TBC's are typically composed of a top-coat and a bondcoat [109]. The lower bound for thickness is conventionally 0.16 mm [109], while the upper bound is 0.4 mm (400 μm)[56].

The original paper presented by Young and Wilcox does not specify a value for the Bi_{tbc}, and the test case does not include a tbc in the calculation scheme. Horlock suggests a value of 0.15 [85], although limited information is provided about this. A range of reasonable values for Bi_{tbc} can be found as a function of temperature based on the value ranges discussed for the three quantities defining this quantity, namely:

- $\lambda_{tbc} = -0.0002 \cdot T + 2.0305$

- $500 \le \alpha_g \le 1200 \ W/m^2K$

- $0.16 \le t_{tbc} \le 0.4 \ mm$

The feasible range of Bi_{tbc} is shown in Figure 6.28. It can be observed that the range varies slightly with temperature, but the upper bound generally lies between 0.25-0.3. This is significantly different from the value proposed by Horlock. Furthermore, the lower bound is observed to lie between 0.04-0.05. This means that if a tbc is modelled in the CTM, Bi_{tbc} may not be less than 0.04. For cases with no tbc, a value of $Bi_{tbc} = 0$ can still be used.
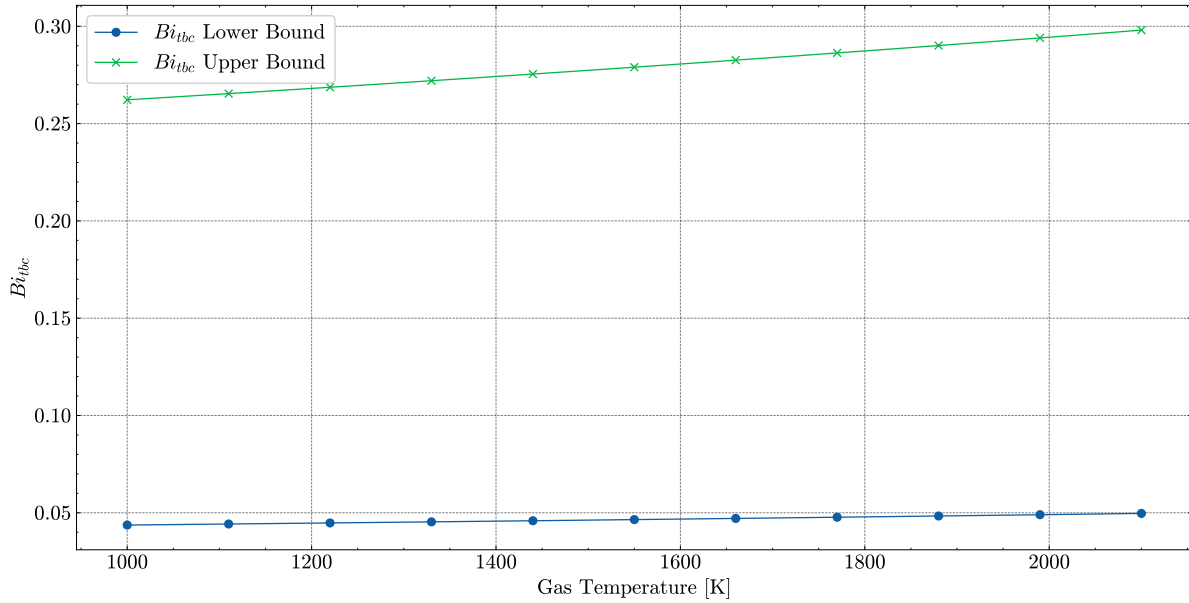
Figure 6.28: Variation in upper and lower bound of Bi_{tbc} with temperature for typical aero-engine turbine conditions and materials. Topcoat of thermal barrier coating is modelled as partially yttria stabilized zirconia (PYSZ).

For turbines, typical blade wall thickness values are in the range 0.8 to 6 mm, based on experimental measurements performed by Zhou et. al. and Goldammer et. al.[110, 111] and the test setup utilized by Lanzilotta [63]. The lower limit is constrained by the accuracy of the manufacturing process, while the upper limit is to minimize blade weight [112]. Thus, similarly to the tbc, the range of Biot numbers for the blade metal can be calculated using:

- $500 \leq \alpha_g \leq 1200 \; W/m^2K$

- $0.8 \leq t_m \leq 3 \; mm$

as well as the Inconel 718 thermal conductivity, as defined in Equation 6.23. The resulting bounds for Bi_m are shown in Figure 6.29.

The range is between 0.02 and 0.33, and tends to reduce the higher the gas temperature. A downward trend is noted in the upper bound due to increasing thermal conductivity of Inconel 718 with temperature. The calculated range is almost centred on the original value prescribed by Young and Wilcox, 0.2. The lower bound is lower than what would be feasible for the blades of a civil aero-engine high pressure turbine, as it requires very thin turbine blades with a low heat transfer coefficient. A more realistic lower bound would be 0.15, as indicated by Horlock [85]. Thereby, the bounds for Bi_{met} would lie between 0.15 and 0.33. Considering the red curve ($Bi_{tbc} = 0.0$) in Figure 6.25, this range in Bi_m makes Ω_{stage} vary between approximately 0.18 and 0.24, a 6% variation in cooling flow. Furthermore, in cases where a tbc is present, the selection of the ratio of Bi_{tbc} to Bi_m is constrained by thermal expansion limits and blade lifetime considerations [99, 113]. This means that the upper bounds cannot be used for both Biot numbers simultaneously. Further investigation is required to establish the exact limitations for the combination of these two factors.

6.7. COOLING MECHANISMS

The film cooling effectiveness,ϵ_f and the internal cooling efficiency, $\eta_{c,int}$ are lumped parameters representing the adopted cooling mechanisms. They have significant impact on the cooling flow requirement calculated for a turbine row, as shown in section 6.1. ϵ_f has a significantly higher influence than $\eta_{c,int}$ on the estimated cooling fraction. In addition to influencing the magnitude of cooling flows, the values of ϵ_f and $\eta_{c,int}$ have a significant influence on the validity of the CTM calculations as discussed in section 5.5.

Considering the internal cooling efficiency, $\eta_{c,int}$, the range presented in literature is between 0.6 and 0.8 [17, 85]. However, the fitting of the CTM model parameters based on the predictions of the Gauntner model in subsection 6.2.2 as well as the validation study of the 2nd stage of the E3 Engine HPT showed that $\eta_{c,int}$ may reach a value of 0.9.
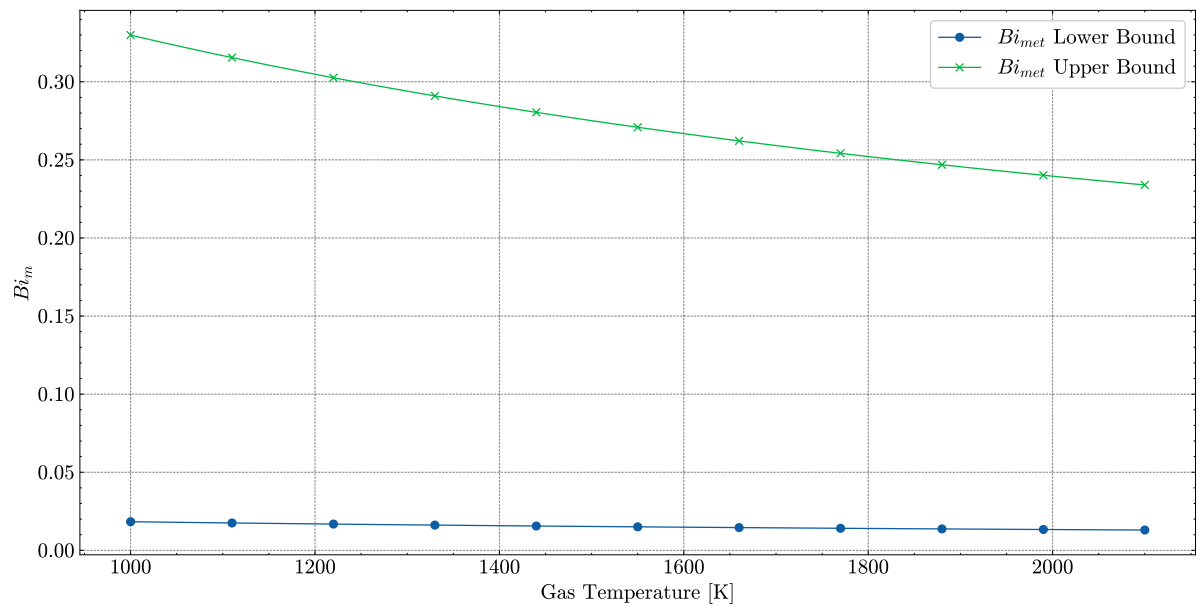
Figure 6.29: Variation in upper and lower bound of Bi_m with temperature for typical aero-engine turbine conditions and materials. Blade material modelled as Inconel 718.

For the film cooling effectiveness, Figure 2.11 showed the strong dependency between the position of the cooling holes and ϵ_f. The literature confirms the upper limit between 0.4 and 0.5 as suggested by Young and Wilcox [17] and no compelling experimental or numerical results have been found disagreeing with this. Locally ϵ_f may exceed 0.4, but this occurs only very close to the cooling holes and with high blowing ratios, as seen in Figure 6.30 [27]. The tuning of the CTM based on the Gauntner model results showed that for film cooled blades without thermal barrier coatings, ϵ_f would need to be around 0.5, in agreement with Horlock's estimate for advanced film cooling techniques [85]. Thus, for ultra advanced cooled blades ϵ_f could take values of 0.5, although for most blades the average value will be slightly lower.
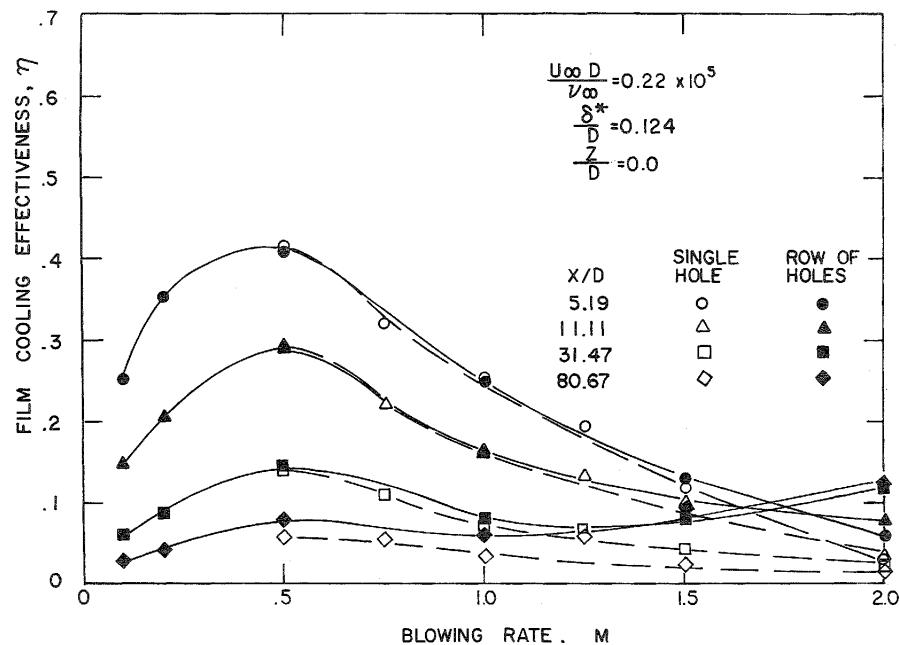
Figure 6.30: Variation in film cooling effectiveness with blowing ratio, M, for various film cooling configurations [27].

6.8. Cooling fraction optimization study

The cooling flow fractions of turbines is expressed in terms of the non-dimensional cooling fraction, m_{c+}, namely:

$$m_{c+} = \frac{\epsilon_0^{max} - \epsilon_f + \epsilon_f \eta_{c,int}(1 - \epsilon_0^{max})}{(1 + Bi_{tbc})\eta_{c,int}(1 - \epsilon_0^{max}) - Bi_m \eta_{c,int}(\epsilon_0^{max} - \epsilon_f)} \quad (6.26)$$

The optimal design of a cooling system can be formulated as an optimization problem, whose objective is to minimize m_{c+}. The optimization requires bounds to be set for the design variables. The problem statement is shown below, using the updated variable ranges discussed in this chapter:

Minimize

$$f(\bar{\mathbf{x}}, \epsilon_0^{max}) = m_{c+}$$

with respect to:

$$\bar{\mathbf{x}} = \left[\epsilon_f, \eta_{c,int}, Bi_{tbc}, Bi_m \right]$$

subject to:

$$f(\bar{\mathbf{x}}) \geq 0.00$$
$$0.0 \leq \epsilon_f \leq 0.5$$
$$0.6 \leq \eta_{c,int} \leq 0.9$$
$$0.15 \leq Bi_m \leq 0.33 \quad (6.27)$$
$$0.04 \leq Bi_{tbc} \leq 0.5$$
$$\epsilon_0^{min} \leq \epsilon_0^{max} \leq 0.9 * \epsilon_0^{asymp}$$

where:

$$\epsilon_0^{asymp} = \frac{(\eta_{c,int} + Bi_{tbc}\eta_{c,int}) + \eta_{c,int}Bi_m\epsilon_f}{\eta_{c,int} + Bi_{tbc}\eta_{c,int} + Bi_m\eta_{c,int}}$$
$$\epsilon_0^{min} = \frac{\epsilon_f - \epsilon_f \eta_{c,int}}{1 - \epsilon_f \eta_{c,int}}$$

The objective function, $f(\bar{\mathbf{x}})$ is non-linear and is constrained directly to be positive. The use of bounds to constrain ϵ_0^{max} also ensure that m_{c+} never drop below zero, or approach the divergence limit, as discussed in section 5.5. The bounds placed on ϵ_f and $\eta_{c,int}$ are based on the values prescribed by Young and Wilcox [17]. For Bi_m, the lower bound is based on the value set by Horlock [85], while the upper bound is raised to 0.33 reflecting the discussion in subsection 6.6.3. Finally, values for Bi_{tbc} are set between 0.04 and 0.5, based on subsection 6.6.3 and Horlock's values for 'super-advanced' technology levels [29]. The chosen optimization algorithm is *Sequential Least Squares Programming* (SLSP), applied through an OpenMDAO wrapper with default settings. Further details on the optimization algorithm and chosen settings are shown in Table 6.11. Results of this optimization for a range of values of ϵ_0^{max} are shown in Figure 6.31. Note that the estimated of m_{c+} values have been multiplied by a value of K_{cool} of 0.045 to facilitate discussion.

As shown in Figure 6.31, for values of ϵ_0^{max} exceeding 0.5, the optimal design vector is consistent. In this scenario, Bi_m is at the permitted lower bound, Bi_{tbc} is at the permitted upper bound, and both internal and film cooling systems operate at maximum efficiency and effectiveness. For lower values of ϵ_0^{max}, the optimal design vector varies with ϵ_0^{max}. This comes from the constraint imposed by ϵ_0^{min}. As ϵ_0^{max} increases, the optimal Bi_{tbc} also increases, highlighting the significance of a thermal barrier coating in minimizing required cooling flows. It is observed that $\eta_{c,int}$ first increases and then decreases around $\epsilon_0^{max} = 0.15$. For ϵ_0^{max} between 0.2 and 0.4, there is significant variation in optimal configurations, with a notable increase in the role of thermal barrier coatings. This aligns with existing engines where thermal barrier coatings are used on blades in high temperature conditions, which correspond to the highest ϵ_0^{max} values. Moreover, it is noted that to satisfy the constraints, the optimal value of $\eta_{c,int}$ decreases for ϵ_0^{max} between 0.2 and 0.4, allowing for an increased film cooling effectiveness. Considering coolant fractions, it is observed that even with optimal values of all parameters, the minimum coolant fraction unavoidably increases with ϵ_0^{max}. The nonlinear increase in cooling fraction is in line with findings by Rao et al [31].

While the trends shown in Figure 6.31 can form a foundation for turbine blade design, there are aspects of cooling system design not considered in the optimization. The first is the constraint between Bi_{tbc} and Bi_m as discussed earlier, with large differences in thermal conductivity not permitted due to possible problems with

Option	Value	Note
Optimization Algorithm	SLSQP	*Nonlinear problem*
Tolerance	1e-06	*SciPy default*
Maximum iterations	200	*SciPy default*

Table 6.11: Optimization algorithm and options used to minimize m_{c+}

the thermal expansion behaviour of the materials. The second is the cost and complexity of manufacturing blades. Finally, the possibility to change the coolant source, thereby changing ϵ_0^{max}, can influence cooling. Therefore, it is not realistic to design a cooling system based only on the predictions of a turbine cooling model.

The optimization problem can be run with the originally prescribed bounds of Young and Wilcox [17, 85], namely:

Minimize

$$f(\bar{\mathbf{x}}, \epsilon_0^{max}) = m_{c+}$$

with respect to:

$$\bar{\mathbf{x}} = \left[\epsilon_f, \eta_{c,int}, Bi_{tbc}, Bi_m\right]$$

subject to:

$$f(\bar{\mathbf{x}}) \geq 0.00$$
$$0.0 \leq \epsilon_f \leq 0.4$$
$$0.6 \leq \eta_{c,int} \leq 0.8$$
$$0.15 \leq Bi_m \leq 0.2$$
$$0.0 \leq Bi_{tbc} \leq 0.3$$
$$\epsilon_0^{min} \leq \epsilon_0^{max} \leq 0.9 * \epsilon_0^{asymp}$$

(6.28)

where:

$$\epsilon_0^{asymp} = \frac{(\eta_{c,int} + Bi_{tbc}\eta_{c,int}) + \eta_{c,int}Bi_m\epsilon_f}{\eta_{c,int} + Bi_{tbc}\eta_{c,int} + Bi_m\eta_{c,int}}$$
$$\epsilon_0^{min} = \frac{\epsilon_f - \epsilon_f\eta_{c,int}}{1 - \epsilon_f\eta_{c,int}}$$

Results are shown in Figure 6.32. The trends are largely the same as observed before. Dixon [4] suggests that a representative value of ϵ_0^{max} is 0.6 in modern engines. For this value of cooling effectiveness, the CTM with original parameter bounds estimates a 3.77% cooling flow, while in the case the updated parameter bounds are used, the CTM estimate is 3.02%. Therefore updating the parameters can reduce the estimated cooling flows by close to 1% of the turbine inflow mass, r by nearly 20% of its original value.

6.9. PARAMETRIC ANALYSIS

Finally a parametric analysis is conducted, to understand trends in cooling fraction calculations with varying conditions. To this end, the case of the GE90 will be used. The design point used will be take-off on an ISA standard day. The data for this test case is presented in Table 6.12.

As the bypass ratio is known, the core massflow can immediately be calculated as:

$$\dot{m}_{core} = \frac{\dot{m}_{air}}{1 + BPR} = \frac{1350}{9.4} = 143.6 \, \text{kg/s}$$

(6.29)

Therefore, the mass flow entering the first stage of the turbine is 147 kg/s. The fuel to air ratio is 0.023. The first parameter to be analysed is the coolant temperature. Figure 6.33 shows the variation in the stage coolant fraction, Ω_{stage}, with coolant temperature.

As is visible from Figure 6.33 a decrease in coolant temperature results in significant reductions in stage coolant fraction, as expected. However, the relationship is not linear and this aligns well with the findings of Rao and Tiemstra [31], who concluded that capturing the non-linearity of the growth in cooling fraction with difference in gas and coolant temperatures is fundamental to accurate modelling of cooled turbines. Effectively, an increase in the coolant temperature is equivalent to applying a harsher constraint to the cooling
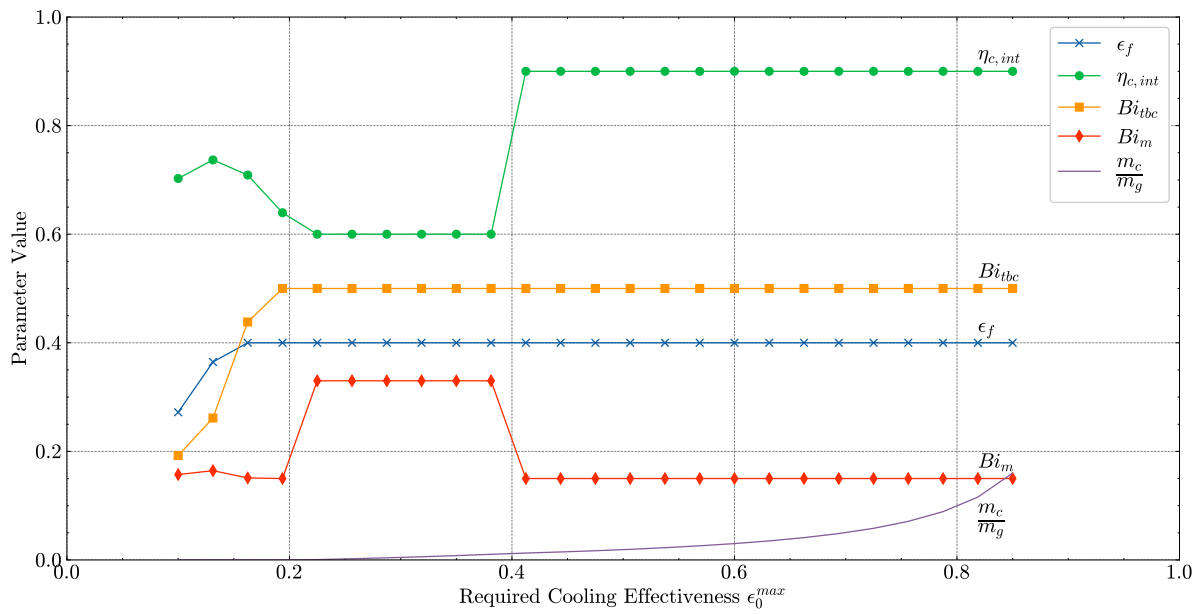
Figure 6.31: Optimal parameter values for minimal m_{c+} at a given value of ϵ_0^{max}, using updated parameter bounds shown in Equation 6.27
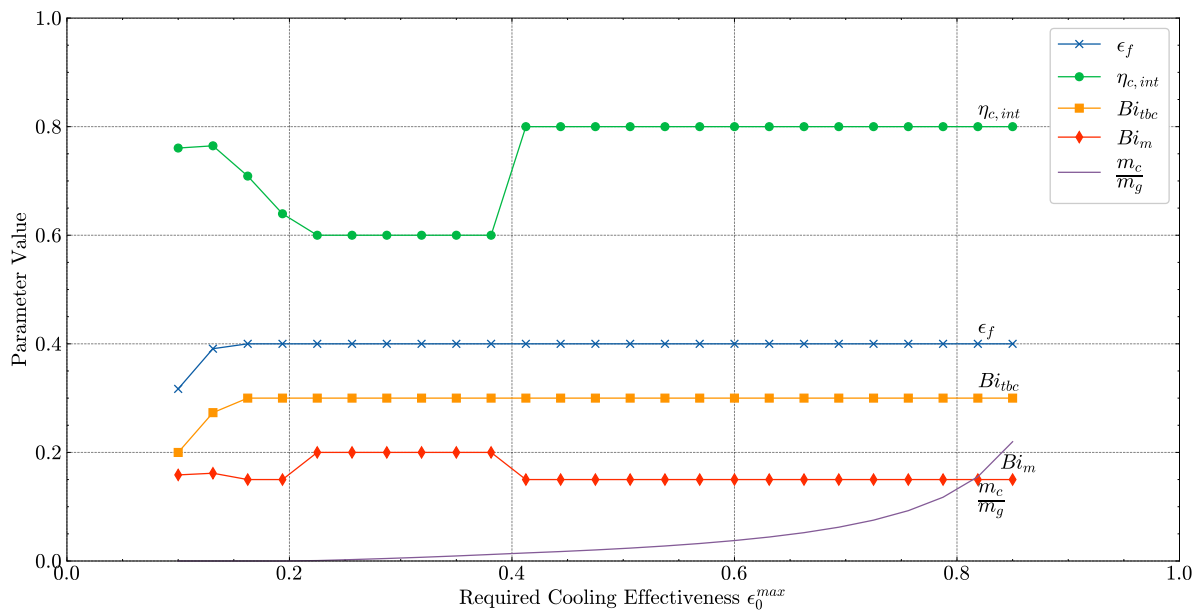
Figure 6.32: Optimal parameter values for minimal m_{c+} at a given value of ϵ_0^{max}, using original parameter bounds shown in Equation 6.28

Quantity	Value	Unit
Turbine Inlet Temperature	1592	K
Inlet mass flowrate	1350	kg/s
Max Blade Temperature	1200	K
Bypass Ratio	8.4	[-]
Fuel Flow Take-off	3.4	kg/s
Combustor Pressure Loss	0.05	[-]
Combustor Inlet Temperature	820	K
Combustor Inlet Total Pressure	40.5	bar
Overall Pressure Ratio	39.97	[-]

Table 6.12: Input parameters for GE90 at Sea Level Static Take Off condition [24, 39, 40]
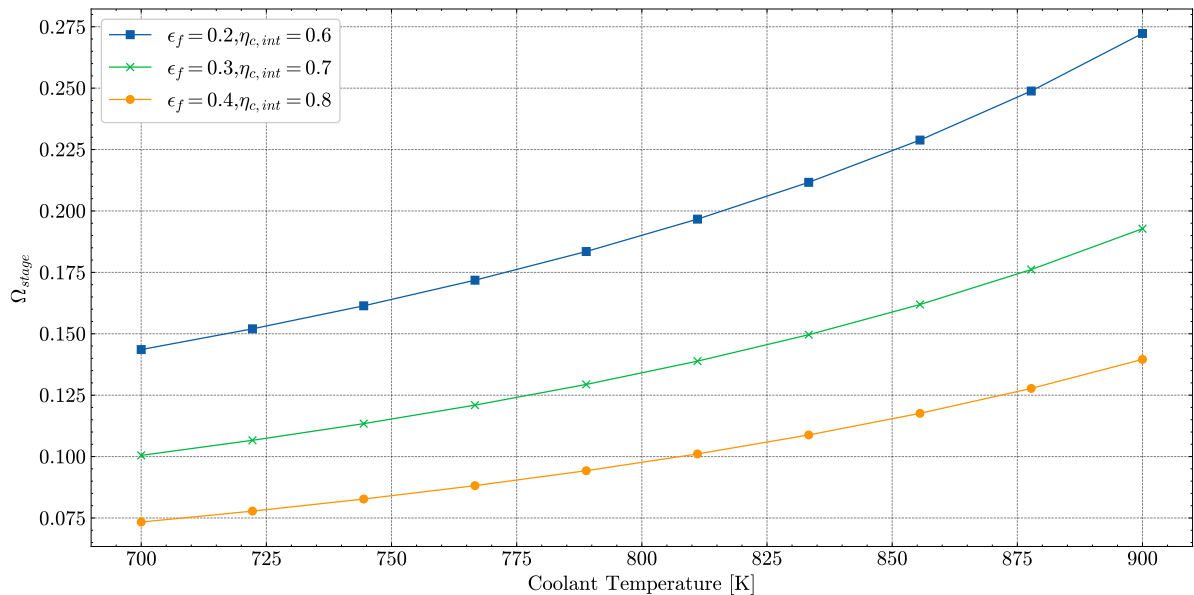
Figure 6.33: Variation in stage cooling fraction with variation in coolant temperature. Fixed turbine inlet temperature of 1529 K.
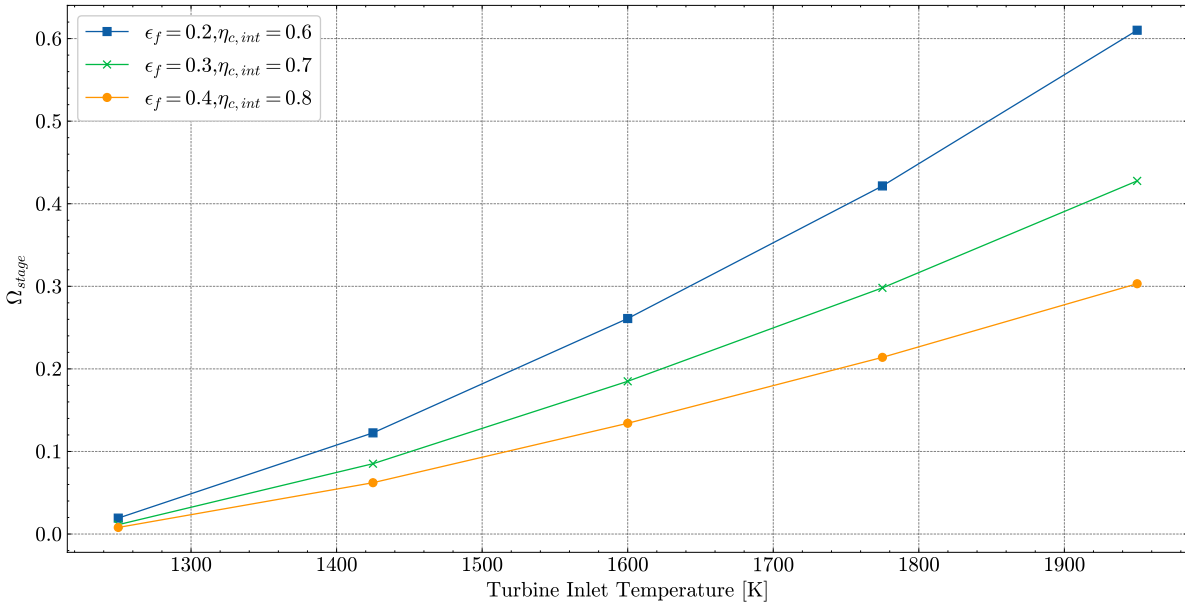
Figure 6.34: Variation in stage cooling fraction, Ω_{stage} with variation in turbine inlet temperature. Fixed coolant temperature of 820 kelvin.

system, that for a fixed performance level (ϵ_f and $\eta_{c,int}$), must increase the amount of the cooling air required. The impact of cooling system technology is also high. Considering the topmost curve, indicating the lowest technology level, it is seen that there is a significantly higher cooling requirement for simpler cooling systems than for more advanced cooling systems.

The second parameter is the turbine inlet temperature. In order to investigate this, the coolant temperature is held constant at 820 K, and the turbine inlet temperature is varied. This replicates certain situations in which power settings may momentarily be raised, resulting in a richer fuel-air mixture, and a higher turbine inlet temperature, albeit with the same compressor delivery temperature. As is visible from Figure 6.34, there is a sharp rise in the required coolant fraction with an increase in turbine inlet temperature. This is expected, as the gap between the turbine inlet temperature and blade metal temperature is increasing, for a fixed coolant temperature. Once again, the non linearity should be noted. Unlike for variations in coolant temperatures, the variation in turbine inlet temperature results in significant divergence behaviour between the respective technology level curves.

Combining the previous results, it is possible to analyze the behaviour of the cooling model for different gas temperatures with variations in cooling temperature, as shown in Figure 6.35. As can be seen, the impact of increasing coolant temperature is more prominent for situations where the gas temperature is higher, likely due to the value of ϵ_0^{max} being closer to the asymptotic value, as all these curves are generated for the same level of technology.
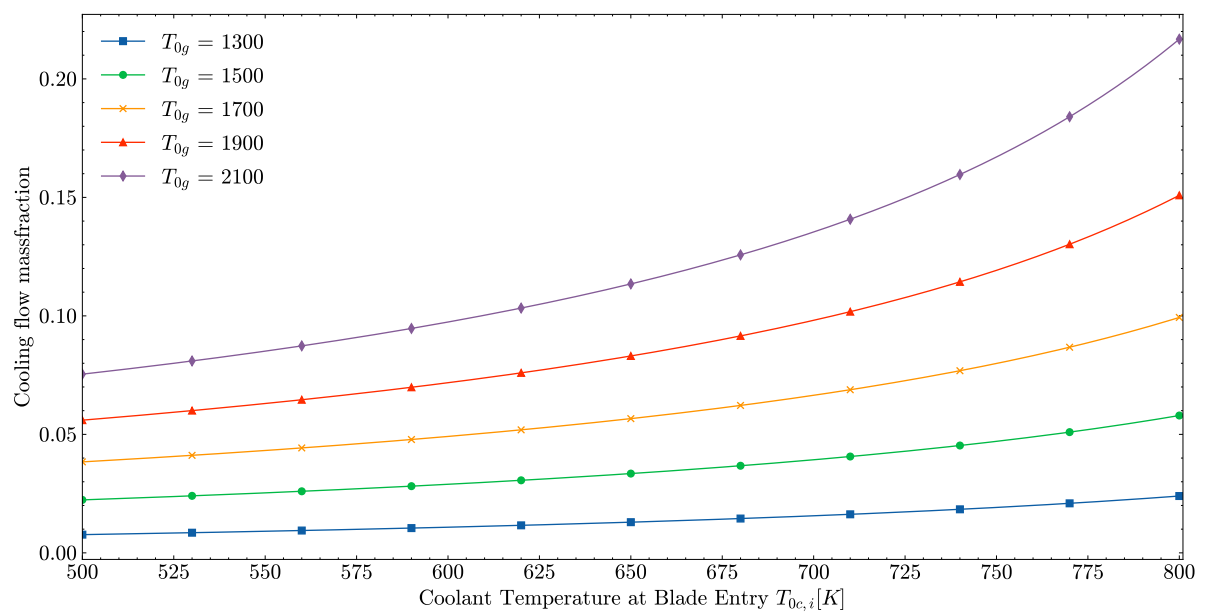
Figure 6.35: Variation in cooling fraction with coolant temperature for varying gas temperatures. Maximum blade temperature = 1100 K, no thermal barrier coating. $\eta_{c,int}$ = 0.7 and ϵ_f = 0.4.

7

CONCLUSIONS & RECOMMENDATIONS

The research objective formulated at the start of this research work was:

Developing a cooled turbine model for use in engine cycle analysis and optimization through implementation and adjustment of an entropy based approach to turbine cooling related performance degradation

In order to realize this objective, this thesis focused on implementation of a cooled turbine model into an engine modelling framework. In order to answer the research objective, the following research (sub-) questions were formulated.

1. What is the state of the art in gas turbine blade cooling performance modelling?

   - What are various approaches that can be used to predict cooling mass flows?
   - What approaches can be used to predict efficiency degradation due to turbine blade cooling?

2. How sensitive are turbine cooling performance models to various parameters?

   - Which parameters drive the cooling mass flow requirements for turbine blade rows?
   - What is the sensitivity of turbine cooling models to design parameters?
   - What is the sensitivity of turbine cooling models to empirical parameters?

3. How can an entropy based performance degradation model be tuned to predict cooling system performance in aero-engine gas turbines?

   - What empirical and experimental data must be available to such a model?
   - What is the effect of tuning empirical parameters with modern gas turbine data on the accuracy of cooling flow estimations?

The following sections will present the conclusions of the performed research, as well as recommendations for future research and development of the Cooled Turbine Model (CTM).

7.1. CONCLUSIONS

In conclusion, this thesis sought to develop a cooled turbine model (CTM) for engine cycle analysis in *PyCycle*. Various cooled turbine models were considered, after which it was decided to implement a model based on entropy creation rates, to account for irreversibility in the turbine cooling process. The original model, developed by Young and Wilcox, was designed for a single blade or blade row. Therefore, the model had to be extended to model a full turbine stage and, subsequently, multi-stage turbines. To do this, three key aspects had to be modelled, namely:

- The thermodynamics of a cooled turbine row
- The work extraction in an equivalent uncooled turbine stage
- The conversion of thermodynamic properties between an absolute and rotating frame of reference

Additionally, the implementation of the CTM in *PyCycle* necessitated the development of a function, or group usign *PyCycle* terminology, capable of modelling thermodynamic properties, using enthalpy-entropy pairs as an input.

Once implemented, the CTM was verified and validated using three different cases. The results of these verification and validation studies suggest that the CTM is able to capture the effects of turbine cooling on bulk flow properties and to accurately predict the required cooling flows.

Furthermore, the sensitivity of the CTM to input parameters, both thermodynamic and empirical ones was studied. Significant dependency was observed on the empirical parameters, with a 100% range of variation in the estimated cooling fractions possible. The film cooling effectiveness was observed to affect the estimated cooling fraction significantly. Following this, an investigation of the feasible range of each individual parameter of the model was performed. This resulted in the definition of value ranges that were different from those prescribed in the literature. To assess the impact of the proposed parameter ranges the cooling fraction estimation was formulated as an optimization problem. It was found that by using the tuned parameter ranges, a nearly 20% reduction in the estimated cooling fraction could be achieved. This equates to approximately 1% less cooling air as a fraction of the turbine entry mass-flow required. Finally, a parametric study of the CTM shows that the model accurately captures the non-linear growth of required cooling flows with gas temperatures.

RESEARCH QUESTIONS

The first research question is related to the state of the art in gas turbine blade cooling performance modelling. To answer this question, a literature review of existing models was performed. It was found that most cooling models suitable for use in cycle analysis require empirical parameters generally tuned based on past experimental work. Concerning cooling fraction estimation, only the Gauntner model was found to be calibrated based on past experimental work. In contrast, most other models used lumped parameters to represent cooling techniques. Tiemstra's model was reviewed and found to be highly detailed regarding the cooling techniques. Furthermore, total pressure loss was often used to measure performance degradation, although most models developed to estimate cooling fractions do not quantify performance degradation at all.

The second research question is related to the sensitivity of turbine cooling models to various parameters. Firstly, the cooling mass flow estimations were found to be driven primarily by K_{cool}, the cooling flow parameter, ϵ_0^{max}, the required cooling effectiveness and to a lower extent by the film cooling effectiveness and internal cooling efficiency, ϵ_f and $\eta_{c,int}$ respectively. Regarding K_{cool}, the estimated cooling fraction scales linearly with this parameter. Additionally, based on a sensitivity study, the maximum metal temperature was found to have the largest influence on the cooling fraction. The turbine cooling estimates are less sensitive to gas and coolant temperatures than $\epsilon_f,\eta_{c,int}$ and the Biot numbers.

The third research question is how a cooled turbine model could be tuned for accurate estimations of cooling flows. To answer this, the CTM results were compared to the data available for various test cases. The first one was the Alfa Romeo NGV test case, for which it was found that selecting average values of the CTM parameters, the model predictions were within 2.5% (relative difference) of the experimental data. The second test case was NASA's E3 Efficient Engine. Here, the use of average values for the CTM parameters resulted in significant differences with the data reported by NASA, for both high-pressure turbine stages. By tuning the model parameters, it was possible to reduce the error in the cooling flow estimate for the stator and rotor of the first turbine stage from 77.5% and 35.9% to 2.1% and -7.6%, respectively.

PARAMETER TUNING

Furthermore, the parameter values for the CTM were tuned based on the predictions of the Gauntner model for a given cooling technique and a large range of gas, metal and coolant temperatures. The fit observed in this tuning process was quite high, with the lowest R^2 value observed being 0.988.

Additionally, the 7 parameters used in the CTM were assessed individually. Firstly, the external flow parameter K_{ext}, was found to be a function of gas path properties. The study of a representative set of engines was used to derive typical fuel-to-air ratios in various flight phases. The flight phases considered were take-off, climb-out, approach and idle. The typical equivalence ratios observed were 0.3-0.35,0.2-0.25,0.05-0.1 and 0.02-0.05 respectively. This information, in combination with estimates of the gas path Mach number, leads to a range of values for K_{ext} between 1.02 - 1.17. However, further data regarding Mach numbers in the first stage of high-pressure turbines is required to confirm this result. For the internal flow parameter, K_{int}, the dependency on flight conditions and pressure ratio was identified. However, the lack of data on coolant

flow Mach numbers prevents a detailed analysis, only a minimum value of 1.01-1.02 was identified for this quantity.

The K_{cool} range indicated in the literature was between 0.01 and 0.1. An attempt to estimate the Stanton number from Reynolds number and gas temperature was performed. The obtained estimates appeared to be accurate, as proven by an initial comparison with the literature. The approach used in this attempt was based on temperature-based correlations for thermal conductivity and dynamic viscosity, neglecting reduced integral collisions. The turbine blade geometry used in the attempt was that of the Von Karman Institute's LS89 turbine cascade. Through this attempt, a new range of values between 0.01 and 0.065 was then established for K_{cool}.

The Biot numbers were analyzed by modelling the variation in thermal conductivity of thermal barrier coatings with chemical compositions and operating temperature. Based on a preliminary estimate of coatings and blade thicknesses, the estimated ranges for thermal barrier coating Biot numbers and metal Biot numbers were 0.04-0.05 and 0.02-0.33 respectively.

Furthermore, the film cooling effectiveness ϵ_f and internal cooling efficiency, $\eta_{c,int}$ were found to impact the validity of the CTM calculations significantly. This was discussed by defining the asymptotic and minimum values of ϵ_0^{max}. Particularly for the application of film cooling, it was noted that there is a minimum value of ϵ_0^{max} for which the CTM can model this technique accurately. For ϵ_f, the upper limit is 0.5 in the case of extremely advanced engines, while values of $\eta_{c,int}$ up to 0.9-0.95 are possible depending on technology levels.

Finally, it was observed that the CTM based on the Young and Wilcox model was more computationally expensive than the Gauntner model, with consistently longer run times observed. In addition, the complexity and time required for development of the CTM based on the Y&W model was high.

7.2. RECOMMENDATIONS

Based on the findings of the research performed and documented in this thesis, a number of recommendations can be made for possible future research and development of the CTM. The recommendations presented in this section include those related directly to expansion of the CTM's capabilities, as well as identification of potential future research areas.

The first recommendation is to verify the key physical quantities in conditions representative of modern gas turbine engines. These quantities are:

- Stanton numbers of (un-)cooled gas turbine blades

- Coolant flow stream Mach numbers

- Bulk (gas) stream Mach numbers

Limited experimental engine data is available, as most details are proprietary information belonging to engine manufacturers. However, experiments or computational fluid dynamics (CFD) studies would allow for more accurate specification of feasible values of these quantities in the CTM. This could involve the use of CFD to model the flow in greater detail and capture the effects of turbulence and other flow phenomena. The findings could subsequently be converted into feasible ranges for CTM parameters.

The second recommendation is adaptation of the CTM's structure to allow for blade rows within a turbine stage to be modelled independently. This would encompass two key aspects:

- Modelling blade rows with different cooling techniques within the same stage

- Modelling blade rows as being supplied by different cooling air flows

The main benefit of this adaptation of the CTM would be that the CTM would more accurately reflect existing cooling systems, as in modern gas turbines stators and rotors are often supplied with cooling air bled from different locations.

A third recommendation is the adaptation of the CTM to model non-blade cooling flows in turbine stages. Modern aero engines use cooling flows for other purposes including sealing, as well as cooling blade disks. The Young and Wilcox model suggests that these flows should be specified by the user, as a fixed fraction. More accurate modelling of the temperature limits of disk and sealing materials would allow for better predictions of total cooling fractions, beyond that required for the blades. In addition to this, the CTM could be expanded by modelling of other cooling techniques. The CTM currently models film cooling and internal

convective cooling, but there are other techniques such as transpiration cooling that could be included in the model for a more complete model.

Furthermore, the capabilities of the CTM could be expanded through integration of a detailed cooling system design tool. An initial base for this could be the design tool developed by Tiemstra et. al. [23]. The tool provides detailed insights into the internal geometries and cooling techniques that can be used in the cooling of turbine blade. As the tool also produces an estimated cooling fraction as an output, setting this tool in an iterative loop with the CTM's calculations could provide users with immediate insight into cooling techniques suitable for a given blade row. This could also support more accurate estimates of parameter ranges for $\eta_{c,int}$ and ϵ_f as these parameters can be calculated based on realistic geometries. However, the effect of this integration on computational cost and complexity must also be considered.

Additionally, there is a need to investigate the impact of turbine cooling on other engine components, such as the influence of extracting cooling air from the compressor. This could involve the development of a more comprehensive engine cycle model that includes all of the relevant components of the turbine cooling system and their interactions.

Considering future research areas, a recommendation would be to investigate the influence of alternative fuels on the cooling requirements for turbine blades. Considering recent blending mandates for sustainable aviation fuels introduced by the European Union, including synthetic fuels and hydrogen, a study into the influence on existing engines in service could serve to inform the decision on when to retire existing engines from service.

Finally, two recommendations are made regarding the modelling of the coolant flow. The first recommendation is to investigate the influence of fluids other than air in the cooling of turbine blades. This could be developed to model liquid cooled aero engines, such as the Water Enhanced Turbofan (WET) engine concept developed by MTU [114]. Additionally, the CTM could be used to further build on existing studies into the feasibility of cooled cooling air. This would be a suitable use case for the MDAO capabilities of *PyCycle* as well.

Overall, there is still much to be further developed in the modelling of cooled turbines for cycle analysis. Continued research in this area will help to improve the understanding of these complex systems and enable the development of more efficient and reliable gas turbine engines.

BIBLIOGRAPHY

[1] J. E. Penner, *Aviation and the global atmosphere: Aspecial report of IPCC Working Groups I and III in collab. with the Scientific Assessment Panel to the Montreal Protocol on Substances that Deplete the Ozone Layer* (Cambridge University Press, Cambridge, 1999).

[2] L. Xu, S. Bo, Y. Hongde, and W. Lei, *Evolution of rolls-royce air-cooled turbine blades and feature analysis,* Procedia Engineering **99**, 1482 (2015).

[3] e. J. Ir van Buijtenen Emeritus Professor, W. Visser, A. Gangoli Rao Associate Professor, e. P. Ir Jos van Buijtenen, W. P. Visser, S. Shakariyants, F. Montella, A. Gangoli Rao, and I. Jitendra Singh, *Aero engine technology, ae4-238,* .

[4] S. Dixon and C. Hall, *Fluid Mechanics and Thermodynamics of Turbomachinery* (Elsevier Science, 2013).

[5] U. Unnikrishnan and V. Yang, *A review of cooling technologies for high temperature rotating components in gas turbine,* Propulsion and Power Research **11**, 293 (2022).

[6] J. Han, J. Park, C. Lei, T. A. . M. U. D. of Mechanical Engineering, and L. R. Center, *Heat Transfer and Pressure Drop in Blade Cooling Channels with Turbulence Promoters*, NASA contractor report (National Aeronautics and Space Administration, Scientific and Technical Information Branch, 1984).

[7] Smith, Lance and Karim, Hasan and Etemad, Shahrokh and Pfefferle, William C., *The Gas Turbine Handbook* (U.S. Department of Energy-National Energy Technology Laboratory, 2006) engineering Faculty Book Gallery. 3.

[8] M. Oldfield, *Lecture on 38 years of gas-turbine research,* (2007).

[9] G. Oates, U. S. A. F. O. of Scientific Research, and A. F. A. P. L. (U.S.), *The Aerothermodynamics of Aircraft Gas Turbine Engines*, The Aerothermodynamics of Aircraft Gas Turbine Engines No. v. 2 (Air Force Aero Propulsion Laboratory, Air Force Wright Aeronautical Laboratories, Air Force Systems Command, 1978).

[10] M. J. Holland and T. F. Thake, *Rotor blade cooling in high pressure turbines,* Journal of Aircraft **17**, 412 (1980).

[11] J. Gray, J. Hwang, J. Martins, K. Moore, and B. Naylor, *Openmdao: An open-source framework for multidisciplinary design, analysis, and optimization,* Structural and Multidisciplinary Optimization (2019), 10.1007/s00158-019-02211-z.

[12] E. S. Hendricks and J. S. Gray, *pycycle: A tool for efficient optimization of gas turbine engine cycles,* Aerospace **6** (2019).

[13] J. S. Gray, J. Chin, T. Hearn, E. S. Hendricks, T. M. Lavelle, and J. R. R. A. Martins, *Thermodynamics for gas turbine cycles with analytic derivatives in OpenMDAO, 57th AIAA/ASCE/AHS/ASC Structures, Structural Dynamics, and Materials Conference,* (2016), 10.2514/6.2016-0669.

[14] J. B. Young and R. C. Wilcock, *Modeling the air-cooled gas turbine: Part 2-Coolant flows and losses,* Journal of Turbomachinery **124**, 214 (2002).

[15] J. Kurzke and I. Halliwell, *Propulsion and Power* (2018).

[16] *Loss Mechanisms in Turbomachines*, Turbo Expo: Power for Land, Sea, and Air, Vol. Volume 2: Combustion and Fuels; Oil and Gas Applications; Cycle Innovations; Heat Transfer; Electric Power; Industrial and Cogeneration; Ceramics; Structures and Dynamics; Controls, Diagnostics and Instrumentation; IGTI Scholar Award (1993) https://asmedigitalcollection.asme.org/GT/proceedings-pdf/GT1993/78897/V002T14A001/4457435/v002t14a001-93-gt-435.pdf .

[17] J. B. Young and R. C. Wilcock, *Modeling the air-cooled gas turbine: Part 1-General thermodynamics,* Journal of Turbomachinery **124**, 207 (2002).

[18] M. De Paepe and E. Dick, *Cycle improvements to steam injected gas turbines,* International Journal of Energy Research **24**, 1081 (2000).

[19] F. Yin and A. G. Rao, *A review of gas turbine engine with inter-stage turbine burner,* Progress in Aerospace Sciences **121**, 100695 (2020).

[20] S. C. Uysal, *Analytical Modelling of the Effects of Different Gas Turbine Cooling Techniques on Engine Performance,* Doctoral dissertation, West Virginia University (2017).

[21] T. T. Halila, E. E. Lenahan, D. T. Thomas, *Energy Efficient Engine: High Pressure Turbine Test Hardware Detailed Design Report.* , 47 (1982).

[22] B. Livingood and A. Kaufman, *Nasa turbine cooling research status report,* (1971).

[23] F. Tiemstra, *Design of a Semi-Empirical Tool for the Evaluation of Turbine Cooling Requirements in a Preliminary Design Stage,* Master's thesis, Delft University of Technology (2014).

[24] ICAO, *Aircraft engine emissions databank,* (2022).

[25] L. Jenkinson, P. Simpkin, and D. Rhodes, *Engine data file,* (2001).

[26] Q. M. U. of London, *Aboutflow - munich 2016 benchmark: Test case 2,* .

[27] E. R. G. Eckert, V. L. Eriksen, R. J. Goldstein, and J. W. Ramsey, *Film cooling following injection through inclined circular tubes,* (1974).

[28] P. Linstrom and W. Mallard, *The nist chemistry webbook: A chemical data resource on the internet,* (2001).

[29] J. B. Young and J. H. Horlock, *Defining the Efficiency of a Cooled Turbine,* Journal of Turbomachinery **128**, 658 (2006), https://asmedigitalcollection.asme.org/turbomachinery/article-pdf/128/4/658/6930526/658_1.pdf .

[30] S. Colantuoni, A. Colella, L. Di Nola, D. Carbone, and D. Marotta, *Aero-thermal design of a cooled transonic ngv and comparison with experimental results,* (1992).

[31] F. Yin, F. S. Tiemstra, and A. G. Rao, *Development of a Flexible Turbine Cooling Prediction Tool for Preliminary Design of Gas Turbines,* Journal of Engineering for Gas Turbines and Power **140** (2018), 10.1115/1.4039732.

[32] E. Stearns, *Energy Efficient Engine core design and performance report,* NASA-Lewis Research Center, NASA CR-168069 (1982).

[33] L. Jenkinson, P. Simpkin, and D. Rhodes, *Civil Jet Aircraft Design,* AIAA education series (American Institute of Aeronautics and Astronautics, 1999).

[34] T. Arts, M. L. de Rouvroit, and A. W. Rutherford, *Aero-thermal investigation of a highly loaded transonic linear turbine guide vane cascade - a test case for inviscid and viscous flow computations,* (1990).

[35] J. Warnatz, U. Maas, and R. Dibble, *Combustion: Physical and Chemical Fundamentals, Modeling and Simulation, Experiments, Pollutant Formation* (Springer Berlin Heidelberg, 2006).

[36] X. SONG, M. XIE, F. ZHOU, G. JIA, X. Hao, and S. An, *High-temperature thermal properties of yttria fully stabilized zirconia ceramics,* Journal of Rare Earths **29**, 155–159 (2011).

[37] S. Kim, J. Chen, T. Cheng, A. Gindulyte, J. He, S. He, Q. Li, B. A. Shoemaker, P. A. Thiessen, B. Yu, L. Zaslavsky, J. Zhang, and E. E. Bolton, *Pubchem 2023 update,* Nucleic Acids Res **51**, D1373 (2023).

[38] J. Nicholls and D. Rickerby, *Thermal barrier coating systems,* Project Result Poster, additional information, e.g., conference location.

[39] B. J. Cantwell, *The ge90 - an introduction - kimerius,* (2011).

[40] J. Mattingly, *Aircraft Engine Design*, AIAA Education Series (American Institute of Aeronautics & Astronautics, 2002).

[41] J. F. O'Connell, *The global airline industry,* (2018) pp. 11–28.

[42] R. K. Pachauri, *Climate Change 2014 Synthesis Report* (2014).

[43] S. Shparberg and B. Lange, *Global Market Forecast 2022,* (2022).

[44] M. Cames, J. Graichen, A. Siemons, and V. Cook, *Directorate general for internal policies - european parliament,* (2015).

[45] *Ryanair cuts carbon emissions by 165,000 tonnes with winglet retrofit,* (2023).

[46] *Fuel efficiency trends for new commercial jet aircraft: 1960 to 2014,* (2022).

[47] *Zeroe - towards the world's first hydrogen-powered commercial aircraft,* .

[48] H. Liu, J. Sun, S. Lei, and S. Ning, *In-service aircraft engines turbine blades life prediction based on multi-modal operation and maintenance data,* Propulsion and Power Research **10**, 360 (2021).

[49] P. Puspitasari, A. Andoko, and P. Kurniawan, *Failure analysis of a gas turbine blade: A review,* IOP Conference Series: Materials Science and Engineering **1034**, 012156 (2021).

[50] J. Alonso, P. LeGresley, and V. Pereyra, *Aircraft design optimization,* Mathematics and Computers in Simulation **79**, 1948 (2009), applied and Computational MathematicsSelected Papers of the Sixth PanAmerican WorkshopJuly 23-28, 2006, Huatulco-Oaxaca, Mexico.

[51] G. Hemighaus, T. Boval, J. Bacha, F. Barnes, M. Franklin, L. Gibbs, N. Hogue, J. Jones, D. Lesnini, J. Lind, and J. Morris, *Aviation fuel technical review,* (2007).

[52] H. Wang, R. Xu, K. Wang, C. T. Bowman, R. K. Hanson, D. F. Davidson, K. Brezinsky, and F. N. Egolfopoulos, *A physics-based approach to modeling real-fuel combustion chemistry - i. evidence from experiments, and thermodynamic, chemical kinetic and statistical considerations,* Combustion and Flame **193**, 502 (2018).

[53] R. Xu, K. Wang, S. Banerjee, J. Shao, T. Parise, Y. Zhu, S. Wang, A. Movaghar, D. J. Lee, R. Zhao, X. Han, Y. Gao, T. Lu, K. Brezinsky, F. N. Egolfopoulos, D. F. Davidson, R. K. Hanson, C. T. Bowman, and H. Wang, *A physics-based approach to modeling real-fuel combustion chemistry – ii. reaction kinetic models of jet and rocket fuels,* Combustion and Flame **193**, 520 (2018).

[54] A. Lefebvre, *GAS Turbine Combustion, Second Edition*, Combustion: An International Series (Taylor & Francis, 1998).

[55] I. Waitz, *Unified propulsion,* (Massachusetts Institute of Technology, 2001).

[56] H. I. H. Saravanamuttoo, G. F. C. Rogers, H. Cohen, and P. V. Straznicky, *Gas Turbine Theory*, 6th ed. (Pearson Prentice Hall, Harlow, England; New York, 2009).

[57] R. Gorla and A. Khan, *Turbomachinery: Design and Theory*, Dekker Mechanical Engineering (Taylor & Francis, 2003).

[58] B. Lakshminarayana, *Fluid Dynamics and Heat Transfer of Turbomachinery*, Wiley-Interscience publication (Wiley, 1995).

[59] P. Walsh and P. Fletcher, *Gas Turbine Performance* (Wiley, 2008).

[60] J. Choi, S. Teng, J.-C. Han, and F. Ladeinde, *Effect of free-stream turbulence on turbine blade heat transfer and pressure coefficients in low reynolds number flows,* International Journal of Heat and Mass Transfer **47**, 3441 (2004).

[61] A. Mills, *Basic Heat and Mass Transfer*, Always Learning (Pearson, 2014).

[62] S. Lau, R. McMillin, and R. Kukreja, *Segmental heat transfer in a pin fin channel with ejection holes,* International Journal of Heat and Mass Transfer **35,** 1407 (1992).

[63] F. Lanzillotta, *Effect of Film Cooling on the Aerodynamic Performance of Turbine Blades,* Ph.D. thesis (2016).

[64] K. Thole, A. Sinha, D. Bogard, and M. Crawford, *Mean temperature measurements of jets with a crossflow for gas turbine film cooling application,* Rotating Machinery Transport Phenomena (1992).

[65] A. Mills, *Turbine cooling,* (2021).

[66] A. Hare, A. Hare, and H. H. Malley, *Cooling modern aero engine turbine blades and vanes,* SAE Transactions , 230 (1967).

[67] A. Apostolidis, *Turbine Cooling and heat transfer modelling for gas turbine performance simulation,* (2015).

[68] F. Yin, F. S. Tiemstra, and A. G. Rao, *Development of a Flexible Turbine Cooling Prediction Tool for Preliminary Design of Gas Turbines,* Journal of Engineering for Gas Turbines and Power **140** (2018), 10.1115/1.4039732.

[69] K. Jordal, L. Torbidoni, and A. F. Massardo, *Convective blade cooling modelling for the analysis of innovative gas turbine cycles,* Proceedings of the ASME Turbo Expo **2,** 1 (2001).

[70] L. Torbidoni and A. F. Massardo, *Analytical blade row cooling model for innovative gas turbine cycle evaluations supported by semi-empirical air-cooled blade data,* Journal of Engineering for Gas Turbines and Power **126,** 498 (2004).

[71] E. S. Hendricks, R. D. Falck, and J. S. Gray, *Simultaneous propulsion system and trajectory optimization,* 18th AIAA/ISSMO Multidisciplinary Analysis and Optimization Conference, 2017 , 1 (2017).

[72] S. S. Chauhan, J. T. Hwang, and J. R. R. A. Martins, *An automated selection algorithm for nonlinear solvers in mdo,* Structural and Multidisciplinary Optimization **58,** 349 (2018).

[73] T. Akba, D. K. Baker, and M. P. Mengüç, *Off-design performance of micro-scale solar brayton cycle,* Energy Conversion and Management **289,** 117187 (2023).

[74] J. Gray, J. Chin, T. Hearn, E. Hendricks, T. Lavelle, and J. Martins, *Chemical-equilibrium analysis with adjoint derivatives for propulsion cycle analysis,* Journal of Propulsion and Power **33,** 1 (2017).

[75] C. E. Bryant and J. L. Rutledge, *Temperature Dependent Property Considerations for Biot Number Matching With Composite Materials,* Journal of Turbomachinery **145,** 041010 (2022), https://asmedigitalcollection.asme.org/turbomachinery/article-pdf/145/4/041010/6941128/turbo_145_4_041010.pdf .

[76] K. Kawaike, N. Kobayashi, and T. Ikeguchi, *Effect of New Blade Cooling System With Minimized Gas Temperature Dilution on Gas Turbine Performance,* Journal of Engineering for Gas Turbines and Power **106,** 756 (1984), https://asmedigitalcollection.asme.org/gasturbinespower/article-pdf/106/4/756/5529483/756_1.pdf .

[77] A. H. Shapiro and W. R. Hawthorne, *The Mechanics and Thermodynamics of Steady One-Dimensional Gas Flow,* Journal of Applied Mechanics **14,** A317 (2021), https://asmedigitalcollection.asme.org/appliedmechanics/article-pdf/14/4/A317/6745741/a317_1.pdf .

[78] S. A. Cole, *The jacobian matrix,* Ph.D. thesis (1970).

[79] A. Razak, *Industrial Gas Turbines - Performance and Operability* (Woodhead Publishing, 2007).

[80] R. H. Aungier, *Turbine Aerodynamics: Axial-Flow and Radial-Flow Turbine Design and Analysis* (ASME Press, 2006).

[81] E. M. Greitzer, C. S. Tan, and M. B. Graf, *Internal Flow: Concepts and Applications*, Cambridge Engine Technology Series (Cambridge University Press, 2004).

[82] Y. Du, M. Zou, J. Man, and X. Haiyi, *Conjugate heat transfer investigation on swirl-film cooling at the leading edge of a gas turbine vane*, Entropy **21**, 1007 (2019).

[83] J. HARTSEL, *Prediction of effects of mass-transfer cooling on the blade-row efficiency of turbine airfoils*, (1972), 10.2514/6.1972-11.

[84] L. Velthausz, *Feasibility of an engine architecture using bypass cooled cooling air,* (2022).

[85] R. C. Wilcock, J. B. Young, and J. H. Horlock, *The Effect of Turbine Blade Cooling on the Cycle Efficiency of Gas Turbine Power Cycles* , Journal of Engineering for Gas Turbines and Power **127**, 109 (2005), https://asmedigitalcollection.asme.org/gasturbinespower/article-pdf/127/1/109/5614162/109_1.pdf .

[86] V. Sethi, *Advanced performance simulation of gas turbine components and fluid thermodynamic properties*, Cranfield University, PhD Thesis (2008).

[87] M. Hussain, *Numerical analysis on thermodynamic performance of simple turbojet engine,* International Journal of Pavement Research and Technology **6**, 61 (2020).

[88] N. Sachdeva, *Techno-Economic feasibility analysis of Solid-Oxide Fuel Cell-Gas Turbine based hybrid propulsion system fu- eled by Hydrogen,* (2022).

[89] M. el Abbassi, *Conceptual design of a flameless combustor for aircraft engines,* (2015).

[90] J. Han, S. Dutta, and S. Ekkad, *Gas Turbine Heat Transfer and Cooling Technology* (Taylor & Francis, 2001).

[91] EASA, *Pratt and whitney pw1500g series engines,* (2022).

[92] M. Pfitzner and W. Waschka, *Development of an Aeroengine Secondary Air System Employing Vortex Reducers,* , 1 (2000).

[93] R. Hackney, T. Nikolaidis, and A. Pellegrini, *A method for modelling compressor bleed in gas turbine analysis software*, Applied Thermal Engineering **172**, 115087 (2020).

[94] E. Hendricks, *Meanline analysis of turbines with choked flow in the object-oriented turbomachinery analysis code,* (2016).

[95] V. Lallini, J. Janikovic, P. Pilidis, R. Singh, and P. Laskaridis, *A Calculation Tool of a Turbine Cooling Air Schedule for General Gas Turbine Simulation Algorithms,* Journal of Turbomachinery **134**, 041003 (2011), https://asmedigitalcollection.asme.org/turbomachinery/article-pdf/134/4/041003/5846997/041003_1.pdf .

[96] P. de la calzada, M. Valdés, and M. Burgos Olmos, *Heat transfer in separated flows on the pressure side of turbine blades*, Numerical Heat Transfer **Part A: Applications,** 666 (2011).

[97] R. B. Rivir, R. Sondergaard, M. Dahlstrom, and E. Ervin, *Low reynolds number turbine blade cascade calculations.* (1996).

[98] A. Khalatov, N. Panchenko, I. Borisov, and V. Severina, *Numerical simulation of film cooling with a coolant supplied through holes in a trench,* Journal of Engineering Physics and Thermophysics **90**, 637 (2017).

[99] J. T. DeMasi, K. D. Sheffler, and M. Ortiz, *Thermal barrier coating life prediction model*, Contractor Report CR-182230 (NASA, 1989).

[100] E. Greitzer, *N+3 aircraft concept designs and trade studies, final report,* (2010).

[101] I. Boersma, *Weight estimation of gas turbine engines,* (2022).

[102] A. S. Agazhanov, D. A. Samoshkin, and Y. M. Kozlovskii, *Thermophysical properties of inconel 718 alloy,* Journal of Physics: Conference Series **1382**, 012175 (2019).

[103] J. Díaz-Álvarez, A. Tapetado, C. Vázquez, and H. Miguélez, *Temperature measurement and numerical prediction in machining inconel 718,* Sensors **17**, 1531 (2017).

[104] Q. Liu, S. Huang, and A. He, *Composite ceramics thermal barrier coatings of yttria stabilized zirconia for aero-engines,* Journal of Materials Science Technology **35**, 2814 (2019), sI: Ultra High Temperature Ceramic Matrix Composites Design and Application.

[105] S. Raghavan, M. J. Mayo, H. Wang, R. B. Dinwiddie, and W. D. Porter, *The effect of grain size, porosity and yttria content on the thermal conductivity of nanocrystalline zirconia,* Scripta Materialia **39** (1998), 10.1016/S1359-6462(98)00290-5.

[106] J. Wu, X. Wei, N. Padture, P. Klemens, M. Gell, E. Garcia, P. Miranzo, and M. Osendi, *Low-thermal-conductivity rare-earth zirconates for potential thermal-barrier-coating applications,* Journal of the American Ceramic Society **85**, 3031 (2004).

[107] G. Azad, J.-C. Han, S. Teng, and R. Boyle, *Heat transfer and pressure distributions on a gas turbine blade tip,* Journal of Turbomachinery-transactions of The Asme - J TURBOMACH-T ASME **122** (2000), 10.1115/1.1308567.

[108] V. K. Garg, *Heat transfer on a film-cooled rotating blade using different turbulence models,* International Journal of Heat and Mass Transfer **42**, 789 (1999).

[109] B. Gleeson, *Thermal barrier coatings for aeroengine applications,* Journal of Propulsion and Power **22**, 375 (2006).

[110] B. Zhou, T. Tian, G. Zhu, J. Zhao, and D. Liu, *An ultrasonic testing method for wall thickness of turbine blades,* Measurement **198**, 111357 (2022).

[111] M. Goldammer and D. Heinrich, *Active thermography for dimensional measurements on gas turbine components,* in *9th European Conference on NDT* (Berlin, Germany, 2006).

[112] K. Wiens, *Airfoil thickness as a life limiting factor of gas turbine blades,* in *Proceedings of the H Symposium of the Industrial Application of Gas Turbines Committee* (Banff, Alberta, Canada, 2024).

[113] S. Stecura, *Optimization of the NiCrAl-Y/ZrO2-Y2O3 Thermal Barrier System,* Technical Memorandum 86905 (NASA, 1985).

[114] M. A. Engines, *Water-enhanced turbofan,* (2024).

A

XDSM - ADAPTED YOUNG AND WILCOX COOLING MODEL

B

ENTROPY GENERATION TERMS AND COOLING PARAMETER
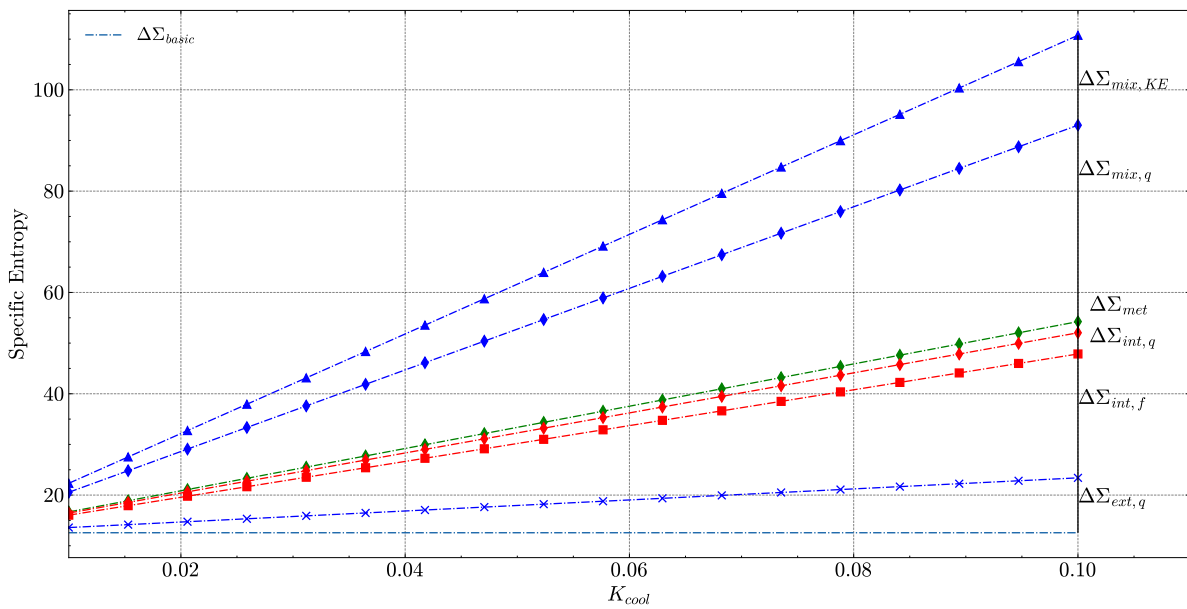
Figure B.1: Variation in loss terms with variation in cooling parameter K_{cool}, loss terms represented by areas between lines.
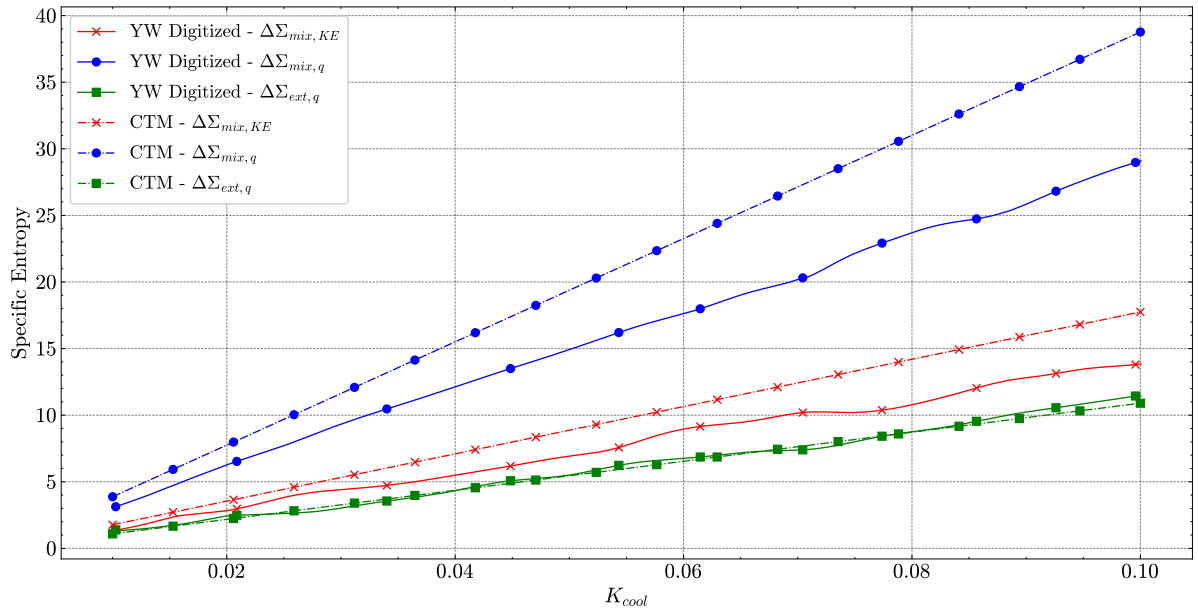
Figure B.2: Variation in external loss terms with variation in cooling parameter K_{cool}
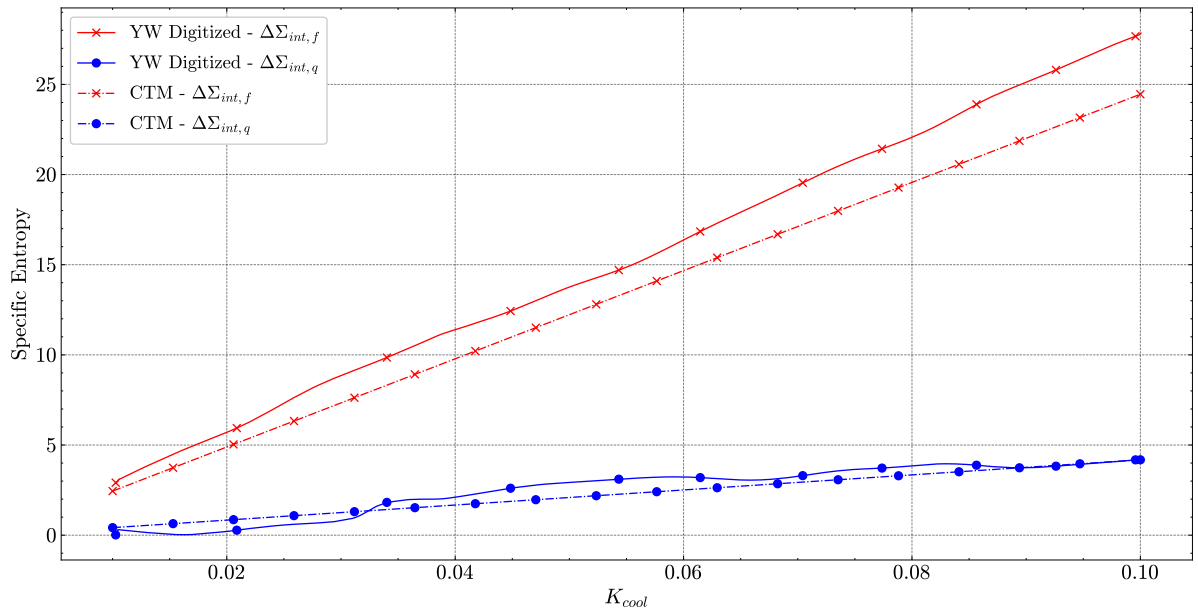
Figure B.3: Variation in internal loss terms with variation in cooling parameter K_{cool}

C

DERIVATIVE TERMS

Derivative	Value at Tg = 1500 K	Value at Tg = 1700 K	Value at Tg = 1900 K	Value at Tg = 2100 K
$\dfrac{\partial}{\partial T_{0g}}$	0.00025	0.00032	0.00043	0.00061
$\dfrac{\partial}{\partial T_{0c,i}}$	0.0005	0.00095	0.00168	0.00295
$\dfrac{\partial}{\partial T_m}$	-0.00075	-0.00127	-0.00212	-0.00357
$\dfrac{\partial}{\partial \epsilon_f}$	-0.24254	-0.43944	-0.7589	-1.31055
$\dfrac{\partial}{\partial \eta_{c,int}}$	-0.1053	-0.20523	-0.33683	-0.51802
$\dfrac{\partial}{\partial Bi_m}$	0.06933	0.23786	0.61245	1.41208
$\dfrac{\partial}{\partial Bi_{tbc}}$	-0.08743	-0.17495	-0.31797	-0.5665

D

UNCOOLED STAGE MODEL - RELATIVE DIFFERENCE
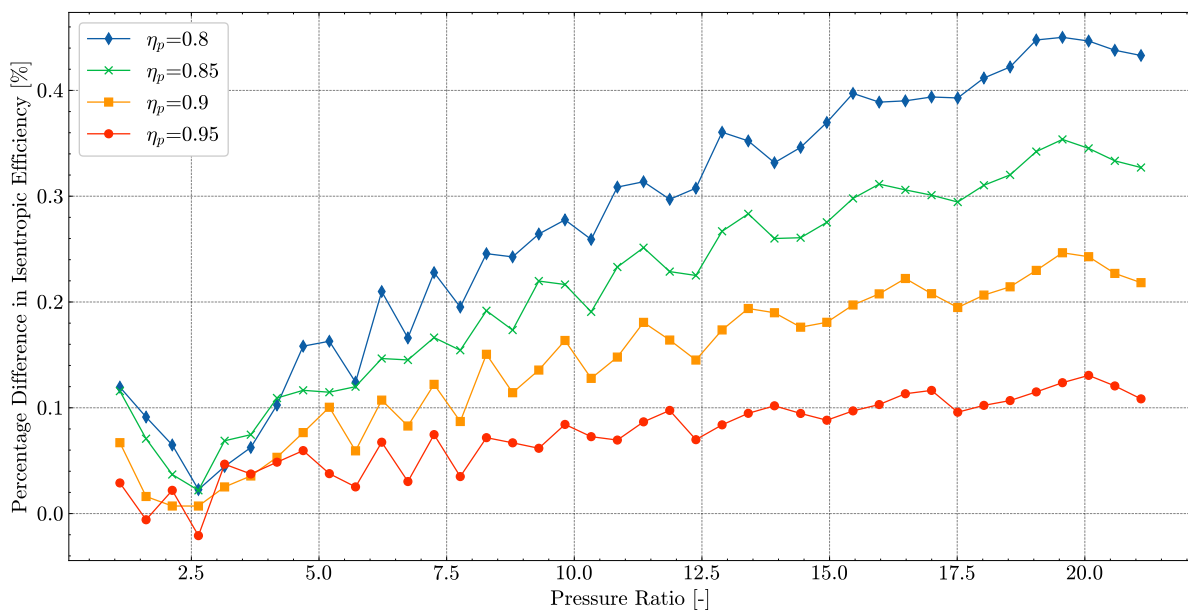
Figure D.1: Variation in relative error between uncooled stage model and theoretical isentropic efficiency calculations.